University of Wollongong

Research Online

2018

Electroactive Fibre Sensor Systems for Fluidics

Syamak Farajikhah
University of Wollongong

Follow this and additional works at: https://ro.uow.edu.au/theses1

Recommended Citation

Electroactive Fibre Sensor Systems for Fluidics

Syamak Farajikhah

Supervisors:

Professor Peter C Innis
Professor Brett Paull
Professor Gordon G Wallace

This thesis is presented as part of the requirement for the conferral of the degree:

Doctor of Philosophy

The University of Wollongong
School of Chemistry

March 2018

Abstract

Due to an increasing demand for development of cost-effective portable microfluidics using textile substrates, a foundation study on the effect of fibre surface chemistry on the performance of textiles was undertaken to elucidate its applicability to textile-based microfluidics (Chapter 3). Composite fibres consisting of low-density polyethylene (LDPE) fibres with liquid crystalline graphene oxide (LCGO) fillers, at a range of loadings, were successfully prepared by a melt spinning process and then incorporated in parallel with commercial polyester yarns (PET), via a tubular knitting process, to produce 3D textile-based microfluidic structures. It was shown that the LCGO filler increased the surface polarity of fibres, as a result of accumulation of oxygen on the polymer surface, and the increase in O/C ratio amplified the surface and inter-fibre capillary fluid driving force in textile structure. Fluid was shown to move up to 6x faster in 3D knitted structures comprised of 5w/w% LCGO/LDPE fibre compared to the knitted structure without any composite fibre. It was demonstrated that the ion rejection and/or absorption phenomenon which occur between fluid ions and fibre surface functional groups played the most important role in determination of fluid flow rate. The flow rate achievable was found to be proportional to the LCGO loading, providing the potential to control flow through fibre composition. Significantly, using this approach fluid pumping of fluid against a gravity feed head height (anti-gravitational) was observed as a consequence of the LCGO filler interactions at the surface of the LDPE/LCGO composite fibres.

Recently, electric fields have been used to move or separate analytes in textile-based microfluidics to achieve a precise control over the fluid flow. However, applying electric fields to move or separate solutes within fluids typically results in Joule-heating which adversely affects the efficiency of the separations. In this thesis, the idea of preparing

thermally conducting fibres and assembling them into 3D textile structures to facilitate dissipating the Joule-heating was investigated (Chapter 4) using LDPE/LCGO composite fibres, where LCGO was partially reduced to impart improved thermal conductivity. LCGO/LDPE composite fibres were successfully prepared and incorporated into a 3D PET knitted structures and their capability to dissipate the Joule-heating in electrofluidic experiments probed. Monitoring the temperature change during electrofluidic experiments showed that incorporation of reduced LCGO/LDPE fibres into 3D knitted structures resulted in lower temperature rise during the experiments and more importantly, final temperature decreased by an increase in the LCGO loading. However, loading more than 5 w/w% LCGO into LDPE fibres, utilising a powder coating and melt spinning approach, proved to be impractical due to agglomeration of LCGO within composite fibres resulting in poor mechanical properties and therefore limited knittability.

To eliminate the issue of poor filler distribution, a solvent-based wet-spinning technique was adopted (Chapter 5). A solvent processable non cross-linked biocompatible grade polyurethane (PU) elastomer was filled with LCGO to produce LCGO/PU fibres. These fibres were successfully incorporated into 3D knitted structures in parallel to the PET yarns and then chemically reduced to improve thermal conductivity. The ability of the reduced LCGO/PU composite fibres as heat dissipators was shown to be limited by their electrical conductivity. Fibres were shown to become effective in Joule-heating dissipation at the point that they became electrically conductive resulting in potential short-circuits which should be avoided in high voltage electrofluidic experiments. As a consequence, boron nitride nanopowder (BNNP) filler was chosen to make BNNP/PU composite fibres as it was thermally conducting but electrically insulating (band gap of ~ 5 eV). It was shown that incorporating BNNP/PU composite fibres into 3D textile structures effectively dissipated the heat generated by Joule-heating and kept the textile structure at low temperature during

electrofluidic experiments. This novel idea of utilizing thermally conducting fibres into textile-based microfluidics could be an advantageous for fibre based capillary electrophoresis studies specifically when proteins, living cells and thermosensitive analytes are being used.

Textile substrates have been widely used to make wearable electrochemical sensors. Therefore, as a proof-of-concept study, two different 3D textile designs (utilizing knitting and braiding techniques) with integrated electrodes as potential wearable electrochemical sensors were investigated (Chapter 6). The electrochemical behaviour of stainless steel (SS) filament working electrodes were shown to be far from ideal (or reversible). These filaments were surface modificated by the electrodeposition of polypyrrole and gold nanoparticles to give improved electrode surface responses. These modified electrodes were successfully incorporated into 3D braided structures, whereby all electrodes were not in direct electrical contact, consisting of two parallel SS (counter and working) electrodes with the addition of a silver-coated nylon yarn as pseudo reference electrode. This braided 3 electrode system was shown to be a functional 3D textile platform capable of electrochemical detection in a similar manner as a classical 3-electrode electrochemical system. In an alternative approach, a 3D knitted structure with 3 separate conductive strips, i.e. two SS yarn and a silver-plated nylon in the middle separated by insulating yarns, was successfully created to perform amperometric detection under a gravity assisted electrolyte flow system.

In summary, this thesis demonstrates the feasibility of the approaches investigated and their incorporation into textile structures. Significantly the approaches shown are relatively simple to fabricate, cheap, flexible and easily incorporated into textile systems to provide real time sensing and monitoring, fluid transportation and heat dissipation, all of which are critical for the implementation of textiles into active and functional devices.

Acknowledgments

I would like to express my sincere gratitude to my parents, Mahmoud and Shahnaz, and my sisters, Sara and Simin, for their endless love and support throughout my life. Finally, very special thanks to my best friend, my partner and the love of my life, Mediya, for her endless patience and unconditional love without her doing this PhD wouldn't be possible. Thanks for being such an amazing wife, supportive to all my decisions and bearing with through thick and thin.

Certification

I, Syamak Farajikhah, declare that this thesis submitted in fulfilment of the requirements for the conferral of the degree Doctor of Philosophy, from the University of Wollongong, is wholly my own work unless otherwise referenced or acknowledged. This document has not been submitted for qualifications at any other academic institution.

_____

Syamak Farajikhah

28$^{\text{th}}$ March 2018

List of Names or Abbreviations

WHO	World Health Organisation
UV	ultra violet
IR	infrared
CV	cyclic voltammetry
µPADs	paper-based microfluidic devices
µTADs	textile-based microfluidic devices
XPS	x-ray photoelectron spectroscopy
SERS	surface-enhanced raman scattering
µFIA	microflow injection analysis
CZE	capillary zone electrophoresis
ITP	isotachophoresis
CEC	capillary electrochromotography
BUN	blood urea nitrogen
MES	2-(n-morpholino) ethanesulfonic acid
Tris	tris(hydroxymethyl)aminomethane
CHES	n-cyclohexyl-2-aminoethanesulfonic acid
GO	graphene oxide
LCGO	liquid-crystalline graphene oxide
BN	boron nitride
BNNP	boron nitride nanopowder
hBN	hexagonal boron nitride
cBN	cubic boron nitride
AuNp	gold nanoparticle
AgNP	silver nanoparticle
PPy	polypyrrole
GOx	glucose oxidase
LDPE	low-density polyethylene
PU	polyurethane
PET	polyester
D.I. water	deionized water
PBS	phosphate buffered saline
Ag/AgCl	silver/silver chloride reference electrode
v/v	volume/volume
wt.%	weight percent
w/w%.	weight/weight percent
DC	direct current
Pt	platinum
SS	stainless steel
λ	thermal conductivity
Cp	specific heat capacity
P	density
PCR	polymerase chain reactions
POC	point-of-care
TGA	thermogravimetric analysis
DSC	dynamic scanning calorimetry
SEM	scanning electron microscope
C^4D	capacitively coupled contactless conductivity detection
UTS	ultimate tensile strength
E	young's modulus
η	thermal conductivity enhancement

Table of contents

List of Figures

List of Tables

Chapter 1:

Introduction

1.1. Introduction; An urgent need for cost-effective diagnostic devices

Rapid spread of serious illnesses such as cancers, immune and infectious disease around the world threatens the lives of millions of people specifically those who are living in remote and developing regions every year. Therefore, development of affordable, rapid, portable and accurate diagnostic devices is a World Health Organisation (WHO) prioritised global challenge and has attracted a great deal of attention among scientists. Early detection along with accurate diagnostics plays a vital role in increasing survivability rates, improving treatment outcomes, reducing risk factors and ultimately minimising financial and spiritual impacts[1–7]. Despite the outstanding advances in the field of public health and diagnostics in recent decades, developed and developing countries cannot benefit equally from these developments. Poverty, insufficient infrastructure and lack of trained personnel often hinder access to new diagnostic technologies for people living in developing countries and remote regions of the world[6,8]. To tackle this issue, development of diagnostic devices that are affordable, sensitive, specific, user-friendly, rapid and robust, equipment free and deliverable to end user called ASSURED has been planned out by World Health Organization[6,8–10]. The emergence of microfluidic technologies with their outstanding features such as ability to process microscale liquids, being rapid, simple and cost-effective, has a great impact on diagnostics and public health. Nowadays, microfluidics' contribution to rapid development of public health and diagnostic devices is undeniable, because of their so called characteristics[2,7,8,11].

1.2. Portable cost-effective microfluidic devices

There is an ever growing demand for integrated diagnostic devices, also known as lab-on-a-chip devices. Portable and cost effective microfluidic devices have attracted a lot of

attention because of their ability to eliminate large expensive laboratory equipment and provide in-situ, at-site and 'at-person' results[12]. Microfluidic technology has many potential applications in the development of diagnostic devices and has provided key components essential for development of lab-on-a-chip devices comprised of micro channels, micromixers, micropumps, etc. Microfluidics makes it possible to integrate sensors into lab-on-a-chip devices offering the potential to provide real-time data on the interaction and exposure of the wearer to his/her environment, in addition to significant opportunities for personal health monitoring. Although, in recent decades, public health has been greatly improved due to the advances in detection techniques, many of these technologies are unaffordable for developing countries due to the poverty and lack of sufficient infrastructure [6,8]. As a result of this increasing demand and the prioritized development of ASSURED diagnostic devices by WHO, new materials have been considered for development of healthcare and environmental monitoring microfluidic devices which are inexpensive yet accurate. Recently, paper and textiles (threads and fabrics) have been demonstrated to have potential in providing desirable characteristics to be utilised in development of affordable healthcare and environmental monitoring microfluidic devices. Consequently, those materials have been extensively used in the development of minimally invasive, accurate, durable, user-friendly, and low cost diagnostic platforms[13–22].

1.2.1. Paper-based microfluidic devices (µPADs)

Paper has been used as a substrate in analytical chemistries since early 1800s. Recently, it has been widely used in expansion of microfluidic analytical devices owing to its unique characteristics such as power-free fluid transport via capillary action[6,23–25] as well as being highly abundant, flexible, cheap, disposable, and ease for surface chemistry functionalisation[23,24,26]. µPADs can be readily patterned and surface functionalised using

inkjet, wax or screen printing making them affordable, equipment free and readable with naked eye. They are stable in many different environments as well as capability of analysing multiple different analytes in a single device [6,10,24,26]. Essential to any µPAD is the need to define hydrophilic and hydrophobic regions on the paper substrate to create channels that may rely on delicate and time consuming processes[13–15,20,21]. Low mechanical strength when wet with solution and low efficiency of sample delivery due to leakage of the samples out of the defined surface channels can be considered as the other shortcomings of using paper as a substrate for making microfluidic devices[27,28]. Due to such limitations, other abundant materials, such as threads and textiles, have considered as a substrates in microfluidic devices.

1.2.2. Textile-based microfluidic devices (µTADs)

Recently, two different research groups, i.e. Li et al. and Reches et al, discovered a similar concept to µPAD based on threads. They found that void space between fibres in a thread or textile can provide capillary channels for fluid movement and as a result they have been investigated as an alternative to µPADs paper substrates in diagnostic devices[13,14]. Although threads and papers have some features in common such as being highly abundant, flexible, cheap, disposable, ease for surface chemistry functionalisation, and independence of external power for fluid movement (due to capillary forces), threads also benefit from some outstanding characteristics such as high mechanical strength when wet and reusability. Also, threads does not need hydrophobic barriers, unlike µPADs, and can be easily converted into 3D structures or be integrated into wearable materials by traditional techniques such as knitting, weaving or sewing. Having these unique features and advantages over paper, make textiles an excellent candidate for microfluidic textile analytical devices (µTAD) [13, 14, 17, 27–29]. These very old yet newly discovered materials in

microfluidics technology have attracted a lot of attention in this field with over 60 publications studying the effect of different yarns and fabrics to form efficient µTADs since the first demonstration of this approach in 2010.

1.3. Wicking properties and surface chemistry in µTADs

Capillary forces generated in the void spaces between fibres drive fluid flow and are the reason for wicking action in threads and textiles. Following Washburn's equation, wetted distance (L) is proportional to the square root function of time (t):

$$L = \sqrt{\frac{Dt\gamma\cos\theta}{4\mu}} \tag{1}$$

Where D is the effective capillary diameter or pore diameter, γ is the interfacial or surface tension, θ is the contact angle between the liquid and the surface, and μ is the viscosity. However, wicking may also be affected by parameters such as evaporation, swelling, gravitational forces or internal pressure variations[29].

Due to the complexity in the internal structures of textiles and threads, along with different surface finishing of the materials being used contact angle measurements on fibres and fabrics, in formulating wicking behaviour in textile materials is complicated. Long fatty acid chains found on natural cotton fibres and contamination on the surface of synthetic threads, such as polyester and nylon, interfere with wicking in threads and lead to non-Washburn behaviour. Removal of these waxes and contamination by surface modifications will enhance the wettability of yarns and increase in wicking by capillary action[13,14,30–33]. Surface modification will change surface chemistry of both synthetic and natural fibres which can be responsible for improvement of their wicking properties. Natural fibres such as cotton, silk and wool are usually covered with a wax that contains fatty acid chains which may hinder or even stop liquid movement along threads. Two common methods that have been used for surface treatment surface was removal of natural fibres include plasma

treatment and scouring in NaOH or Na_2CO_3. Many researchers have reported using plasma treatment to enhance wicking properties of cotton fibres[13,14,33–39] where it oxidizes the cotton surface and removes the wax. X-ray photoelectron spectroscopy (XPS) data shows an increase in concentration of oxygen, due to the generation of O-C-O, C=O, O-C=O and C-O, at the cotton surface, therefore, increase in surface polarity that leads to improvement of wicking properties in cotton fibres[14,33,38,39]. Jeon et al. have also reported the use of plasma treatment to increase the wettability of another natural fibre, i.e. wool fibres, by degumming fatty acid on its surface[40]. They found that wool's flowrate depends on the gas (O_2, N_2 and Ar gases) that the plasma treatment was performed, enabling then flow control of micro-mixing devices.

Another widely reported method for increasing the wettability of natural fibres is boiling[15] or scouring in NaOH or Na_2CO_3[30,41–51]. These chemical are reported to attack aliphatic chains of the wax on the surface of cotton fibres, removing the wax and exposing the underlying cellulose structure which has negative charge and abundant hydroxyl (-OH) group functionality. Treatment with NaOH also increases O/C ratio which generally makes the fibre surface more hydrophilic[30,42,45,46,49]. Safavieh et al. visually demonstrated the effect of surface treatment upon the wicking properties of cotton, Figure 1.1A. Also, Jeon et al. showed the effect of different plasma treatments and/or time on the wicking properties of wool fibres, Figure 1.1B.
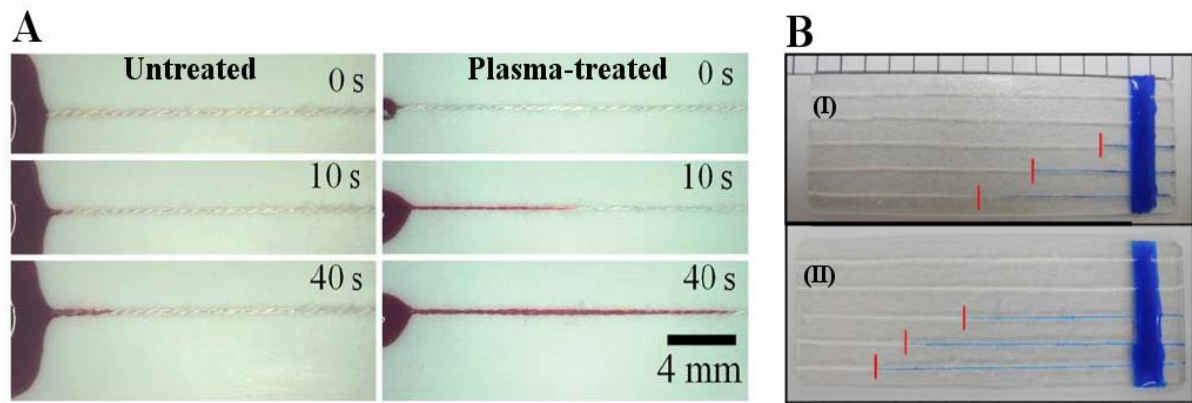
Figure 1.1: Improvement in wicking properties of yarns. (A) Cotton treated with plasma treatment[34] and (B) Wool treated with I. Oxygen and II. Argon plasma. Pristine wool fiber and fibers treated for 0, 15, 30, 45 and 60 min, respectively from upside[40]

Reports on using plasma surface treatment to increase surface wettability and improve liquid movement of thread-based microfluidic devices are not limited to natural fibres. As this treatment increases surface polarity and removes surface contamination on the thread, a large number of research groups used the same method on µTADs made from polyester threads. [13,19,32,52–54]. Furthermore, as demonstrated by Reches et al. plasma treatment significantly increases the wicking rate of different threads. Table 1.1 summarizes these findings[13].

Table 1.1: Increase in wicking rate after plasma treatment for different types of threads[13]

Thread	Wicking rate before treatment (cm s⁻¹)	Wicking rate after treatment (cm s⁻¹)
Rayon	0.29 ± 0.06	1.01 ± 0.69
Hemp	0.02 ± 0.01	0.55 ± 0.55
Nylon	0.03 ± 0.00	0.04 ± 0.01
Cotton	0.23 ± 0.04	1.89 ± 0.52
Polyester	0.13 ± 0.03	1.98 ± 0.79
Wool	Did not wick	2.20 ± 0.40
50% Cotton, 50% Acrylic	Did not wick	2.11 ± 0.30
Acrylic	Did not wick	1.91 ± 0.42
Natural silk	Did not wick	0.60 ± 0.21

1.4. Fabricating µTADs using threads and fabrics

Threads can be used to perform a variety of analytical experiments ranging from simple colourimetric detection to more complex procedures such as isolation and separation of biomolecules and bacteria cells. Different approaches have been reported to develop µTADs using threads. One of the simplest approaches is utilizing hydrophilic threads to provide predefined paths for liquid movement. Two different research groups demonstrated the capability of using threads to make microfluidic devices. They have shown twisting threads can be used for fluid mixing (Figure 1.2A)[14]. Reches et al. also demonstrated different designs for incorporation of hydrophilic threads into a hydrophobic substrate to develop µTADs, such as sewing cotton threads through a hydrophobic substrate to incorporate an assayable zone into a bandage (Figure 1.2B)[13]. Sewing hydrophilic threads into other substrates to create a 3D µTADs has been also reported[14,41]. Some research groups have focused on demonstration of more complex functionalities feasible using threads. Using different knots with different topologies to provide control over mixing and splitting of the fluid in µTADs have been demonstrated by Safavieh et al.[34]. In other work, Ballerini et al. demonstrated different mechanisms of flow control ranging from simple binary on/off style switches, to micro-selectors, and micro-mixers on polyester threads as potential functions that can be utilized for designing complex yet low-cost µTADs[39]. Surface acoustic waves were employed by Ramesan and co-workers to demonstrate feasibility of externally driving fluid flow in a network of threads. This method was also utilized to perform the serial dilution in a thread network embedded in a transparent hydrogel that mimics in vivo tissue microenvironment (Figure 1.2C)[55]. Threads have also been used as reactors for synthesising ferric hydroxide and 2,4-dichloro-N-(2-morpholinoethyl) benzamide in addition to being used have also synthesised on thread reactors and as microchannel for chemical sensing[56].

Recently, using integrated surface functionalized threads capable of sensing electrochemically into µTAD platforms to measure both physical (strain and temperature), and chemical (pH and glucose) properties for in vivo and in vitro studies have also reported by Mostafalu and co-authors[57]. Haemoglobin detection on threads with high sensitivity and low levels of nonspecific adsorption utilising functionalized filaments of cellulose nanofibrils conjugated with antihuman haemoglobin (anti-Hb) antibodies has also been reported[58]. Cabot et al. recently reported the use of commercial threads and novel 3D printed supporting platform to create low-cost µTADs. The proposed device has been demonstrated to be able to facilitate controlled protein delivery, electrophoresis isolation and separation of biomolecules and bacteria cells[59]. µTADs equipped with electrochemical[19,21,32,60–64] and optical[36,51,65–69] detection devices have also been reported.
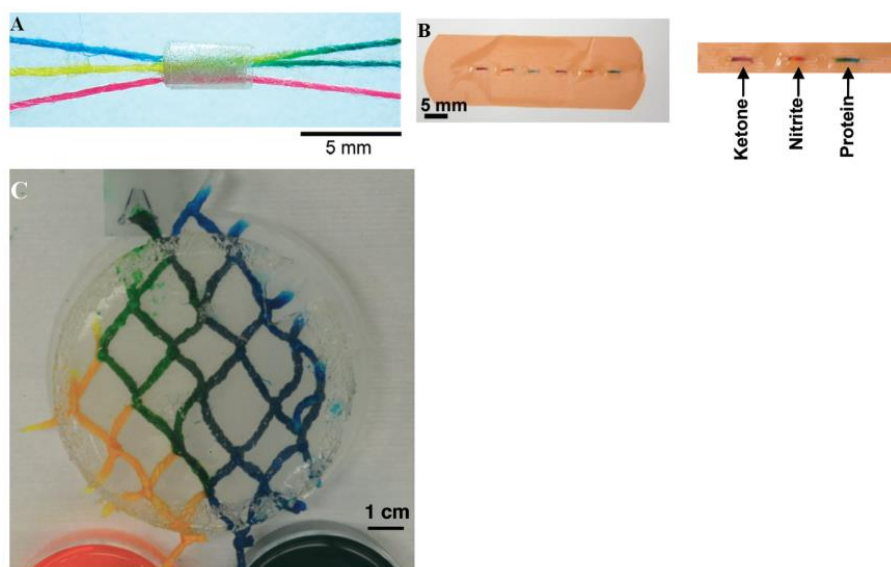
Figure 1.2: Demonstration of some reported thread and cloth-based microfluidic devices. (A) Fluid mixing by twisting threads. The top and the middle threads that transport cyan and yellow liquids are twisted and sleeved inside a heat shrink tube; the bottom thread that transports magenta liquid is not twisted with the other two threads and passes through the mixing zone from outside of the heat shrink tube[14], (B) Colorimetric assay performed with sewn array design[13]. (C) Acoustically-driven fluid into a thread network embedded in transparent hydrogel[55].

Although threads can be used solely to develop µTADs, using hydrophilic/hydrophobic contrast in fabrics to provide a path for fluid movement is an alternate method for

fabricating μTADs. It has been demonstrated that flow in fabric is controllable by systematic change in the placement of hydrophilic and hydrophobic threads in a fabric design[70].

Using hydrophilic and hydrophobic types of silk threads in a fabric to make a μTAD (Figure 1.3A) by Bhandari et al. was one of the first to report on using fabrics for immunoassay[15]. Another report on using hydrophilic/hydrophobic contrast on fabric was using polypropylene (hydrophobic) and hydrophilic poly(ethylene terephthalate) yarns in a fabric to develop pH-sensitive microfluidic device reported by Vatansever et al[71].

Another method to a define path for liquid movement in textiles can be achieved by using patterning techniques to create hydrophobic zones on hydrophilic textile structure, such as cotton fabrics. These methods have been widely used to develop 2D and 3D μTADs to perform colorimetric bioassays for qualitative measurements or using in combination with electrochemical detections[30,42,43,45,72–74]. Liu et al. utilized wax and carbon ink screen printings on hydrophilic cotton fabrics to develop μTADs used to perform wireless electrochemiluminescence. Proposed devices combine inherent features of μTADs with sensitivity and selectivity[75,76]. The photolithography technique has also been utilized with different research groups to define hydrophobic barriers on hydrophilic textile structures to develop μTADs. Baysal and co-workers used this technique to define physical barriers using a hydrophobic photo-resist polymer on a hydrophilic non-woven fabric as a base structure. They successfully developed a flexible and disposable μTADs with proposed applications in rapid detection of various kinds of important analytes or monitoring an athlete's physical status during exercise[53,77]. In another work, the same patterning technique was employed to developed a μTAD capable of performing colorimetric assays of glucose and protein in artificial urine samples[49].

Curto et al. demonstrated a wearable, flexible and electronic-free μTADs for real-time

monitoring of sweat pH (Figure 1.3B)[78]. Development of fabric-based electrophoretic platforms which are aimed for protein separation have been reported utilizing metallic electrodes and metal-coated fibres and incorporating them into textile substrates[20]. Novel low-cost µTADs for monitoring biomarkers or environmental pollutants have been introduced by Robinson et al. These devices have been made by treating fabrics with silver nanoparticles (AgNPs) to develop low cost Surface-enhanced Raman scattering (SERS) wearable sensors[79]. Recently, a non-invasive method for determining glucose level has been proposed by Marcolino Junior research group. They have created an integrated µTAD by combining a simple poly(toluidine blue O) - glucose oxidase(GOx) amperometric biosensor and low cost cotton threads[80] (Figure 1.3C). Microflow injection analysis (µFIA) was then implemented on that device to measure glucose level in human tears. Phenol detection in tap water using electrochemical biosensors combined with threads has been also reported by this research group[81].
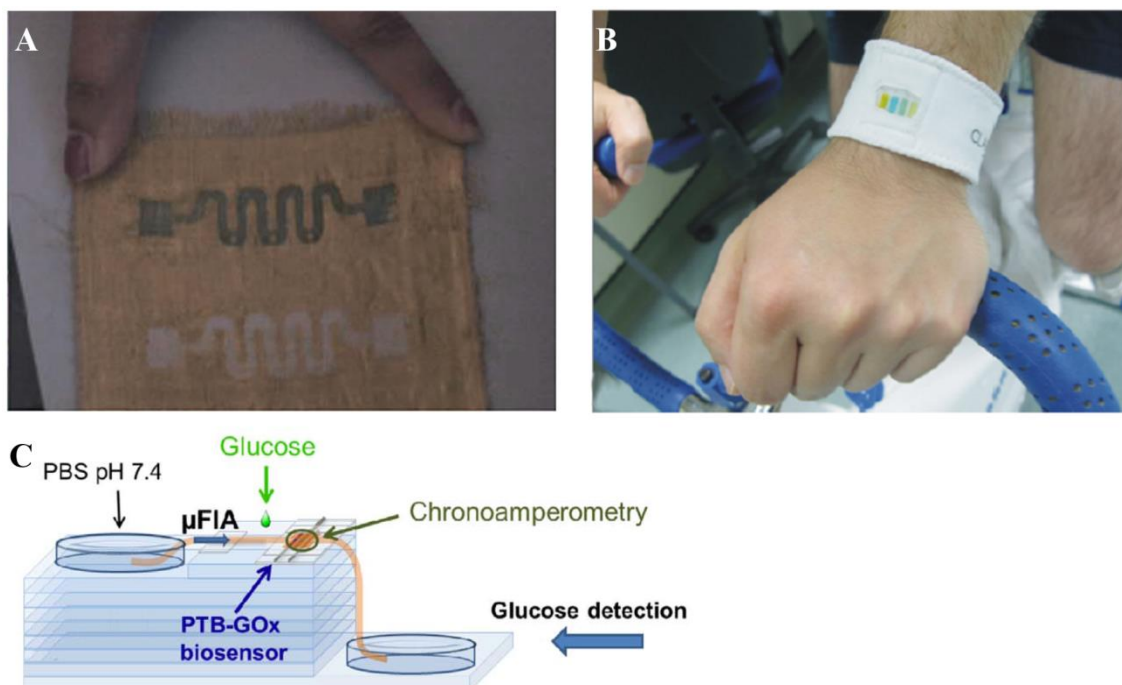
Figure 1.3: (A) A fabric chip comprising hydrophilic (white) and hydrophobic (gold) silk fibres, a green die was deposited and spread on one of hydrophilic parts[15] , (B) A wearable micro-fluidic system for monitoring sweat pH[78], (C) Glucose determination using µFIA on an integrated biosensor and µTAD[80]

1.5.   Electrophoretic separation on µTADs

Although textile-based microfluidics is still in its infancy, it provides significant opportunities for the development of portable analytical devices that meet the WHO defined ASSURED criteria. To-date most research groups have explored simple fluid wicking in this area and the great potential of using precise controlled fluid movement in µTADs utilizing different methods such as controlled electrophoretic systems has been neglected with only a few research groups reporting on these approaches. Textiles benefit from power-free fluid movement because of capillary forces or simple wicking. However, this movement is not controllable and accurate devices have not been developed by purely relying upon wicking methods. Therefore, creating novel controllable devices with precise fluid control greatly depends on employing a driving force other than simple capillary action or 'wicking'. Electric fields have shown great potential for movement, pre-concentration and separation of solutes within fluids. Some researchers have utilized electrophoresis to achieve controllable fluid and solute movement on µTADs. Employing electrophoresis on textiles, controlled electroosmotic force and solute electroosmotic migration may take place within the surface layer of fluid formed on a thread or fabric.

Over past three decades, capillary electrophoresis and specifically three common types of them including capillary zone electrophoresis (CZE), isotachophoresis (ITP) and capillary electrochromotography (CEC) have been widely employed in analytical chemistry as a powerful tool for separation of charged analytes which includes inorganic and organic ions as well as charged biomolecules of various sizes, up to and including proteins. These above-mentioned electrophoresis based separation techniques have been greatly popular in analytical chemistry due to their outstanding selectivity (compared to what is feasible using current standard liquid chromatographic methods) along with their very high efficiency. However, they also have some inherent limitations as a consequence of the small inner

diameters of the capillaries used which results in very limited sample loading capacity. A fundamental disadvantage of capillary-based separation technique is that it is impractical to access to the analyte within the capillary during the actual separation process. Typically, detection of the limited amounts of separated analytes typically occurs as they finally elute from the column, resulting in difficulties in the post-capillary analytical processes using these techniques[82,83]. Interestingly, utilizing close environmental control, similar separations achievable in enclosed capillary systems may be achieved on the surface of threads and fabrics. Significantly, using threads or fabrics instead of conventional closed capillaries can eliminate most of the analyte accessibility issues as they are accessible everywhere on textiles with tunable loading capacity depending upon the textile structure. Although using textile substrates can eliminate the intrinsic issues associated with closed capillaries, it should be noted that volumetric Joule heating phenomenon, due to current passing the fluid, could be a greater challenge in textile-based microfluidics compared to closed capillary tubes which accommodate smaller volumes of buffer solution. µTADs utilising these approaches are discussed below.

Electrochemical detection of inorganic ion samples[32], e.g. Cl, Br and I, blood urea nitrogen (BUN) in whole blood[19] and on-site detection of BUN and glucose in serum[21] (Figure 1.4A) by incorporating an enzyme-doped thread into a µTAD using polyester thread has been reported by Lin research group. Buffer solution of 1.0 mM of MES (2-(N-morpholino) ethanesulfonic acid) pH = 5 was used and 300-500 V cm^{-1} potential was applied to perform separations and detections. Narahari et al. demonstrated a scalable µTAD consisting of cotton fabric to hold large volumes of aqueous buffer and nylon- or polyester-based fabric as a separation substrate. The proposed µTAD eliminated the loading capacity issue in conventional capillary electrophoretic systems. Finally, as shown in Figure 1.4B, the separation of human albumin and human IgG using glycine−NaOH pH

8.58 as buffer while applying a 35 V cm^{-1} potential was demonstrated on proposed device[20]. Recently, Cabot et al. demonstrated the use electrophoresis applying 200 V cm^{-1} on Nylon thread substrates pre-concentrated with and connected to reservoirs containing 2.5 mM TRIS/CHES buffer solution of pH 8.5 to perform selective movement of proteins in branching structures and fluorescent dye separations[59]. They also showed the feasibility of physically concentrating fluorescent dyes on textiles. Different types of yarns, i.e. nylon, silk and cotton were linked by simple knotting and fluorescent dyes were physically concentrated in different locations as a result of chromatographic interaction. They proposed a practical potential diagnostic platform for urinary tract infection for this technique by trapping and detecting bacteria cells from urine by demonstrating cell survival after the on-fibre electrophoretic concentration (Figure 1.4C).
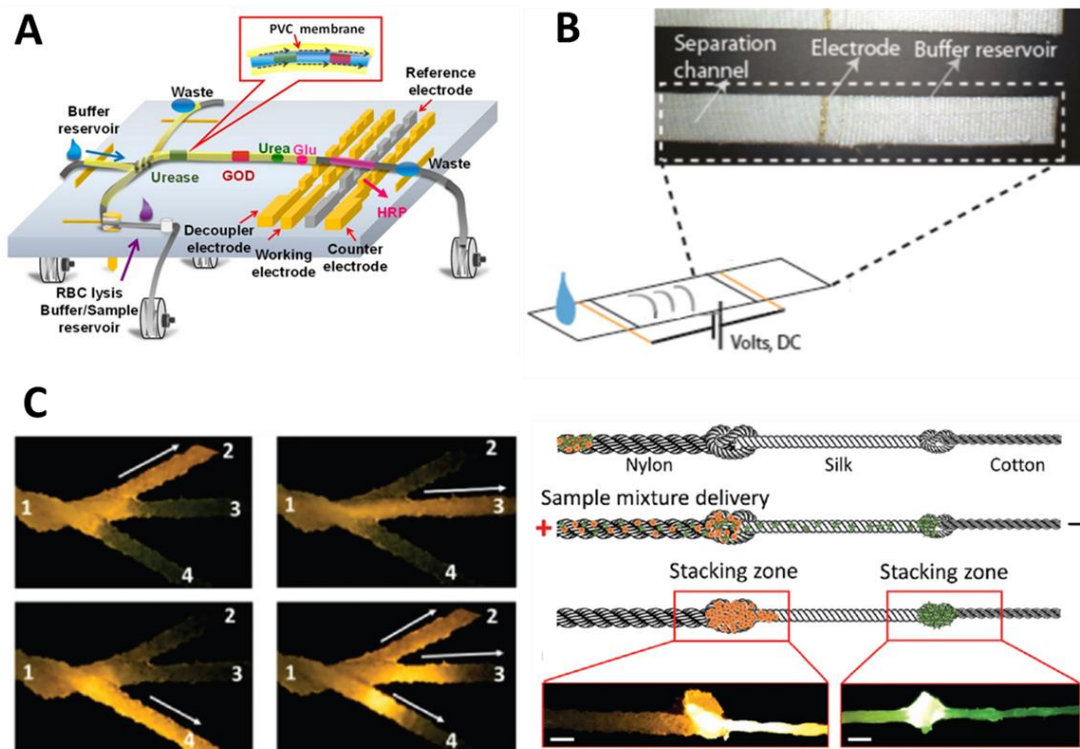
Figure 1.4: Utilising electrophoresis on µTAD. (A) Enzyme-doped thread-based microfluidic system for electrophoretic separation and detection of blood urea nitrogen and glucose in serum [19]. (B) Scalable fabric-based platform for a separation of proteins[20]. (C) Selective delivery of proteins in branching structures using electrophoresis, and the use of knotting to link different thread materials to trap bacteria for urinary tract infection[59].

1.6. Reported applications for µTADs to date

There are some inherent differences in using threads and fabrics as a platform for microfluidics. Threads can accommodate much lower solutions compare to fabrics, also, the flow within a thread is confined to one direction, while in woven fabric-based microfluidic devices is two dimensional. Finally, fabric-based platforms provide a greater sampling zone, allowing also higher area for detection zones. Despite these differences, a wide range of applications such as bacteria isolation and quantification, chemotaxis studies for cell culture systems, immunoassay, blood typing, chemical synthesis, bioanalysis, and the determination of nucleic acids, protein, glucose, drugs , small ions and metals has been reported on both thread- and fabric-based structures. Despite the relatively low sensitivity, colourimetric detection featuring simplicity and robustness has been the most popular technique that has been employed on µTADs. To tackle the low sensitivity issue, different methods such as using functionalised thread or nanoparticles, patterned electrodes, electrophoretic separations or other detection systems, e.g. amperometry, electrochemistry, conductivity, SERS, fluorescence or electrochemiluminescence, has been investigated on textile-based microfluidic platforms. Figure 1.5 shows some examples of colorimetric, amperometric, electrochemiluminescence assisted detections as well as DNA detection which have been demonstrated using µTADs.
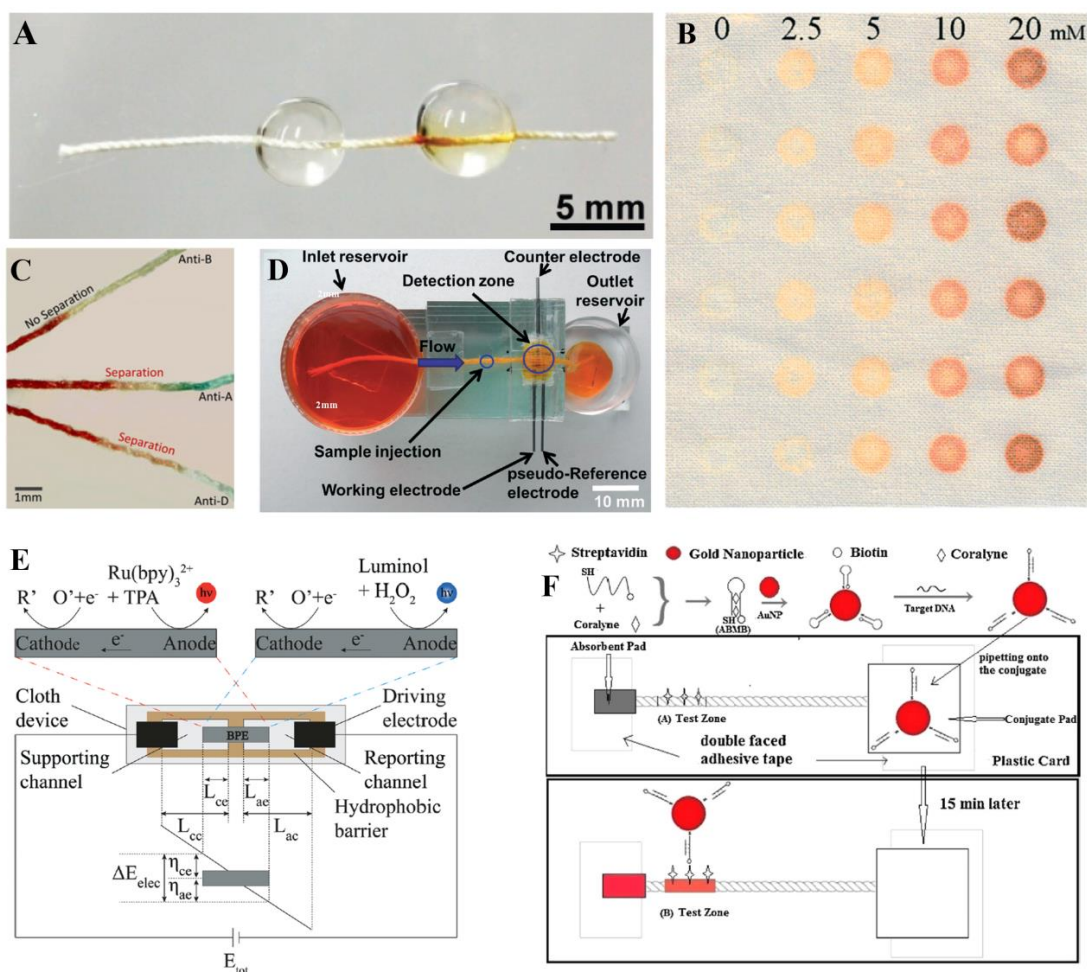
Figure 1.5: (A) Glucose detection in a thread-based microfluidic device, colourless iodide is oxidized to brown iodine on the thread in the presence of glucose[13], (B) Colorimetric detection of glucose with different concentrations[49], (C) A single-step blood grouping test [52], (D) µTAD device for detection of acetaminophen (ACT) and diclofenac (DCF) using multiple pulse amperometry (MPA)[28] (E) Scheme of a µTAD for doing wireless electrochemiluminescence[75] and (F) The principle of cotton thread-based device for DNA detection[44]

As discussed above, threads and textiles have been attracted a lot of attention in the field of microfluidics and diagnostics for development of low-cost portable devices. Different applications ranging from simple fluid wicking properties to complicated diagnostics have been reported using textile platforms. Different fibrous materials, and textile structures, including threads, woven and non-woven fabrics have been used to create µTADs. Moreover, different pre-treatment techniques have been utilised to increase hydrophilicity of or to add functionality to the textile structure. Reported µTAD applications to date organised based on material, textile structure used for the device, and pre-treatment employed are summarised in Table 1.2.

Table 1.2: Applications reported for textile-based microfluidic devices

Material	Textile structure	Pre-treatment	Application
Cotton	Thread	Nil	Simultaneous determination of acetaminophen and diclofenac by exploring of the multiple pulse amperometry detection modes[28]
			Design of the thread-based devices incorporating pins as electrodes[61]
			Amperometric determination of estriol[62]
			Electrochemical detection of naproxen[64]
			Developing a µTAD for wireless elechrochemiluminescese detection of TriPropylamine and H_2O_2[76]
			Tunable acoustically driving fluid in a thread network and a thread network embedded in hydrogel.[55]
		Plasma treatment	Introducing functionalized thread substrates as disposable, low-cost-per-test diagnostics, for routine SERS spectroscopy[36]
			Calorimetrically detecting of NO_2^- to show the potential of producing low-cost portable diagnostics[14]
		Air plasma treatment	Constructing passive microfluidic systems[34]
		Oxygen plasma treatment	A new type of manufacturing process for the development of particle-like arrays for a multiplexed bioassay platform

		using individually functionalized thread strands was introduced[38]
	Oxygen plasma treatment. Fabrication by sequentially passing the core through multiple wells containing conductive inks (silver/silver chloride, carbon nanopowders, carbon nanotubes, polyaniline)	Electrochemical sensing of physical and chemical markers both In vivo and In vitro[57]
	Sodium carbonate treatment	Blood plasma separation[51]
	Nil	Amperometric detection of tear glucose [80]
	Nil	Electrochemical detection of phenol in tap water[81]
Non-woven fabric	Nil	A wearable, electronic-free and flexible microfluidic system based on ionic liquid polymer gels for monitoring in real-time the pH of the sweat generated during an exercise period was presented[78]
	Patterning using PDMS-coating. Hydrophilic patterning on hydrophobic substrate.	Presenting patterned fabric allowed selective permeation of water-based reagents through the hydrophilic regions[84]
Non-woven fabric (wax patterning)	Nil	Simultaneous quantifying small concentrations of multiple biomarkers of disease using 2D and 3D microfluidic devices[72]
	Sodium carbonate treatment	Quantitatively determination of human chorionic

		gonadotropin[42]
	Sodium hydroxide and sodium carbonate treatment	Bovine Serum Albumin detection in artificial urine[30]
Woven fabric (wax patterning)	Nil	Glucose determination in different sample resources[73]
	Sodium carbonate treatment	Determination of lactate concentration in saliva samples[43]
	Boiling followed by Sodium carbonate treatment	Quantitative colorimetric detection of glucose or bovine serum albumin in artificial urine[45]
Woven fabric (photolithographic patterning)	Sodium hydroxide treatment	Colorimetric assays of glucose and protein in artificial urine [49]
Woven fabric (wax printing)	Nil	Wax patterning to create a µTAD for detection of Cr(III) in water[74] Developing a µTAD for wireless elechrochemiluminescese detection of TriPropylamine and H2O2[75]
Fabric (Woven hydrophobic fabric as the substrate and hydrophilic threads	Sodium carbonate and hand soap treatment	Applicability toward facilitated and controlled biofluid removal, such as skin surfaces experiencing heavy perspiration was demonstrated[41]

	as channels)		
Mercerized cotton	Thread	Nil	Detection of protein, nitrite and ketones and glucose in artificial urine. And alkaline phosphatase in artificial blood plasma[13] Visual detection of lung cancer related biomarker, i.e. human ferritin antigen using carbon nanotubes reporters[68] Electrochemical detection of human ferritin using gold nanorod reporters[63]
		Boiling with sodium chloride followed by treatment in a solution of hydrogen peroxide and hydrochloric acid	Room temperature DNA detection device[44] Human ferritin detection[47] A novel enhanced dry-reagent cotton thread device for Squamous cell carcinoma antigen detection based on two kinds of gold nanoparticles and a novel room temperature DNA detection device by using adenosine based molecular beacon probe were introduced[48]
Cellulose	Thread	Nil	Detection of different electro-active compounds[60]
	Nanofibril Filaments	Nil	Highly sensitive detection of human hemoglobin[58]
Nylon	Thread	Nil	Controlled protein delivery, electrophoretic separation and isolation of analytes[59] Colorimetric assessment of acetylcholinesterase activity[67]

Polyester	Thread	Nil	blood urea nitrogen and glucose detection in human whole blood[21]
		Plasma treatment	ABO and Rh/D blood typing[52] Blood typing[54]
		Oxygen Plasma treatment	Separation and detection of mixed ion samples and bio-samples [32] capillary electrophoresis electrochemical detection of blood urea nitrogen in whole blood[19]
Silk	Woven fabric	Metal coated Silk yarns (Zari)	Low cost SERS substrates[79]
	Woven fabric (Hydrophilic and hydrophobic threads)	Boiling	Immunoassay[15]
Wool	Thread	Plasma treatment	Effect of different plasma treatments and treatment times on wettability of wool fibres. A simple microfluidic device was designed to do micro-mixing[40]
Polypropylene	Hollow and liquid core fibres	Nil	Demonstration of the potential of using hollow or liquid core fibres as microfluidic channels[85].
PVA (Poly(vinyl alcohol))	Electrospun nanofibres	Nil	Creating patterns on the Poly(methyl methacrylate) chip with gold electrodes and integrated into polymer-based microfluidic channels to create functionalized microfluidic systems[86]

Multi-material	Mercerized cotton and silk threads Nylon bundle	Nil	Knotting to link different thread materials, providing the ability to physically concentrate solutes by chromatographic interaction. Application of trapping and detection of bacteria cells for urinary tract infection[59]
	Mercerized Cotton threads Nylon bundle	Air plasma treatment (for cotton)	Detection of three target molecules in serum was performed to demonstrate a multiplexed assay as well as singleplex assay[35]
	Mercerized cotton and artificial silk threads	Nil	Performing chemical synthesis and sensing and bovine serum albumin detection and quantification of glucose present a human blood plasma [56]
	Cotton and polyester threads	Vacuum plasma treatment	Describes a semiquantitative method for analytical detection by measuring the length of colour change on indicator treated threads using a ruler[33]
		Plasma treatment	Various mechanisms of flow control in yarns were shown and discussed[39]
	Cotton and silk threads	Vacuum plasma treatment	The effect of the surface morphologies of silk and cotton fibers on the separation properties for the application of blood typing based on the principal of chromatographic elution[37]
	Blend of cotton and polyester threads	Sodium hydroxide treatment (with ultrasonic)	Quantitative assays of hydrogen peroxide and glucose[46]
	Cotton threads Cotton and polyester	Sodium hydroxide and sodium dodecylbenzenesulfonate (SDS)	sequential determination of Cu(II) and Zn(II)[50]

threads	treatment	
Nylon threads, paper for analysis sites	Nil	Colourimetric assessing of glucose in artificial urine[69]
Cotton thread for microfluidics Fabric of Nylon-Lycra for detection zone	Nil	Real-time chemical analysis of sweat composition, in particular pH[65]
Polyester and nylon non-woven fabric (Photolithographic patterning)	Nil	Detecting lactate in sweat[53] An enzyme biosensor based on colorimetric detection of hydrogen peroxide was reported[77]
Polypropylene and poly(ethylene terephthalate) woven fabric	Nil	Making microfluidic fibre channels with switchable water transport[71]
Cotton fabric for reservoirs and polyester for channels Woven and knitted fabric strips	Nil	Separation of small molecule as well as macromolecule (protein) analytes[20]
Poly(ethylene terephthalate) copolyester	Nil	Flow control by systematic change in fabric design.[70]

	(Hydrophilic part) Polypropylene (Hydrophobic part) Woven fabric		

Although, a lot of research work has been done in the field of textile-based microfluidics, it's still in its early stages. Most importantly, to the best of our knowledge, there is no report on utilizing custom-built functionalized composite fibres in textile structures to induce desired characteristics to µTADs. Hence, in the following sections, principles of textile fibre making methods and textile fabrication techniques as key elements in making textile structures with desired characteristics will be briefly reviewed.

1.7. Polymeric fibre spinning

The process of converting polymer liquid into continuous fibre form is called fibre spinning. Continuous solidification of polymer liquid is an undetectable part of any spinning process, regardless of the materials involved. This process can involve heat removal or solvent removal by using a solvent non-solvent process. Making a processable or spinnable form of polymer by either melting or dissolving polymer in a proper solvent is the first step of spinning. Depending on the thermal and chemical properties of polymers, different methods including melt spinning, wet spinning, dry spinning and electrospinning can be employed to make polymeric fibres from a spinnable state of fibres constituent polymer[87,88].

1.7.1. Melt spinning

In this method of fibre making, heat is applied to the polymer to melt it then molten polymer passed through a spinneret via a spinning pump. Therefore, only thermoplastic polymers (polymers that melt) can be used for melt spinning technique. Spinning temperature in which viscosity of molten polymer fulfils the requirements for spinning is often about 30K higher than melting temperature. Consequently, polymers used in melt spinning method should exhibit good thermal stability under melt condition. Solidification

of molten polymer occurs as a result of heat transfer (cooling the molten polymer in cooling chamber or air). Although production speed in this system is relatively high, it has some disadvantages such as being able to process only thermoplastic polymers which are resistant to thermal oxidation and rapid solidification which sometimes results in poor internal micro-structure in spun fibres[89]. Figure 1.6 shows schematic of a melt spinning process.
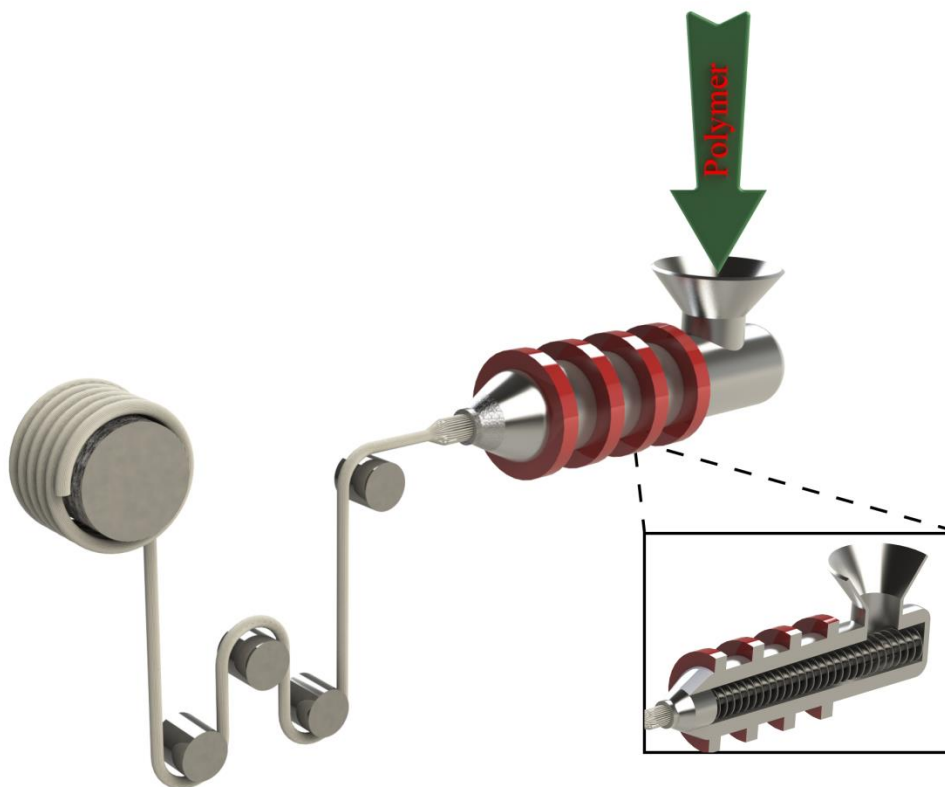
Figure 1.6: Schematic of melt spinning process includes polymer feeding, heating zones and collector.

1.7.2. Wet spinning

In this method of spinning, polymer first dissolved in a suitable solvent to make spinning solution. Then fibres are formed by injecting prepared solution into a coagulation bath through spinnerets and at a controlled flow rate.   The coagulation bath contains a miscible solvent compatible with the spinning solvent in which the polymer is dissolved but

importantly the coagulant should be a non-solvent to the polymer, being spun which results in polymer precipitation and fibre formation. Fibre morphology and cross-section shape greatly depends on the mass transfer rate occurring in coagulation bath. Some drawbacks of this process includes a relatively low fibre production rate and the need for the non-solvent which can make the wet spinning process costly[87,88,89]. Schematic of wet spinning process is shown in Figure 1.7.
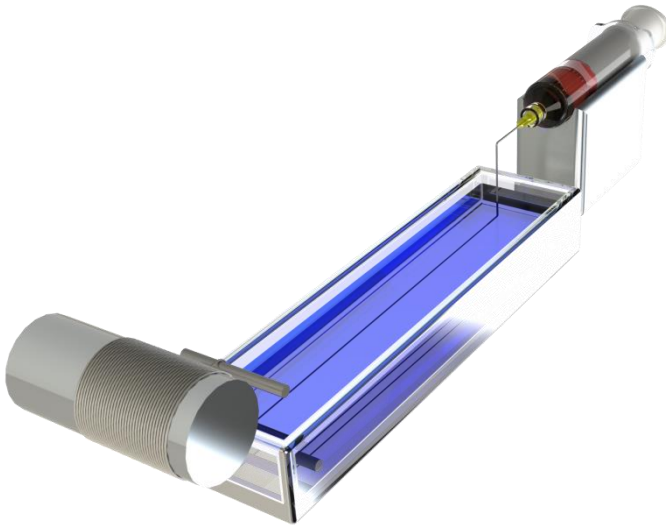
Figure 1.7: Scheme of wet spinning technique includes syringe pump that pumps the polymer solution into the coagulation bath and a collector for fibres

1.7.3. Dry spinning

Dry spinning and wet spinning share a number of basic principles. Similar to wet spinning method, polymer spinning solution is preparation by dissolving polymer into a compatible solvent system. Then solution is injected through a spinneret into a chamber of circulating warp air to form fibre gels. In this method, solidification occurs as a result of solvent evaporation within the chamber. In this process two simultaneous phenomena, i.e. inward heat transfer and outward mass transfer occurs typically results in non-circular fibre cross-sections due to the collapse of the outer skin. This method can be used to make fibres from

27

heat-sensitive polymers. Application of this method is limited to flammable, non-hazardous solvents with low boiling points[87–90].

1.7.4. Electrospinning

This technique is a well-known method for making fibres with sub-micron dimension that exhibit outstanding characteristics such as very large surface area to volume ratio, flexibility in surface functionalities and very good mechanical performance. This technique is often applied to polymer solutions, however there are some reports on electrospinning of molten polymer include making 3D scaffolds by melt electrowritting[91,92]. This method essentially comprised of three components: a high voltage supplier, a needle of small diameter (or a capillary tube) and a metal collector (Figure 1.8). In electrospinning, an electrically charged jet of polymer is created by the high voltage supplier (One electrode is attached to the tip of the needle which contains spinning solution/melt and the other to the collector). This jet is applying a very high amount of tension to the polymer that results in formation of sub-micron fibres. Solution or molten polymer solidifies by either solvent evaporation or cooling before reaching the collector and an interconnected web of very fine fibres is formed on the collector[93,94].
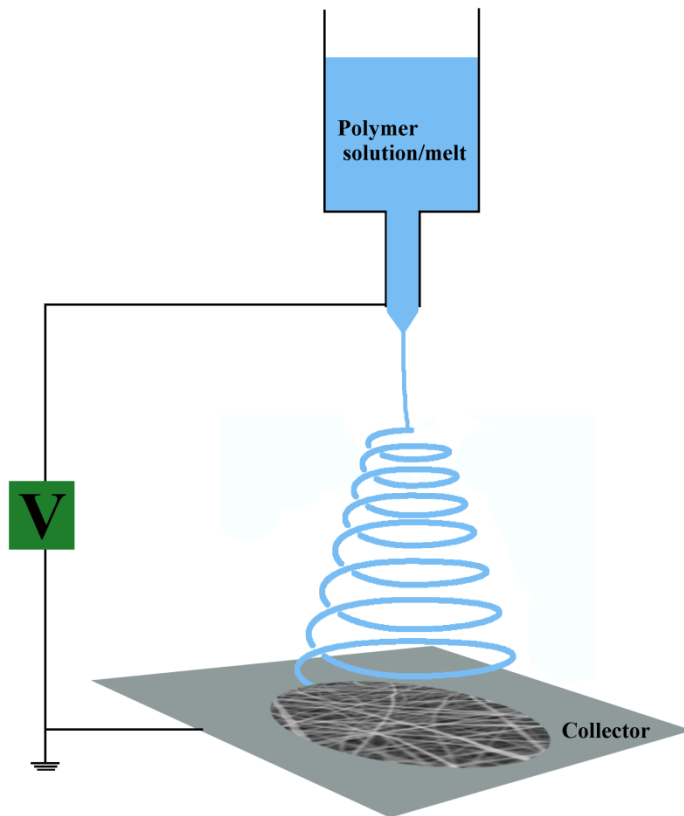
Figure 1.8: Scheme of electrospinning process which includes polymer solution, high voltage DC power supply and a collector

1.8.   Textile fabrication techniques

Textile fabric can be defined as an assembly of fibres, yarns or their combinations. Fabric manufacturing can be done in different ways and each of them is capable of producing wide variety of fabrics depending on raw materials used, equipment and machinery employed and setup control elements during the process. Most commonly fabric forming methods can be categorized in weaving, knitting, braiding, and nonwoven manufacturing[95] (Figure 1.9).
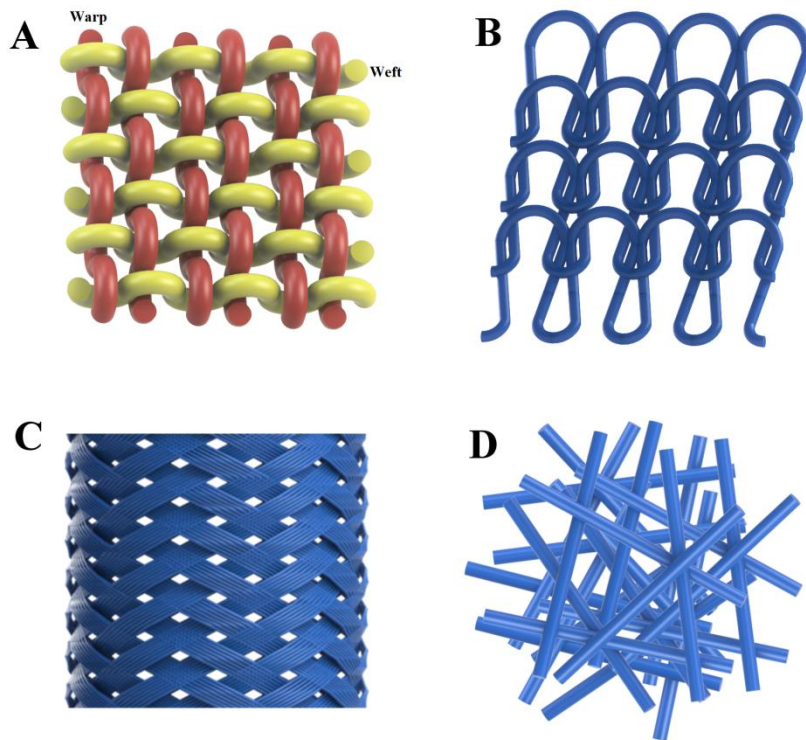
Figure 1.9: Schematic of fabrics produced by (a) Weaving, (b) knitting, (c) braiding and (d) nonwoven manufacturing.

1.8.1. Weaving

Woven fabrics are made by which two sets of yarns (i.e. warp and weft) interlaced perpendicular to each other [95,96]. In the simplest two dimensional woven fabrics, threads run vertically along the length of the fabric are called warps and wefts are the threads are lay across the width of the fabric perpendicular to war threads[97,98]. Woven fabrics can be made in triaxial and three dimensional shapes as well[97].

1.8.2. Knitting

The knitting is the second most common method of textile fabric formation and consists of continuous lengths of yarns which are formed into columns and rows of intermeshed loops using either hand or machine. This technique can be categorized into two main streams i.e.

Weft knitting and warp knitting techniques[96,99–102]. Weft knitting is the method being used in hand knitting. Weft knitted structures are made by loops formed by one continuous end of yarn across the width of the cloth (**Figure 1. 10**a). In warp knitting method, multiple yarn ends are formed columns of loops then warp knitted fabric is made by diagonal intermeshing of loops with the adjacent vertical columns (Figure 1. 10b)[97,98]. Weft knitting has some unique features which includes;

- The capability of making fabrics using minimum number of yarns (even only one yarn),

- Varying the size of loops,

- Possibility of loop transfer from one needle to another,

- Stability and extensibility of the fabric can be engineered,

- Tunable porosity and compactness,

- Shaping can be done during knitting process,

- Unsuitable yarns for knitting can be knitted as in-lays,

- Selective variation of the number of yarns to be knitted in the same fabric,

- Possibility of variation in needle numbers for loop formation from one cycle to another,

- Easy flow of yarn from one loop to another under tension and

- Negligible wastage of yarn during yarn conversion in knitting which make it greatly popular.
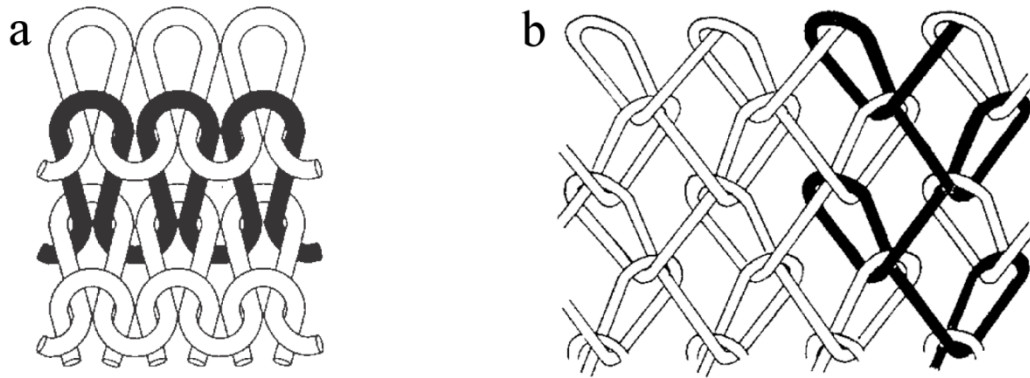
Figure 1. 10. Intermeshed loops in (a) weft- and (b) warp-knitted structures[97]

1.8.3. Braiding

Braiding is probably the simplest and the first method of fabric formation used by ancient civilizations. Braided structures are formed by interlacing three or more sets of yarns on the bias over and under each other[95,102]. Braiding is the ideal technique for developing structures comprising of mixed materials and for rapid production.

1.8.4. Non-woven

Non-woven textile structures are made by bonding and/or interlocking of fibres. Bonding fibres can be done mechanically, chemically, thermally, or by using solvent and the combination of them[103].

Weaving and warp knitting methods are costly techniques of fabric formation because they require significant preparation such as warping and winding. Fabric formation using these methods typically requires a large amount of yarns which make them not suitable for lab scale productions. In this thesis, weft knitting and braiding have been selected as fabric formation methods for producing textiles substrates for fluidics because of ease of fabrication. Moreover, characteristics of knitted and braided structures can be easily adjusted by changing production parameters. In addition, weft knitting needs almost no

preparation and can be performed using only one yarn. Braiding technique benefits from having independent tension mechanism for each individual yarn, unlike weaving and warp knitting, also, this method has been designed to easily make multi-material structures.

1.9. Common nano-fillers for composite fibres

In recent decades, nanocomposite materials owing to their outstanding characteristics such as being strong, durable, multifunctional materials with low nanofiller content have been attracted a lot of attention and it have been known as 'radical alternative to conventional filled polymers or polymer blends'. Such materials including nanocomposite fibres have been utilized to a wide range of applications[104,105]. Following a brief review of two common fillers, i.e. graphene and boron nitride, will be provided.

1.9.1. Graphene

In recent years, graphene sheets, one-atom thick two dimensional layers of sp^2-bonded carbon, is a remarkable carbonaceous material demonstrated unusual properties such as extraordinary optical properties, mechanical strength, electrical and thermal conductivity. Such features result in an increasing attention for development of nanocomposite materials for different applications[104–106]. Graphene is a flat monolayer of carbon atoms arranged in a two dimensional honeycomb lattice, Figure 1.11. This network is the basic building block of other important carbon materials, i.e. 3D graphite, one-dimensional carbon nanotube and zero-dimensional fullerenes[107].
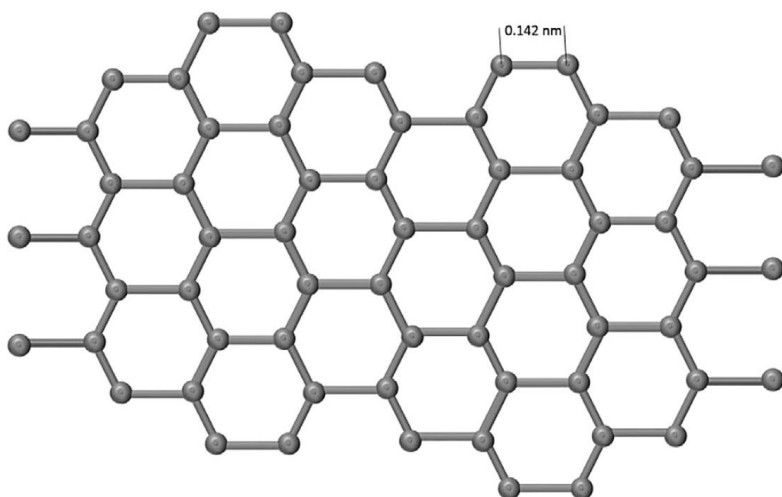
Figure 1.11: Schematic structure of graphene sheets in which carbon atoms bonded in a honeycomb lattice[106].

For a long time it was believed that two-dimensional crystals were thought to be thermodynamically unstable at finite temperatures till Geim et al. first isolated single-layer samples from graphite in 2004. This great discovery was awarded a Nobel Prize in physics[106,107].

Apart from mechanical exfoliation of graphite proposed in 2004, graphene sheets are mainly synthesized using three main approaches: liquid-phase exfoliation of graphite[108], chemical vapour deposition method[109] and reduction of graphene oxide[110]. Graphene exhibits a very poor dispersibility which limited its application. In 2006, Ruoff's group presented water dispersible graphene oxide (GO) sheets by chemical modification of graphite. They showed oxidation of graphite results in GO which is a layered material which is heavily oxygenated, having hydroxyl and epoxide functional groups on their basal planes as well as carbonyl and carboxyl groups at the sheet edges. These functional groups make the GO hydrophilic and therefore, dispersible in water[110]. Due to disruption of graphitic network, GO is electrically insulating which limits its application for the synthesis of conductive nanocomposites. However, graphene oxide can be reduced chemically,

thermally or using ultraviolet-assisted methods to make a significant increase in its electrical conductivity[104,110].

Using graphene sheets, with their ultrahigh aspect ratio, as a filler to make composites results in large changes in its properties at very low percolation thresholds. Therefore, graphene has been widely used as a filler to develop composites for a wide range of applications[106].

1.9.2. Boron nitride

Boron nitride (BN) has three different crystal structures; layered known as hexagonal boron nitride (hBN), cubic (cBN) and tubular structures. hBN also known as "white graphite" is the isoelectric analogue of graphite and naturally comprised of layered structures. In this structure, boron and nitrogen atoms are bound together by strong covalent bonds with an interlayer spacing of ~0.33 nm forming a honeycomb lattice, while different layers are attached by a weak van der Waals force[111–113]. While graphene sheets adopt AB stacking to form 3D graphite solid, hBN layers prefer AA' stacking arrangement. However, non- AA' stacking in BN sheets is also possible as a result of basal plane sliding[114]. Different views (top, side and end views) of structural diagram of AA' stacked BN is shown in Figure 1.12.
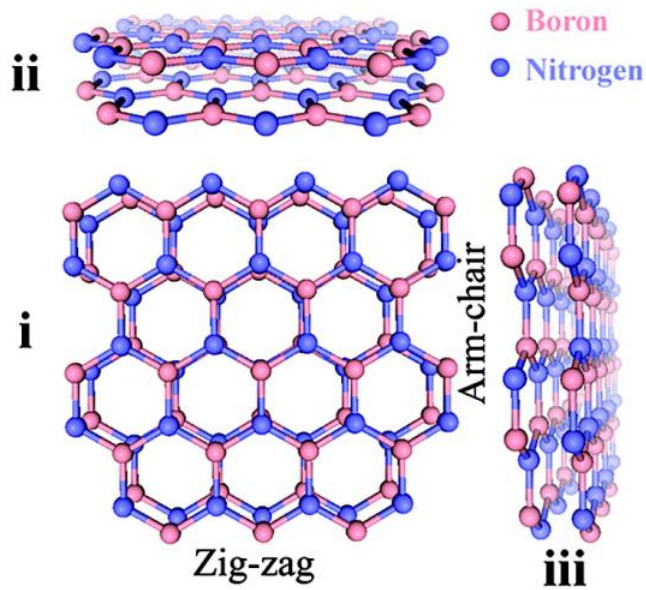
Figure 1.12: (i) top view, (ii) end view, and (iii) side view of structural diagram of AA' stacked BN sheet[114]

In addition to high mechanical strength and thermal conductivity of hBN, similar to those of graphene, it also exhibits outstanding characteristics such as high temperature stability, high hardness and corrosion resistance, deep ultraviolet photon emission and a low dielectric constant. These features make it popular for a wide range of applications. Although hBN has a very high thermal conductivity like graphene, it has a large band gap (∼4-6 eV), making it an insulator (or a wide-band-gap semiconductor)[111–118].

First synthesis of BN from boric acid and calcium cyanide was reported by W.H. Balmain in 1842. BN remained as a lab-scale production until mid-1940s when improved process of producing BN was presented which led to more economical and higher quality BN production[111,118]. This material has been used in a wide range of applications such as solid lubricant in rigorous environments, as an ultraviolet-light emitter, or as an insulating thermally conductive filler in composites for different industries like metallization, metal industry, cosmetics, the automotive industry, high-temperature furnaces, thermal management, etc[111,112].

1.10. Thesis outline

As discussed above, application of textiles as a low-cost abundant substrate in the field of microfluidics is increasing. This thesis aims to develop functionalized composite fibres to be incorporated into textile structures (either 2D or 3D structures) to induce desired characteristics to the substrate and improve the performance of textile-based microfluidic device.

Considering the fact that textile-based microfluidics is a relatively recent technology, many different aspects of this novel field are yet to be unravelled. For instance, a huge potential exists to exploit the separation potential of electrophoresis in multiple dimensions. These either may include applying potential upon single threads in simple mono-directional arrangements, or systematically designed multi-dimensional and woven fluidics comprising of multiple types of interconnected threads with different arrangements. Another interesting field that needs to be explored is the use of modified and functionalized composite fibres made specifically to satisfy the specific needs. For instance, 'on-fibre' trapping, isolation and derivatisation can be achieved by incorporation of functionalized composite fibres into textile platforms. The first step would be the understanding of the fundamental underlying principles of the nature and role of the fibre material in the electrophoretic separations. Taking into account that the electrophoresis technique, as a well-established technology, has the capacity to provide solutions to the analysis of small molecules to large biomolecules (and even whole cells), the approach taken in this thesis will be to;

- Develop an understanding the impact of materials' composition in the final performance of μTADs.
- Investigate the preparation and incorporation of functionalized composite fibres into 3D textile platforms to facilitate electrophoresis experiments.

- Investigate segmented functionalized textile platforms equipped with electrochemical and amperometric detection techniques to perform some diagnostic assays.

Chapter 2 presents the materials used to perform experiments in this thesis, explains the experimental procedures including preparing composites, fibre spinning formulations for wet-spinning experiments, melt spinning conditions, electrophoresis tests and characterisation methods used.

Chapter 3 investigates the effect of surface chemistry and surface charge in the performance of a μTAD. In this chapter different 3D knitted structures comprising of LCGO/low-density polyethylene composite fibres are produced and the effect of their changing surface chemistry in the wicking properties of those structures in different solutions are assessed.

Recently, electrophoresis technique as a powerful tool has been used in textile-based microfluidics to precisely control the flow. However, the drawback of using this method is Joule-heating caused as a result of applying electric field passing electrolyte to move and/or separate solutes. Joule-heating not only increases the fluid temperature, but also produces temperature gradients in cross-stream and axial directions. These temperature effects, cause non-uniformity in fluid properties, and more importantly affect the mass species transport [119]. Therefore, next two chapters of this thesis have been focused on development of thermally conducting fibres incorporated into textile substrates to minimize the Joule-heating effect.

Chapter 4 presents the development of a thermally conducing fibres using low-density polyethylene as polymeric matrix along with liquid-crystalline graphene oxide (LCGO) as filler then incorporation of these fibres into 3D textile structure for dissipating the Joule-heating caused by electrophoresis.

Utilising solution-based methods to produce composite fibres using polyurethane polymeric matrix and two different fillers, i.e. LCGO and hBN nanopowders, their mechanical and thermal properties, and finally, the effect of incorporating those thermally conducting fibres into 3D textile structures in dissipation of Joule-heating and keeping the working temperature low is explained in chapter 5.

Then final experimental chapter of this thesis dedicated to making a μTAD in which electroactive electrodes have been prepared and incorporated into textile structures using two different fabrication techniques, i.e. knitting and braiding. Then cyclic voltammetry and amperometric methods have been employed to perform potassium ferricyanide detection on textile-based microfluidic device to demonstrate the capability of using these devices as wearable electrochemical sensors.

1.11. References

(1)   Etzioni, R.; Urban, N.; Ramsey, S.; McIntosh, M.; Schwartz, S.; Reid, B.; Radich, J.; Anderson, G.; Hartwell, L. The Case for Early Detection. *Nat. Rev. Cancer* **2003**, *3* (4), 243–252.

(2)   Lazar, I. M. Microfluidic Devices in Diagnostics: What Does the Future Hold? *Bioanalysis* **2015**, *7* (20), 2677–2680.

(3)   Smith, R. a.; von Eschenbach, A. C.; Wender, R.; Levin, B.; Byers, T.; Rothenberger, D.; Brooks, D.; Creasman, W.; Cohen, C.; Runowicz, C.; et al. American Cancer Society Guidelines for the Early Detection of Cancer: Update of Early Detection Guidelines for Prostate, Colorectal, and Endometrial Cancers. Also: Update 2001--Testing for Early Lung Cancer Detection. *CA. Cancer J. Clin.* **2001**, *51* (1), 38-75-80.

(4)   Locatelli, F.; Vecchio, L. Del; Pozzoni, P. The Importance of Early Detection of Chronic Kidney Disease. *Nephrol. Dial. Transplant* **2002**, *17 Suppl 1*, 2–7.

(5)   Smith, R. a; Cokkinides, V.; Eyre, H. J. American Cancer Society Guidelines for the Early Detection of Cancer, 2006. *CA. Cancer J. Clin.* **2003**, *56* (1), 11-25-50.

(6)   Martinez, A. W.; Phillips, S. T.; Whitesides, G. M.; Carrilho, E. Diagnostics for the Developing World: Microfluidic Paper-Based Analytical Devices. *Anal. Chem.* **2010**, *82* (1), 3–10.

(7)   Gervais, L.; De Rooij, N.; Delamarche, E. Microfluidic Chips for Point-of-Care Immunodiagnostics. *Adv. Mater.* **2011**, *23* (24), H151-76.

(8)   Yager, P.; Edwards, T.; Fu, E.; Helton, K.; Nelson, K.; Tam, M. R.; Weigl, B. H. Microfluidic Diagnostic Technologies for Global Public Health. *Nature* **2006**, *442* (7101), 412–418.

(9)   Peeling, R. W.; Holmes, K. K.; Mabey, D.; Ronald, a. Rapid Tests for Sexually Transmitted Infections (STIs): The Way Forward. *Sex. Transm. Infect.* **2006**, *82 Suppl 5*, v1–v6.

(10)   Parolo, C.; Merkoci, A. Paper-Based Nanobiosensors for Diagnostics. *Chem. Soc. Rev.* **2013**, *42* (2), 450–457.

(11)   Sackmann, E. K.; Fulton, A. L.; Beebe, D. J. The Present and Future Role of Microfluidics in Biomedical Research. *Nature* **2014**, *507* (7491), 181–189.

(12)   Whitesides, G. M. The Origins and the Future of Microfluidics. *Nature* **2006**, *442* (7101), 368–373.

(13)   Reches, M.; Mirica, K. A.; Dasgupta, R.; Dickey, M. D.; Butte, M. J.; Whitesides, G. M. Thread as a Matrix for Biomedical Assays. *ACS Appl. Mater. Interfaces* **2010**, *2* (6), 1722–1728.

(14)   Li, X.; Tian, J.; Shen, W. Thread as a Versatile Material for Low-Cost Microfluidic Diagnostics. *ACS Appl. Mater. Interfaces* **2010**, *2* (1), 1–6.

(15)   Bhandari, P.; Narahari, T.; Dendukuri, D. "Fab-Chips": A Versatile, Fabric-Based Platform for Low-Cost, Rapid and Multiplexed Diagnostics. *Lab Chip* **2011**, *11* (15), 2493.

(16)   Wei, Y.; Lin, C.; Wang, Y.-N.; Fu, L.-M. Capillary Electrophoresis Electrochemical (CE-EC) Detection on a Novel Thread-Based Microfluidic Device with 3D Sensing Electrodes. In *6th IEEE International Conference on Nano/Molecular Medicine and Engineering*; 2012; pp 101–105.

(17)   Wei, Y.-C.; Fu, L.-M.; Lin, C.-H. Electrophoresis Separation and Electrochemical Detection on a Novel Thread-Based Microfluidic Device. *Microfluid. Nanofluidics* **2012**, *14* (3–4), 583–590.

(18)   Yang, Y.; Kuo, W.; Lin, C. ENZYME-DOPED POLYESTER THREAD COATED WITH PVC MEMBRANE FOR ON-SITE UREA AND GLUCOSE DETECTION ON A THREAD-BASED MICROFLUIDIC SYSTEM. In *MEMS 2014*; San Francisco, 2014; Vol. i, pp 959–962.

(19)   Yang, Y.-A. A.; Lin, C.-H. H.; Wei, Y.-C. C. Thread-Based Microfluidic System for Detection of Rapid Blood Urea Nitrogen in Whole Blood. *Microfluid. Nanofluidics* **2014**, *16* (5), 1–8.

(20)   Narahari, T.; Dendukuri, D.; Murthy, S. K. Tunable Electrophoretic Separations Using a Scalable, Fabric-Based Platform. *Anal. Chem.* **2015**, *87* (4), 2480–2487.

(21)   Yang, Y.; Lin, C. Multiple Enzyme-Doped Thread-Based Microfluidic System for Blood Urea Nitrogen and Glucose Detection in Human Whole Blood. *Biomicrofluidics* **2015**, *9* (2), 1–13.

(22)   Yamada, K.; Henares, T. G.; Suzuki, K.; Citterio, D. Paper-Based Inkjet-Printed Microfluidic Analytical Devices. *Angew. Chemie - Int. Ed.* **2015**, *54* (18), 5294–5310.

(23)   Yetisen, A. K.; Akram, M. S.; Lowe, C. R. Paper-Based Microfluidic Point-of-Care Diagnostic Devices. *Lab Chip* **2013**, *13* (12), 2210–2251.

(24)   Cate, D. M.; Adkins, J. a; Mettakoonpitak, J.; Henry, C. S. Recent Developments in Paper-Based Micro Fluidic Devices. *Anal. Chem.* **2015**, *87*, 19–41.

(25)   Hu, J.; Wang, S.; Wang, L.; Li, F.; Pingguan-Murphy, B.; Lu, T. J.; Xu, F. Advances in Paper-Based Point-of-Care Diagnostics. *Biosens. Bioelectron.* **2014**, *54*, 585–597.

(26)   Weian, Z.; Berg, A. Lab on Paper. *Lab Chip* **2008**, *8*, 1988–1991.

(27)   Ballerini, D. R.; Li, X.; Shen, W. Patterned Paper and Alternative Materials as Substrates for Low-Cost Microfluidic Diagnostics. *Microfluid. Nanofluidics* **2012**, *13* (5), 769–787.

(28)   Agustini, D.; Bergamini, M. F.; Marcolino-Junior, L. H. Low Cost Microfluidic Device Based on Cotton Threads for Electroanalytical Application. *Lab Chip* **2016**, *16*, 345–352.

(29)   Washburn, E. W. The Dynamics of Capillary Flow. *Phys. Rev.* **1921**, *17* (3), 273–283.

(30)   Nilghaz, A.; Wicaksono, D. H. B.; Gustiono, D.; Abdul Majid, F. A.; Supriyanto, E.; Abdul Kadir, M. R. Flexible Microfluidic Cloth-Based Analytical Devices Using a Low-Cost Wax Patterning Technique. *Lab Chip* **2012**, *12* (1), 209.

(31)   Nilghaz, A.; Ballerini, D. R.; Shen, W. Exploration of Microfluidic Devices Based on Multi-Filament Threads and Textiles: A Review. *Biomicrofluidics* **2013**, *7* (5).

(32)   Wei, Y. C.; Fu, L. M.; Lin, C. H. Electrophoresis Separation and Electrochemical Detection on a Novel Thread-Based Microfluidic Device. *Microfluid. Nanofluidics* **2013**, *14* (3–4), 583–590.

(33)   Nilghaz, A.; Ballerini, D. R.; Fang, X. Y.; Shen, W. Semiquantitative Analysis on Microfluidic Thread-Based Analytical Devices by Ruler. *Sensors Actuators, B Chem.* **2014**, *191*, 586–594.

(34)   Safavieh, R.; Zhou, G. Z.; Juncker, D. Microfluidics Made of Yarns and Knots: From Fundamental Properties to Simple Networks and Operations. *Lab Chip* **2011**, *11* (15), 2618–2624.

(35)   Zhou, G.; Mao, X.; Juncker, D. Immunochromatographic Assay on Thread. *Anal. Chem.* **2012**, *84* (18), 7736–7743.

(36)   David R. Ballerini, Ying H. Ngo, Gil Garnier, Bradley P. Ladewig, and W. S. Gold Nanoparticle-Functionalized Thread as a Substrate for SERS Study of Analytes Both Bound and Unbound to Gold. *AIChE J.* **2014**, *60*, 1598–1605.

(37)   Nilghaz, A.; Zhang, L.; Li, M.; Ballerini, D. R.; Shen, W. Understanding Thread Properties for Red Blood Cell Antigen Assays : Weak ABO Blood Typing. *ACS Appl. Mater. Interfaces* **2014**, *6*, 22209–22215.

(38)   Kim, J.; Bae, S.; Song, S.; Chung, K.; Kwon, S. Fiber Composite Slices for Multiplexed Immunoassays. *Biomicrofluidics* **2015**, *9* (4), 44109.

(39)   Ballerini, D. R.; Li, X.; Shen, W. Flow Control Concepts for Thread-Based Microfluidic Devices. *Biomicrofluidics* **2011**, *14* (5), 14105.

(40)   Jeon, S.-H.; Hwang, K.-H.; Lee, J. S.; Boo, J.-H.; Yun, S. H. Plasma Treatments of Wool Fiber Surface for Microfluidic Applications. *Mater. Res. Bull.* **2015**, *69*, 65–70.

(41)   Xing, S.; Jiang, J.; Pan, T. Interfacial Microfluidic Transport on Micropatterned Superhydrophobic Textile. *Lab Chip* **2013**, *13* (10), 1937–1947.

(42)   Bagherbaigi, S.; Corcoles, E. P.; Wicaksono, D. H. B. Cotton Fabric as an Immobilization Matrix for Low-Cost and Quick Colorimetric Enzyme-Linked Immunosorbent Assay (ELISA). *Anal. Methods* **2014**, *6* (18), 7175–7180.

(43)   Malon, R. S. P.; Chua, K. Y.; Wicaksono, D. H. B.; Córcoles, E. P. Cotton Fabric-Based Electrochemical Device for Lactate Measurement in Saliva. *Analyst* **2014**, *139* (12), 3009–3016.

(44)   Du, T.-E.; Wang, Y.; Zhang, Y.; Zhang, T.; Mao, X. A Novel Adenosine-Based Molecular

Beacon Probe for Room Temperature Nucleic Acid Rapid Detection in Cotton Thread Device. *Anal. Chim. Acta* **2015**, *861*, 69–73.

(45)   Liu, M.; Zhang, C.; Liu, F. Understanding Wax Screen-Printing: A Novel Patterning Process for Microfluidic Cloth-Based Analytical Devices. *Anal. Chim. Acta* **2015**, *891*, 234–246.

(46)   Lu, F.; Mao, Q.; Wu, R.; Zhang, S.; Du, J.; Lv, J. A Siphonage Flow and Thread-Based Low-Cost Platform Enables Quantitative and Sensitive Assays. *Lab Chip* **2015**, *15* (2), 495–503.

(47)   Mao, X.; Du, T.-E.; Meng, L.; Song, T. Novel Gold Nanoparticle Trimer Reporter Probe Combined with Dry-Reagent Cotton Thread Immunoassay Device for Rapid Human Ferritin Test. *Anal. Chim. Acta* **2015**, *889*, 172–178.

(48)   Mao, X.; Du, T.-E.; Wang, Y.; Meng, L. Disposable Dry-Reagent Cotton Thread-Based Point-of-Care Diagnosis Devices for Protein and Nucleic Acid Test. *Biosens. Bioelectron.* **2015**, *65*, 390–396.

(49)   Wu, P.; Zhang, C. Low-Cost, High-Throughput Fabrication of Cloth-Based Microfluidic Devices Using a Photolithographical Patterning Technique. *Lab Chip* **2015**, *15* (6), 1598–1608.

(50)   Yan, Y.; Kou, B.; Yan, L. Thread-Based Microfluidic Three Channel Device in Combination with Thermal Lens Detection for the Determination of Copper and Zinc. *Anal. Methods* **2015**, *7* (20), 8757–8762.

(51)   Ulum, M. F.; Maylina, L.; Noviana, D.; Wicaksono, D. H. B. EDTA-Treated Cotton-Thread Microfluidic Device for One-Step Whole Blood Plasma Separation and Assay. *Lab Chip* **2016**.

(52)   Ballerini, D. R.; Li, X.; Shen, W. An Inexpensive Thread-Based System for Simple and Rapid Blood Grouping. *Anal. Bioanal. Chem.* **2011**, *399* (5), 1869–1875.

(53)   Baysal, G.; Onder, S.; Gocek, I.; Trabzon, L.; K z l, H.; Kok, F. N.; Kayao lu, B. K. Microfluidic Device on a Nonwoven Fabric: A Potential Biosensor for Lactate Detection. *Text. Res. J.* **2014**, *84* (16), 1729–1741.

(54)   Nilghaz, A.; Ballerini, D. R.; Guan, L.; Li, L.; Shen, W. Red Blood Cell Transport Mechanisms in Polyester Thread-Based Blood Typing Devices. *Anal. Bioanal. Chem.* **2016**.

(55)   Ramesan, S.; Rezk, A. R.; Cheng, K. W.; Chan, P. P. Y.; Yeo, L. Y. Acoustically-Driven Thread-Based Tuneable Gradient Generators. *Lab Chip* **2016**, *16* (15), 2820–2828.

(56)   Banerjee, S. S.; Roychowdhury, A.; Taneja, N.; Janrao, R.; Khandare, J.; Paul, D. Chemical Synthesis and Sensing in Inexpensive Thread-Based Microdevices. *Sensors Actuators, B Chem.* **2013**, *186*, 439–445.

(57)   Mostafalu, P.; Akbari, M.; Alberti, K. A.; Xu, Q.; Khademhosseini, A.; Sonkusale, S. R. A Toolkit of Thread-Based Microfluidics, Sensors, and Electronics for 3D Tissue Embedding for Medical Diagnostics. *Microsystems Nanoeng.* **2016**, *2* (April), 16039.

(58)   Vuoriluoto, M.; Orelma, H.; Lundahl, M.; Borghei, M.; Rojas, O. J. Filaments with Affinity Binding and Wet Strength Can Be Achieved by Spinning Bifunctional Cellulose Nanofibrils. *Biomacromolecules* **2017**, acs.biomac.7b00256.

(59)   Cabot, J. M.; Macdonald, N. P.; Phung, S. C.; Breadmore, M. C.; Paull, B. Fibre-Based Electrofluidics on Low Cost Versatile 3D Printed Platforms for Solute Delivery, Separations and Diagnostics; from Small Molecules to Intact Cells. *Analyst* **2016**, *141* (23), 6422–6431.

(60)   Sekar, N. C.; Mousavi Shaegh, S. A.; Ng, S. H.; Ge, L.; Tan, S. N. Simple Thick-Film Thread-

Based Voltammetric Sensors. *Electrochem. commun.* **2014**, *46*, 128–131.

(61)   Glavan, A. C.; Ainla, A.; Hamedi, M. M.; Fernández-Abedul, M. T.; Whitesides, G. M. Electroanalytical Devices with Pins and Thread. *Lab Chip* **2016**, *16* (1), 112–119.

(62)   Ochiai, L. M.; Agustini, D.; Figueiredo-Filho, L. C. S.; Banks, C. E.; Marcolino-Junior, L. H.; Bergamini, M. F. Electroanalytical Thread-Device for Estriol Determination Using Screen-Printed Carbon Electrodes Modified with Carbon Nanotubes. *Sensors Actuators B Chem.* **2017**, *241*, 978–984.

(63)   Song, T. T.; Wang, W.; Meng, L. L.; Liu, Y.; Jia, X. B.; Mao, X. Electrochemical Detection of Human Ferritin Based on Gold Nanorod Reporter Probe and Cotton Thread Immunoassay Device. *Chinese Chem. Lett.* **2017**, *28* (2), 226–230.

(64)   Agustini, D.; Bergamini, M. F.; Marcolino-Junior, L. H. Characterization and Optimization of Low Cost Microfluidic Thread Based Electroanalytical Device for Micro Flow Injection Analysis. *Anal. Chim. Acta* **2017**, *951*, 108–115.

(65)   Curto, V. F.; Coyle, S.; Byrne, R.; Angelov, N.; Diamond, D.; Benito-Lopez, F. Concept and Development of an Autonomous Wearable Micro-Fluidic Platform for Real Time pH Sweat Analysis. *Sensors Actuators, B Chem.* **2012**, *175*, 263–270.

(66)   Erenas, M. M.; De Orbe-Payá, I.; Capitan-Vallvey, L. F. Surface Modified Thread-Based Microfluidic Analytical Device for Selective Potassium Analysis. *Anal. Chem.* **2016**, *88* (10), 5331–5337.

(67)   Gonzalez, A.; Gaines, M.; Gomez, F. A. Thread-Based Microfluidic Chips as a Platform to Assess Acetylcholinesterase Activity. *Electrophoresis* **2017**, *38* (7), 996–1001.

(68)   Meng, L. L.; Song, T. T.; Mao, X. Novel Immunochromatographic Assay on Cotton Thread Based on Carbon Nanotubes Reporter Probe. *Talanta* **2017**, *167* (November 2016), 379–384.

(69)   Gonzalez, A.; Estala, L.; Gaines, M.; Gomez, F. A. Mixed Thread/paper-Based Microfluidic Chips as a Platform for Glucose Assays. *Electrophoresis* **2016**, *37* (12), 1685–1690.

(70)   Owens, T. L.; Leisen, J.; Beckham, H. W.; Breedveld, V. Control of Microfluidic Flow in Amphiphilic Fabrics. *ACS Appl. Mater. Interfaces* **2011**, *3* (10), 3796–3803.

(71)   Vatansever, F.; Burtovyy, R.; Zdyrko, B.; Ramarantnam, K.; Andrukh, T.; Minko, S.; Owens, J. R.; Kornev, K. G.; Luzinov, I. Toward Fabric-Based Flexible Microfluidic Devices: Pointed Surface Modification for pH Sensitive Liquid Transport. *ACS Appl. Mater. Interfaces* **2012**, *4*, 4541–4548.

(72)   Nilghaz, A.; Bagherbaigi, S.; Lam, C. L.; Mousavi, S. M.; Córcoles, E. P.; Wicaksono, D. H. B. Multiple Semi-Quantitative Colorimetric Assays in Compact Embeddable Microfluidic Cloth-Based Analytical Device (µCAD) for Effective Point-of-Care Diagnostic. *Microfluid. Nanofluidics* **2015**, 317–333.

(73)   Guan, W.; Liu, M.; Zhang, C. Electrochemiluminescence Detection in Microfluidic Cloth-Based Analytical Devices. *Biosens. Bioelectron.* **2016**, *75*, 247–253.

(74)   Liu, R.; Zhang, P.; Li, H.; Zhang, C. Lab-on-Cloth Integrated with Gravity/capillary Flow Chemiluminescence (GCF-CL): Towards Simple, Inexpensive, Portable, Flow System for Measuring Trivalent Chromium in Water. *Sensors Actuators, B Chem.* **2016**, *236*, 35–43.

(75)   Liu, M.; Liu, R.; Wang, D.; Liu, C.; Zhang, C. A Low-Cost, Ultraflexible Cloth-Based Microfluidic Device for Wireless Electrochemiluminescence Application. *Lab Chip* **2016**, *16* (15), 2860–2870.

(76) Liu, R.; Liu, C.; Li, H.; Liu, M.; Wang, D.; Zhang, C. Bipolar Electrochemiluminescence on Thread: A New Class of Electroanalytical Sensors. *Biosens. Bioelectron.* **2017**, *94* (February), 335–343.

(77) Baysal, G.; Önder, S.; Göcek, İ.; Trabzon, L.; Kızıl, H.; Kök, F. N.; Karagüzel Kayaoğlu, B. Design and Fabrication of a New Nonwoven-Textile Based Platform for Biosensor Construction. *Sensors Actuators B Chem.* **2015**, *208*, 475–484.

(78) Curto, V. F.; Fay, C.; Coyle, S.; Byrne, R.; O'Toole, C.; Barry, C.; Hughes, S.; Moyna, N.; Diamond, D.; Benito-Lopez, F. Real-Time Sweat pH Monitoring Based on a Wearable Chemical Barcode Micro-Fluidic Platform Incorporating Ionic Liquids. *Sensors Actuators B Chem.* **2012**, *171–172*, 1327–1334.

(79) Robinson, A. M.; Zhao, L.; Shah Alam, M. Y.; Bhandari, P.; Harroun, S. G.; Dendukuri, D.; Blackburn, J.; Brosseau, C. L. The Development of "fab-Chips" as Low-Cost, Sensitive Surface-Enhanced Raman Spectroscopy (SERS) Substrates for Analytical Applications. *Analyst* **2015**, *140* (3), 779–785.

(80) Agustini, D.; Bergamini, M. F.; Marcolino-Junior, L. H. Tear Glucose Detection Combining Microfluidic Thread Based Device, Amperometric Biosensor and Microflow Injection Analysis. *Biosens. Bioelectron.* **2017**, *98* (May), 161–167.

(81) Caetano, F. R.; Carneiro, E. A.; Agustini, D.; Figueiredo-Filho, L. C. S.; Banks, C. E.; Bergamini, M. F.; Marcolino-Junior, L. H. Combination of Electrochemical Biosensor and Textile Threads: A Microfluidic Device for Phenol Determination in Tap Water. *Biosens. Bioelectron.* **2018**, *99* (May 2017), 382–388.

(82) Bush, D. R.; Zang, L.; Belov, A. M.; Ivanov, A. R.; Karger, B. L. High Resolution CZE-MS Quantitative Characterization of Intact Biopharmaceutical Proteins: Proteoforms of Interferon-β1. *Anal. Chem.* **2016**, *88* (2), 1138–1146.

(83) Li, Y.; Champion, M. M.; Sun, L.; Champion, P. A. D.; Wojcik, R.; Dovichi, N. J. Capillary Zone Electrophoresis-Electrospray Ionization-Tandem Mass Spectrometry as an Alternative Proteomics Platform to Ultraperformance Liquid Chromatography-Electrospray Ionization-Tandem Mass Spectrometry for Samples of Intermediate Complexity. *Anal. Chem.* **2012**, *84* (3), 1617–1622.

(84) Wang, Y.; Li, X.; Hu, H.; Liu, G.; Rabnawaz, M. Hydrophilically Patterned Superhydrophobic Cotton Fabrics and Their Use in Ink Printing. *J. Mater. Chem. A* **2014**, *2* (21), 8094–8102.

(85) Leal, A. A.; Naeimirad, M.; Gottardo, L.; Schuetz, P.; Zadhoush, A.; Hufenus, R. Microfluidic Behavior in Melt-Spun Hollow and Liquid Core Fibers. *Int. J. Polym. Mater. Polym. Biomater.* **2016**, *65* (9), 451–456.

(86) Cho, D.; Matlock-Colangelo, L.; Xiang, C.; Asiello, P. J.; Baeumner, A. J.; Frey, M. W. Electrospun Nanofibers for Microfluidic Analytical Systems. *Polymer (Guildf).* **2011**, *52* (15), 3413–3421.

(87) Mirabedini, A.; Foroughi, J.; Farajikhah, S.; Wallace, G. G. Developments in Conducting Polymer Fibres: From Established Spinning Methods toward Advanced Applications. *RSC Adv.* **2016**, *6* (110), 108152–108152.

(88) Seyedin, S. Z. Fabrication of Conducting Elastomeric Composite Fibres. *Univ. Wollongong Thesis Collect. 1954-2016* **2014**.

(89) Ullmann, F. *Ullmann's Fibers.*; Wiley-VCH, 2008.

(90) Zhang, D. *Advances in Filament Spinning of Polymers and Textiles.*

(91) Hochleitner, G.; Jüngst, T.; Brown, T. D.; Hahn, K.; Moseke, C.; Jakob, F.; Dalton, P. D.; Groll, J. Additive Manufacturing of Scaffolds with Sub-Micron Filaments via Melt Electrospinning Writing. *Biofabrication* **2015**, *7* (3).

(92) Dalton, P. D. Melt Electrowriting with Additive Manufacturing Principles. *Curr. Opin. Biomed. Eng.* **2017**, *2*, 49–57.

(93) Teo, W. E.; Ramakrishna, S. A Review on Electrospinning Design and Nanofibre Assemblies. *Nanotechnology* **2006**, *17* (14), R89–R106.

(94) Huang, Z. M.; Zhang, Y. Z.; Kotaki, M.; Ramakrishna, S. A Review on Polymer Nanofibers by Electrospinning and Their Applications in Nanocomposites. *Compos. Sci. Technol.* **2003**, *63* (15), 2223–2253.

(95) Adanur, S. *Handbook of Weaving*; CRC Press, 2000.

(96) Naik, S. *Weaving and Knitting Technology*; APH Publishing Corporation, 2013.

(97) Horrocks, A. R.; Anand, S. C. *Handbook of Technical Textiles*; Woodhead Publishing Limited, 2000.

(98) Sinclair, R. *Textiles and Fashion : Materials, Design and Technology*; 2014.

(99) Ray, S. C. *Fundamentals and Advances in Knitting Technology*; Woodhead Publishing Limited, 2011.

(100) Spencer, D. J. *Knitting Technology: A Comprehensive Handbook and Practical Guide*; CRC Press, 2001.

(101) Corbman, B. P. *Textiles: Fiber to Fabric*; MCGRAW-HILL Professional, 1983.

(102) Wingate, I. B.; Mohler, J. F. *Textile Fabrics and Their Selection*; Prentice-Hall, 1984.

(103) Hutten, I. M. *Handbook of Nonwoven Filter Media*; Elsevier, 2007.

(104) Stankovich, S.; Dikin, D. A.; Dommett, G. H. B.; Kohlhaas, K. M.; Zimney, E. J.; Stach, E. A.; Piner, R. D.; Nguyen, S. T.; Ruoff, R. S. Graphene-Based Composite Materials. *Nature* **2006**, *442* (7100), 282–286.

(105) Ramanathan, T.; Abdala, A. A.; Stankovich, S.; Dikin, D. A.; Herrera-Alonso, M.; Piner, R. D.; Adamson, D. H.; Schniepp, H. C.; Chen, X.; Ruoff, R. S.; et al. Functionalized Graphene Sheets for Polymer Nanocomposites. *Nat. Nanotechnol.* **2008**, *3* (6), 327–331.

(106) Phiri, J.; Gane, P.; Maloney, T. C. General Overview of Graphene: Production, Properties and Application in Polymer Composites. *Mater. Sci. Eng. B* **2017**, *215*, 9–28.

(107) Allen, M. J.; Tung, V. C.; Kaner, R. B. Honeycomb Carbon -- A Study of Graphene. *Am. Chem. Soc.* **2009**, 184.

(108) Hernandez, Y.; Nicolosi, V.; Lotya, M.; Blighe, F. M.; Sun, Z.; De, S.; McGovern, I. T.; Holland, B.; Byrne, M.; Gun'Ko, Y. K.; et al. High-Yield Production of Graphene by Liquid-Phase Exfoliation of Graphite. *Nat. Nanotechnol.* **2008**, *3* (9), 563–568.

(109) Petrone, N.; Dean, C. R.; Meric, I.; Van Der Zande, A. M.; Huang, P. Y.; Wang, L.; Muller, D.; Shepard, K. L.; Hone, J. Chemical Vapor Deposition-Derived Graphene with Electrical Performance of Exfoliated Graphene. *Nano Lett.* **2012**, *12*, 2751–2756.

(110) Park, S.; Ruoff, R. S. Chemical Methods for the Production of Graphenes. *Nat. Nanotechnol.* **2009**, *4* (4), 217–224.

(111) Eichler, J.; Lesniak, C. Boron Nitride (BN) and BN Composites for High-Temperature Applications. *J. Eur. Ceram. Soc.* **2008**, *28* (5), 1105–1109.

(112) Zhi, C.; Bando, Y.; Tang, C.; Kuwahara, H.; Golberg, D. Large-Scale Fabrication of Boron Nitride Nanosheets and Their Utilization in Polymeric Composites with Improved Thermal and Mechanical Properties. *Adv. Mater.* **2009**, *21* (28), 2889–2893.

(113) Lin, Y.; Williams, T. V.; Connell, J. W. Soluble, Exfoliated Hexagonal Boron Nitride Nanosheets. *J. Phys. Chem. Lett.* **2010**, *1* (1), 277–283.

(114) B., B. Atomic Resolution Imaging and Topogarphy of Boron Nitride Sheet Produced by Chemical Exfoliation. *ACS Nano* **2010**, *4* (3), 1299.

(115) Dmitri Golberg,* Yoshio Bando, Yang Huang, Takeshi Terao, Masanori Mitome, Chengchun Tang, and C. Z. Boron Nitride Nanotubes and Nanosheets. *ACS Nano* **2010**, *4* (6), 2979–2993.

(116) Divincenzo, D. P.; Duer, W.; Cirac, J. I.; Zoller, P.; Steel, D. G.; Rice, T. M.; Stahl, A.; Gotoh, H.; Temmyo, J.; Takagahara, T.; et al. Deep Ultraviolet Light – Emitting Hexagonal Boron Nitride Synthesized at Atmospheric Pressure. *Science (80-.).* **2007**, *317*, 932–935.

(117) Shi, Y.; Hamsen, C.; Jia, X.; Kim, K. K.; Reina, A.; Hofmann, M.; Hsu, A. L.; Zhang, K.; Li, H.; Juang, Z. Y.; et al. Synthesis of Few-Layer Hexagonal Boron Nitride Thin Film by Chemical Vapor Deposition. *Nano Lett.* **2010**, *10* (10), 4134–4139.

(118) Lipp, A.; Schwetz, K. A.; Hunold, K. Hexagonal Boron Nitride: Fabrication, Properties and Applications. *J. Eur. Ceram. Soc.* **1989**, *5* (1), 3–9.

(119) Xuan, X.; Li, D. Analytical Study of Joule Heating Effects on Electrokinetic Transportation in Capillary Electrophoresis. *J. Chromatogr. A* **2005**, *1064* (2), 227–237.

Chapter 2:

Materials and methods

2.1. Materials

Low-density polyethylene (LDPE) pellets were kindly supplied by CSIRO and hydrophilic thermoplastic biocompatible polyurethane elastomers (PU) pellets were purchased from Advansource HydroThane^{TM} AL 25-80A. Boron nitride nanopowders (<150 nm average particle size (BET), 99% trace metals basis), Tris(hydroxymethyl)aminomethane (TRIS), N-Cyclohexyl-2-aminoethanesulfonic acid (CHES), 3-aminopropyltriethoxysilane, hydrochloric acid (HCl), Hypophosphorous acid solution (H_3PO_4), Gold (III) trichloride, Potassium ferricyanide and phosphate buffered saline (PBS) were purchased from Sigma-Aldrich and used without modification. Ethanol (EtOH) and perchloric acid ($HClO_4$) was sourced from Ajax Finechem and pyrrole was purchased from Merck and used without further purification. Stainless steel filaments were purchased from Bekaert, silver-plated nylon yarns from 3L Tex Co.,Ltd and polyester threads from Shijiazhuang Yunchong Trading Co., Ltd.

Millipore (Sartorius Stedim Biotech) water was used in entire project. Liquid crystalline graphene oxide (LCGO) aqueous dispersions at a concentration of 8 mg mL^{-1} were supplied by the Materials Node of the Australian National Fabrication Facility (ANFF).

2.2. Experimental

2.2.1. LCGO/LDPE composites

LDPE pellets were ground into ca. 200 μm size powders suitable for use in a bench top melt extrusion system utilizing Cyro grinder machine. Polymer pellets and machine's mechanical parts (rotating blades) were cooled down constantly using liquid nitrogen.

To make LCGO/LDPE composites, first LDPE powders were mixed with LCGO aqueous dispersion to achieve the desired LCGO loading in final composite. Then LDPE powders

were coated with LCGO by evaporation of water in dispersion using BUCHI Rotovapor R-210 rotary evaporator machine utilising a 70°C water bath temperature at 70 mbar vacuum.

2.2.2. Melt spinning

LDPE and LCGO/LDPE fibres were made using a Barrell twin-screw extruder (http://www.barrell.com.au/engineering-products/mini-laboratory-extruder/). Figure 2.1 shows the screw setup used for making polymeric fibres. The temperature profile for the 10 different extrusion zones and die are given in Table 2.1.
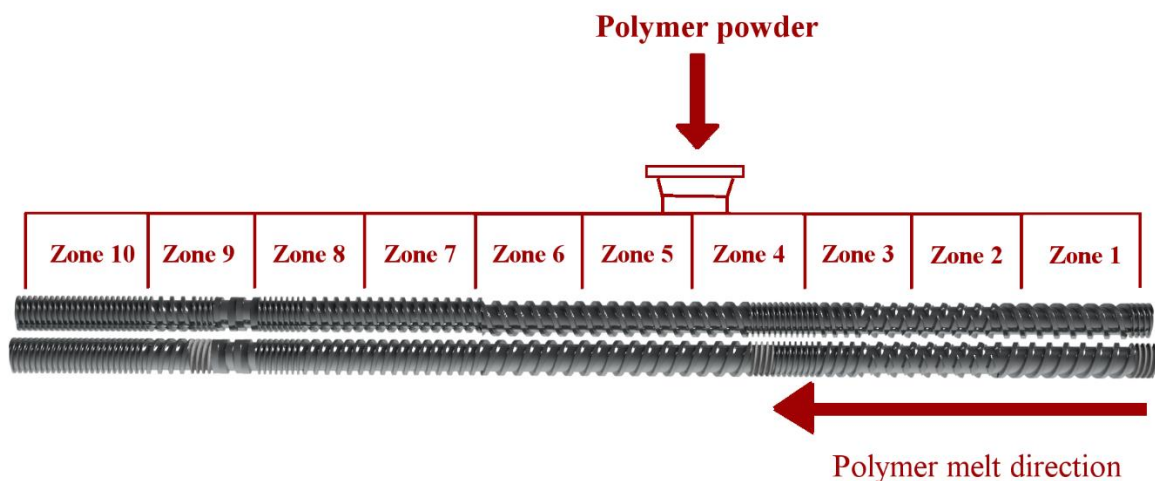
Figure 2.1: Scheme of screw setup used for melt spinning, ten heating zones and polymer melt direction

Table 2.1: Heat profile for making melt spun fibres

Zone	Temperature (^{o}C)
Zone 1	70
Zone 2	110
Zone 3	130
Zone 4	150
Zone 5	160
Zone 6	160
Zone 7	160
Zone 8	160
Zone 9	150
Zone 10	140
Extrusion die	140

Fibres were made using a Ø 700μm extrusion die. Fibres were stretched using custom fabricated roller stretching system before being collected onto a bobbin. The melt spinning setup comprising of twin-screw melt extruder, stretching unit and winding unit as shown in Figure 2.2.

Figure 2.2: melt spinning setup, I: twin-screw melt extrusion, II: stretching unit and III: winding unit

2.2.3. Wet Spinning of LCGO/PU composites

2.2.3.1. Making PU solutions

To make LCGO/PU composites, first PU polymer was dissolved in EtOH/Water (85:15 v/v) at 70°C with constant stirring to make a 100 mg mL^{-1} PU solution.

2.2.3.2. Making LCGO dispersion in EtOH

To replace water with EtOH in the LCGO dispersion, first a LCGO aqueous dispersion was transferred into centrifuge tubes and some EtOH was added to each tube. Then solutions were centrifuged (Eppendorf Centrifuge 5804) at 8000 rpm for 90 minutes. Supernatants were pippeted out and the remaining was washed with EtOH. This procedure was repeated 10 times to replace water with EtOH in LCGO dispersion.

2.2.3.3. Composite making

LCGO/PU composites were prepared by gradual addition of PU (100 mg mL^{-1}) solution to its equal volume of EtOH/water (85:15 v/v) solution that contained desired amount of LCGO in EtOH while constantly stirred on a hot plate.

LCGO/PU films for characterisation were produced by casting the composite solution in glass petri dishes under fume hood.

2.2.4. Reduction of LCGO/PU composites

LCGO/PU samples were reduced in 5 wt.% hypophosphorous acid at 80 °C overnight. To remove the excess acid, reduced samples were washed with DI water and finally vacuum dried at 80 °C.

2.2.5. BN/PU composites

Desired amount of BN nanopowder was weighed and a uniform dispersion in EtOH/Water (85:15 v/v) was prepared by 60 minutes of bath sonication (Branson B5500R-DTH). Then BN/PU composites were made by gradual addition of PU (100 mg mL^{-1}) solution to its equal volume of BN dispersion in EtOH/water (85:15 v/v) while dispersion was constantly stirred on a hot plate.

BN/PU films for characterisation were then prepared by casting the composite solution in glass petri dishes under fume hood.

2.2.6. Wet spinning

Fibres were made from different spinning formulations using horizontal wet-spinning setup which is shown in Figure 2.3. Spinning formulation was injected into a 50 cm horizontal coagulation bath filled with non-solvent composition. Injections of spinning formulation, transferred into a Ø 15.75 mm syringe, were performed with a controlled flow rate by utilizing a syringe pump. A 20 gauge needle with blunt tip was used as spinneret. Solvent/non-solvent interaction between spinning formulation and non-solvent composition in coagulation bath resulted in formation of solid fibres. Spun fibres were then collected on a speed-controlled winder.

Figure 2.3: Scheme of horizontal wet-spinning configuration includes syringe filled with solution, coagulation bath and collector.

2.2.7. Knitting

3D knitted structure substrates for electrofluidic tests were prepared on a Harry Lucas (R_RR3-1S-2zoll) circular knitting machine with the head size of 1/12 in.; gauge, 28 and 8 needles (http://www.lucas-elha.de/products/ckmsinglejersey/r_rr3-1s-2zoll.php). A feeding tension setting of 3.2 and pickup tension of 32 were applied to threads and knitted structures, respectively. Different 3D textile structures were prepared from commercially available polyester (PET) threads and combination of PET with composite fibres by feeding PET yarns or PET yarns in parallel composite fibres into a Harry-Lucas knitting machine. To achieve knitted structures with similar architectures, a constant feeding tension of 3.2 for PET threads and pick-up tension 32 (an empirical machine specific setting) for the knitted structure were applied for making all structures. Schematic of knitting procedure is shown in Figure 2.4.

Figure 2.4. scheme of making 3D knitted structures with commercial PET and a composite fibre

2.2.8. Braiding

3D braided structures were prepared using Trenz-Export (12/80) circular braiding machine (http://www.braiding-machines.net/productos.php?IDpro=12). 12 different spools of threads were fitted into machine and different core materials were used to make 3D braid structures.

2.2.9. Electrofluidic experiments

3D printed reservoirs filled with buffer solutions were used to perform electrophoresis tests on textile structures. DC voltages were supplied by a high voltage sequencer purchased from LabSmith, Inc. (HVS 448LC 3000D high voltage sequencer). Micro-clip terminators and 23 gauge, ca. 0.5 mm diameter, Platinum (Pt) electrodes were used to apply voltages to the textile structures. HVS connections were secured in a box to avoid electrical shocks.

2.3. Characterisation methods
2.3.1. Polymers, solutions and dispersions characterisations
2.3.1.1. LCGO sheet size measurement

LCGO sheets were first deposited on pre-cleaned and silanized silicon wafer (300 nm SiO_2 layer). Silane solution was prepared by mixing 3-aminopropyltriethoxysilane with water (1:9 v/v) and one drop of hydrochloric acid. Pre-cut silicon substrates were silanized by immersing in aqueous silane solution for 30 min followed by washing thoroughly with D.I. water. LCGO sheets were then deposited onto the silanized silicon substrates by immersing a silicon substrate into the LCGO dispersion (50 µg mL^{-1}) for a few seconds then immersing in D.I. water and air-drying. The as-deposited LCGO sheets were directly examined by scanning electron microscopy analysis. The lateral size distributions of 256

isolated LCGO sheets were determined and analysed using imageJ[1] image analysis software. The lateral size of LCGO sheets was defined as the diameter of an equal area circle.

2.3.1.2. Zeta potential on LCGO

Zeta potential of LCGO aqueous dispersions were measured by dynamic light scattering (DLS) technique using a zetasizer (Malvern Instruments Nano-ZS) using dip cell cuvettes. The zeta potential for each sample was reported as an average of 10 measurements.

2.3.1.3. Rheological tests of PU composite spinning formulations

Rheology tests on PU and PU composites (LCGO/PU and BN/PU) solutions were performed using a rheometer (TA Instruments AR-G2) at room temperature (25 $^{\circ}$C) using a flow test from $0.01 - 400$ s^{-1}. Cone plate geometry (cone angle 2°, diameter 40 mm and truncation 55µm) was used to do viscosity tests. Solutions were protected from solvent evaporation and/or change in decomposition by placing a protective chamber around the geometry. 2-minute holds at each shear rate were used to equilibrate the solutions. Measurements were made logarithmically at 10 points per decade of shear rates.

2.3.1.4. Thermogravimetric Analysis (TGA)

TGA analysis on polymeric samples was performed on TA instruments Q500 in under nitrogen flow with the flow rate of 90 mL min^{-1} using Platinum pans. To measure the mass loss of samples with temperature, samples were heated up to 600 $^{\circ}$C with 10 $^{\circ}$C min^{-1} heating rate and mass loss was recorded.

---

[1] ImageJ. https://imagej.nih.gov/ij/

2.3.1.5. Differential scanning calorimetry (DSC)

Differential scanning calorimetry (DSC) experiments were performed to determine the melting temperature of polymeric samples using a TA instrument Q100. Samples were sealed in standard Aluminium pans then placed in the instrument.

2.3.1.6. UV-Vis spectroscopy

UV-1800 Shimadzu UV spectrophotometer was used to carry out spectroscopy on different aqueous solutions in standard plastic cuvettes. Absorbance of solutions were measured in the wave length rang of 400 to 700 nm.

2.3.1.7. Capacitively Coupled Contactless Conductivity (C4D) measurement

An output signal measured by volts for different concentrations of solutions, was obtained and measured using a commercial C^4D (TraceDec), supplied by Innovative Sensor Technologies GmbH (Strasshof, Austria), with a capillary head- stage that specifically accommodates a 660 μm fused silica capillary. Solutions were injected into capillary tube to fill the tube. Measurement frequency and gain were adjusted for different solutions to maximum signal did not exceed 2.5 volts. Capillary was washed thoroughly with DI water before each measurement.

2.3.2. Films and Fibres characterisation
2.3.2.1. Mechanical test

To ensure that fibres were held vertically between clamps, fibres were initially mounted into paper frames which were then transferred to the tensile tester machine. After mounting and before testing the frame sides were cut. Fibres of 3 cm in length were fixed vertically between two clamps and stretched at a 10 mm min^{-1} rate using a mechanical

testing system (Shimadzu EZ mechanical tester) equipped with a computer-based control/analysis system. A 10 N load cell was used in all experiments. Ultimate strength was determined as the maximum stress before the fibre fractured and the corresponding strain was determined as the elongation at break. Young's modulus for fibres were calculated using the equation 1 in the initial linear part of stress-strain curves.

$$E = \frac{\sigma}{\varepsilon}$$
(1)

Where E, σ and ε represent Young's modulus, stress and strain, respectively.

2.3.2.2. Scanning electron microscopy

Fibre and textile cross-sections were observed using scanning electron microscope (JEOL JSM 7500-FA). Fibres and textiles were freeze-fractured while immersed in liquid nitrogen to obtain smooth surfaces. Samples were sputter coated with a layer of about 5 nm of Pt using a sputter coater (EDWARDS Auto 306). LCGO sheets and BN nanoparticles deposited on silicon wafers were also coated with Pt and analysed using the same microscope.

2.3.2.3. Fibre diameter and film thickness measurements

An optical microscope (Leica DM6000 Optical Microscope) was used to measure the fibre diameters as well as film thicknesses utilising the built-in image analysis tool in the associated Leica software. The average value of at least 5 measurements was considered as the fibre diameter or film thickness.

2.3.2.4. Raman spectroscopy

Raman spectroscopy was performed on different samples including spun composite fibres, LCGO film and BN nanopowders utilising a Jobin Yvon Horiba HR800 confocal Raman microscope with a 632 nm laser and a 300-line grating under 100X objective to achieve a

resolution of ± 1.25 cm^{-1}. Calculations such as I_D/I_G were made after a common baseline correction was applied to all acquired spectra.

2.3.2.5. Fourier Transform Infrared Spectroscopy (FTIR) analysis

FTIR spectra were obtained using Shimadzu IRPrestige-21 infrared spectrometer.

2.3.2.6. Specific heat capacity (C_P) measurement

Modulated differential scanning calorimetry (MDSC) experiments in standard aluminium pans using TA instrument Q100 were performed to measure specific heat capacity of polymeric samples. TA instrument first calibrated in MDSC mode with standard sapphire material with known heat capacity at desired temperature range. Around 5mg of the sample was sealed into a standard aluminium pan and heated from 10 to 75 °C at the heating rate of 5 °C min^{-1}, with the oscillation amplitude of ±1 °C and oscillation period of 60 s.

2.3.2.7. Thermal diffusivity measurements

To perform thermal diffusivity experiments, film samples prepared by casting solutions in petri-dishes were first cut into Ø 12.5 mm disks using punches and then they all coated with graphite powder using commercial graphite powder spray. The thermal diffusivity was then measured using the NETZSCH laser flash apparatus LFA 457 MicroFlash®. Thermal diffusivity of samples at each temperature was measured three times.

The Laser Flash (LFA) technique is a fast, non-destructive and non-contact method for determining thermal diffusivity and specific heat. The front surface of a plane-parallel sample is heated by a short energy light pulse. From the resulting temperature of the rear face measured with an infrared (IR) detector, thermal diffusivity is determined. Having thermal diffusivity, sample density and sample specific heat capacity, thermal

58

conductivity can be calculated using equation 2.

$$\lambda(T) = a(T) \cdot c\rho(T) \cdot \rho(T) \tag{2}$$

Where λ represents thermal conductivity [W $(m \cdot K)^{-1}$], a represents thermal diffusivity [mm² s^{-1}], Cp is specific heat capacity [J $(g \cdot K)^{-1}$] and ρ shows sample bulk density [g cm^{-3}].

Chapter 3:

Tunable Flow Rate in Textile-based Microfluidics Utilizing Composite Fibers

3.1. Introduction

Threads and textiles have recently shown immense promise for the mass production of cheap microfluidic devices with outstanding characteristics [1-3]. Threads and textiles possess unique features that make them suitable for production of next generation microfluidics. Features such as flexibility, high mechanical strength in wet state, reusability, disposability, an independence of external power for fluid movement (due to capillary channels between fibers), no bubbles that may plague microfluidic systems, an ease of chemical surface functionalization and a readily accessible analyte at the open surface at the textile-solvent interface [1,2,4-7].

Since the first introduction of thread-based microfluidics [2,1], the nature of the textiles and threads deployed have attracted a lot of attention. A variety of threads have been used in microfluidics for applications ranging from simple fluid wicking properties to complicated microfluidic textile platforms for portable diagnostics such as textile-based real-time sweat monitoring devices [8-13].

Since, power-free fluid movement due to capillary action in textile-based microfluidics is a key element, a great deal of research work have been done to enhance the wicking rate of textiles by surface modification and removal of contamination utilizing chemical or plasma treatments [2,1,14,5,15,16]. However, these techniques have some major drawbacks. Wet chemical treatments are harsh and can potentially result in loss of mechanical properties. The reproducibility of the degree of surface modification is also affected by different molecular weight, crystallinity or tacticity. Generation of hazardous chemical waste and irregular surface etching are also need to be noted [17-19]. Plasma-treatment is also an expensive methods and enhanced wicking in textiles is a temporary effect and will not last for long [20].

In this chapter, we have utilized composite making approach a novel, easy, tunable and cost-effective method with long-lasting (permanent) effect that improves the mechanical properties of fibres to tune the surface chemistry of fibres. It has been also demonstrated that a tunable flow rate in 3D knitted structures comprised of liquid crystalline graphene oxide (LCGO) / low-density polyethylene (LDPE) composite fibres embedded into a 3D polyester (PET) knitted structure with an internal (hollow) channel as textile-based microfluidics can be achieved through modifying the surface chemistry of polymeric fibers utilizing the proposed approach. Herein, we show how surface chemistry within a 3D knitted structure can deliver controlled flow rates, well in excess of that typically achieved using standard fibers. The proposed technique can be potentially implemented in a range of applications in textile-based analytical devices includes tuning the analyte's movement, physical analyte concentration or entrapment and opens up new routes in textile-based point-of-care diagnostics.

As fluid movement in textiles and yarns requires capillaries formed between fibres in a thread, a single fibre cannot make a textile-based microfluidic structure. In this thesis fibre-based microfluidics refers to a thread-based microfluidic structure which is made by threads (yarns). Fabrics are also made of yarns and filaments arranged in a specific way.

3.2. Experimental
3.2.1. Composite development

LCGO/LDPE composite with LCGO loadings of 0.5, 1, 2 and 5 w/w% using a rotary evaporator at 70 °C at 70 mbar vacuum were prepared as described in 2.2.1 Figure 3.1.

Figure 3.1: left to right: LDPE, 0.5, 1, 2 and 5 w/w% LCGO/LDPE powders

3.2.2. Fibre spinning

To confirm extrusion parameters of LDPE and LCGO/LDPE composites, pristine LDPE and LCGO/LDPE coated powders were characterized using TA Dynamic scanning calorimetry (DSC) and TA thermogravimetric analysis (TGA), to evaluate their melting and decomposition temperature, respectively. DSC results show that LDPE melts at about 125 $^\circ$ C and LCGO coatings having no effect (Figure 3.2). LDPE and LCGO coated samples decomposed at about 400° C without noticing any effect resulting from addition of LCGO (Figure 3.3).
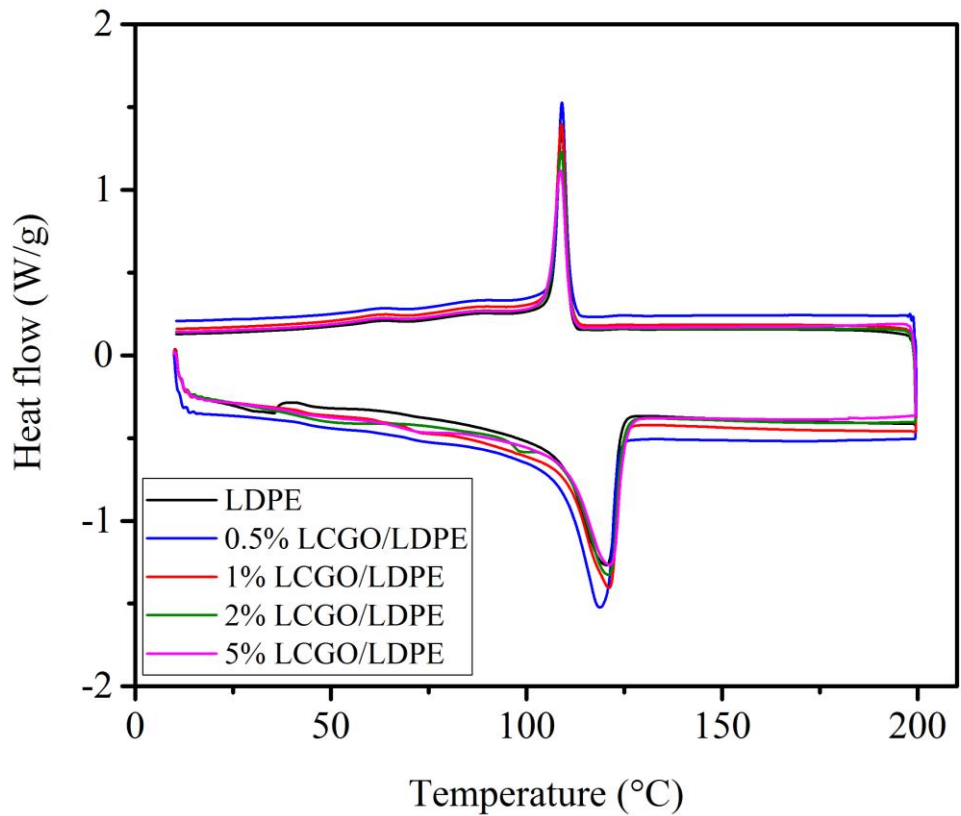
Figure 3.2: DSC spectra of LDPE and LCGO/LDPE composite fibres showing melting temperature at 125 °C
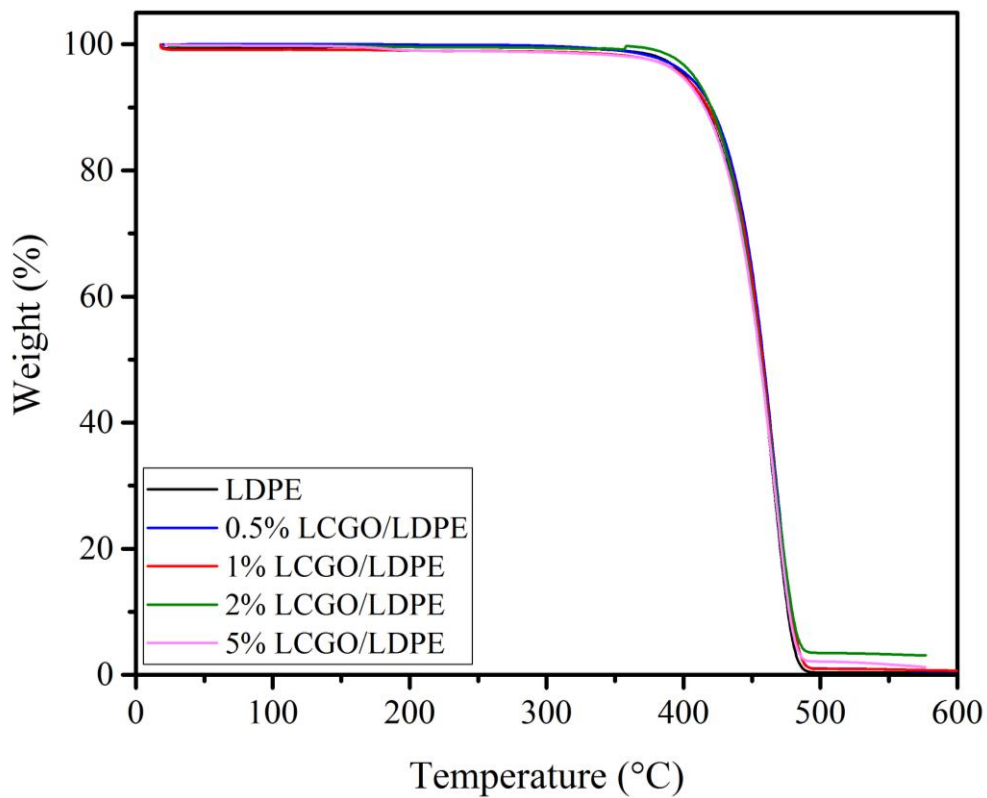
Figure 3.3: Decomposition temperature for LDPE and LCGO/LDPE powders acquired from TGA

Powders were melt extruded into fibres using a mini laboratory twin-screw melt extruder as described in 2.2.2. Melt spinning setup used is shown in Figure 3.4a. A screw speed of 20 rpm was used to extrude filament from which fibres were produced by stretching and collecting on a winder spool (Figure 3.4b). Circular cross-section shape LDPE and LCGO/LDPE composite fibres of about 100 μm in diameter were successfully produced, Figure 3.5.

Figure 3.4: (a) melt spinning setup, I: twin-screw melt extrusion, II: stretching unit and III: winding unit, and (b) left: pure and right: LCGO-coated LDPE powder.
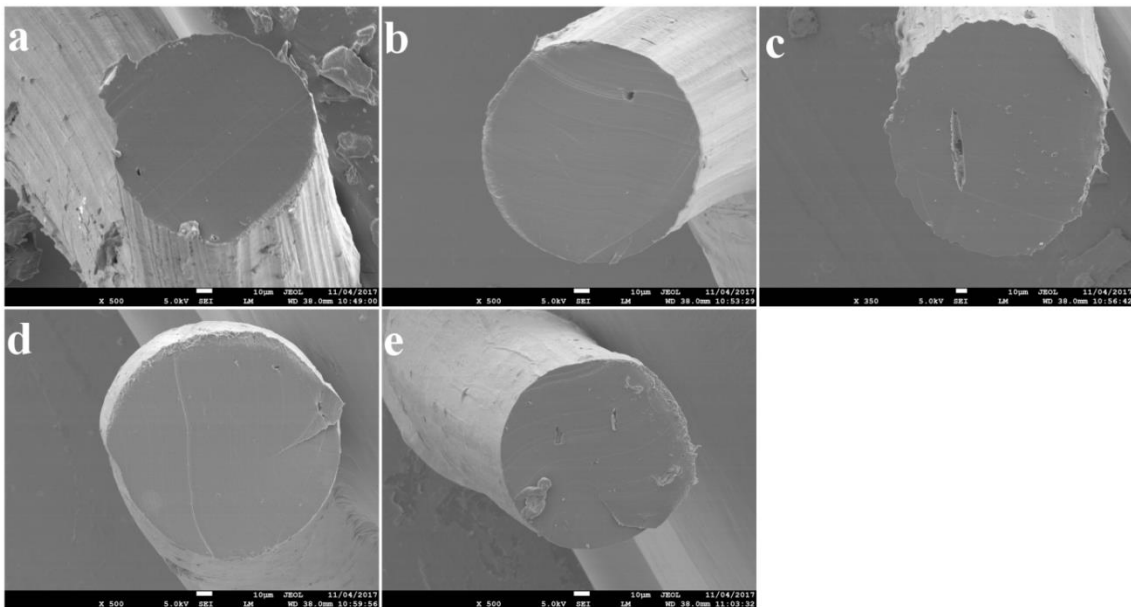
Figure 3.5: SEM images for cross-sections of (a) LDPE, (b) 0.5 w/w%, (c) 1 w/w%, (d) 2 w/w% and (e) 5 w/w% LCGO/LDPE fibres.

3.2.3. Making 3D structures

Since capillary action cannot be occur on a single fibre, only yarns (threads) and fabrics can be used as a suitable substrate for textile-based microfluidics. In this thesis (and most of the literature relating to textile-based microfluidics) fibre-based microfluidics refers to microfluidic devices in which yarns (threads) are the substrates. Utilising knitting and braiding techniques in this thesis, tubular structures with a hollow core were prepared which are referred to as 3D knitted or 3D braided structures and are different when compared to two-dimensional fabrics prepared by weaving or as non-woven mats.

Due to the good performance of polyester (PET) substrates in textile-based microfluidic devices,[21–23] PET was chosen as the base material. 3D knitted structures composed of commercial PET and LCGO/LDPE composite fibres were prepared as described in 2.2.7 and cross-section optical micrographs of knitted structures are shown in Figure 3.6.
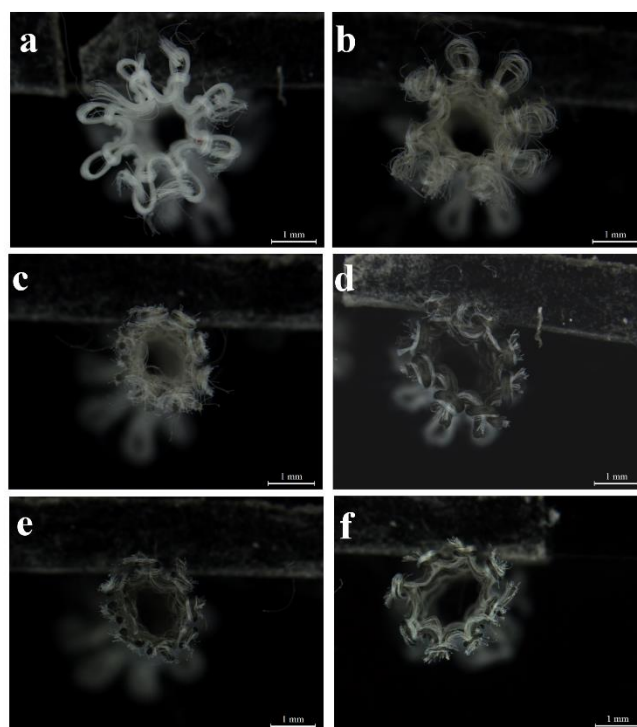
Figure 3.6: (a)-(f) optical micrographs showing cross-sections of a knitted structures comprised of 2 PET yarns, PET yarns parallel with LDPE, 0.5, 1, 2 and 5 w/w% LCGO/LDPE composite fibres, respectively

3.2.4. Characterisation

3.2.4.1. LCGO characterisation

Zeta-potential of LCGO aqueous dispersions were measured by dynamic light scattering (DLS) technique using a zetasizer (Malvern Instruments Nano-ZS) to determine the stability of the dispersions. The Zeta-potential of LCGO dispersions were found to be -28.7 ± 0.7 mV, a potential which is indicative of a stable dispersion. This value is close to the values reported in literature indicating a stable dispersion of LCGO[24].

3.2.4.2. Raman spectra on fibres

Raman spectra of LDPE and LCGO/LDPE composite fibres, shown in Figure 3.7, clearly shows that the LCGO was incorporated into LDPE matrix and formed a uniform composite. A typical Raman spectra of LDPE polymer with peaks that are attributed to

different vibration modes of CH_2 groups and C-C bonds was observed[25,26]. The characteristic D and G bands of graphene were observed at 1347 and 1586 cm^{-1}, respectively, in Raman Spectra of LCGO[27]. These peaks were also clearly observable in the Raman spectra of LCGO/LDPE composite fibres indicating the integration of LCGO into LDPE polymeric matrix.
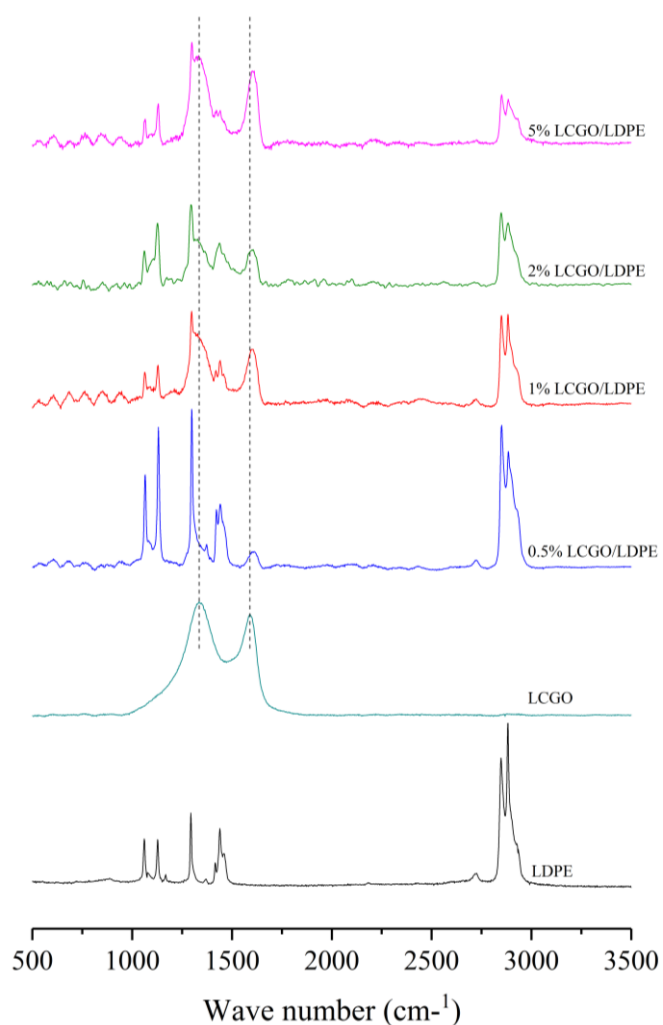
Figure 3.7: Raman spectra for LCGO films, LDPE and LCGO/LDPE fibres.

3.2.4.3. Fibre mechanical properties

To evaluate the mechanical properties of LDPE and LCGO/LDPE composite fibres, initially fibres diameters were measured using inbuilt image analysis application of optical

Leica microscope software. Then 30 mm lengths of fibres were fixed in a paper frame to ensure the fibres were held in a vertical position between the clamps of tensile tester machine. Prior to testing the paper frame was cut and the fibres stretched at the rate of 10 mm min^{-1} until fracture. Figure 3.8 shows stress-strain curves for LDPE and LCGO/LDPE composite fibres. Ultimate strength was determined as the maximum stress before the fibre fractured and the corresponding strain was determined as the elongation at break. Young's moduli for pure LDPE and LCGO/LDPE composite fibres were calculated using a MATLAB code (see appendix I).
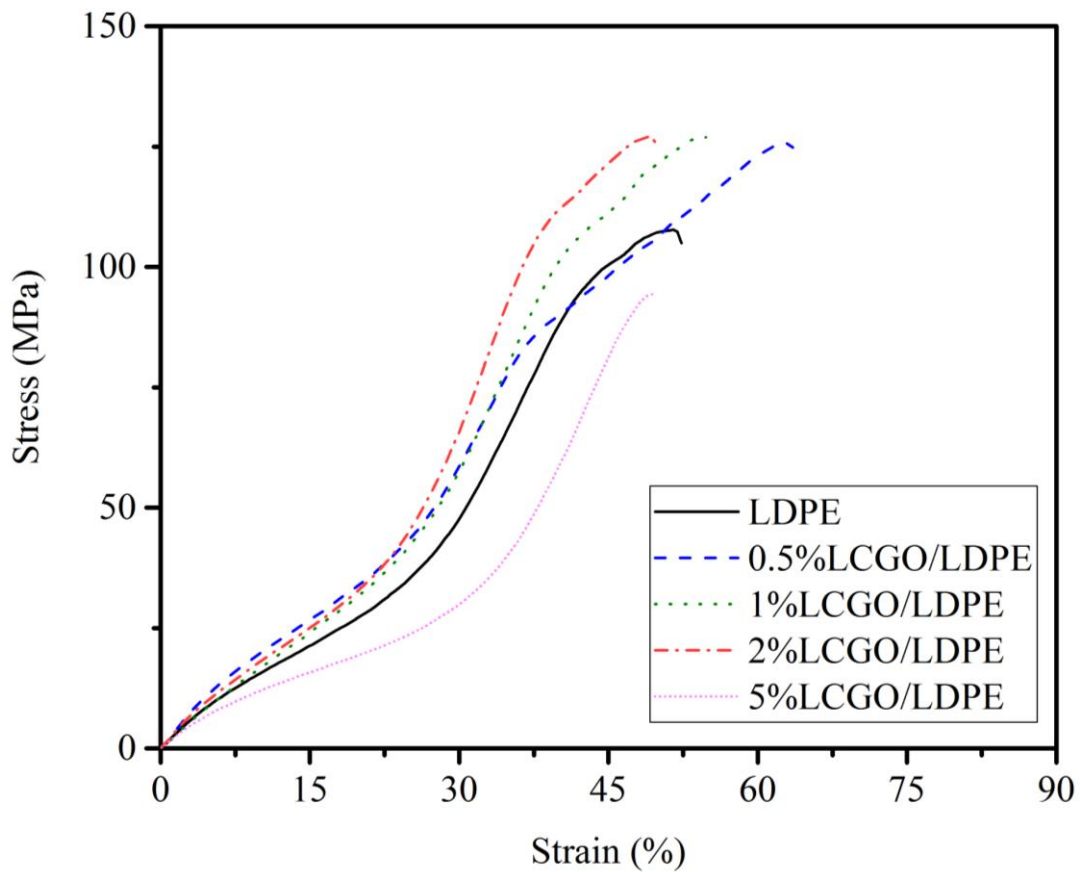
Figure 3.8: Stress-strain curve for LDPE and LCGO/LDPE composite fibres.

3.2.5. Wicking tests

3.2.5.1. Solutions and calibration curves

3.2.5.1.1. Wicking experiment setup

The wicking properties of 3D knitted structures comprising of PET threads with and without LDPE and LCGO/LDPE composite fibres were assessed by the amount of fluid transferred from one reservoir to the other across an 11 cm distance, holding both reservoirs at the same height as shown in Figure 3.9. Textile structures were pre-concentrated with the transfer solution prior to mounting between the two reservoirs. One reservoir was filled with 1 mL of solution and the amount of fluid transferred to the other reservoir was measured at 5, 10, 15 and 20 minutes intervals.
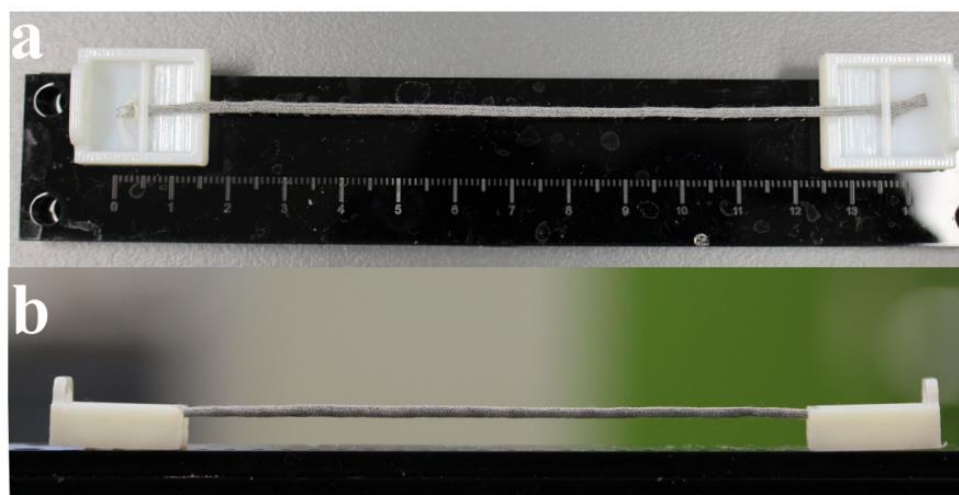
Figure 3.9: (a) top view and (b) side view of the experimental setup for wicking tests

3.2.5.1.2. Calibration curves for wicking tests

Three different solutions, i.e. deionized (D.I.) water with addition of commercial Pillar Box Red Food Colour to increase visibility, sodium chloride (NaCl) aqueous solution and tris(hydroxymethyl)aminomethane (Tris)/ N-Cyclohexyl-2-aminoethanesulfonic acid (CHES) ion pair as a typical electrolyte medium used in electrophoretic separation studies[28], were chosen for wicking experiments. 80 µg mL^{-1}(ppm) red dye, 20 mMolar

(mM) NaCl and 100 mM Tris/CHES aqueous solutions were used to perform wicking experiments. Calibration curves for different transfer solutions were established for the red dye, NaCl and Tris/CHES salts in D.I. water, used in wicking experiments. For the red dye, UV-Vis spectra were obtained for different solutions from 0.1-40.0 µg mL^{-1} and a linear UV-Vis absorption curve observed, Figure 3.10.
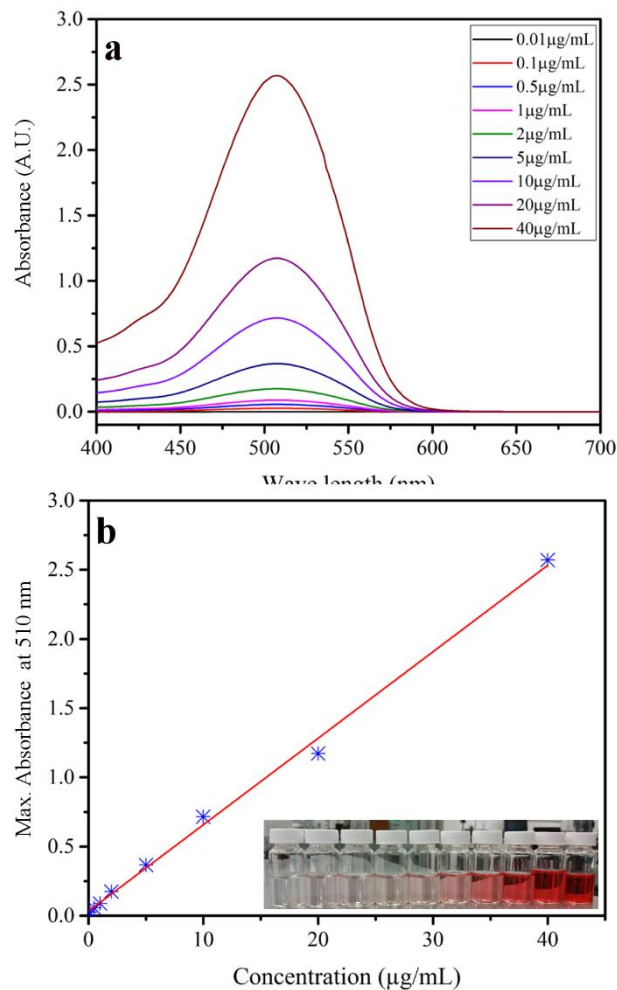
Figure 3.10: (a) UV-Vis spectra for dyes in different concentrations and (b) linear calibration curve for different concentrations of red dye in D.I. water (inset)

Calibration curves for NaCl and Tris/CHES solutions with different concentrations were obtained utilizing Capacitively Coupled Contactless Conductivity Detection (C^{4}D)[29] technique. The C^{4}D system was used due to the very small volumes on analyte being used

which made direct ionic conductivity tests impractical. A C^4D signal in volts was obtained for different concentrations of salts in D.I. water. In both cases, voltage signal increased rapidly with small increase in concentration of salts; however, the rate of increase levelled off at higher concentrations resulting in a non-linear calibration curve[30]. Consequently, as shown in Figure 3.11a and Figure 3.11b, power function calibration curves were obtained for NaCl and Tris/CHES aqueous solutions.
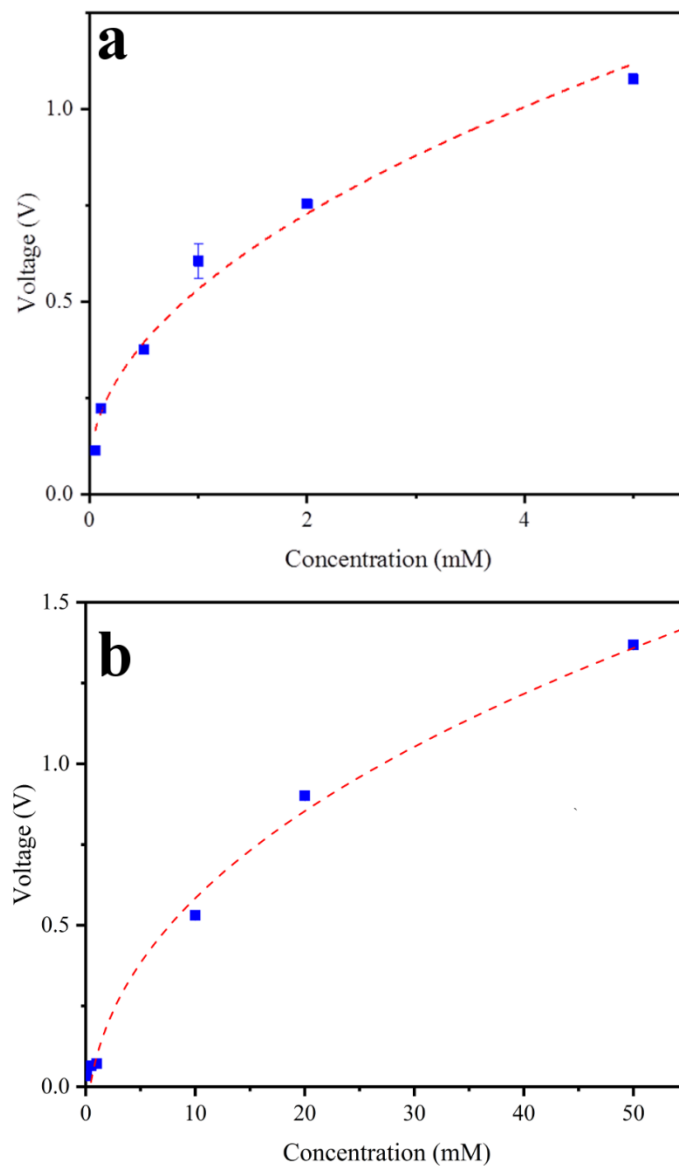
Figure 3.11: Calibration curves for (a) Signal(volts) for different concentrations of NaCl in D.I. water, and (b) Signal(volts) for different concentrations of Tris/CHES in D.I. water.

3.2.5.1.3. Flow rate measurements

Fluid in the receiver reservoir collected at different time intervals, was diluted to a volume of 1 mL. Final concentration was calculated according to the corresponding calibration curve, i.e. UV-Vis absorption or C^4D signal value. The total amount of fluid which was transferred to the reservoir was calculated using Equation 1 where m_1, V_1, m_2 and V_2 represents initial concentration, initial volume, final concentration and final volume, respectively.

$$V_1 = \frac{m_2 \times V_2}{m_1} \tag{1}$$

Finally, knowing the time intervals and amount of transferred fluid, flow rates were calculated.

3.3. Results and discussion

3.3.1. Mechanical test

The Ultimate tensile strength (UTS), Young's modulus (E) and elongation at break for different fibre samples, i.e. LDPE and LCGO/LDPE composite fibres were determined, Figure 3.12. An improvement in UTS and modulus were observed by addition of LCGO to LDPE up to 2 w/w%. This improvement may be attributed to the contribution of LCGO sheets in reinforcement of LDPE by aligning along the fibres axis[31]. As shown in Figure 3.12b, addition of 0.5 w/w% LCGO into LDPE polymeric matrix led to an increase in in elongation at break compared to pure LDPE; while elongation at break showed a gradual decrease by increasing the loading of LCGO to more than 1 w/w%.
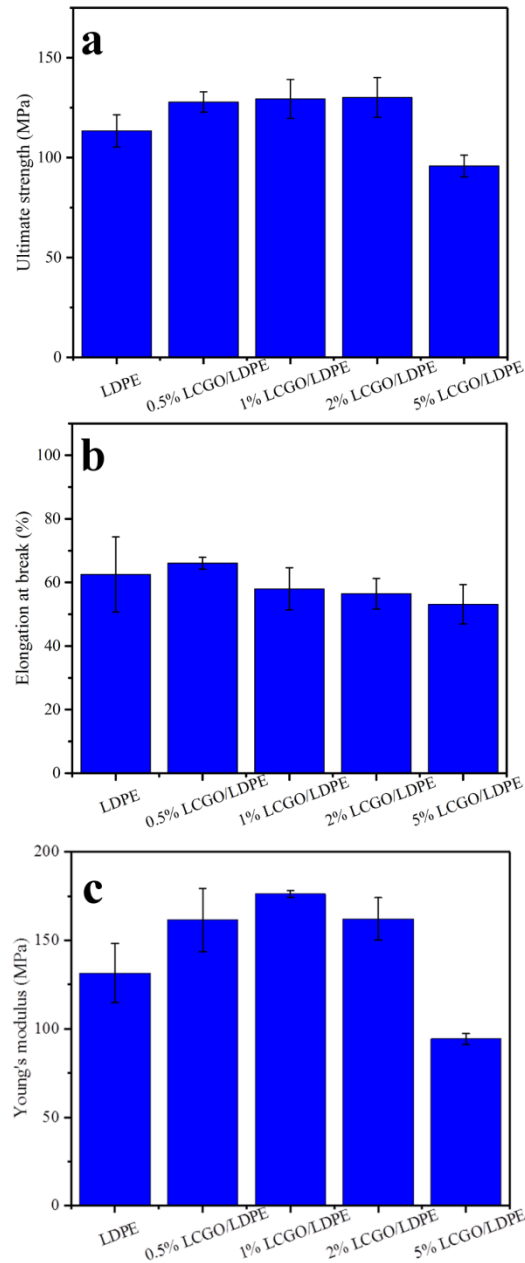
Figure 3.12: (a) Ultimate tensile strength, (b) Elongation at break and (c) Young's modulus for LDPE and LCGO/LDPE composite fibres

The observed improvements are likely to have been as a result of the strong interfacial interaction between the filler and the polymeric matrix. These interactions enabled the load to be transferred effectively from matrix to the filler at the interface at low concentrations of the filler, i.e. 0.5 w/w% LCGO in LDPE. However, at higher loadings non-uniformity in filler distribution was observed to result in agglomeration. Figure 3.13

illustrated the agglomeration of LCGO filler in a 5 w/w% LCGO/LDPE fibre. At these higher loadings weak points were produced as a result of non-uniform filler distribution which assisted in crack initiation that contributed to the observed drop in ultimate tensile strength and modulus for 5 w/w% LCGO/LDPE and a decrease in elongation at break for LCGO/LDPE composites containing more than 0.5 w/w% LCGO[32].
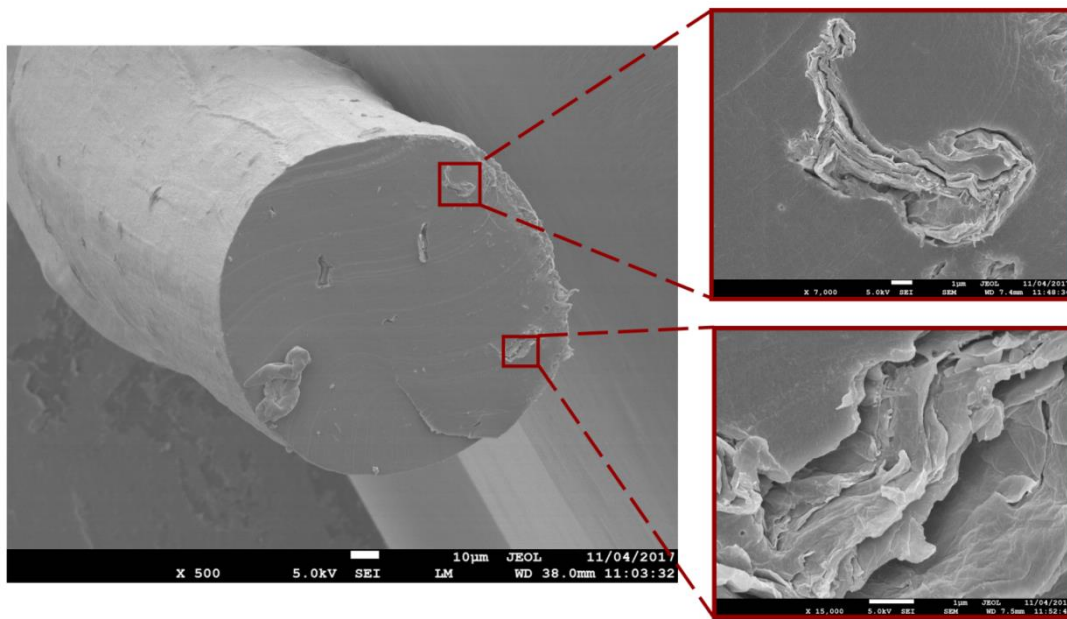
Figure 3.13: LCGO agglomerations formed in a 5 w/w% LCGO/LDPE composite fibre.

3.3.2. Wicking behaviour in knitted textile structures

The wicking behaviour of the knitted textile structures, described above, was observed and the flow rates (μL min^{-1}) for different samples measured in D.I. water and NaCl aqueous solution determined, Figure 3.14a and Figure 3.14b respectively.
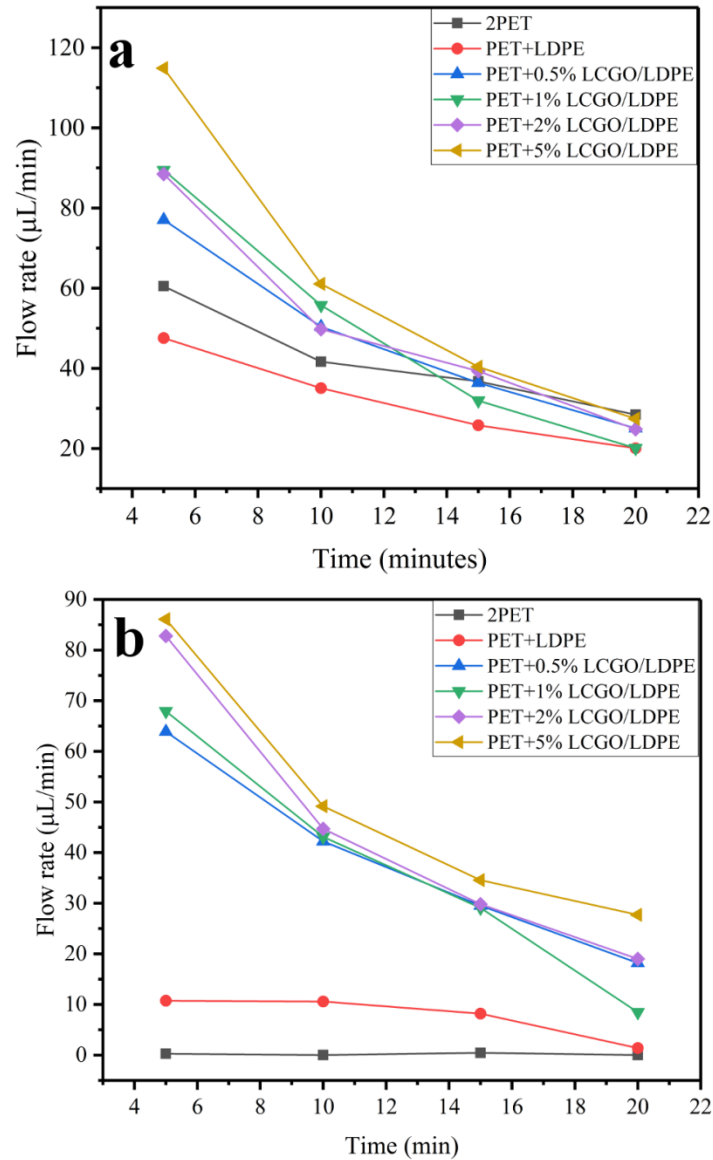
Figure 3.14: Flow rates achieved by different samples in (a) D.I. water and (b) NaCl aqueous solution

In both electrolyte systems, a gradual decrease in wicking flow rate over the time was observed. This decrease was a consequence of an increase in backpressure as fluid was transferred from the first reservoir to the receiving reservoir. As discussed earlier, fluid moves through a textile as a result of capillary networks generated in the gaps between the fibres. This force, and consequently wicking properties of textile structures, is greatly affected by surface chemistry and functional groups at the fibres surface and can be influenced by surface modifications[1,2]. As illustrated in Figure 3.14. the knitted structure
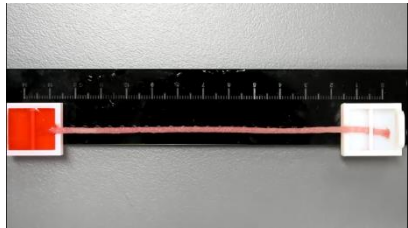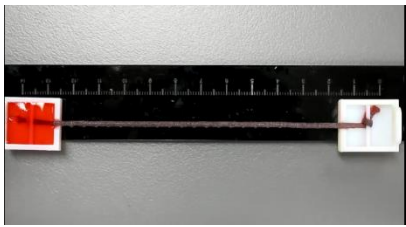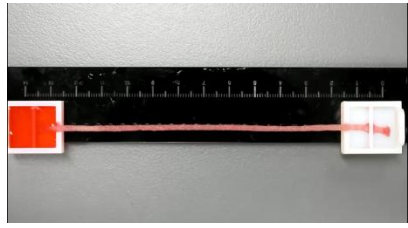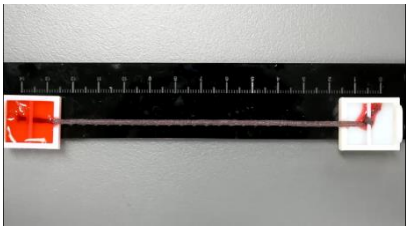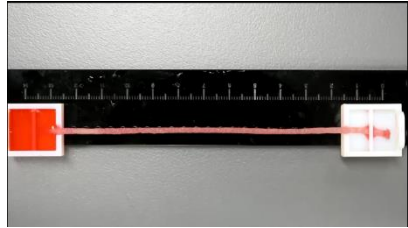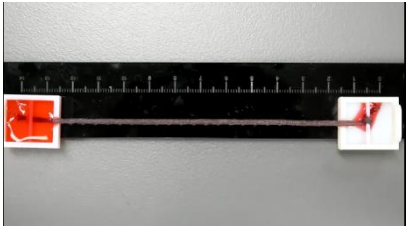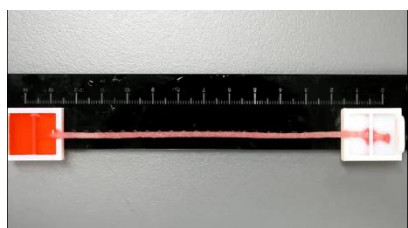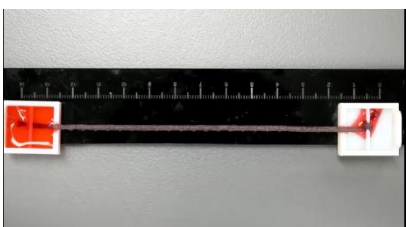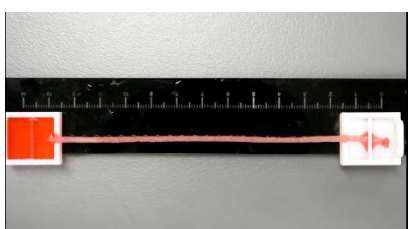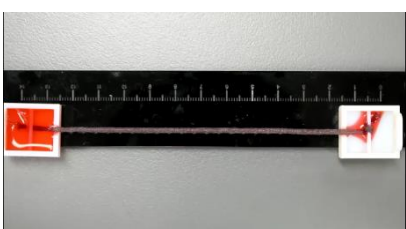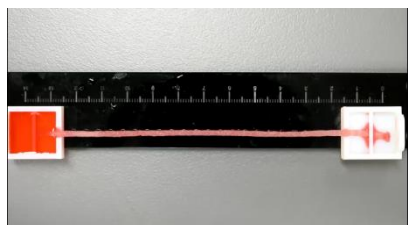
which comprised of 5 w/w% LCGO/LDPE composite fibre showed the highest flow rate while knitted structure made from 2PET threads, one with PET thread and LDPE fibres presented the lowest flow rate,

Addition of LCGO/LDPE composite fibres into 3D knitted structures of PET threads, is presumed to have led to an increase in the surface concentration of charged hydrophilic surface functionalisation, owing to the hydroxyl (–OH) and carboxyl (–COOH) functional groups on LCGO, and consequently increased the surface polarity of structures[33,34]. Following the well-known Young-Laplace equation, higher polarity would consequently lead to a higher surface tension, creating lower capillary pressure at the second reservoir and therefore increase its liquid flow. Unfortunately, surface contact angle measurements of hot pressed films of the LDPE/LCGO films proved unenlightening, as there was a stronger dependence upon surface roughness. The increase in the flow rate for the 3D knitted samples, which comprised higher loadings of LCGO in the LDPE fibres, when compared to those without the LCGO composite fibres further proved the increase in surface polarity. Significantly the flow rate in samples containing the LCGO composite fibres were proportional to the LCGO content, i.e. higher the LCGO content, higher the flow rate, that can be attributed to the increase in surface polarity.

Table 3.1 illustrates the differences in flow rates that were achieved by the knitted structures comprised of LDPE and LCGO/LDPE composite fibres.

Table 3.1: Comparing the amount of DI water displacement using knitted structures comprising LDPE and LCGO/LDPE composite fibres

Time (sec)	LDPE	LCGO/LDPE composite
0		
30		
60		
90		
120		
180		

300
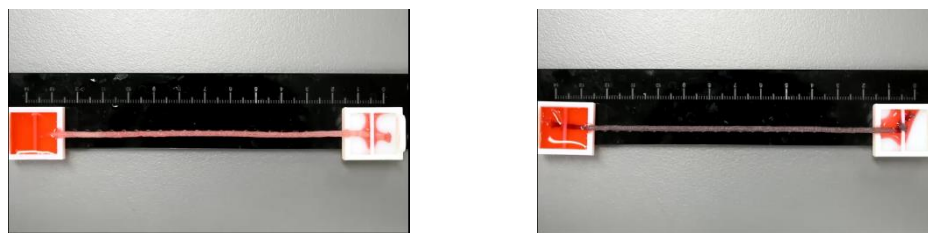
In NaCl aqueous solution the observed wicking flow rates trends were similar to what was achieved in D.I. water. The maximum flow rate values for the 3D knitted structures comprised of LCGO/LDPE composite fibres (at different loadings of LCGO) was lower and closer to each other in the NaCl aqueous solution than for D.I. water. In the presence of NaCl the electrostatic interaction between ions in electrolyte fluid and negatively charged LCGO functional groups (–OH and –COOH groups) on the surface of composite fibres, which plays a crucial role in determining the driving force for fluid movement,[35–37] is effectively screened by the ionic environment. Similar to the trend that was observed in D.I. water, higher loadings of LCGO also led to higher flow rates owing to increase in the concentrations of surface functional groups. However the net flow in NaCl was significantly lower due to ionic screening effects. The huge difference between the flow rate for structures comprising composite fibres and the structure with LDPE in NaCl solution when compared to D.I. water highlights the importance of the ionic interactions of the wicking fluid upon movement in the textile structure.

Surface chemistry of knitted structures was clearly affected by the incorporation of LCGO/LDPE composite fibres into 3D PET textile structures led to addition of active functional groups to the surface resulting in an increased wicking due to capillary and ionic interactions. Confirming this observation, the observed flow rate in the presence of Tris/CHES aqueous solution followed a completely reverse trend compared to trends in D.I. water and NaCl aqueous solution, Figure 3.15.
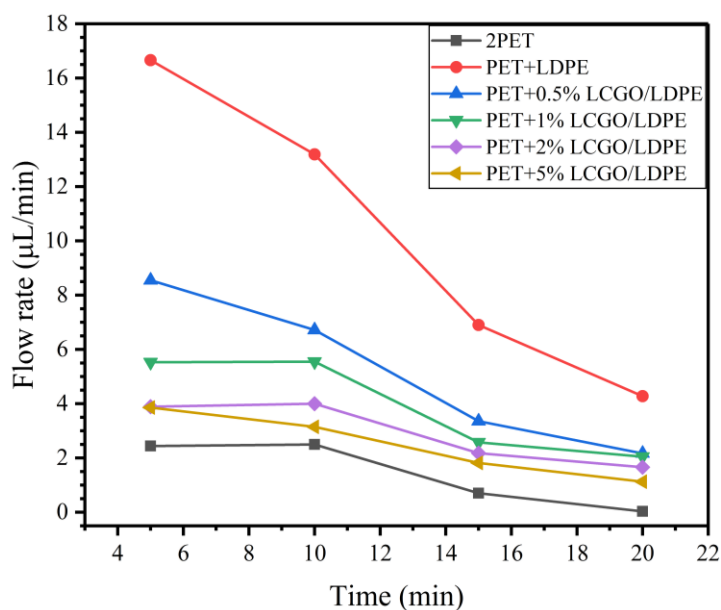
Figure 3.15: Flow rates achieved by different samples in Tris/CHES aqueous solution

The inverse behaviour can be explained by the absorption of ions in Tis/CHES solution on the surface of composite fibres due to interactions among carboxyl and hydroxyl functional groups of the LCGO and amino groups in Tris/CHES solution[38]. These absorptions blocked the LCGO functional groups (-OH and –COOH groups) and consequently, led to a declining the flow rate through the addition of LCGO/LDPE composite fibre into the 3D knitted structure. A subsequent increase in the amount of LCGO loading to the composite fibres resulted in an increase in absorption at sites on fibre surfaces which causes lower flow rate.

In order understand Tris/CHES ion surface absorption and probe the effect of Tris/CHES treatment on the performance of LCGO/LDPE fiber-containing 3D textiles, pure LCGO sheets were treated with a 100mM Tris/CHES aqueous solution and the physiochemical characteristics of the resulting films studied. 300 μm thick LCGO films were immersed in a 100 mMolar Tris/CHES solution for 2hrs then thoroughly washed with and immersed in D.I. water to remove non-adsorbed materials from the surface. As shown in Figure 3.16, colour of the LCGO sheet changed from brownish yellow in pure LCGO to deep black in the treated sample. The observed colour change was indicative of the chemical reduction

of LCGO samples upon treatment.
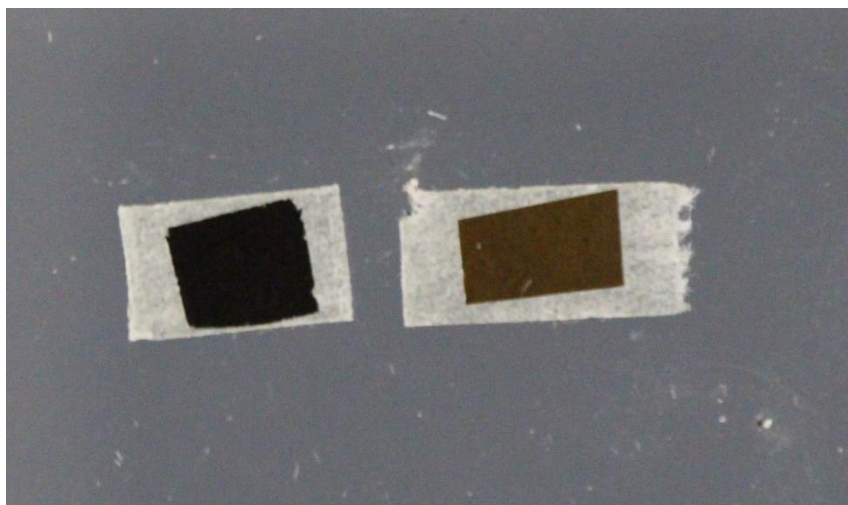
Figure 3.16: right: pure and left: Tris/CHES treated LCGO films

In addition to the observed colour change, FTIR and Raman spectroscopy were utilised to further prove this phenomenon. Common characteristic peaks of GO were observed in FTIR spectrum of LCGO samples (Figure 3.17a) at 1045, 1227, 1618 and 1731 cm^{-1} corresponding to C-O stretching of epoxy and phenolic groups, C=C stretching vibration of aromatic groups and C=O stretching vibration of carboxylic acid groups, respectively[39–41]. The partial reduction of the LCGO, due to treatment with 100 mM Tris/CHES aqueous solution, was confirmed by appearance of peaks at 1221, 1561, 2856 and 2924 cm^{-1} attributed to stretching vibration of C-N groups (in the C-NH group), bending vibration of N-H (in the C-NH group) and stretching vibration of –CH$_2$ groups due to attachment of TRIS molecules to LCGO sheets (via amine mediated reduction of LCGO epoxide rings) [38,42,43]. Partial reduction of LCGO was also confirmed utilizing Raman spectroscopy (Figure 3.17b). Peaks associated with D and G band of LCGO at 1328 and 1587 cm^{-1}, respectively, were observed for both pure and Tris/CHES treated LCGO. However, the intensity ratio of D to G bands (I_D/I_G) increased from 1.20 for pure to 1.28 for treated LCGO indicating an increase in the number of sp^2 domains confirming the chemical reduction of LCGO upon treatment with Tris/CHES[44,45].
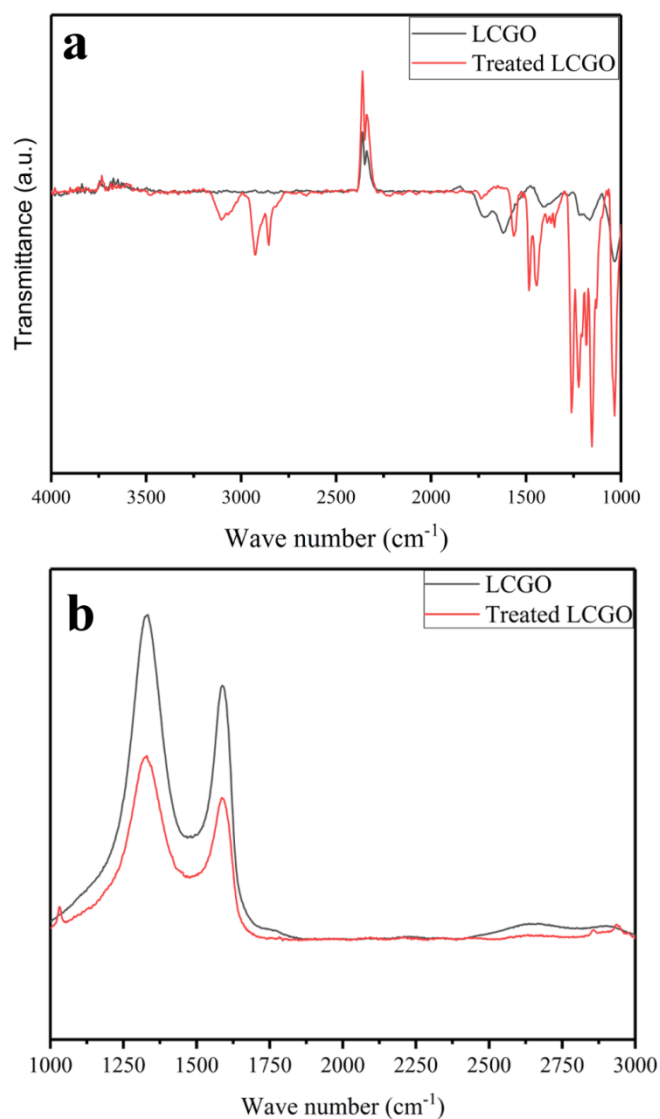
Figure 3.17: (a) FTIR and (b) Raman spectra of pure and Tris/CHES treated LCGO sheets

This data confirmed chemical reduction of LCGO due to treatment with Tris/CHES aqueous solution, which led to elimination of LCGO functional groups and subsequently attenuated the wicking performance of the textile structures containing LCGO/LDPE composite fibres.

From these observations it is clear that the wicking properties of textile structures strongly depend on the surface chemistry and surface functional groups. Significantly, the capability of tuning surface chemistry to alter the wicking properties (achieving different

flow rates) has been demonstrated.

Due to significant differences in experimental designs (some measures in horizontal and the others in vertical setup) and structure volumes (yarns, fabrics and non-woven structures were used), unfortunately, a meaningful comparison with previously reported work cannot be made.

3.3.3. Anti-Gravity pumping capabilities

In the next section, pumping capability of knitted structures comprising LCGO/LDPE composite fibres using water as fluid is discussed. Since anti-Gravity pumping would dramatically lower the flow rate, the fluid which showed the highest flow rate in same height reservoir experiments, i.e. D.I. water, was chosen for this experiment.

In order to demonstrate the pumping capability, wicking tests using the setup shown in Figure 3.18a were modified so that the receiving reservoir was 4 mm higher than the first reservoir were performed on different knitted structures using D.I. water. Reservoirs were connected with a pre-concentrated knitted structure. Then lower reservoir was filled with 1 mL of D.I. water and flow rate of fluid transfer to the higher reservoir was measure as previously described. As shown in Figure 3.18b, similar trend of achieved flow rates to that was observed in wicking test using water was observed in this experiment which confirms the action of similar driving forces. Incorporation of LCGO/LDPE fibres into knitted structures greatly affected their wicking properties by increasing the surface polarity as a result of increase in the surface oxygen concentration. Increasing the surface polarity amplified the driving force which is capillary force in this case and was proportional to the amount of LCGO loadings, i.e. higher driving forces were achieved at higher LCGO loadings.

Therefore, it was demonstrated that 3D knitted structure comprised of 5 w/w% LCGO/LDPE fibre and PET yarn can act as power-free textile-based microfluidic pump

and transfer water from a lower reservoir to the one 4 mm higher at the maximum flow rate of ca. 16 μL min^{-1} without the need for an external power supply or any chemical reaction.
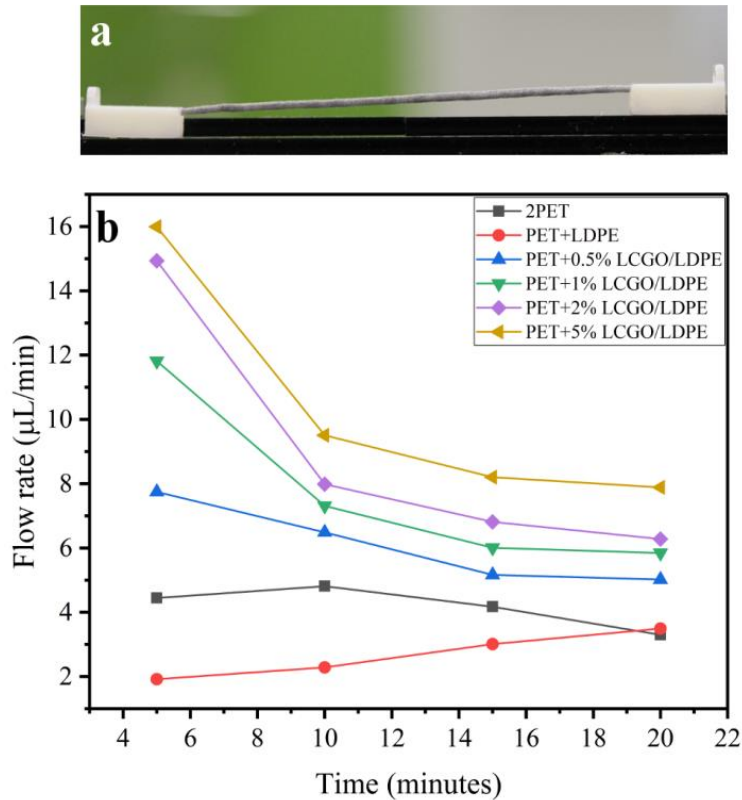
Figure 3.18: (a) experiment setup for pumping effect and (b) flow rate for different samples

3.4. Conclusion

Polymeric composite fibres using LDPE polymeric matrix and LCGO fillers are successfully fabricated and converted into 3D textile structures parallel with commercially available PET threads. The influence of the amount of LCGO loaded into the polymer matrix on fibre surface chemistry and surface polarity of the resultant 3D textile is also shown. The increase in surface polarity, as a result of accumulation of oxygen on the polymer surface and increase in O/C ratio, augments the fluid driving force in textile structure. It was demonstrated that, based on the ion rejection and/or absorption phenomenon which occur between fluid ions and functional groups on textile surface,

these 3D textile structures are capable of acting as a microfluidic pump with relatively high throughput. The presented power-free textile-based microfluidic pumps feature low-cost production, flexibility, ease of use that make them excellent candidates for the production of ASSURED devices. Moreover, proposed pumps, capable of being integrated into garments using well-established textile manufacturing techniques such as weaving or sewing, may be used to tackle the intrinsic miniaturization issue of microfluidic pumps, which has hindered the development of POCs and other integrated microfluidic chips, and expand the application of textiles in development of portable analytical and diagnostic devices.

3.5. References

(1)   Li, X.; Tian, J.; Shen, W. Thread as a Versatile Material for Low-Cost Microfluidic Diagnostics. *ACS Appl. Mater. Interfaces* **2010**, *2* (1), 1–6.

(2)   Reches, M.; Mirica, K. A.; Dasgupta, R.; Dickey, M. D.; Butte, M. J.; Whitesides, G. M. Thread as a Matrix for Biomedical Assays. *ACS Appl. Mater. Interfaces* **2010**, *2* (6), 1722–1728.

(3)   Nilghaz, A.; Bagherbaigi, S.; Lam, C. L.; Mousavi, S. M.; Córcoles, E. P.; Wicaksono, D. H. B. Multiple Semi-Quantitative Colorimetric Assays in Compact Embeddable Microfluidic Cloth-Based Analytical Device (μCAD) for Effective Point-of-Care Diagnostic. *Microfluid. Nanofluidics* **2015**, 317–333.

(4)   Wei, Y.-C.; Fu, L.-M.; Lin, C.-H. Electrophoresis Separation and Electrochemical Detection on a Novel Thread-Based Microfluidic Device. *Microfluid. Nanofluidics* **2012**, *14* (3–4), 583–590.

(5)   Nilghaz, A.; Ballerini, D. R.; Shen, W. Exploration of Microfluidic Devices Based on Multi-Filament Threads and Textiles: A Review. *Biomicrofluidics* **2013**, *7* (5).

(6)   Ballerini, D. R.; Li, X.; Shen, W. Patterned Paper and Alternative Materials as Substrates for Low-Cost Microfluidic Diagnostics. *Microfluid. Nanofluidics* **2012**, *13* (5), 769–787.

(7)   Agustini, D.; Bergamini, M. F.; Marcolino-Junior, L. H. Low Cost Microfluidic Device Based on Cotton Threads for Electroanalytical Application. *Lab Chip* **2016**, *16*, 345–352.

(8)   Bhandari, P.; Narahari, T.; Dendukuri, D. "Fab-Chips": A Versatile, Fabric-Based Platform for Low-Cost, Rapid and Multiplexed Diagnostics. *Lab Chip* **2011**, *11* (15), 2493.

(9)   Gonzalez, A.; Estala, L.; Gaines, M.; Gomez, F. A. Mixed Thread/paper-Based Microfluidic Chips as a Platform for Glucose Assays. *Electrophoresis* **2016**, *37* (12), 1685–1690.

(10)   Erenas, M. M.; De Orbe-Payá, I.; Capitan-Vallvey, L. F. Surface Modified Thread-Based Microfluidic Analytical Device for Selective Potassium Analysis. *Anal. Chem.* **2016**, *88* (10), 5331–5337.

(11)   Curto, V. F.; Fay, C.; Coyle, S.; Byrne, R.; O'Toole, C.; Barry, C.; Hughes, S.; Moyna, N.; Diamond, D.; Benito-Lopez, F. Real-Time Sweat pH Monitoring Based on a Wearable Chemical Barcode Micro-Fluidic Platform Incorporating Ionic Liquids. *Sensors Actuators B Chem.* **2012**, *171–172*, 1327–1334.

(12)   Leal, A. A.; Naeimirad, M.; Gottardo, L.; Schuetz, P.; Zadhoush, A.; Hufenus, R. Microfluidic Behavior in Melt-Spun Hollow and Liquid Core Fibers. *Int. J. Polym. Mater. Polym. Biomater.* **2016**, *65* (9), 451–456.

(13)   Jeon, S.-H.; Hwang, K.-H.; Lee, J. S.; Boo, J.-H.; Yun, S. H. Plasma Treatments of Wool Fiber Surface for Microfluidic Applications. *Mater. Res. Bull.* **2015**, *69*, 65–70.

(14)   Nilghaz, A.; Wicaksono, D. H. B.; Gustiono, D.; Abdul Majid, F. A.; Supriyanto, E.; Abdul Kadir, M. R. Flexible Microfluidic Cloth-Based Analytical Devices Using a Low-Cost Wax Patterning Technique. *Lab Chip* **2012**, *12* (1), 209.

(15)   Wei, Y. C.; Fu, L. M.; Lin, C. H. Electrophoresis Separation and Electrochemical Detection on a Novel Thread-Based Microfluidic Device. *Microfluid. Nanofluidics* **2013**, *14* (3–4), 583–590.

(16)   Nilghaz, A.; Ballerini, D. R.; Fang, X. Y.; Shen, W. Semiquantitative Analysis on Microfluidic Thread-Based Analytical Devices by Ruler. *Sensors Actuators, B Chem.* **2014**, *191*, 586–594.

(17)   Goddard, J. M.; Hotchkiss, J. H. Polymer Surface Modification for the Attachment of Bioactive Compounds. *Prog. Polym. Sci.* **2007**, *32* (7), 698–725.

(18)   Desmet, T.; Morent, R.; De Geyter, N.; Leys, C.; Schacht, E.; Dubruel, P. Nonthermal Plasma Technology as a Versatile Strategy for Polymeric Biomaterials Surface Modification: A Review. *Biomacromolecules* **2009**, *10* (9), 2351–2378.

(19)   Li, X.; Tabil, L. G.; Panigrahi, S. Chemical Treatments of Natural Fiber for Use in Natural Fiber-Reinforced Composites: A Review. *J. Polym. Environ.* **2007**, *15* (1), 25–33.

(20)   Morent, R.; De Geyter, N.; Desmet, T.; Dubruel, P.; Leys, C. Plasma Surface Modification of Biodegradable Polymers: A Review. *Plasma Process. Polym.* **2011**, *8* (3), 171–190.

(21)   Yang, Y.; Lin, C. Multiple Enzyme-Doped Thread-Based Microfluidic System for Blood Urea Nitrogen and Glucose Detection in Human Whole Blood. *Biomicrofluidics* **2015**, *9* (2), 1–13.

(22)   Ballerini, D. R.; Li, X.; Shen, W. An Inexpensive Thread-Based System for Simple and Rapid Blood Grouping. *Anal. Bioanal. Chem.* **2011**, *399* (5), 1869–1875.

(23)   Nilghaz, A.; Ballerini, D. R.; Guan, L.; Li, L.; Shen, W. Red Blood Cell Transport Mechanisms in Polyester Thread-Based Blood Typing Devices. *Anal. Bioanal. Chem.* **2016**.

(24)   Li, D.; Müller, M. B.; Gilje, S.; Kaner, R. B.; Wallace, G. G. Processable Aqueous Dispersions of Graphene Nanosheets. *Nat. Nanotechnol.* **2008**, *3* (2), 101–105.

(25)   Sato, H.; Shimoyama, M.; Kamiya, T.; Amari, T.; ?a?ic, S.; Ninomiya, T.; Siesler, H. W.; Ozaki, Y. Raman Spectra of High-Density, Low-Density, and Linear Low-Density Polyethylene Pellets and Prediction of Their Physical Properties by Multivariate Data Analysis. *J. Appl. Polym. Sci.* **2002**, *86* (2), 443–448.

(26)   Gall, M. J.; Hendra, P. J.; Peacock, C. J.; Cudby, M. E. A.; Willis, H. A. Laser-Raman Spectrum of Polyethylene: Part 1. Structure and Analysis of the Polymer. *Polymer (Guildf).* **1972**, *13* (3), 104–108.

(27)   Gambhir, S.; Murray, E.; Sayyar, S.; Wallace, G. G.; Officer, D. L. Anhydrous Organic Dispersions of Highly Reduced Chemically Converted Graphene. *Carbon N. Y.* **2014**, *76*, 368–377.

(28)   Cabot, J. M.; Macdonald, N. P.; Phung, S. C.; Breadmore, M. C.; Paull, B. Fibre-Based Electrofluidics on Low Cost Versatile 3D Printed Platforms for Solute Delivery, Separations and Diagnostics; from Small Molecules to Intact Cells. *Analyst* **2016**, *141* (23), 6422–6431.

(29)   Cabot, J. M. . b; Duffy, E. .; Currivan, S. .; Ruland, A. .; Jalili, R. .; Mozer, A. J. .; Innis, P. C. .; Wallace, G. G. .; Breadmore, M. . b; Paull, B. . b. Characterisation of Graphene Fibres and Graphene Coated Fibres Using Capacitively Coupled Contactless Conductivity Detector. *Analyst* **2016**, *141* (9), 2774–2782.

(30)   Nesbitt, B. E. Resistivities of Crustal Fluids Resistive at 102 to 105 Fl M . The Values Vary with the Type Crust , from More Resistive Fl M) in Precambrian Shields to Less Resistive Fl M) in Regions. *J. Geophys. Res. Solid Earth* **1993**, *98* (9), 4301–4310.

(31)   Seyedin, M. Z.; Razal, J. M.; Innis, P. C.; Jalili, R.; Wallace, G. G. Achieving Outstanding Mechanical Performance in Reinforced Elastomeric Composite Fibers Using Large Sheets of Graphene Oxide. *Adv. Funct. Mater.* **2015**, *25* (1), 94–104.

(32)   Chee, C. Y.; Song, N. L.; Abdullah, L. C.; Choong, T. S. Y.; Ibrahim, A.; Chantara, T. R. Characterization of Mechanical Properties: Low-Density Polyethylene Nanocomposite Using Nanoalumina Particle as Filler. *J. Nanomater.* **2012**, *2012*.

(33)   Szabo, T.; Tombacz, E.; Illes, E.; Dekany, I. Enhanced Acidity and pH-Dependent Surface Charge Characterization of Successively Oxidized Graphite Oxides. *Carbon N. Y.* **2006**, *44* (3), 537–545.

(34)   Joshi, R. K.; Alwarappan, S.; Yoshimura, M.; Sahajwalla, V.; Nishina, Y. Graphene Oxide: The New Membrane Material. *Appl. Mater. Today* **2015**, *1* (1), 1–12.

(35)   Teixeira, M. R.; Rosa, M. J.; Nyström, M. The Role of Membrane Charge on Nanofiltration Performance. *J. Memb. Sci.* **2005**, *265* (1–2), 160–166.

(36)   Nicolini, J. V.; Borges, C. P.; Ferraz, H. C. Selective Rejection of Ions and Correlation with Surface Properties of Nanofiltration Membranes. *Sep. Purif. Technol.* **2016**, *171*, 238–247.

(37)   Hong, B. J.; Compton, O. C.; An, Z.; Eryazici, I.; Nguyen, S. T. Successful Stabilization of Graphene Oxide in Electrolyte Solutions: Enhancement of Biofunctionalization and Cellular Uptake. *ACS Nano* **2012**, *6* (1), 63–73.

(38)   Deng, Y.; Li, Y.; Dai, J.; Lang, M.; Huang, X. Functionalization of Graphene Oxide towards Thermo-Sensitive Nanocomposites via Moderate in Situ SET-LRP. *J. Polym. Sci. Part A Polym. Chem.* **2011**, *49* (22), 4747–4755.

(39)   Navaee, A.; Salimi, A. Efficient Amine Functionalization of Graphene Oxide through the Bucherer Reaction: An Extraordinary Metal-Free Electrocatalyst for the Oxygen Reduction Reaction. *RSC Adv.* **2015**, *5* (74), 59874–59880.

(40)   Aboutalebi, S. H.; Jalili, R.; Esrafilzadeh, D.; Salari, M.; Gholamvand, Z.; Aminorroaya Yamini, S.; Konstantinov, K.; Shepherd, R. L.; Chen, J.; Moulton, S. E.; et al. High-Performance Multifunctional Graphene Yarns: Toward Wearable All-Carbon Energy Storage Textiles. *ACS Nano* **2014**, No. Xx.

(41)   Li, M.; Wang, Y.; Liu, Q.; Li, Q.; Cheng, Y.; Zheng, Y.; Xi, T.; Wei, S. In Situ Synthesis and Biocompatibility of Nano Hydroxyapatite on Pristine and Chitosan Functionalized Graphene Oxide. *J. Mater. Chem. B* **2013**, *1* (4), 475–484.

(42) Stankovich, S.; Dikin, D. A.; Piner, R. D.; Kohlhaas, K. A.; Kleinhammes, A.; Jia, Y.; Wu, Y.; Nguyen, S. T.; Ruoff, R. S. Synthesis of Graphene-Based Nanosheets via Chemical Reduction of Exfoliated Graphite Oxide. *Carbon N. Y.* **2007**, *45* (7), 1558–1565.

(43) Compton, O. C.; Dikin, D. A.; Putz, K. W.; Brinson, L. C.; Nguyen, S. T. Electrically Conductive "alkylated" graphene Paper via Chemical Reduction of Amine-Functionalized Graphene Oxide Paper. *Adv. Mater.* **2010**, *22* (8), 892–896.

(44) Pei, S.; Cheng, H. M. The Reduction of Graphene Oxide. *Carbon N. Y.* **2012**, *50* (9), 3210–3228.

(45) Mehrali, M.; Sadeghinezhad, E.; Akhiani, A. R.; Tahan Latibari, S.; Talebian, S.; Dolatshahi-Pirouz, A.; Metselaar, H. S. C.; Mehrali, M. An Ecofriendly Graphene-Based Nanofluid for Heat Transfer Applications. *J. Clean. Prod.* **2016**, *137*, 555–566.

Chapter 4:

Thermally conducting LCGO-filled composite fibres for heat dissipation in textile-based microfluidic

4.1. Introduction

Although fluid can be transport in textile-based microfluidics by simple wicking, in order to obtain controllable devices with precise fluid control, a driving force other than simple capillary action may be required. Electric fields are widely used to move, pre-concentrate and separate solutes within fluids[1]. When this fluid is held as a surface layer upon a thread or fibre, both electroosmotic force and solute electroosmotic migration can take place in a controlled manner. More significantly, separations that are achievable in capillaries systems can be simulated on the surface of fibres using close environmental control. This opens a new area of analytical platforms and opportunities specifically 'on-fibre' detection. However, applying electric field to move and/or separate solutes within fluids causes Joule-heating. This not only increases the fluid temperature, but also produces temperature gradients in cross-stream and axial directions. These temperature effects, cause non-uniformity in fluid properties, and more importantly affect the mass species transport, efficiency and reproducibility of the seperations[1,2].

The use of heat sinks or heat spreaders, which are materials with high thermal conductivity as an attachment to a device for dissipation of heat from the device, is a method that has been widely used to tackle the heating issue of different electroosmotic devices. A range of materials including polymer-matrix composites have been developed to satisfy this need[3,4]. One of the most common methods of making thermally conducting polymeric composites is by adding thermally conducting fillers such as aluminium nitride, wollastonite, silicon carbide whisker, boron nitride, etc. into a thermally insulating polymeric matrix[5,6].

Polyethylene because of its simplicity (simple chemical structure) with its strain induced crystallinity, thereby giving it a degree of thermal conductivity tunability, has been widely used for thermal conductivity studies[7–9]. Thermal conductivity of 37.5 W m^{-1} K^{-1} in the

drawing direction has been reported for and stretched polyethylene by Choy et al.[10]. Thermal conductivity of polyethylene increases rapidly by increasing the drawing ratio with thermal conductivities of 70 W m^{-1} K^{-1} reported by Pietralla[11] for fully aligned polyethylene. Recently, high thermal conductivities with the values as high as ∼104 W m^{-1} K^{-1} was reported for polyethylene nanofibers. It has also been theoretically estimated that the thermal conductivity of polyethylene nanofibers may be improved to be competitive with aluminium[12].

Carbon allotropes and their derivatives specifically one- and two-dimensional materials such as carbon nanotubes and graphene sheets have attracted a lot of attentions as thermally conductive fillers for different applications[13]. Liquid crystalline graphene oxide (LCGO) which is produced using a novel protocol with extremely high aspect ratio and lateral size of up to ca. 100 μm was chosen as filler to make composite fibres. Its unique characteristics such as ability to form liquid crystals in very low concentrations, very large sheet size that can effectively improve desired properties in a composite material in relatively low loadings compare to conventional graphene oxides. Extraordinary high thermal conductivity of ca. 1500 W m^{-1} K^{-1} was achieved using LCGO[14,15].

For the first time, we formulated LCGO and low density polyethylene (LDPE) composite fibres and introduced them into 3D polyester (PET) knitted structures, to minimize Joule-heating effects. Different potentials, i.e. from 20 to 250 V cm^{-1}, were applied to the structures and corresponding currents were measured. Also, temperature changes in samples were monitored when 250 V cm^{-1} was applied to the structures.

4.2. Experimental

LDPE powders were evapouratively surface coated as described in Chapter 3 to obtain LCGO/LDPE coated powers which utilised for melt spinning fibres. These fibres were

characterised using DSC and TGA techniques using methods described earlier in Chapter 3 (Figure 3.1 to Figure 3.3).

LDPE fibres were made with two different methods. First, undrawn LDPE fibres were made using a 500µm circular extrusion die and directly collected on a winder spool (Figure 3.4a) without any additional drawing steps. In the second approach fibres were spun using a 700µm circular extrusion die and passed through a drawing passage utilizing the stretching unit before being collected on a winder spool (Figure 3.4b) to obtain drawn LDPE and LCGO/LDPE fibres. The heat profile, screw setup and screw speed for both experiments were same as what was described earlier in Chapter 3 (3.2.2. Fibre Spinning section). SEM micrographs of cross-sections of drawn LDPE and drawn LCGO/LDPE composite fibres are shown in Chapter 3 (Figure 3.5).

Figure 4.1: (a) melt spinning setup for making (a) undrawn LDPE fibres, I: twin-screw melt extrusion, II: winding unit and (b) drawn LDPE fibres, I: twin-screw melt extrusion, II: stretching unit and III: winding unit

4.2.1. Fabricating 3D structures

Similar to what was described earlier in Chapter 3 (3.2.3. Making 3D structures), 3D knitted structures comprised of commercial polyester (PET) threads and LDPE (or LCGO/LDPE) fibres were successfully prepared (see Figure 3.6).

4.2.2. Characterisations

LCGO aqueous dispersion was characterized by Zeta potential technique same as what was reported earlier in Chapter 3. Incorporation of LCGO in LDPE fibres and fibre mechanical properties were also characterized by Raman spectroscopy and tensile mechanical tester as previously described in Chapter 3 (Figure 3.7 and Figure 3.8).

4.2.3. Joule-heating dissipation experiment

For Joule-heating dissipation tests, 3D textile samples were held between two 3D printed reservoirs containing 500 μL of buffer solution.

The distance between adjacent reservoirs were 6 cm and 1.25 mM Tris/CHES buffer solution with the pH of 8.5 used to pre-wet 3D textile structures and fill the two reservoirs. Different electric fields from 20, 40, 60, 80, 100, 120, 140, 160, 180, 200 and 250 V cm^{-1}, was applied using LabSmiths high voltage sequencer across the reservoirs equipped with platinum (Pt) electrodes. The corresponding current flow was monitored utilizing the supplied LabSmiths software and the samples temperature change measured using an infrared thermographic camera (thermoIMAGER TIM 160, Micor-Epsilon, Germany). The experimental setup is shown in Figure 4.2.
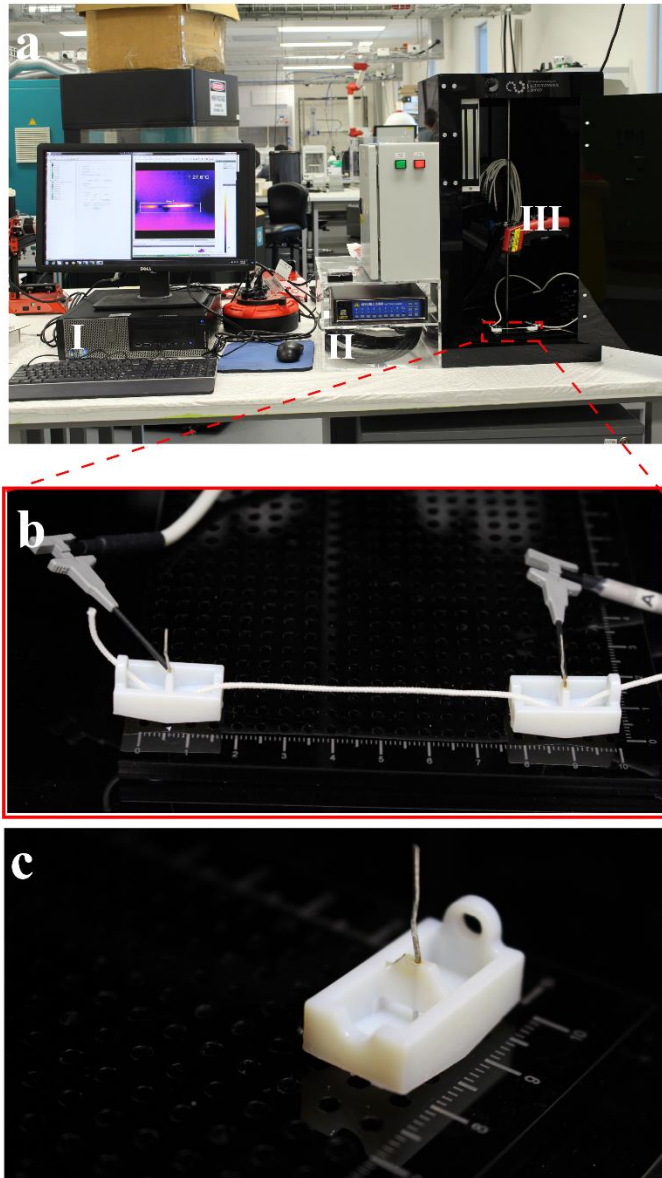
Figure 4.2: (a) experimental setup, I: PC, II: high voltage sequencer, III: thermal camera, (b) two reservoirs connected with a textile structure and high voltage connectors connected to Pt electrodes and (c) 3D printed reservoir with Pt electrode.

4.2.4. Results and discussion

4.2.4.1. Mechanical test

The mechanical properties of drawn and undrawn LDPE fibres were compared. Figure 4.3 shows stress-strain curves for drawn and undrawn LDPE fibres. Figure 4.3 shows 956% elongation at break for undrawn and only 64% for drawn LDPE. Undrawn LDPE had the

ultimate strength of 18 MPa while this value was 113 MPa for drawn LDPE fibres. Undrawn LDPE showed rubber like behaviour with very low ultimate strength and very high elongation at break (ca. 1000% strain) indicating amorphous nature of the fibre while drawn LDPE demonstrated much higher modulus, ultimate strength and much lower elongation at break. These were observed as a result of polymer chain orientation along the fibre axis (stretch direction) and consequently alteration of amorphous regions into 3D crystalline structures[16–18]. Thermal conductivity of LDPE has been reported to be increased by increasing the degree of crystallinity. This could be attributed to the fact that phonons are predominantly being conducted through crystalline regions[19]. Since the aim of this chapter is production of thermally conductive fibres to be incorporated into 3D textile structures for Joule-heating dissipation, only drawn LDPE and LCGO/LDPE composite fibres were used to make 3D textile structures.
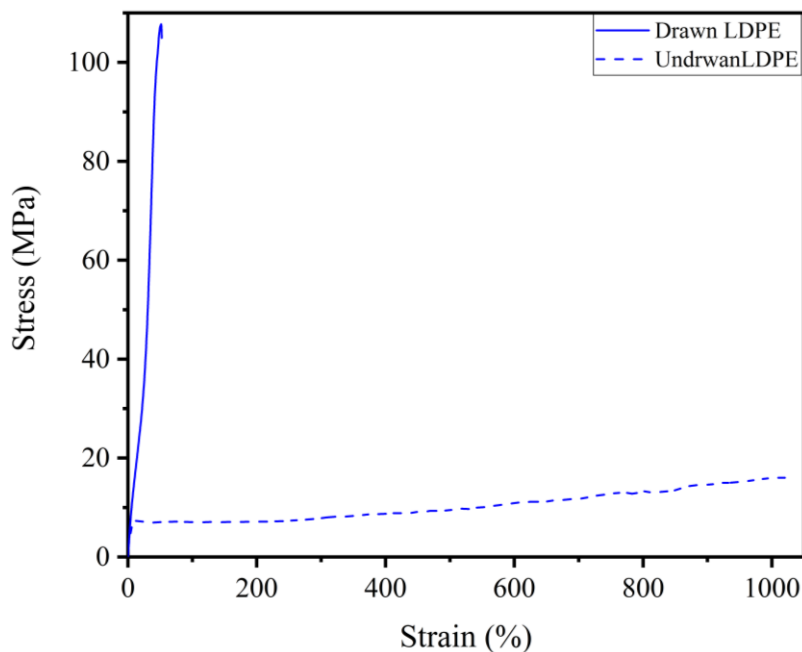
Figure 4.3: Stress-strain curve for drawn and undrawn LDPE fibres

4.2.4.2. Joule-heating dissipation experiment

Current passing through pre-concentrated 3D knitted structures comprising of PET threads or PET threads parallel with LDPE and LCGO/LDPE composite fibres were measured when different potentials were applied, i.e. 20, 40, 60, 80, 100, 120, 140, 160, 180, 200 and 250 V cm^{-1}. As shown in Figure 4.4, the current and applied electric field for all 3D knitted structures had a non-linear relationship which was be attributed to the Joule-heating effect[1]. In the absence of Joule-heating effects, the observed electric current would be a linear function of the applied electric field and follow Ohm's law. With a Joule-heating effect present a higher electric current would be expected at every electric field proportional to the electric current to the power of two ($P=VI=I^2R$)[20],according to the power law, due to an enhanced electrolyte ionic conductivity resulting from the elevated electrolyte temperatures which then results in the current-electric field deviating from linearity. Joule-heating effects will also be higher in textile samples with lower thermal conductivities as a result the material being unable to dissipate heat which leads to more non-linearity in the observed current-electric field.
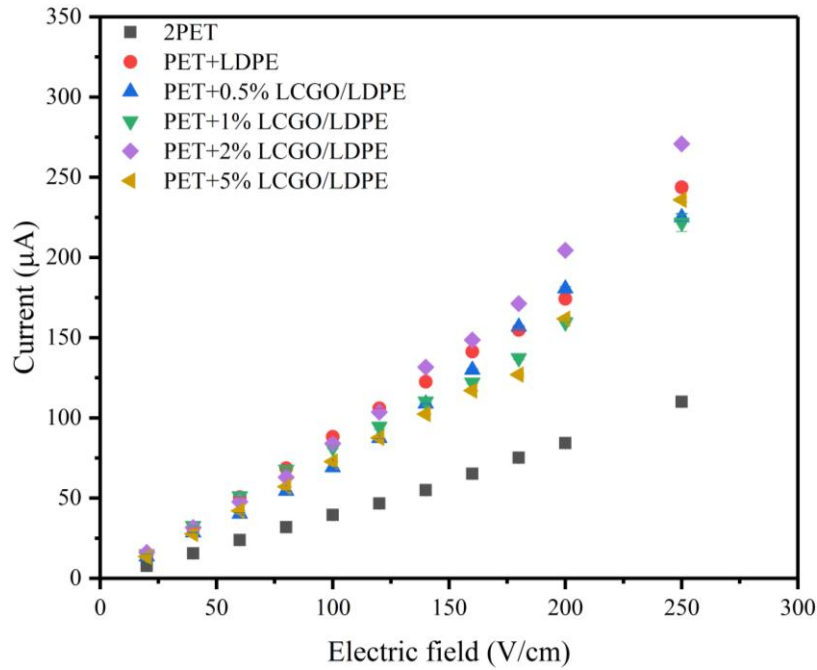
Figure 4.4: Current in each applied electric field for different 3D textile structures

Higher applied potentials led to larger rise in temperature. This can be explained by the fact that higher potentials (higher power) heated the system faster while heat dissipation rate of the system was much lower [2]. Figure 4.5(a) shows the typical temperature change, measured by the thermal camera, on a 3D textile structure over 60 seconds when a 250 V cm^{-1} electric field was applied. Rathore et al[2]. measured the temperature in a capillary tube with the lumen size of about 37.5 µm while 310 V cm^{-1} was applied across the tube shown in Figure 4.5(b).
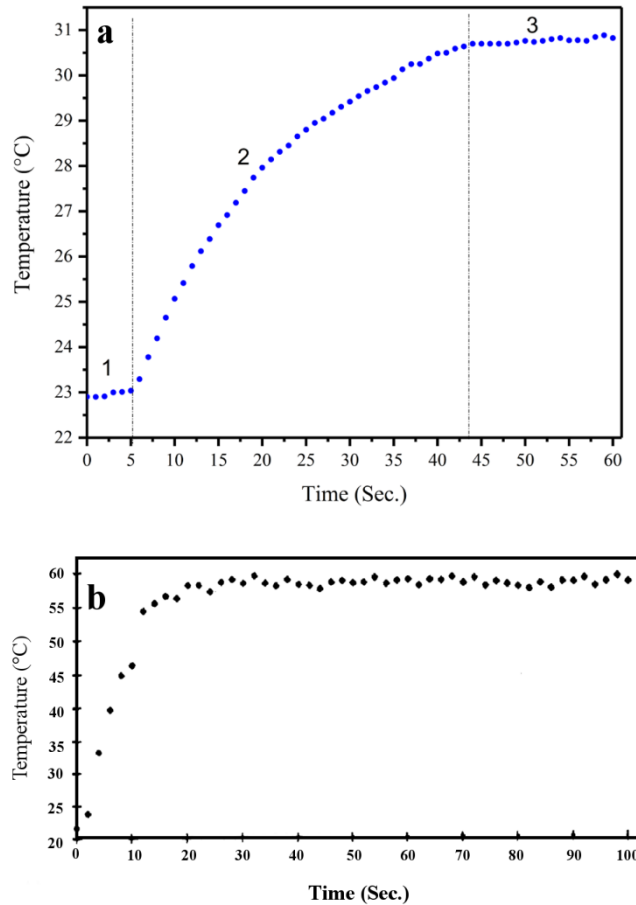
Figure 4.5: temperature rise as a function of time in (a) a 3D textile structure when 250 V cm^{-1} was applied and (b) a capillary tube with the lumen size of about 37.5 µm while 310 V cm^{-1} was applied adopted from [2].

As demonstrated in Figure 4.5(b), applying a constant potential to a capillary tube causes an immediate rise in temperature followed by a steady state. Contrasting this, applying a constant potential to a 3D knitted structures did not cause an immediate temperature change and temperature remained relatively unchanged for a while, as shown in area 1 of Figure 4.5(a). A temperature rise followed by a steady state was observed for textiles in an observation similar to results reported for capillary tubes, (areas 2 and 3 in Figure 4.5(a)). The difference in behaviours of 3D knitted textiles and capillary tubes can be attributed to the thermal lag resulting from the structural difference between textiles, which are large textile structures of diameters of about Ø 1.5 mm, and the smaller diameter capillary tubes. Capillary tubes are closed environments where generated heat cannot escape though and air

cannot enter while open geometry of the knitted sutures facilitates the occurrence of heat transfer between the fluid inside the knitted structure and its neighbouring air flow which leads to cooling down the fluid and plateau region at the beginning of the graph shown in Figure 4.5(a).

Changes in temperature due to the Joule-heating effect were observed using the thermal camera for 60 seconds while 250 V cm^{-1} was applied to the samples. Temperature change with respect to the initial temperature was measured for different samples (Figure 4.6).
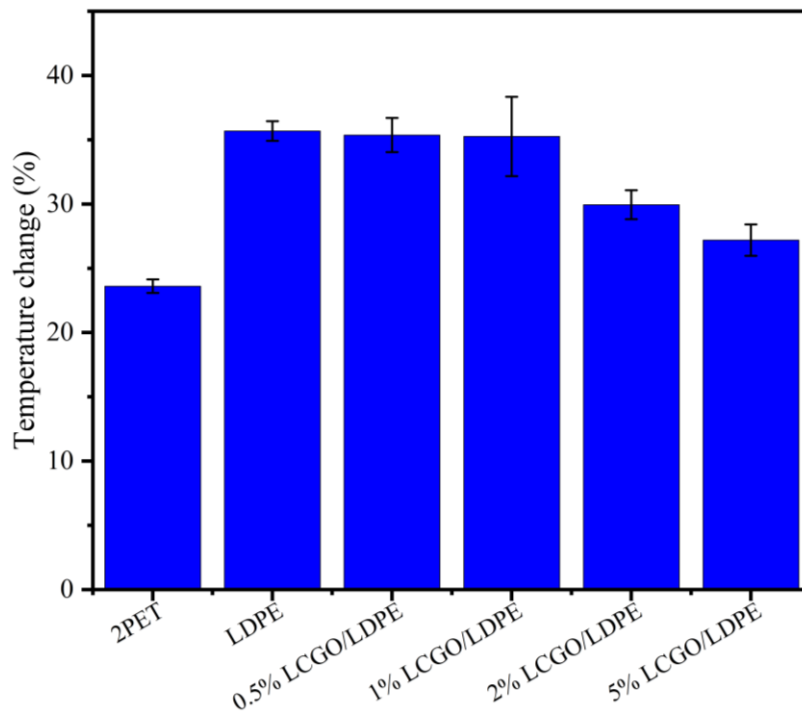
Figure 4.6: Temperature change with respect to the initial temperature for different samples while 250 V cm^{-1} was applied

As shown in Figure 4.6, replacing one PET thread with LDPE fibre led to an increase in temperature change with respect to the initial temperature. This shift may be attributed to the fact that the knitted structure composed of two PET threads was not as stiff as the structures comprising of PET thread and LDPE (or LCGO/LDPE) fibres which can it collapsed under tension during the experiment. Collapsed structures accommodated lower

99

amount of fluid compare to the other structures. Since Joule-heating is a volumetric phenomenon and its magnitude is directly affected by the volume of the channel used[21], lower Joule-heating generated in those collapsed structures that resulted in lower working temperature.

An increase in thermal conductivity of structures containing LCGO loaded into the LDPE can be explained by the in situ reduction of LCGO to Graphene during the extrusion process, as confirmed by Raman spectroscopy, (Figure 3.7). The elevated thermal extrusion process clearly induces a partial elimination of the oxygen containing groups of GO and restores the pi-electron structure to some extent[22]. The observed Raman spectra of the fibres, D and G bands shifted compare to those of LCGO provides an indication for reduction of graphene oxide[23]. Similarly, the ratio of the D/G bands (I_D/I_G) was noted to increase after extrusion of samples containing LCGO (measured to be 1.11 in LCGO to 1.44 in 0.5 w/w%, 1.12 in 1w/w%, 1.21 in 2 w/w% and 1.18 in 5 w/w% composite fibres). This D/G ratio change has been attributed to formation of new smaller graphitic domains confirming the reduction of LCGO[24–27]. As a result of the thermal reduction of LCGO during the melt spinning process, an increase in thermal conductivity of LCGO and consequently LDPE/LCGO composite fibres can be expected[15,28].

In LCGO/LDPE composites with low amounts of LCGO filler content, i.e. up to 1 w/w%, the LCGO sheets were separated from each other by the LDPE polymer matrix which had much lower thermal conductivity compare to that of LCGO and reduced LCGO sheets. This poor degree of interconnectivity limited the composites ability to form a heat conduction path. This led to huge phonon scatterings at the boundaries (between polymeric matrix and the filler) as a result of interruption in phonon movements as well as internal contact thermal resistance. These effects led to negligible improvement in thermal conductivity of the composite and therefore, only a slight decrease were observed in

system's temperature change in structures comprised of by 0.5 w/w% and 1 w/w% LCGO/LDPE composite fibres compare to that contained LDPE fibre. By increasing the LCGO loadings between 2 and 5 w/w% an improved inter-connection of LCGO sheets resulted thereby providing a heat conduction pathway. This phenomenon, along with the ability of LCGO to fully integrate into LDPE polymeric matrix due because of its extremely large aspect ratio, leads to a significant increase in composites' thermal conductivity and therefore its ability to dissipate the heat generated by Joule-heating in the system[29–31]. Therefore, as shown in Figure 4.6, the drop in the temperature that was observed for knitted structures containing LCGO/LDPE fibres with loadings above 2 w/w% was consistent with the formation of improved reduced LCGO interconnected pathways. Although integrating thermally conducting LCGO/LDPE fibres into PET knitted structure resulted in decrease in system's temperature change, the final temperature change for structure with 5w/w% composite was still higher than that of the structure with pure PET. Unfortunately due to graphene oxide agglomeration within these fibres at LCGO/LDPE loadings more than 5w/w% the resultant in drop in ultimate strength and modulus limited the utility of the pre-mixing method. Consequently, another method for composite making (and fibre production) needed to be considered to resolve this issue.

Thermal conductivity measurements by the LFA technique (described in Chapter 2 and Chapter 5) is a common method for characterizing the thermal diffusivity (and consequently thermal conductivity) of materials. Performing LFA on LCGO/LDPE composites proved to be impractical due to some significant limitations; firstly, hot pressing the composite powders (LCGO-coated LDPEs) resulted in very non-uniform films, and secondly, hot pressing the spun fibers was impractical because of the limited amount of spun materials available. More importantly, hot pressing the spun drawn LDPE fibres would destroys the LDPE orientation induced by drawing and consequently thermal

conductivity measurements would not reflect the effect of strain-induced thermal conductivity enhancement.

4.3. Conclusion

The wide variety of fibrous materials and composite formulations available in textiles opens new possibilities for exploitation of specific surface interactions providing opportunities to develop low-cost thread-based structures for biosensing and diagnostic devices. In this chapter, the novel idea of incorporating thermally conductive fibres into 3D textile microfluidic devices to minimize the effects of Joule-heating which is the most important side effect of electrophoresis technique was investigated. Thermally conducting graphene oxide-filled LDPE fibres with different graphene oxide loadings were successfully made and incorporated into 3D knitted structures in combination with PET threads to make novel textile-based microfluidics. Different electric fields were applied to 3D knitted structures and resultant current and temperature change were monitored. It was shown that incorporating thermally conductive fibres into 3D textile structures as heat dissipater potentially can be used as an effective method to dissipate the heat generated by Joule-heating and keep the system as cool as possible. This new capability of producing thermally conducting textile materials opens up new opportunities for fibre based capillary electrophoresis studies in areas such as protein separation and detections where high electrical fields are required to perform separations. Although a promising trend was shown in temperature change with respect to the initial temperature for 3D knitted structures comprising of LCGO-filled thermally conducting composite fibres, loading LCGO up to 5 w/w% was not sufficient to effectively dissipate the heat generated by Joule-heating effect. Making LCGO/LDPE composite fibres with more than 5 w/w% LCGO using pre-mixing method used in this chapter was impractical due to agglomeration of LCGO which causes

weakening in composite fibres. Therefore, making composite fibres with solvent-based methods, i.e. making a composite solution and using wet-spinning to make fibre, were proposed which could eliminate this issue.

4.4. References

(1)   Xuan, X.; Li, D. Analytical Study of Joule Heating Effects on Electrokinetic Transportation in Capillary Electrophoresis. *J. Chromatogr. A* **2005**, *1064* (2), 227–237.

(2)   Rathore, A. S. Joule Heating and Determination of Temperature in Capillary Electrophoresis and Capillary Electrochromatography Columns. *J. Chromatogr. A* **2004**, *1037* (1–2), 431–443.

(3)   Sim, L. C.; Ramanan, S. R.; Ismail, H.; Seetharamu, K. N.; Goh, T. J. Thermal Characterization of Al2O3 and ZnO Reinforced Silicone Rubber as Thermal Pads for Heat Dissipation Purposes. *Thermochim. Acta* **2005**, *430* (1–2), 155–165.

(4)   Xu, Y.; Luo, X.; Chung, D. D. L. Sodium Silicate Based Thermal Interface Material for High Thermal Contact Conductance. *J. Electron. Packag.* **2000**, *122* (June), 128–131.

(5)   Lee, G. W.; Park, M.; Kim, J.; Lee, J. I.; Yoon, H. G. Enhanced Thermal Conductivity of Polymer Composites Filled with Hybrid Filler. *Compos. Part A Appl. Sci. Manuf.* **2006**, *37* (5), 727–734.

(6)   Xu, Y.; Chung, D.D.L.; Mroz, C. Thermally Conducting Aluminum Nitride Polymer Matrix Composites. *Compos. Pt. A-Appl. S* **2001**, *32*, 1749–1757.

(7)   Choy, C. L. Thermal Conductivity of Polymers. *Polymer (Guildf).* **1977**, *18* (April 1976), 984–1004.

(8)   Anderson, D. R. Thermal Conductivity of Polymers. *Chem. Rev.* **1966**, *66* (6), 677–690.

(9)   Liu, J.; Yang, R. Tuning the Thermal Conductivity of Polymers with Mechanical Strains. *Phys. Rev. B - Condens. Matter Mater. Phys.* **2010**, *81* (17), 1–9.

(10)   Choy, C. L.; Wong, Y. W.; Yang, G. W.; Kanamoto, T. Elastic Modulus and Thermal Conductivity of Ultradrawn Polyethylene. *J. Polym. Sci. Part B Polym. Phys.* **1999**, *37* (23), 3359–3367.

(11)   Pietralla, M. High Thermal Conductivity of Polymers: Possibility or Dream? *J. Comput. Mater. Des.* **1996**, *3* (1–3), 273–280.

(12)   Shen, S.; Henry, A.; Tong, J.; Zheng, R.; Chen, G. Polyethylene Nanofibres with Very High Thermal Conductivities. *Nat. Nanotechnol.* **2010**, *5* (4), 251–255.

(13)   Balandin, A. A. Thermal Properties of Graphene and Nanostructured Carbon Materials. *Nat. Mater.* **2011**, *10* (8), 569–581.

(14)   Aboutalebi, S. H.; Gudarzi, M. M.; Zheng, Q. Bin; Kim, J. K. Spontaneous Formation of Liquid Crystals in Ultralarge Graphene Oxide Dispersions. *Adv. Funct. Mater.* **2011**, *21* (15), 2978–2988.

(15)   Jalili, R.; Aboutalebi, S. H.; Esrafilzadeh, D.; Shepherd, R. L.; Chen, J.; Aminorroaya-Yamini, S.; Konstantinov, K.; Minett, A. I.; Razal, J. M.; Wallace, G. G. Scalable One-Step Wet-Spinning of Graphene Fibers and Yarns from Liquid Crystalline Dispersions of Graphene Oxide: Towards Multifunctional Textiles. *Adv. Funct. Mater.* **2013**, *23* (43), 5345–5354.

(16) Takayanagi, M.; Imada, K.; Kajiyama, T. Mechanical Properties and Fine Structure of Drawn Polymers. *J. Polym. Sci. Part C Polym. Symp.* **2007**, *15* (1), 263–281.

(17) Ward, I. M. (Ian M.; Sweeney, J. (John). *Mechanical Properties of Solid Polymers.*

(18) Hosemann, R. Crystalline and Paracrystalline Order in High Polymers. *J. Appl. Phys.* **1963**, *34* (1), 25–41.

(19) Fujishiro, H.; Ikebe, M.; Kashima, T.; Yamanaka, A. Drawing Effect on Thermal Properties of High-Strength Polyethylene Fibers. *Jpn. J. Appl. Phys.* **1998**, *37*, 1994–1995.

(20) Sasagawa, K.; Saka, M.; Abé, H. Current Density and Temperature Distributions near the Corner of Angled Metal Line. *Mech. Res. Commun.* **1995**, *22* (5), 473–483.

(21) Horiuchi, K.; Dutta, P. Joule Heating Effects in Electroosmotically Driven Microchannel Flows. *Int. J. Heat Mass Transf.* **2004**, *47* (14–16), 3085–3095.

(22) Tegou, E.; Pseiropoulos, G.; Filippidou, M. K.; Chatzandroulis, S. Low-Temperature Thermal Reduction of Graphene Oxide Films in Ambient Atmosphere: Infra-Red Spectroscopic Studies and Gas Sensing Applications. *Microelectron. Eng.* **2016**, *159*, 146–150.

(23) Gambhir, S.; Murray, E.; Sayyar, S.; Wallace, G. G.; Officer, D. L. Anhydrous Organic Dispersions of Highly Reduced Chemically Converted Graphene. *Carbon N. Y.* **2014**, *76*, 368–377.

(24) Stankovich, S.; Dikin, D. A.; Piner, R. D.; Kohlhaas, K. A.; Kleinhammes, A.; Jia, Y.; Wu, Y.; Nguyen, S. T.; Ruoff, R. S. Synthesis of Graphene-Based Nanosheets via Chemical Reduction of Exfoliated Graphite Oxide. *Carbon N. Y.* **2007**, *45* (7), 1558–1565.

(25) Tuinstra, F.; Koenig, J. L. Raman Spectrum of Graphite. *J. Chem. Phys.* **1970**, *53* (3), 1126.

(26) Mehrali, M.; Sadeghinezhad, E.; Akhiani, A. R.; Tahan Latibari, S.; Talebian, S.; Dolatshahi-Pirouz, A.; Metselaar, H. S. C.; Mehrali, M. An Ecofriendly Graphene-Based Nanofluid for Heat Transfer Applications. *J. Clean. Prod.* **2016**, *137*, 555–566.

(27) Pei, S.; Cheng, H. M. The Reduction of Graphene Oxide. *Carbon N. Y.* **2012**, *50* (9), 3210–3228.

(28) Aboutalebi, S. H.; Jalili, R.; Esrafilzadeh, D.; Salari, M.; Gholamvand, Z.; Yamini, S. A.; Konstantinov, K.; Shepherd, R. L.; Chen, J.; Moulton, S. E.; et al. High-Performance Multifunctional Graphene Yarns: Toward Wearable All-Carbon Energy Storage Textiles. *ACS Nano* **2014**, *8* (3), 2456–2466.

(29) Zhao, Y. H.; Zhang, Y. F.; Bai, S. L. High Thermal Conductivity of Flexible Polymer Composites due to Synergistic Effect of Multilayer Graphene Flakes and Graphene Foam. *Compos. Part A Appl. Sci. Manuf.* **2016**, *85*, 148–155.

(30) Guo, H.; Li, X.; Li, B.; Wang, J.; Wang, S. Thermal Conductivity of Graphene/poly(vinylidene Fluoride) Nanocomposite Membrane. *Mater. Des.* **2017**, *114*, 355–363.

(31) Zhao, Y. H.; Wu, Z. K.; Bai, S. L. Study on Thermal Properties of Graphene Foam/graphene Sheets Filled Polymer Composites. *Compos. Part A Appl. Sci. Manuf.* **2015**, *72*, 200–206.

Chapter 5:

Processable thermally conducting composite fibres

5.1. Introduction

In recent decades, a lot of work has been done in the area of incorporation of electronic components into textiles and garments so as to equip traditional textiles with functionality such as sensing, health and environment monitoring and energy storage[1–7]. Owing to rapid development of nanoscience and technology, it is possible to build electronic functions inside or on the surface of fibres and consequently incorporate it into a garment using well-established textile fabrication techniques[1]. As a result of this increasing demand for wearable electronics, a great deal of research has been made to produce electrically conducting fibres for different application including strain sensing, energy storage, etc.[8–11]. Heat removal and heat management in microelectronics are becoming very important by ever growing demand for miniaturization and development of wearable electronics[12]. While a significant amount of work has been performed to produce electrically conducting composite fibres, making these fibres thermally conducting for heat dissipation has been almost neglected. Thermally conducting fibres may be used as heat sink which is one of the necessary compartments in integrated electronics. One of the most commonly used methods to tackle heating issues in devices the use of heat sinks or heat spreaders. These are materials with high thermal conductivity which are typically used as an attachment to a device to facilitate heat dissipation from the device. A range of composite materials including polymer-matrix composites have been developed to satisfy this need[13,14]. One of the most common methods of making thermally conducting polymeric composites is adding thermally conducting fillers such as aluminium nitride, wollastonite, silicon carbide whisker, boron nitride, etc. into a thermally insulating polymeric matrix[15,16].

Carbon allotropes and their derivatives, specifically one- and two-dimensional materials

such as carbon nanotubes and graphene sheets have attracted a lot of attention as thermally conductive fillers for different applications[17]. Liquid crystalline graphene oxide (LCGO) which is produced using a novel protocol with extremely high aspect ratio and lateral size of up to ca. 100 μm was chosen as one of the fillers to make composite fibres. Its unique characteristics such as ability to form liquid crystals in very low concentrations, very large sheet size that can effectively improve desired properties in a composite material in relatively low loadings compare to conventional graphene oxides. Extraordinary high thermal conductivity of ca. 1500 W m^{-1} K^{-1} was achieved using LCGO[18,19].

Boron nitride (BN), also known as white graphite, is an isoelectronic with carbon and has a wide range of attractive properties such as high thermal conductivity, low coefficient of thermal expansion, high electrical resistivity in a wide temperature range, high temperature stability, high mechanical strength and hardness, high corrosion resistance and chemically stable with respect to most molten metals and glasses, organic solvents, and polymers, even at high temperature. Such characteristics make it a widely used ceramic material for different applications[20–23]. Therefore, BN was also chosen to be used as another filler to make thermally conducting polymeric composite fibres.

It has been reported that composites made using solution mixing process exhibit higher thermal conductivity compare to those prepared with melt mixing method (similar to those made in Chapter 4) at the same filler concentration[24]. More uniform filler distribution was achieved by solution-mixing resulting in a lower level of aggregation. This resulted in the improved performance of solution-mixed thermally conducting composites compared to those which were melt-mixed. Therefore, solution mixing and wet-spinning methods have been chosen to make LCGO/PU or BN/PU composites and fibres, respectively. Polyurethane (PU) exhibits mechanical properties of rubber while non

cross-linked variants can be solvent processed or melt processed such that it has been described as "bridging the gap between rubber and plastics". The combination of high elasticity with high abrasion resistance makes PU very popular for a wide range of applications[25]. Importantly, non-crosslinked PU may be soluble in organic solvents and PU composite structures with different fillers can be readily made[5,8,9,26]. HydroThane® 80A (AdvanSource Biomaterials) was selected for composite fibre development in this Chapter as it was a polyurethane that was biocompatible, thermoplastic, hydrophilic and soluble in organic solvents (non-crosslinked).

The aim of this chapter is to produce and characterize processable thermally conducting composite fibres using polyurethane polymeric matrix and two different filler materials with very high thermal conductivity, i.e. liquid crystalline graphene oxide (LCGO) and boron nitride nanopowders (BNNP). For this purpose, initially the spinning parameters were optimized to produce pristine PU (AdvanSource Biomaterials HydroThane® 80A) and its composite fibres with LCGO or BNNP. These spun fibres were then incorporated into 3D polyester (PET) knitted structures and finally, the effect of incorporation of these fibres into 3D textile structures to minimize Joule-heating effect was investigated under electrophoretic conditions. Different streaming potentials, from 20 to 250 V cm^{-1}, were applied to the fabricated 3D textile structures and corresponding currents were measured, with temperature changes in the structures monitored when 250 V cm^{-1} was applied to the structures.

5.2. Experiments
5.2.1. Solvent for PU

Solubility of PU (AdvanSource Biomaterials HydroThane® 80A) was investigated in DMF and different rations of EtOH and water. Loadings of up to 750 mg of PU powder in 15 mL of solvent at 70°C of constant stirring were investigated.

5.2.2. Composite development

5.2.2.1. LCGO/PU composite

LCGO was initially redispersed in EtOH (replacing water with EtOH in LCGO dispersion). For this purpose, 10 mL of the aqueous LCGO was transferred into a centrifuge tube and about 20 mL of EtOH was added to that and mixed by vortex shaking. Then mixture was centrifuged at 8000 rpm for 99 minutes. After centrifugation, the supernatant was pipetted out and replaced with EtOH followed by vigorously mixing by vortex shaking. This process was repeated 4-5 times to replace the water with the EtOH[27]. DI water was then gradually added to LCGO depression in EtOH to make LCGO dispersion in EtOH/water (85:15 v/v). Finally, LCGO/PU composites were prepared via the gradual addition of the PU solution in EtOH/water (85:15 v/v) to the LCGO dispersion under constant stirring.

5.2.2.2. BNNP/PU composite

BNNP was weighed and dispersed in EtOH/water (85:15 v/v) followed by 60 minutes of bath sonication. BNNP/PU composites were prepared by the gradual addition of the PU solution in EtOH/water (85:15 v/v) under constant stirring.

5.2.3. Fibre wet spinning

Pristine PU fibres as well as LCGO/PU and BNNP/PU composite fibres were made using a wet-spinning method in horizontal configuration as previously described in Chapter 2. Water was used as coagulant in coagulation bath with addition of about 5 % (v/v) EtOH. PU solutions (or PU composite solutions) were injected into the coagulation bath at flow rates of 2-4 mL h^{-1} and needle 20G was used to spin all fibres. PU fibres were then continuously collected on a circular collector and air dried before being knitted.

5.2.4. Fabrication of knitted 3D structures

As previously discussed in Chapter 3, polyester (PET) substrates were chosen as the base

material to make textile-based microfluidics. 3D knitted structures were prepared by parallel feeding of PET with the wet-spun fibres into the knitting machine (using knitting parameters the same as described in Chapter 3). Spun fibres, i.e. PU, LCGO/PU or BNNP/PU fibres, were fed into the knitting zone by passive feeding. Cross-section optical micrographs of the resulting knitted structures as shown in Figure 5.1.
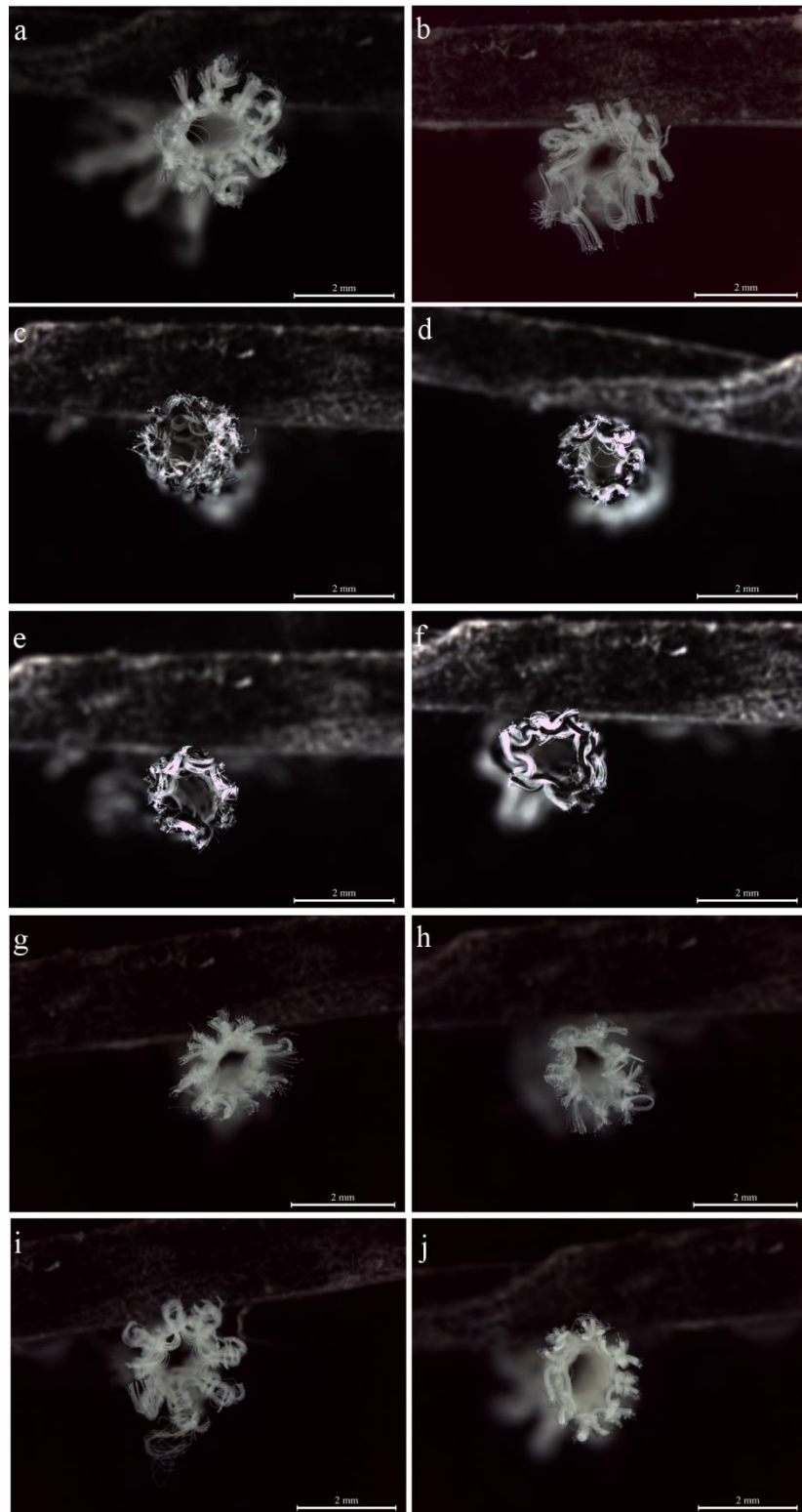
Figure 5.1: Optical micrographs showing cross-sections of knitted structures comprised of (a) 2 PET yarns, (b) PET yarns parallel with PU, (c)-(f) PET yarns parallel with 0.25, 0.5, 1 and 2 w/w% LCGO/PU composite fibres, (g)-(j) PET yarns parallel with 0.5, 1, 2 and 5 w/w% BNNP/PU composite fibres respectively.

5.2.5. Reduction of LCGO/PU

LCGO/PU fibres were chemically reduced using 5 wt.% hypophosphorous acid at 80 °C overnight[27,28]. Excess acid was then removed by dialysis and finally structures were vacuum dried at 80 °C for 1 hour.

5.2.6. Characterisation

5.2.6.1. Zeta-potential

The LCGO dispersion Zeta-potential was determined as discussed in Chapter 3.

5.2.6.2. Rheology test

The viscosity of polymer and composite solutions were measured by a rheometer (TA Instruments AR-G2) at 25°C. Details of the experiment were previously described in Chapter 2.

5.2.6.3. Thermal diffusivity

Thermal diffusivity of PU, LCGO/PU and BNNP/PU films were characterized at 30 °C using the NETZSCH laser flash apparatus LFA 457 MicroFlash® as described in Chapter 2. Discs of 12.5 mm in diameter prepared for each sample and their thicknesses were measured using an inbuilt image analysis application on an optical Leica microscope system.

5.2.6.4. Specific heat capacity (C_p)

Specific heat capacity of the samples was measured using DSC as described in Chapter 2. The thermal conductivities of PU and its composites with BNNP and LCGO were calculated using equation 1.

$$\lambda(T) = a(T) \cdot C_\rho(T) \cdot \rho(T) \tag{1}$$

Where λ represents thermal conductivity [W $(m \cdot K)^{-1}$], a represents thermal diffusivity [mm² s^{-1}], Cp is specific heat capacity [J $(g \cdot K)^{-1}$] and ρ shows sample bulk density [g cm^{-3}].

5.2.6.5. Fibre mechanical properties

To evaluate the mechanical properties of pristine PU and its composite fibres with LCGO and BNNP, first fibres' diameters were measured using the inbuilt image analysis application of optical Leica microscope software. 30 mm lengths of fibres were fixed into a paper frame to ensure the fibres were held in a vertical position between the clamps of tensile tester machine and the frames cut to leave a free mounted fibre. Then fibres were stretched at the rate of 10 mm min^{-1} until fracture.

5.2.7. Joule-heating dissipation experiment

For Joule-heating dissipation tests, the same experimental setup as described in Chapter 4 was used. Similar to the electrofluidic experiments in Chapter 4, different potentials were applied to the structures and corresponding currents were measured by LabSmiths® software. Temperature changes were also measured by an infrared thermographic camera (thermoIMAGER TIM 160, Micor-Epsilon, Germany).

5.3. Results and discussion
5.3.1. Solvent for PU

The solubility of PU in DMF and a range of EtOH/Water mixture were tested. Table 5.1 shows the results of solubility test. It was found that PU was soluble in DMF along with two different ratios of EtOH/water solvent, i.e 85:15 v/v and 95:5 v/v. Figure 5.2 shows PU in different ratios of EtOH and water after being stirred at 70°C for 2 hours. As the EtOH/water mixture had a similar performance to DMF and given that it was is less toxic and importantly more volatile, an important for making uniform composite films via casting methods, this mixture was chosen as the preferred PU solvent.

Table 5.1: Solubility of PU in different solvents

Solvent	PU solubility
DMF	Yes
EtOH	No
EtOH/water (95:5 v/v)	Yes
EtOH/water (85:15 v/v)	Yes
EtOH/water (50:50 v/v)	No
EtOH/water (70:30 v/v)	No
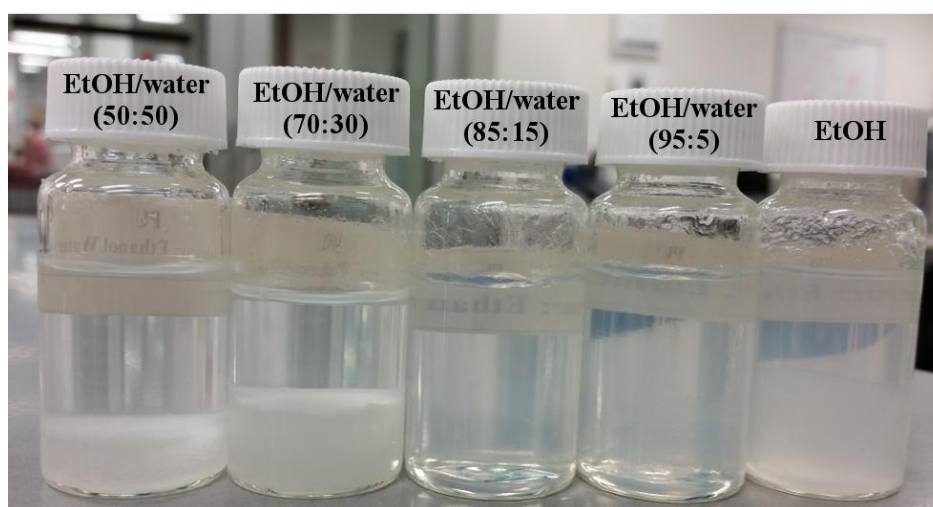
Figure 5.2: PU in different ratios of EtOH and water after being stirred at 70°C for 2 hours.

5.3.2. Spinning solutions and parameters

50 mg mL^{-1} PU solutions in EtOH/water (85:15 v/v) and EtOH/water (95:5 v/v) were prepared and their rheological properties, one of the most important factors in wet-spinning process, were compared. Figure 5.3 compares the viscosities of these solutions at

different shear rates, 0.01 to 400 s^{-1}.
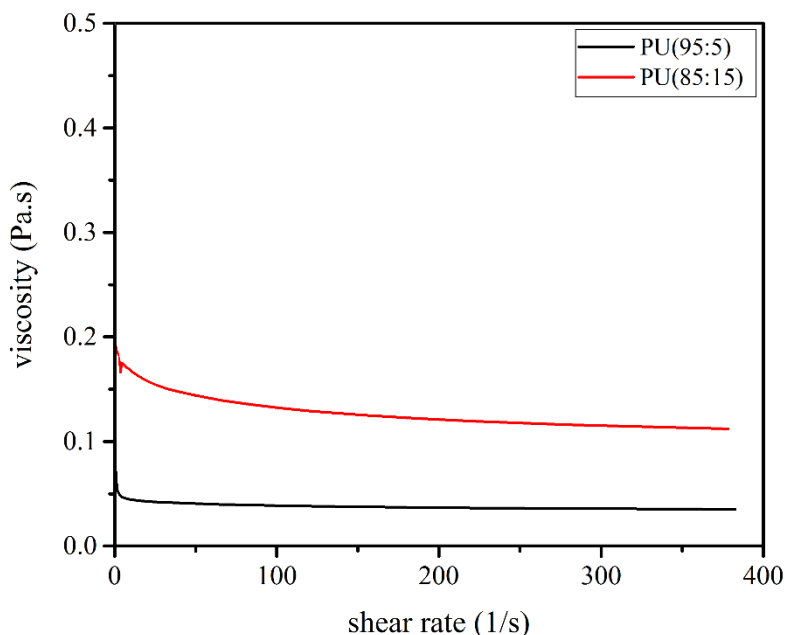
Figure 5.3: Viscosities vs. shear rate for 50 mg mL^{-1} PU solutions in EtOH/water (85:15 v/v) and EtOH/water (95:5 v/v)

As shown in Figure 5.3, in both solutions the viscosity decreased with an increase in the shear rate known as shear thinning phenomenon[29]. This phenomenon occurs as a result of gradual breaking of molecular entanglement with an increase in the shear rate. The degree of intermolecular association dominates the slope of the decreasing viscosity with increasing shear rate, i.e. the lower the molecular entanglement, the lower the slope[30]. The PU solution in EtOH/water (85:15 v/v) showed a higher viscosity with respect to shear force compared to a PU solution in EtOH/water (95:5 v/v) at the same concentration of PU. This indicates that dissolving PU in EtOH/water (85:15 v/v) resulted in a less intertwined solution with less decay of viscosity by shear force[29]. Therefore, the mixture of EtOH/water (85:15 v/v) was chosen as the preferred solvent for making PU solution for all fibres including LCGO/PU and BNNP/PU composite solutions.

Injection of the spinning solution into the coagulation bath causes shearing forces to the solution, therefore, rheological study of spinning solutions, i.e. PU and its composite

solutions, under shear was necessary.

PU fibres were spun from 50 mg mL^{-1} PU solution in EtOH/water (85:15 v/v). Water was used as coagulant as previously reported for spinning of pure or PU composite fibres[5,8]. About 5% (v/v) EtOH was added to the coagulation to adjust the density of coagulation bath to make the fibre sink in coagulation bath and to adjust the mass transfer rate difference[8] during the coagulation process in the spinning bath so as to form fibres that were more circular in cross-sectional shape. PU fibres were successfully spun using a horizontal wet-spinning configuration at flow rates of 2-4 mL h^{-1} using a gauge 20 needle as the spinneret. Figure 5.4 and Figure 5.5 show PU spun fibres collected on a collector and optical and SEM micrographs of PU fibres.
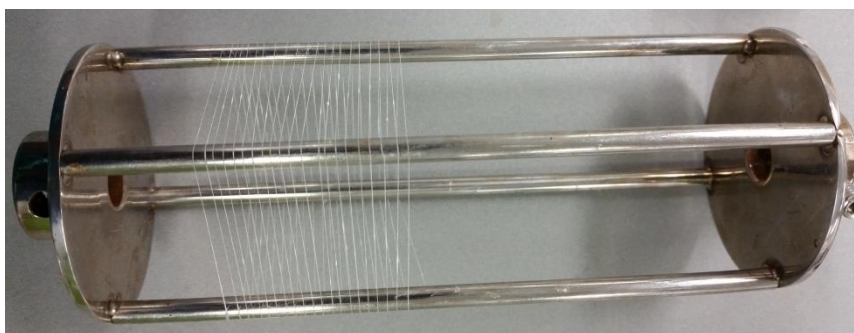
Figure 5.4: PU spun fibre collected on a collector
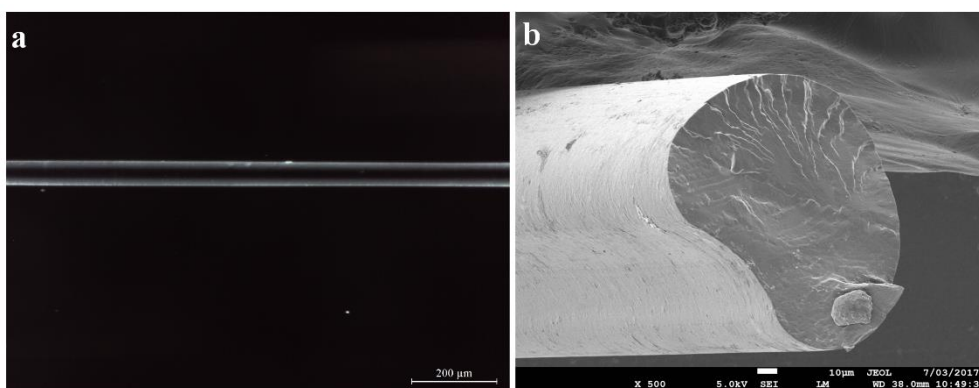
Figure 5.5: (a) optical micrographs of length and (b) SEM image of cross-section of PU spun fibre

Beads were noted to be formed at injection flow rates lower than 2 mL h^{-1}. Bead

formation was noted to result in spinneret blockage and fibre breakage. PU fibres were also not formed at injection rates higher than 4 mL h^{-1}. For these reasons an injection flow rate of 3mL h^{-1} was chosen to produce LCGO/PU and BNNP/PU composite fibres. Figure 5.6 and Figure 5.7 show optical micrographs of length and SEM images of cross-sections of LCGO/PU composite fibres, respectively.
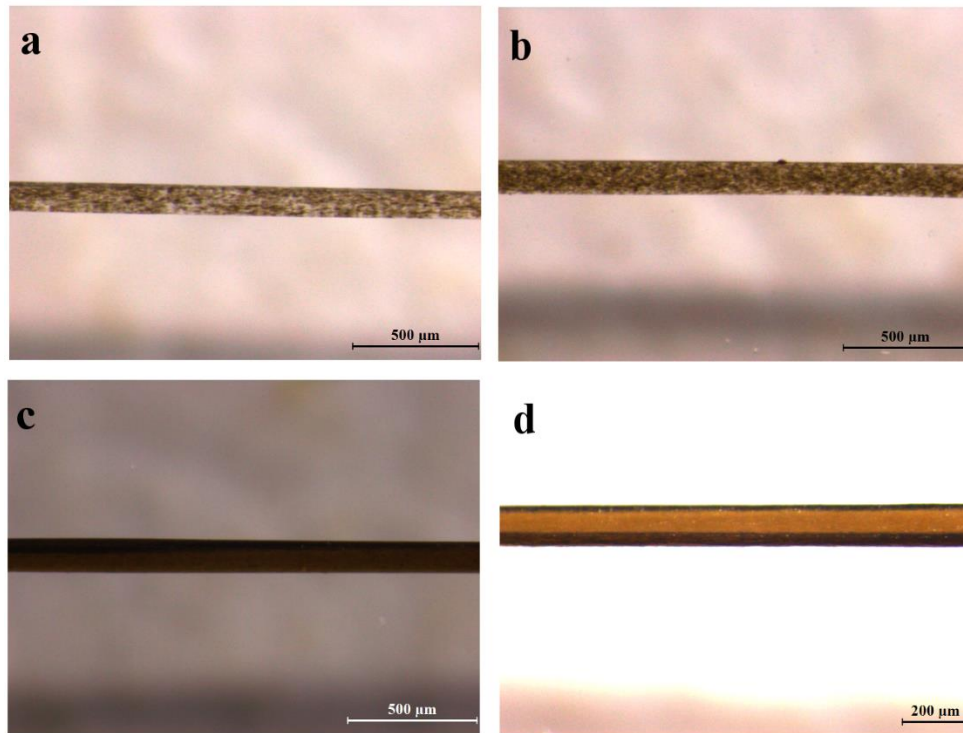
Figure 5.6: Optical micrographs of (a) 0.25 , (b) 0.5, (c) 1 and (d) 2 w/w% LCGO/PU composite fibres.
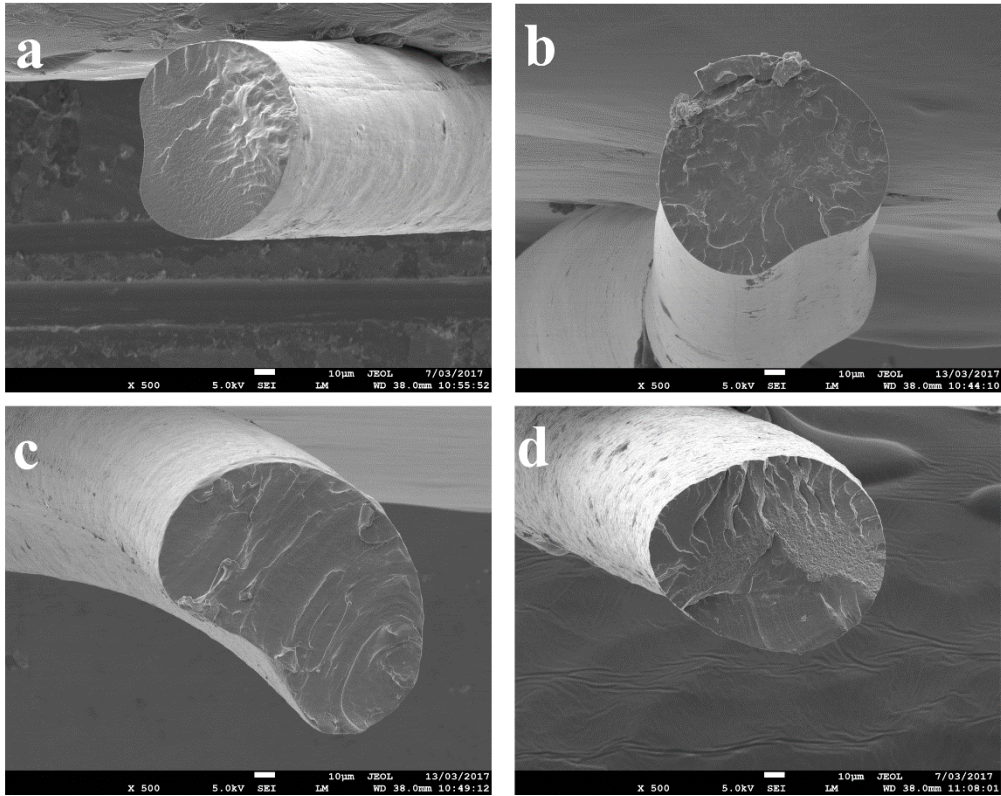
Figure 5.7: SEM images of cross-sections of (a) 0.25 , (b) 0.5, (c) 1 and (d) 2 w/w% LCGO/PU composite fibres.

BNNP/PU composite fibres were also made using the same method. Figure 5.8 and Figure 5.9 show optical micrographs of length and SEM images of cross-sections of BNNP/PU composite fibres, respectively.
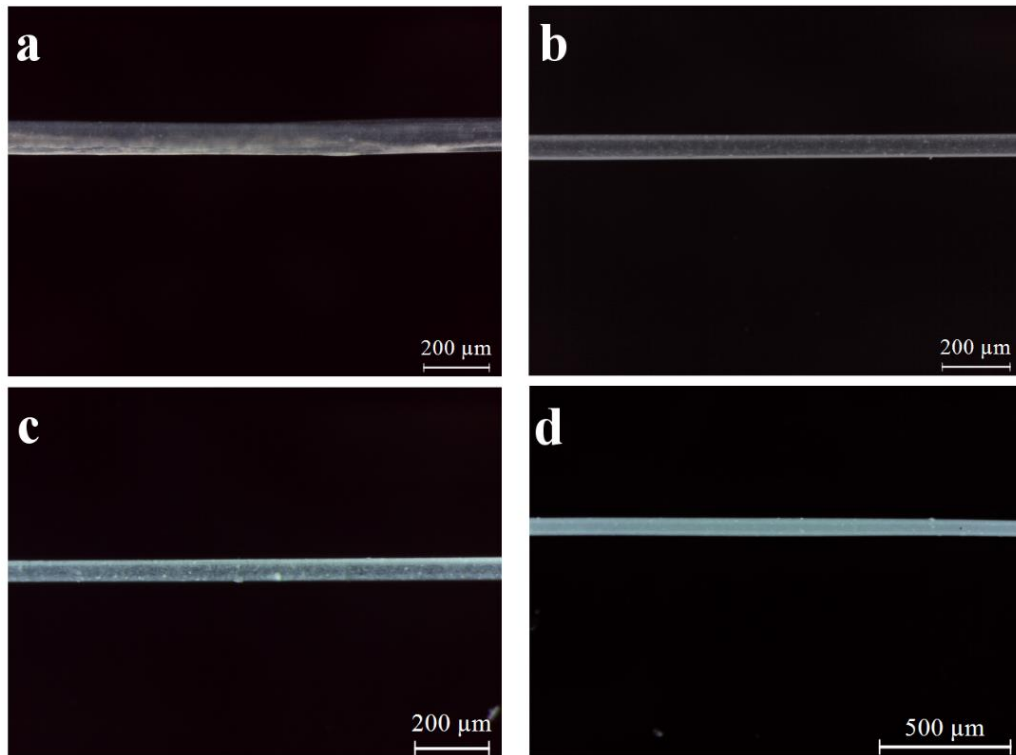
Figure 5.8: Optical micrographs of (a) 0.5 , (b) 1, (c) 2 and (d) 5 w/w% BNNP/PU composite fibres.
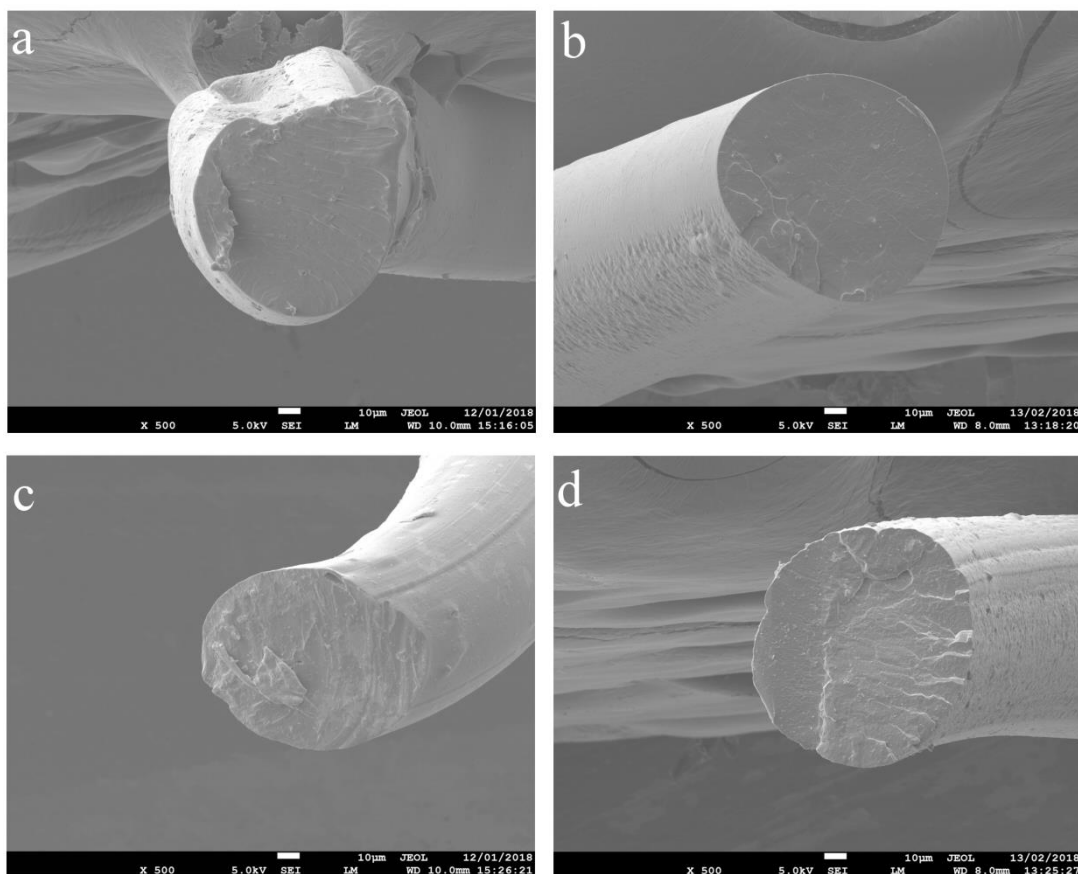
Figure 5.9: SEM images of cross-sections of (a) 0.5 , (b) 1, (c) 2 and (d) 5 w/w% BNNP/PU composite fibres

As shown in Figure 5.5, Figure 5.7 and Figure 5.9, the cross section of PU and its composite fibres with LCGO and BNNP were nearly circular indicating that coagulation solvent diffused into the injected spinning solution at almost the same rate that solvent of spinning solution extracted into the coagulation bath[8].

5.3.3. Raman spectroscopy on composites

Raman spectra of PU and chemically reduced LCGO/PU composites, shown in Figure 5.10, clearly indicate that LCGO was uniformly distributed into PU matrix. Typical PU peaks were observed in the Raman spectra[31]. Characteristics D and G peaks of the carbonaceous LCGO were observed at 1347 and 1586 cm^{-1}, respectively were observed in spectrum of itself LCGO[32,33]. These peaks were also clearly observable in Raman spectra of LCGO/PU composites indicating the integration of LCGO into PU polymeric matrix.

Addition of LCGO into the PU matrix resulted in weakening of PU Raman peaks with these disappearing at 2 w/w% loading as a result of the PU Raman spectra signal being significantly weaker than the LCGO[34]. Chemical reduction of LCGO/PU composites, partially eliminates oxygen containing groups of GO and restores the pi-electron structure to some extent[35]. The observed Raman spectra of the reduced LCGO/PU structures, D and G bands shifted compare to those of LCGO which is an indication for reduction of graphene oxide[32]. Similarly, the ratio of the D/G bands (I_D/I_G) was noted to increase after reduction of samples containing LCGO (it was measured to be 1.18 in LCGO to 1.43 in 0.25 w/w%, 1.58 in 0.5 w/w%, 1.49 in 1 w/w% and 1.28 in 2 w/w% composite fibres), which has also been attributed to formation of new smaller graphitic domains confirming the reduction of LCGO[36–39]. Considering the indications of chemical reduction of LCGO, the increase in thermal conductivity of the LCGO/PU composite fibres as a consequence of the LCGO reduction can be expected[10,19].
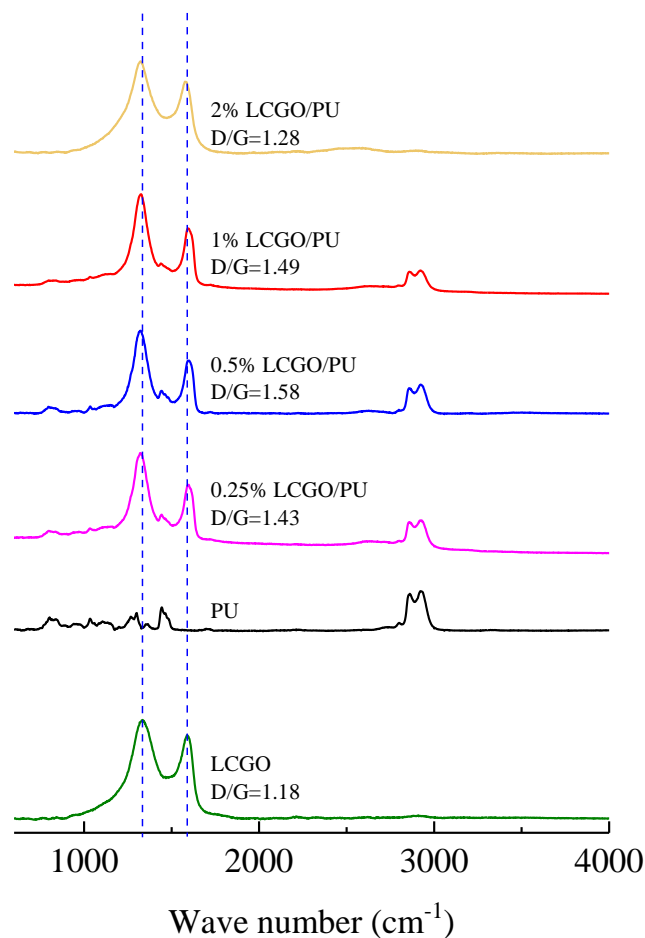
Figure 5.10: Raman spectra of PU, LCGO and chemically reduced LCGO/PU composites

Figure 5.11 shows Raman spectra of PU, BNNP and BNNP/PU composites. Boron nitride exhibited a dominant peak at 1366 cm^{-1}. This peak is analogous to the G peak in graphene and is due to the E_{2g} phonon mode[40,41]. This peak was also observable in all BNNP/PU composites indicating the incorporation of BNNP into PU polymeric matrix. As for the LCGO this BNNP peak becomes more dominant compare to PU Raman peaks as the BNNP loading was increased.
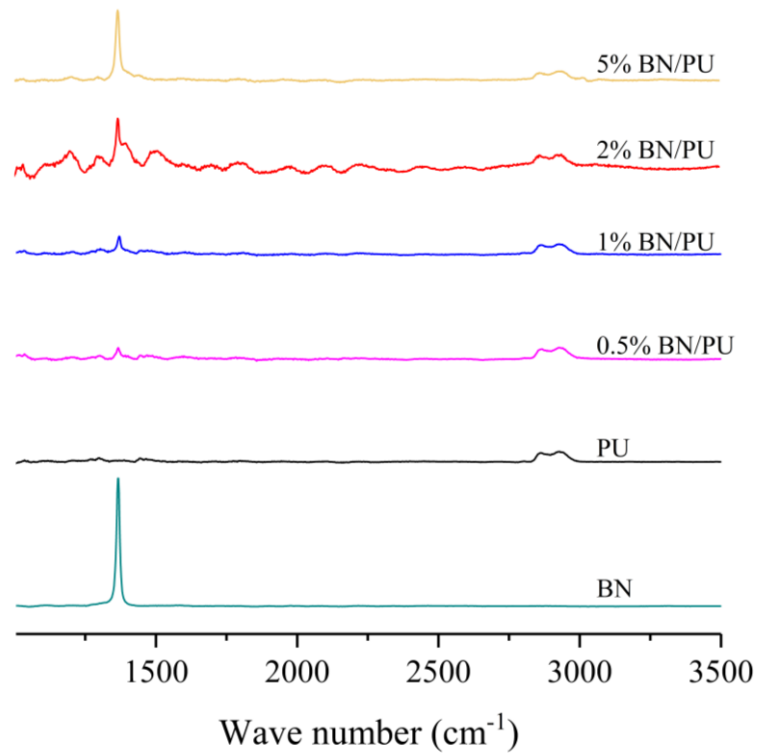
Figure 5.11: Raman spectra of PU, BNNP and BNNP/PU composites

5.3.4. Mechanical test

As spun PU and its composite fibres, i.e. BNNP/PU and LCGO/PU, exhibited similar uniaxial tensile behaviour to what has been reported for thermoplastic polymers, Figure 5.12. This includes an initial modulus region, region I, followed by strain-induced softening which is a plateau region of almost constant stress, region II, and finally, strain hardening zone, region III[26,42,43].
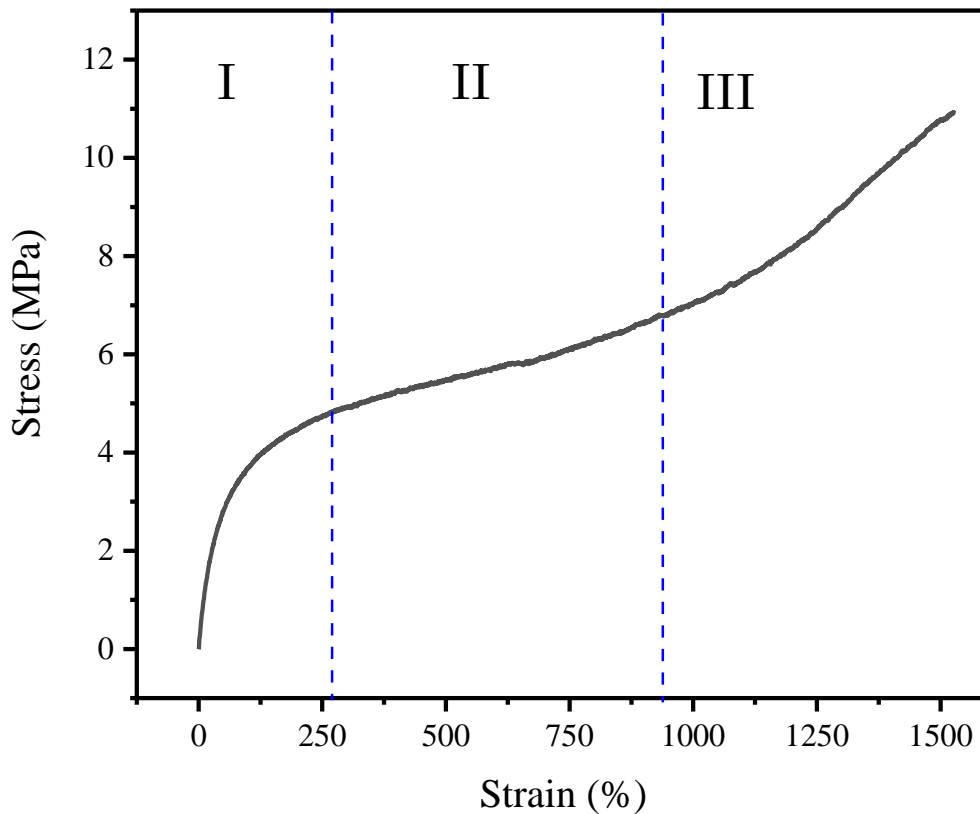
Figure 5.12: A typical stress-strain curve for PU and its composite fibres with BNNP or LCGO

The effect of addition of LCGO into PU polymeric matrix on ultimate stress, elongation at break and Young's modulus is shown in Figure 5.13. See Appendix II for MATLAB code designed to calculate Young's modulus for LCGO/PU composite fibres.

PU polymers are composed of two different parts, i.e. soft segments and hard segments. Viscous behaviour, elongation, of PU is attributed to its soft segment while stiffness and elastic behaviour is originated from hard segment[26,27,43]. As Figure 5.13 clearly shows, the addition of LCGO filler into the PU matrix led to an increase in Young's modulus and ultimate tensile strength with an associated decrease in elongation at break, which is in agreement with previous studies[26,27,31,33,44]. Increase in ultimate stress can be attributed to the fact that adding filler into elastomers reinforces them in two ways. Firstly, by broadening the relaxation spectrum and therefore, enhancing the capability of dissipating

strain energy in the presence of fillers. Secondly, fillers may decelerate or even stop the cracks initiated in the polymer.[43] Strong interfacial adhesion between LCGO and PU matrix is likely to have formed as a result of hydrogen bonds between hydroxyl and carboxyl functional groups on the surface of the LCGO and PU polymer chains. Therefore, the applied mechanical load may be effectively transferred from the weak matrix to the strong LCGO filler resulting in increase in Young's modulus[31,33]. The initial increase in ultimate stress and Young's modulus while elongation at break remained relatively unchanged suggested that loading lower loadings of LCGO had reinforcement effect on PU hard segments while soft segments remained intact[26,27,31,33,43]. LCGO loadings higher than 0.5 w/w% starts to influence soft segments of PU. The fracture of PU samples is likely due to the strain hardening and strain-induced crystallization of soft segments, regions II and III in Figure 5.12. It can be suggested that higher loadings of LCGO (more than 1 w/w%) may reduce ultimate stress by increasing the rate of strain hardening and strain-induced crystallization of the soft segments by hydrogen bonding[33]. Drops in elongation at break at higher LCGO loadings further proves that LCGO fillers interferes with soft segment domains of PU[9].
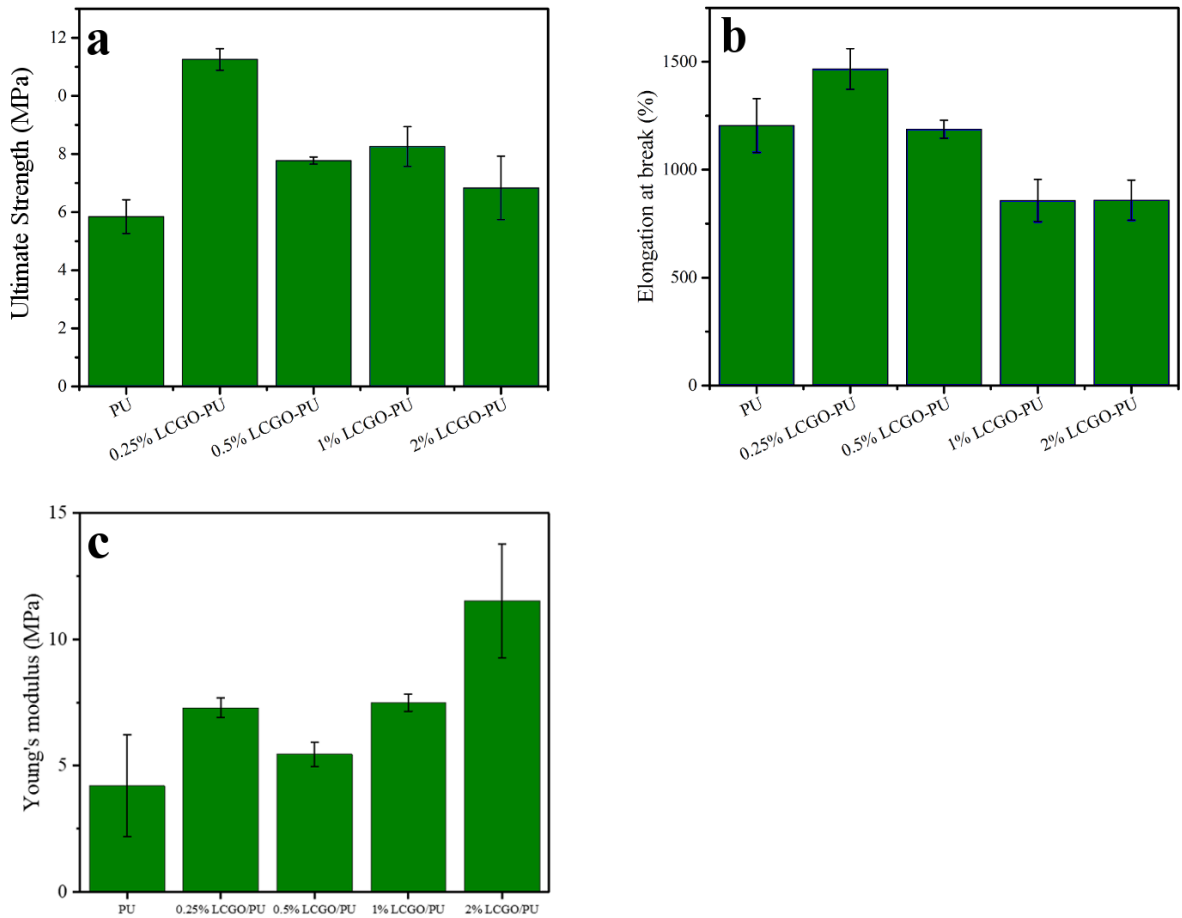
Figure 5.13: (a) Ultimate strength, (b) elongation at break and (c) Young's modulus of PU and LCGO/PU composite fibres

Figure 5.14 shows variations in ultimate stress, elongation at break and Young's modulus as a result of the addition of BNNP filler into the PU polymeric matrix. Similar to what was achieved with LCGO fillers, an increase in the loading of BNNP into PU matrix resulted in increase in Young's modulus and ultimate stress. These changes may be attributed to increasing the ability of strain energy dissipation of polymer due to the interfacial adhesion of filler into PU polymeric matrix[31,33,43]. In contrast to LCGO filler, the addition of BNNP into PU polymer resulted in increase in elongation at break. Since that BNNP has different morphology and much lower aspect ratio (~1) compare to LCGO sheets, Figure 5.15, this phenomenon was anticipated and in agreement with previous

results obtained for silica nanocomposite-filled PU[45] and low loadings of carbon black in

PU[9].
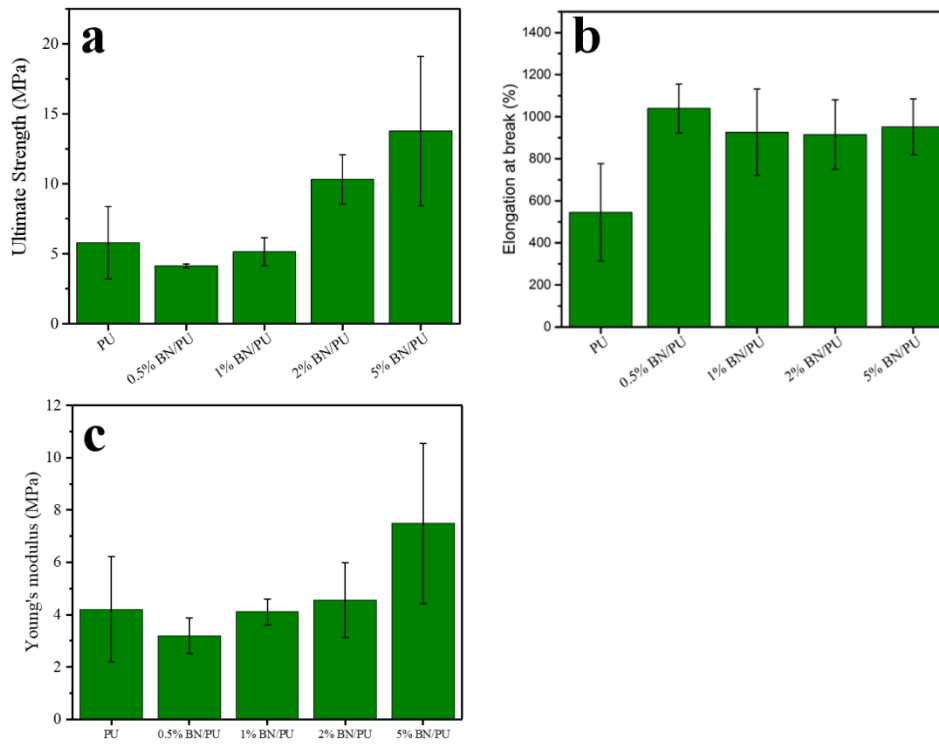
Figure 5.14: (a) ultimate strength, (b) elongation at break and (c) Young's modulus of PU and
BNNP/PU composite fibres
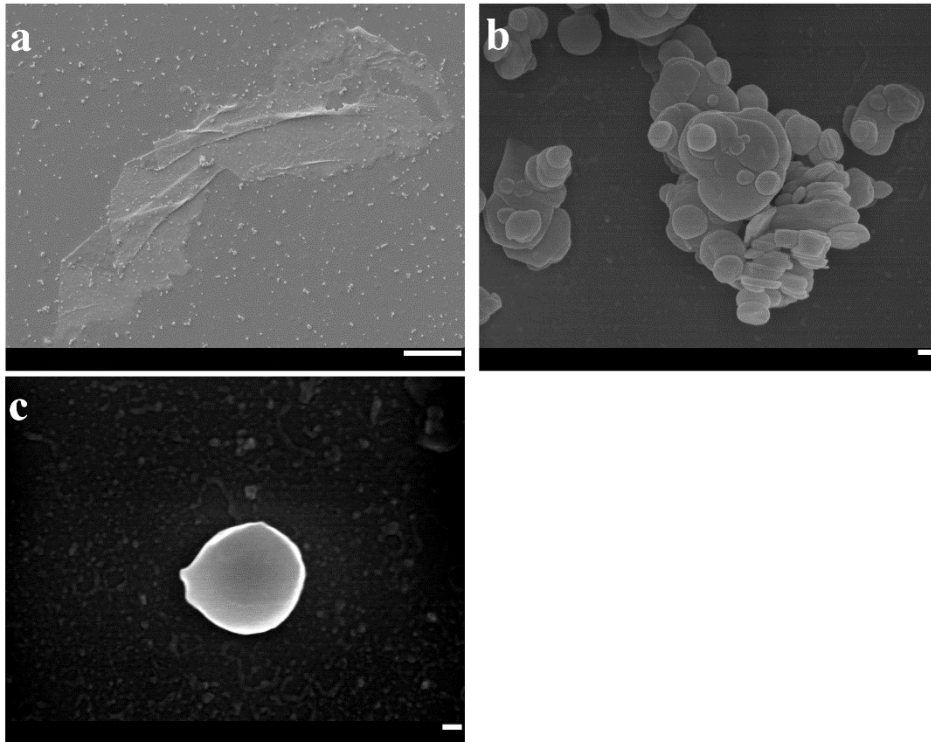
Figure 5.15: SEM micrographs of (a) isolated LCGO sheet (scale bar: 10 μm), (b) aggregated BNNPs (scale bar:100 nm) and (c) isolated BNNP (scale bar:100 nm)

5.3.5. Thermal conductivity

Specific heat capacity of polyurethane in the temperature range of 20 to 60 °C and its composites with LCGO and BNNP show a gradual increase by temperature which agrees with previous reports for PU and PU nanocomposites[46,47], Figure 5.16.
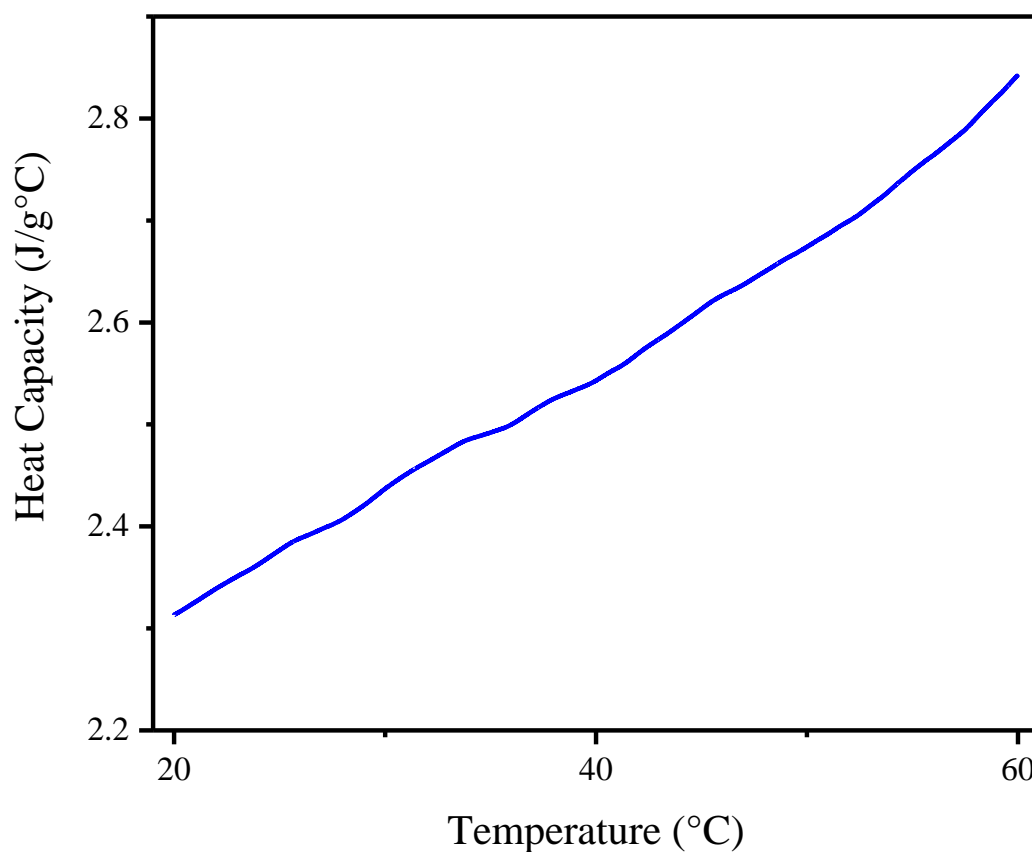
Figure 5.16: Temperature dependence of specific heat capacity of PU and its composites with LCGO and BNNP

Specific heat capacities (C_p) at 30 °C and densities of pure PU, LCGO/PU and BNNP/PU composite samples were measured and shown in Table 5.2. While specific heat capacity of PU/BNNP decreased with increase in filler loadings, which agrees with previous reports on nanoclay- and boron nitride-filled PU[24,47], C_p did not follow the same trend for LCGO fillers. Such fluctuations in C_P was also already reported for graphene-filled epoxy composites[48].

Table 5.2: Specific heat capacities at 30 °C and densities of PU, LCGO/PU and BNNP/PU samples

Sample	Specific heat capacity $(J\,g^{-1}\,{}^{\circ}C^{-1})$	Density $(g\,cm^{-3})$
PU	2.444	1.064
0.25 w/w% LCGO/PU	2.452	1.085
0.5 w/w% LCGO/PU	2.218	1.102
1 w/w% LCGO/PU	2.438	1.119
2 w/w% LCGO/PU	2.413	1.122
0.5 w/w% BNNP/PU	2.41	1.087
1 w/w% BNNP/PU	2.408	1.145
2 w/w% BNNP/PU	2.386	1.165
5 w/w% BNNP/PU	2.225	1.271

Thermal diffusivities of all samples were measured by LFA method. Figure 5.17 and Figure 5.18 show thermal diffusivity of reduced LCGO/PU and BNNP/PU composite structures, respectively
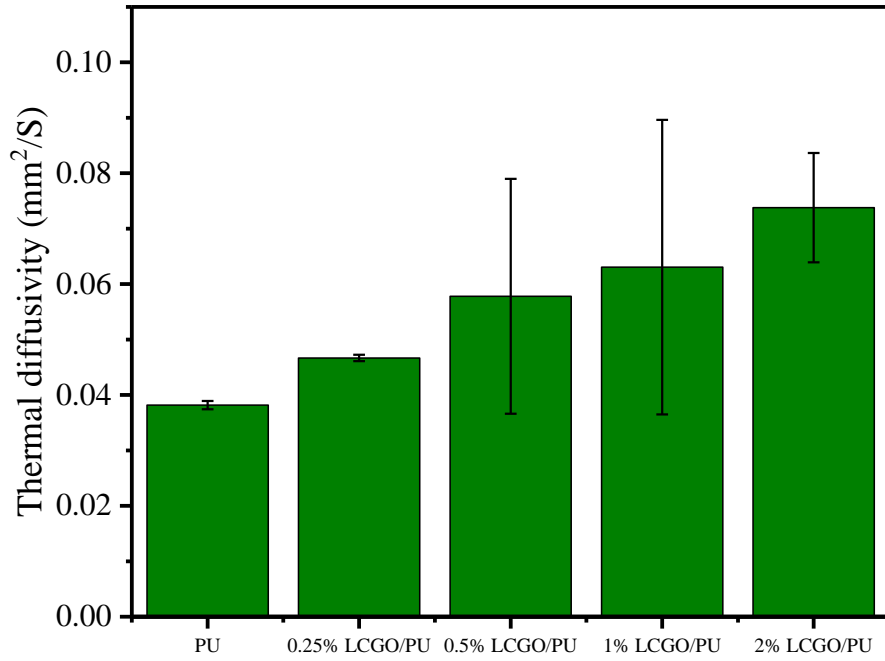
Figure 5.17: Thermal diffusivity of PU and reduced LCGO/PU composite structures
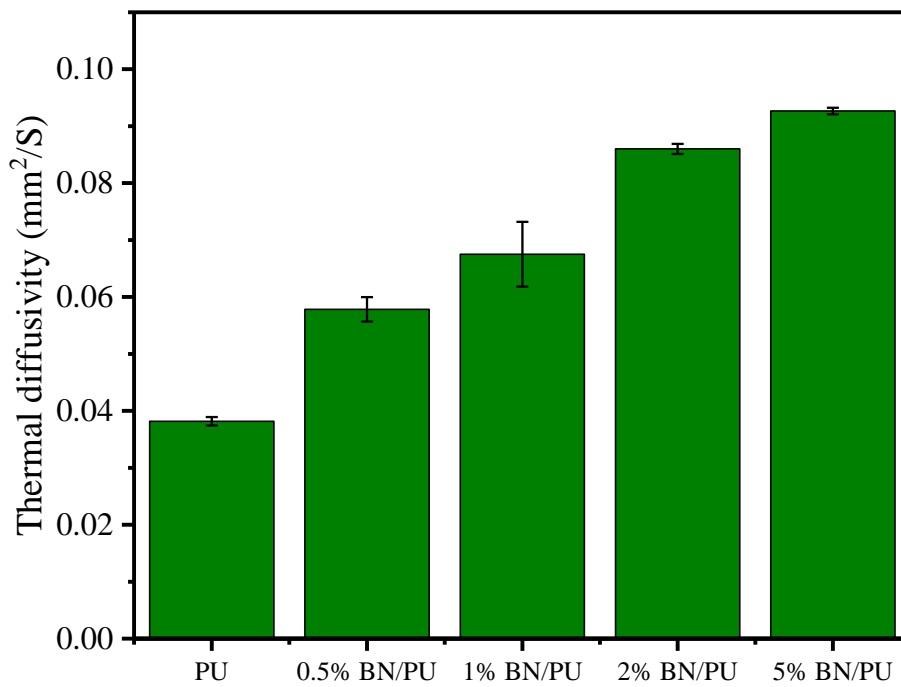
Figure 5.18: Thermal diffusivity of PU and BNNP/PU composite structures

Finally, thermal conductivities of LCGO- and BNNP-filled PU composites were calculated shown in Figure 5.19. Thermal conductivity enhancements[17] (η) were also calculated for both above mentioned composites using Equation 1 and

shown in Figure 5.20.

$$\eta = \frac{\lambda - \lambda_0}{\lambda_0} \quad\quad (1)$$

Where, λ and λ_0 represent thermal conductivity of composite and unfilled polymer, PU matrix, respectively. Addition of thermally conducting fillers, i.e. reduced LCGO and BNNP, into an insulating polymeric matrix, PU, enhanced the heat transfer rate in polymer and consequently increased thermal conductivity.
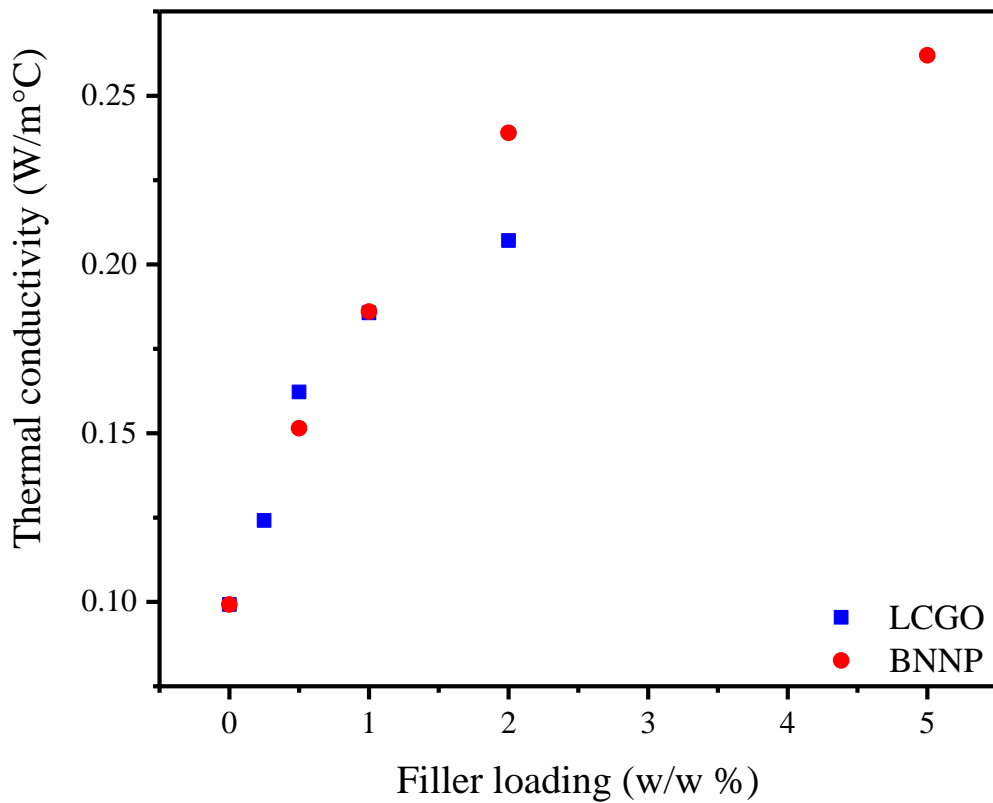
Figure 5.19: Thermal conductivity of PU and its composites with reduced LCGO and BNNP at different loadings
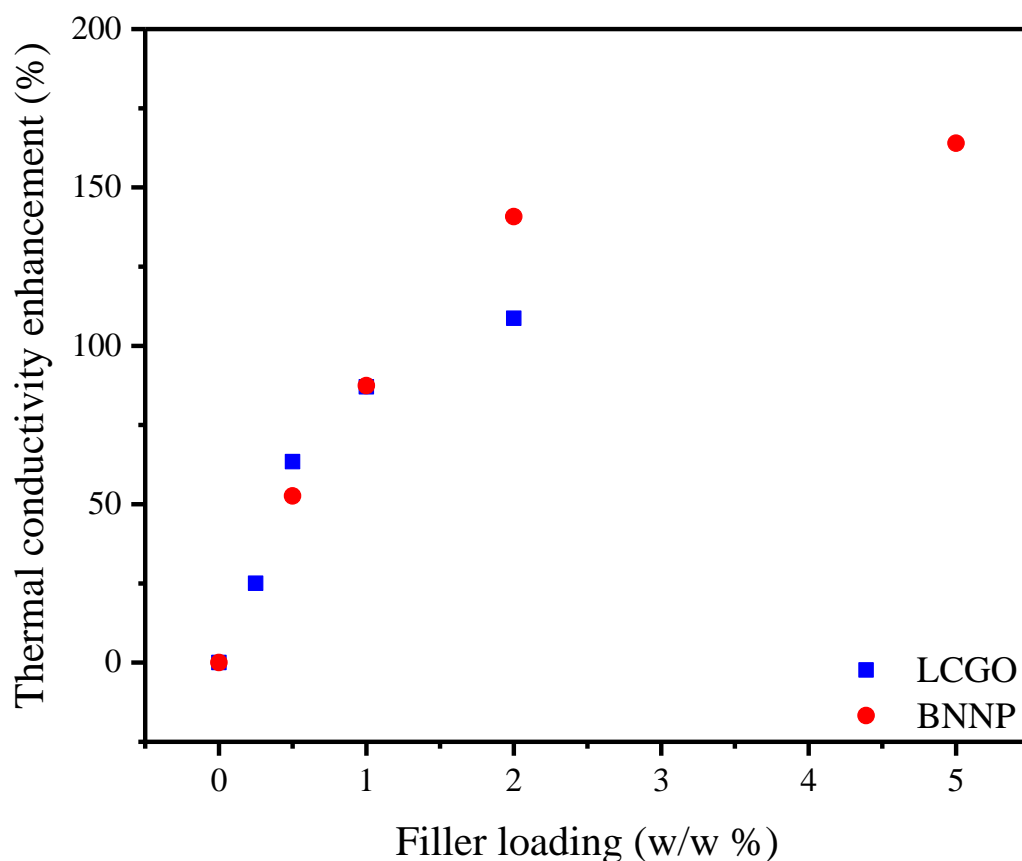
Figure 5.20: Thermal conductivity enhancement by addition of reduced LCGO and BNNP at different loadings

Although LCGO has been considered as one of the best filler materials for making thermally conducting polymer composites, where it has been reported that with a 1 wt.% loading the thermal conductivity of the base polymer could be doubled[17], in this study this advantage was observable only lodgings less than 1 w/w%. Contrasting this the thermal conductivity was enhanced using BNNP at higher concentrations of the filler. This phenomenon can be explained as follows: thermal conductivity of amorphous polymers greatly depends on phonon movements which is the dominant mode of thermal conduction. To increase thermal conductivity of such polymers, phonon scattering should be minimized by reducing the acoustic impedance mismatch at the interface between polymeric matrix and filler. It can be assumed that LCGO owing to its carboxyl and

hydroxyl functional groups (unlike neutral BNNPs) interact strongly to the PU chains and effectively transfer phonon movements with minimal phonon energy loss, i.e. interfacial heat transfer was improved at the boundaries of LCGO filler and PU polymeric matrix[48]. In addition, LCGO sheets with their extraordinary high aspect ratio start to interact with each other and low filler concentrations making conducting path networks. The result of this a decreasing thermal contact resistance by the formation of a compact packing structure which results in the polymeric matrix between the adjacent filler particles smaller and thinner. These interactions facilitate the enhancement of thermal conductivity at low concentrations of filler [49,50]. By increase in filler loadings, the thermal conductivity of LCGO/PU composite increased slowly. In this case many of the LCGO sheets were already interacting and there is no significant increase in the number of newly formed thermally conductive pathways. Therefore, the thermal conductivity will no longer be enhanced notably by increase in the concentration of fillers. In contrast, BNNP fillers with very fine dimensions easily aggregates at lower loadings, also, they have a very large surface area that causes high phonon scatterings at interfaces. Therefore, lower concentrations of BNNP did not effectively improve PU's thermal conductivity. With respect to the almost similar density value of BNNP to LCGO (2.29 g cm^{-3} for BNNP and 2.2 g cm^{-3} for graphene oxide[9]), at higher filler concentrations, BNNP occupies a very high volume fraction in composite (compare to that of LCGO/PU composites at the same mass fraction) and begin to form a highly compact packing structures and consequently thicker heat-conductive pathways in the PU polymeric matrix and improved thermal conductivity of PU polymer more effectively [24,50].

5.3.6. Joule-heating dissipation experiment

Current passing through a pre-concentrated 3D knitted structures comprising of PET threads or PET threads parallel with PU and reduced LCGO/PU composite fibres were measured when different potentials were applied, i.e. 20, 40, 60, 80, 100, 120, 140, 160, 180, 200 and 250 V cm^{-1}. As shown in Figure 5.21, the current and applied electric field for most of 3D knitted structures showed some non-linearity due to the Joule-heating effect[51]. The observed current increased more linearly with electric field in these structures compare to those of LCGO/LDPE composite fibres in Chapter 4. This observation may be attributed to the fact that Joule-heating is a volumetric phenomenon and its magnitude is directly affected by the volume of the channel used.[52] In this case the reduced LCGO/PU knitted structures had much lower diameter when compared to LCGO/LDPE knitted ones. Therefore, lower Joule-heating was generated in these structures. In the absence of Joule-heating effects, the observed electric current should be a linear function of the applied electric field and follow Ohm's law. With a Joule-heating effect present a higher electric current would be expected at every electric field proportional to the electric current to the power of two ($P=VI=I^2R$),[53] according to the power law, due to an enhanced electrolyte ionic conductivity resulting from the elevated electrolyte temperatures which then results in the current-electric field deviating from linearity. Joule-heating effects will also be higher in textile samples with lower thermal conductivities due to being unable to dissipate heat which leads to more non-linearity in the observed current-electric field.
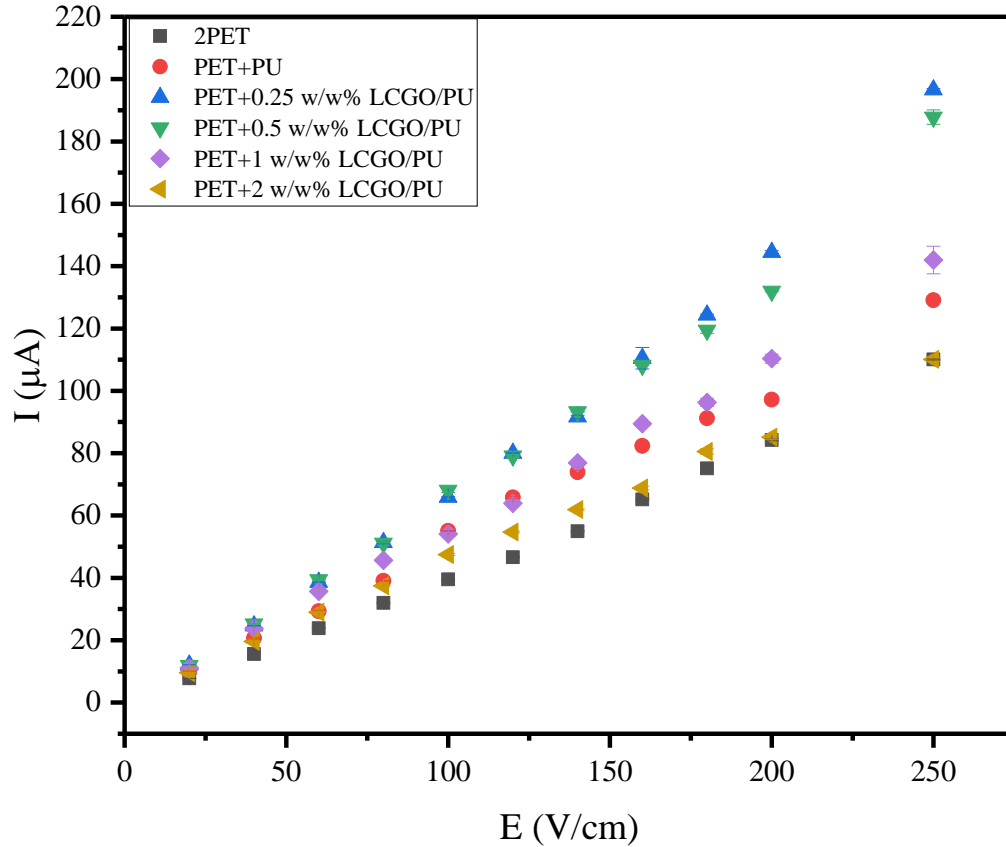
Figure 5.21: current vs. electric field for 3D knitted structures composed of PET and reduced LCGO/PU composite fibres

Higher applied potentials led to larger rise in temperature. This can be explained by the fact that higher potentials (higher power) heated the system faster while heat dissipation rate of the system was much lower than that[54]. Figure 5.22 demonstrated the temperature change with respect to the initial temperature in 3D textile structures composed of PET yarn, PU fibres and/or reduced LCGO/PU composite fibres over 60 seconds when 250 V cm^{-1} was applied.
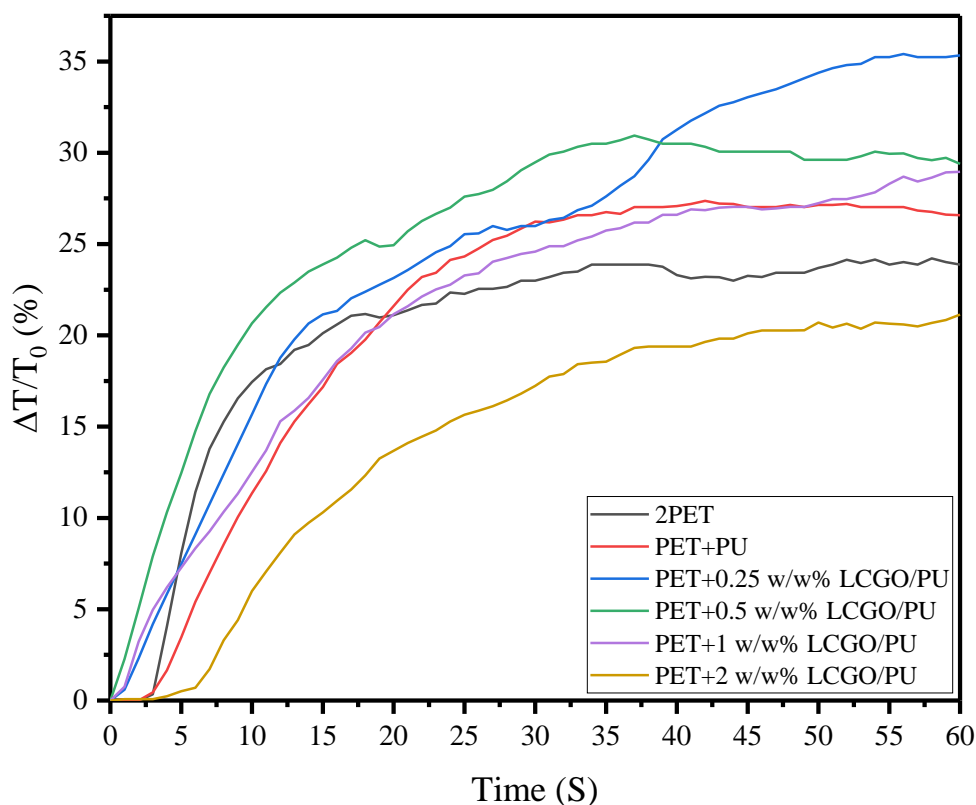
Figure 5.22: Temperature change with respect to the initial temperature as a function of time in 3D textile structures composed of reduced LCGO/PU fibres when 250 V cm^{-1} was applied.

Compared to a similar experiment that has been done on closed capillary tubes[54], shown in Figure 4.7b, in which applying a constant potential causes an immediate rise in temperature followed by a steady state, applying a constant potential to a 3D knitted structures did not cause an immediate temperature change and temperature remained plateau for a while. Then similar to what was reported for capillary tubes, a temperature rise followed by a steady state was observed for textiles as well. This difference in behaviours of 3D knitted textiles and capillary tubes can be attributed to the structural difference between textiles and capillary tubes. Capillary tubes are closed environments where generated heat cannot escape through and air cannot enter while open geometry of the knitted sutures facilitates the occurrence of heat transfer between the fluid inside the knitted structure and its neighbouring air flow which leads to cooling down the fluid and plateau region at the beginning of the graph shown in Figure 5.22.

Changes in temperature due to the Joule-heating effect were observed for 60 seconds while 250 V cm^{-1} was applied to the samples. Final temperature change with respect to the initial temperature was measured for different samples and shown in Figure 5.23.
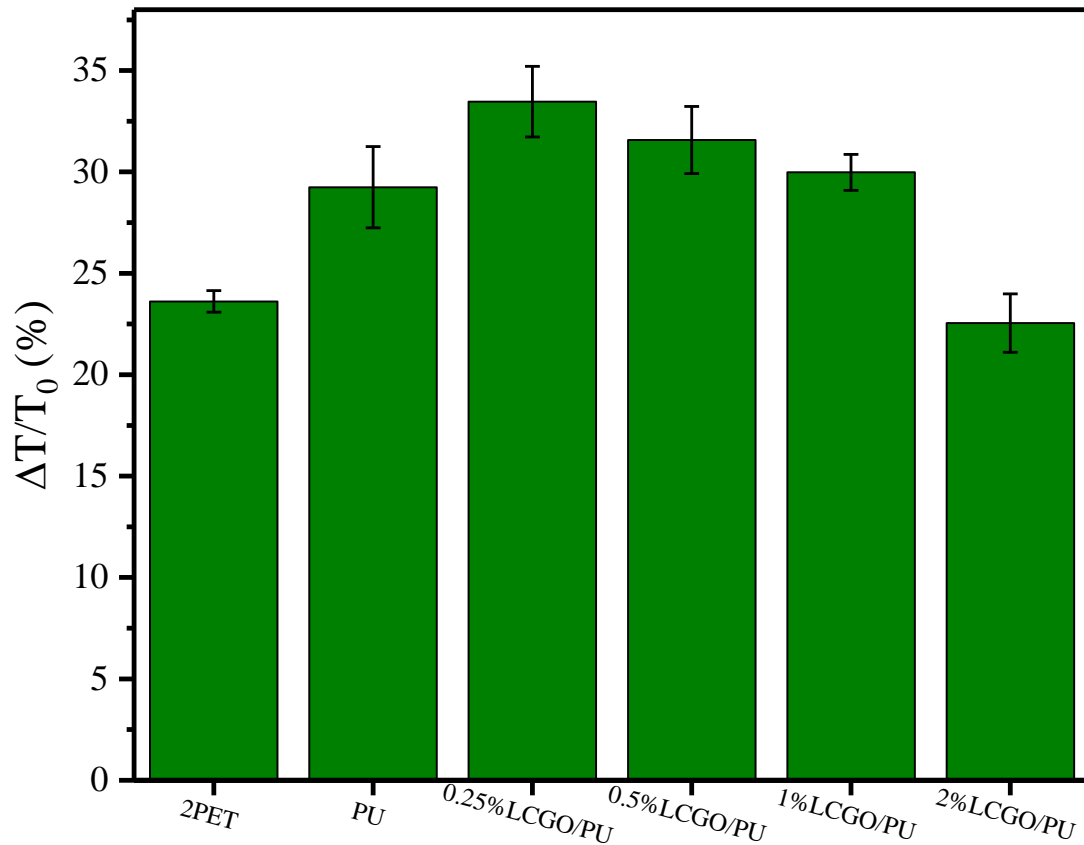
Figure 5.23: Final temperature change with respect to the initial temperature for different samples while 250 V cm^{-1} was applied

As shown in Figure 5.23, replacing one PET thread with PU fibre led to an increase in temperature change with respect to the initial temperature. This could be attributed to differences in crystallinity and therefore thermal conductivity of fully drawn PET thread and undrawn amorphous PU fibre. Thermal conductivity of polymers increased with increase in degree of crystallinity[55–57]. Therefore, it could be assumed that PET threads were more crystalline polymers than PU fibres and have a higher thermal conductivity. Therefore knitted structures with 2PET threads were more capable of dissipating Joule-

heating compare to the one with PET thread and PU fibre.

Despite the increase in thermal conductivity of reduced LCGO/PU composites compare to pure PU as shown in Figure 5.19 and Figure 5.20, no improvement in heat-dissipation ability was observed (Figure 5.23). This can be attributed to the huge difference in in-plane and cross-plane thermal conductivity of graphene. Although in-plane thermal conductivity of graphene is among the highest of known materials 2000-4000 W m^{-1} K^{-1}, its cross-plane direction thermal conductivity is as low as 6 W m^{-1} K^{-1} due to weak interplane van der Waals interactions[58]. Therefore, orientation of LCGO sheets in LCGO/PU composites with respect to the heat flow direction plays a vital role in determining thermal conductivity of composite polymer[59]. It can be assumed that LCGO sheets were randomly oriented in the composite films used to measure thermal conductivity values while most of LCGO sheets in LCGO/PU fibres were parallel to fibre axis because of shear applied to polymer solution in spinning process (schematically shown in Figure 5.24). Since, heat flow in thermal dissipation experiment was in radial direction of fibres, i.e. perpendicular to LCGO sheet plane, enhancement shown in reduced LCGO/PU structures with lower than 2 w/w% loading, were not capable of dissipating heat generated by Joule-heating effect because of polymer layers between LCGO sheets in one hand and low thermal conductivity of LCGO sheets in cross-planar direction in the other hand. Increasing the filler content to 2 w/w% assumed to make fully packed LCGO structures and reduce the thickness of polymeric layer between fillers in both longitudinal and radial fibres' direction[49,50] and resulted in an enhancement in Joule-heating dissipation, shown in Figure 5.23. Although reduced LCGO concentrations more than 1 w/w% in PU matrix started to improve matrix's thermal conductivity and make it capable of dissipating Joule-heating effect, reduced LCGO/PU composite with 2 w/w% LCGO became electrically conductive. These samples showed an electrical resistivity of

44.9 ± 1.2 MΩ/cm which is a draw back for electrophoresis tests as the electrical conductivity makes short circuits. As a result of the electrical conductivity issues, LCGO filler was replaced by thermally conductive and electrically insulating filler, i.e. BNNPs.

Figure 5.25 shows current values for 3D knitted structures comprising of PET threads or PET threads parallel with PU and BNNP/PU composite fibres when different potentials were applied, i.e. 20, 40, 60, 80, 100, 120, 140, 160, 180, 200 and 250 V cm^{-1}. Current vs. electric field in these structures show similar trend to what was achieved by reduced LCGO/PU composite fibres because of similarity in diameters which led to almost similar Joule-heating effects.
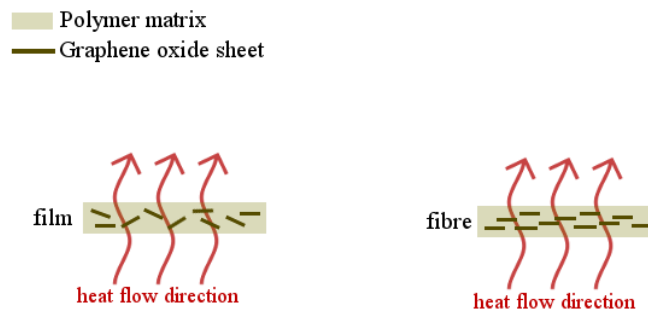
Figure 5.24: Direction of LCGO sheets in PU films and fibres
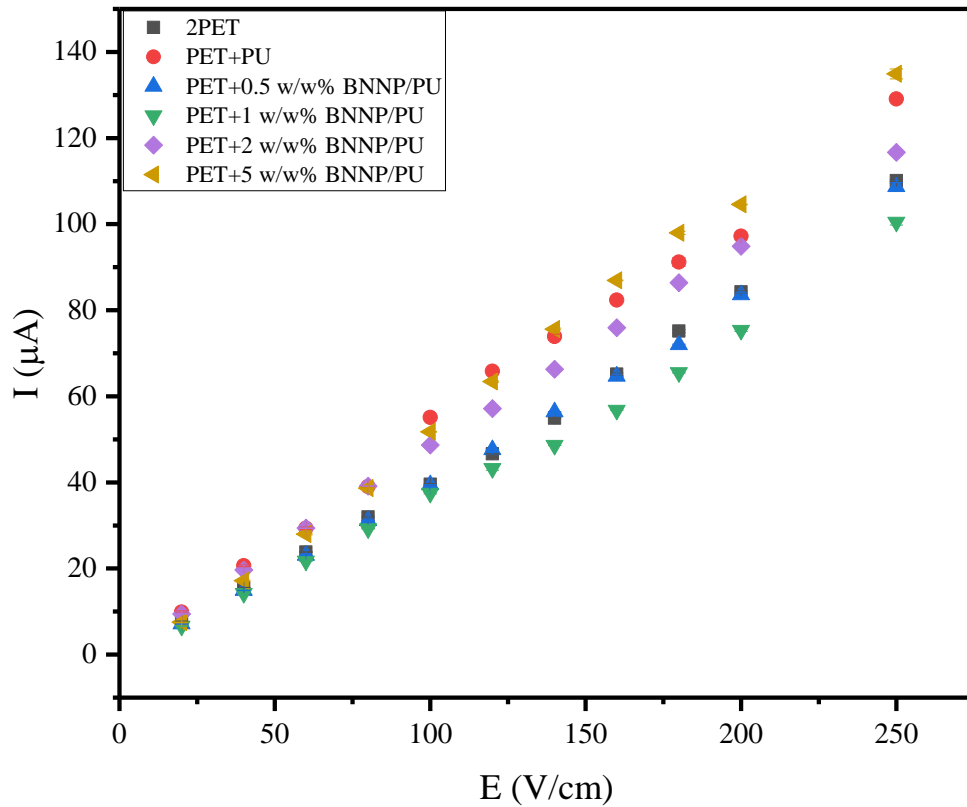
Figure 5.25: current vs. electric field for 3D knitted structures composed of PET and BNNP/PU composite fibres

The temperature changes with respect to the initial temperature in 3D textile structures composed of PET yarn, PU fibres and/or BNNP/PU composite fibres over 60 seconds when 250 V cm^{-1} was applied were monitored and shown in Figure 5.26.
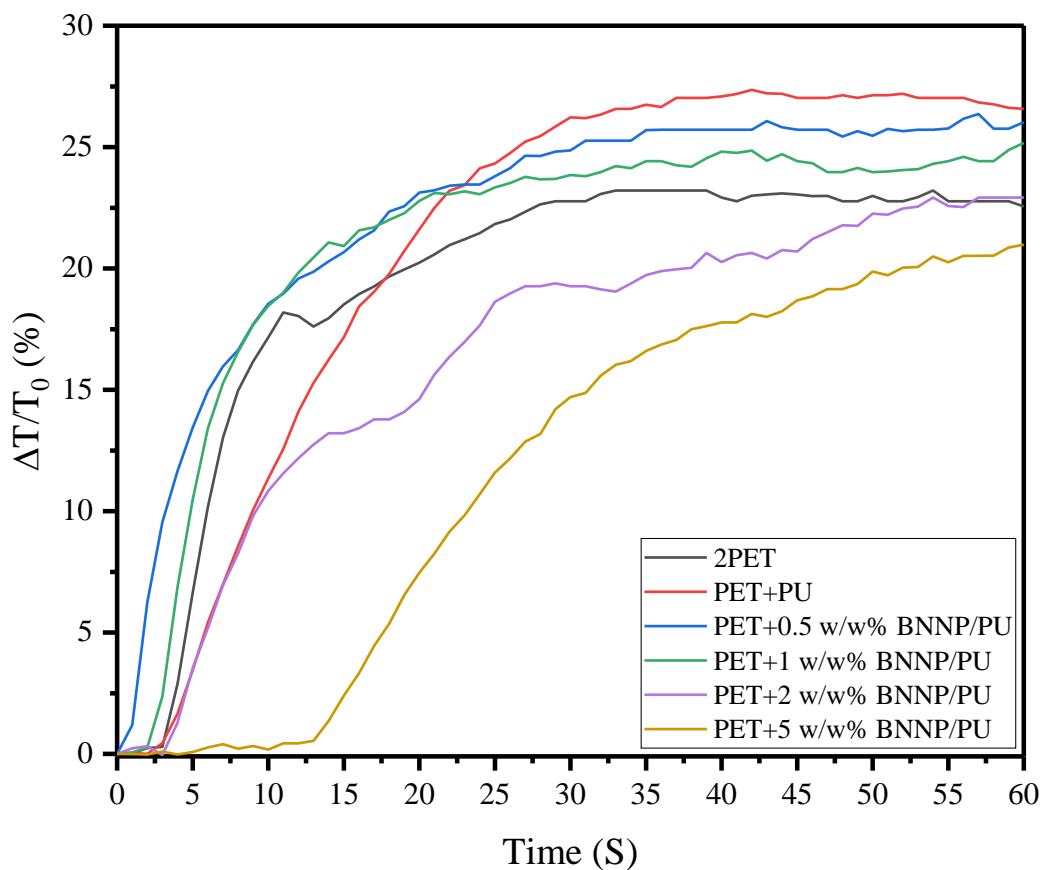
Figure 5.26: temperature change with respect to the initial temperature as a function of time in 3D textile structures composed of BNNP/PU fibres when 250 V cm^{-1} was applied

Temperature rose with a similar pattern to that of obtained by 3D knitted structures with reduced LCGO/PU and LCGO/LDPE fibres, i.e. a plateau region followed by increase and a steady state at the end. Final temperature change with respect to the initial temperature for knitted structures containing BNNP/PU fibres were measured and summarized in Figure 5.27.
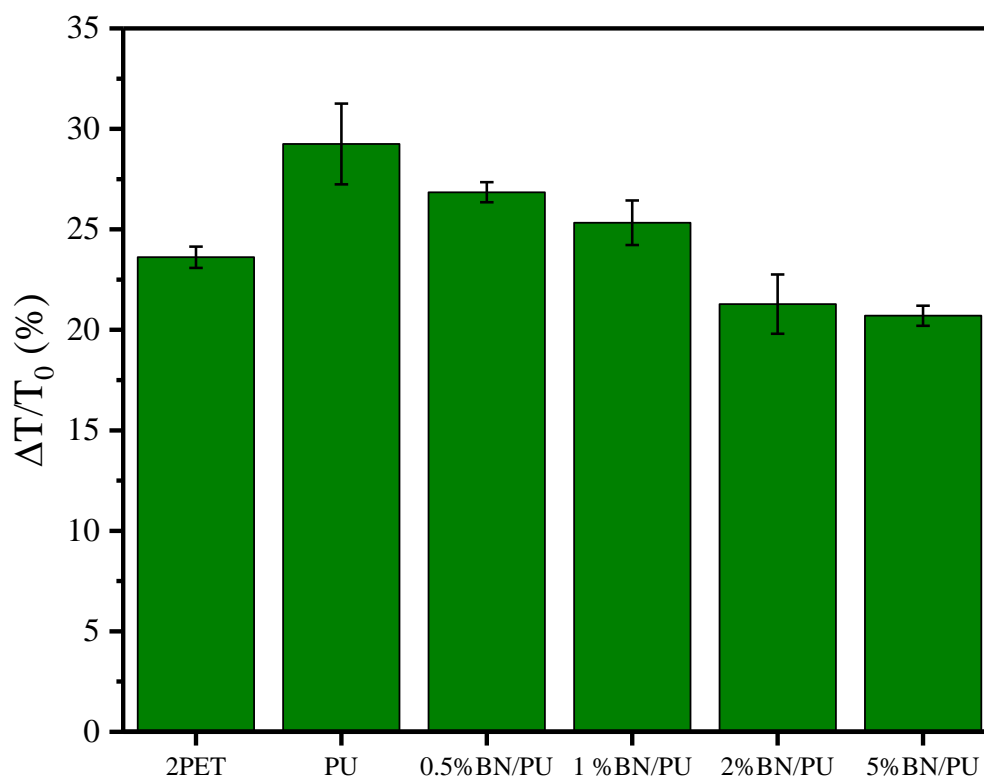
Figure 5.27: Final temperature change with respect to the initial temperature for different samples while 250 V cm^{-1} was applied

As shown in Figure 5.27, replacing one PET thread with PU fibre led to an increase in temperature change with respect to the initial temperature as described earlier in this Chapter. A temperature decreased was noted by replacing the PU fibre with 0.5 w/w% BNNP/PU composite fibres. The observed temperature decrease continued with the increase in the BNNP filler concentration. Considering BNNP's spherical morphology with very low aspect ratio (~1), Figure 5.15, an isotropic thermal conductivity in either flow induced oriented BNNP fillers in BNNP/PU spun fibres or randomly oriented BNNP/PU films[24] could be expected. Decreasing trend in final temperature change in knitted structure by increase in filler concentration, Figure 5.27, is in agreement with increase of thermal conductivity of PU by increase in BNNP filler concentration, Figure 5.19, and confirms that orientation of BNNP did not have a significant effect on heat dissipation ability of BNNP-filled composite fibres. Figure 5.26 shows that addition of

BNNP into PU by more than 2 w/w% led to effective heat dissipation and consequently kept the structure at lower working temperatures for longer times, i.e. longer plateau region at the beginning. This could be an advantage for electrophoresis studies that involves living cells or temperature sensitive analytes.

5.4. Conclusion

The novel idea of incorporating thermally conductive fibres into 3D textile microfluidic devices to minimize the effects of Joule-heating which is the most important side effect of electrophoresis technique was investigated. As discussed in Chapter 4, LCGO/LDPE fibres prepared by pre-mixing and subsequent melt spinning that had limitations in the amount of filler loadings that were achievable through this approach. In this chapter, solution mixing and wet-spinning methods were used to produce polymeric thermally conducting fibres using PU polymeric matrix and two different filler materials, i.e. LCGO and BNNP. Thermally conducting fibres with different filler loadings were successfully made and incorporated into 3D knitted structures in combination with PET threads to make novel textile-based microfluidics. Different electric fields were applied to 3D knitted structures and resultant current and temperature change were monitored. It was found that thermally conducting reduced LCGO-filled fibres became effective in Joule-heating dissipation at the point that they became electrically conductive. Therefore, LCGO was replaced by thermally conducting and electrically insulating BNNP filler. It was shown that incorporating thermally conductive fibres into 3D textile structures as heat dissipater potentially can be used as an effective method to dissipate the heat generated by Joule-heating and keep the system as cool as possible for the longer time during electrophoresis experiment. This could be an advantageous and opens up new opportunities for fibre based capillary electrophoresis studies specifically when proteins, living cells and temperature sensitive analytes are being used.

5.5. References

(1)   Zeng, W.; Shu, L.; Li, Q.; Chen, S.; Wang, F.; Tao, X. M. Fiber-Based Wearable Electronics: A Review of Materials, Fabrication, Devices, and Applications. *Adv. Mater.* **2014**, *26* (31), 5310–5336.

(2)   Service, R. F. Electronic Textiles Charge Ahead. *Science (80-.).* **2003**, *301*, 909–911.

(3)   Textiles, E. A Logical Step. *Nat. Mater.* **2007**, *6* (May), 328–329.

(4)   Coyle, S.; Curto, V. F.; Benito-lopez, F.; Florea, L.; Diamond, D. Wearable Bio and Chemical Sensors. In *Wearable sensors: Fundamentals, Implementation and Applications*; Academic Press (via Elsevier), 2014; pp 65–83.

(5)   Seyedin, S.; Razal, J. M.; Innis, P. C.; Jeiranikhameneh, A.; Beirne, S.; Wallace, G. G. Knitted Strain Sensor Textiles of Highly Conductive All-Polymeric Fibers. *ACS Appl. Mater. Interfaces* **2015**, *7* (38), 21150–21158.

(6)   Zhao, C.; Farajikhah, S.; Wang, C.; Foroughi, J.; Jia, X.; Wallace, G. G. 3D Braided Yarns to Create Electrochemical Cells. *Electrochem. commun.* **2015**, *61*, 27–31.

(7)   Stoppa, M.; Chiolerio, A. Wearable Electronics and Smart Textiles: A Critical Review. *Sensors (Switzerland)* **2014**, *14* (7), 11957–11992.

(8)   Seyedin, M. Z.; Razal, J. M.; Innis, P. C.; Wallace, G. G. Strain-Responsive polyurethane/PEDOT:PSS Elastomeric Composite Fibers with High Electrical Conductivity. *Adv. Funct. Mater.* **2014**, *24* (20), 2957–2966.

(9)   Seyedin, S.; Razal, J. M.; Innis, P. C.; Wallace, G. G. A Facile Approach to Spinning Multifunctional Conductive Elastomer Fibres with Nanocarbon Fillers. *Smart Mater. Struct.* **2016**, *25* (3), 35015.

(10)   Aboutalebi, S. H.; Jalili, R.; Esrafilzadeh, D.; Salari, M.; Gholamvand, Z.; Yamini, S. A.; Konstantinov, K.; Shepherd, R. L.; Chen, J.; Moulton, S. E.; et al. High-Performance Multifunctional Graphene Yarns: Toward Wearable All-Carbon Energy Storage Textiles. *ACS Nano* **2014**, *8* (3), 2456–2466.

(11)   Jalili, R.; Razal, J. M.; Innis, P. C.; Wallace, G. G. One-Step Wet-Spinning Process of poly(3,4-Ethylenedioxythiophene): Poly(styrenesulfonate) Fibers and the Origin of Higher Electrical Conductivity. *Adv. Funct. Mater.* **2011**, *21* (17), 3363–3370.

(12)   Wei, X.; Joshi, Y. Stacked Microchannel Heat Sinks for Liquid Cooling of Microelectronic Components. *J. Electron. Packag.* **2004**, *126* (1), 60.

(13)   Sim, L. C.; Ramanan, S. R.; Ismail, H.; Seetharamu, K. N.; Goh, T. J. Thermal Characterization of Al2O3 and ZnO Reinforced Silicone Rubber as Thermal Pads for Heat Dissipation Purposes. *Thermochim. Acta* **2005**, *430* (1–2), 155–165.

(14)   Xu, Y.; Luo, X.; Chung, D. D. L. Sodium Silicate Based Thermal Interface Material for High Thermal Contact Conductance. *J. Electron. Packag.* **2000**, *122* (June), 128–131.

(15)   Lee, G. W.; Park, M.; Kim, J.; Lee, J. I.; Yoon, H. G. Enhanced Thermal Conductivity of Polymer Composites Filled with Hybrid Filler. *Compos. Part A Appl. Sci. Manuf.* **2006**, *37* (5), 727–734.

(16)   Xu, Y.; Chung, D.D.L.; Mroz, C. Thermally Conducting Aluminum Nitride Polymer Matrix Composites. *Compos. Pt. A-Appl. S* **2001**, *32*, 1749–1757.

(17)   Balandin, A. A. Thermal Properties of Graphene and Nanostructured Carbon Materials. *Nat. Mater.* **2011**, *10* (8), 569–581.

(18)   Aboutalebi, S. H.; Gudarzi, M. M.; Zheng, Q. Bin; Kim, J. K. Spontaneous Formation of Liquid Crystals in Ultralarge Graphene Oxide Dispersions. *Adv. Funct. Mater.* **2011**, *21* (15), 2978–2988.

(19)   Jalili, R.; Aboutalebi, S. H.; Esrafilzadeh, D.; Shepherd, R. L.; Chen, J.; Aminorroaya-Yamini, S.; Konstantinov, K.; Minett, A. I.; Razal, J. M.; Wallace, G. G. Scalable One-Step Wet-Spinning of Graphene Fibers and Yarns from Liquid Crystalline Dispersions of Graphene Oxide: Towards Multifunctional Textiles. *Adv. Funct. Mater.* **2013**, *23* (43), 5345–5354.

(20)   Eichler, J.; Lesniak, C. Boron Nitride (BN) and BN Composites for High-Temperature Applications. *J. Eur. Ceram. Soc.* **2008**, *28* (5), 1105–1109.

(21)   Li, T.; Hsu, S. L. Enhanced Thermal Conductivity of Polyimide Films via a Hybrid of Micro- and Nano-Sized Boron Nitride. *J. Phys. Chem. B* **2010**, *114*, 6825–6829.

(22)   Tang, C.; Bando, Y.; Liu, C.; Fan, S.; Zhang, J.; Ding, X.; Golberg, D. Thermal Conductivity of Nanostructured Boron Nitride Materials. *J. Phys. Chem. B* **2006**, *110* (21), 10354–10357.

(23)   Shi, Y.; Hamsen, C.; Jia, X.; Kim, K. K.; Reina, A.; Hofmann, M.; Hsu, A. L.; Zhang, K.; Li, H.; Juang, Z. Y.; et al. Synthesis of Few-Layer Hexagonal Boron Nitride Thin Film by Chemical Vapor Deposition. *Nano Lett.* **2010**, *10* (10), 4134–4139.

(24)   Ng, H. Y.; Lu, X.; Lau, S. K. Thermal Conductivity of Boron Nitride-Filled Thermoplastics: Effect of Filler Characteristics and Composite Processing Conditions. *Polym. Compos.* **2005**, *26* (6), 778–790.

(25)   Qi, H. J.; Boyce, M. C. Stress–strain Behavior of Thermoplastic Polyurethanes. *Mech. Mater.* **2005**, *37* (8), 817–839.

(26)   Seyedin, M. Z.; Razal, J. M.; Innis, P. C.; Jalili, R.; Wallace, G. G. Achieving Outstanding Mechanical Performance in Reinforced Elastomeric Composite Fibers Using Large Sheets of Graphene Oxide. *Adv. Funct. Mater.* **2015**, *25* (1), 94–104.

(27)   Javadi, M.; Gu, Q.; Naficy, S.; Farajikhah, S.; Crook, J. M.; Wallace, G. G.; Beirne, S.; Moulton, S. E. Conductive Tough Hydrogel for Bioapplications. *Macromol. Biosci.* **2017**.

(28)   Liu, Y.; Weng, B.; Razal, J. M.; Xu, Q.; Zhao, C.; Hou, Y.; Seyedin, S.; Jalili, R.; Wallace, G. G.; Chen, J. High-Performance Flexible All-Solid-State Supercapacitor from Large Free-Standing Graphene-PEDOT/PSS Films. *Sci. Rep.* **2015**, *5* (October), 1–11.

(29)   Um, I. C.; Ki, C. S.; Kweon, H.; Lee, K. G.; Ihm, D. W.; Park, Y. H. Wet Spinning of Silk Polymer: II. Effect of Drawing on the Structural Characteristics and Properties of Filament. *Int. J. Biol. Macromol.* **2004**, *34* (1–2), 107–119.

(30)   Kopperud, H. M.; Hansen, F. K.; Nystrom, B. Effect of Surfactant and Temperature on the Rheological Properties of Aqueous Solutions of Unmodified and Hydrophobically Modified Pol Yacrylamide. *Macromol Chem. Phys.* **1998**, *2394* (11), 2385–2394.

(31)   Cai, D.; Jin, J.; Yusoh, K.; Rafiq, R.; Song, M. High Performance Polyurethane/functionalized Graphene Nanocomposites with Improved Mechanical and Thermal Properties. *Compos. Sci. Technol.* **2012**, *72*, 702–707.

(32)   Gambhir, S.; Murray, E.; Sayyar, S.; Wallace, G. G.; Officer, D. L. Anhydrous Organic Dispersions of Highly Reduced Chemically Converted Graphene. *Carbon N. Y.* **2014**, *76*,

368–377.

(33)   Wu, C.; Huang, X.; Wang, G.; Wu, X.; Yang, K.; Li, S.; Jiang, P. Hyperbranched-Polymer Functionalization of Graphene Sheets for Enhanced Mechanical and Dielectric Properties of Polyurethane Composites. *J. Mater. Chem.* **2012**, *2*, 7010–7019.

(34)   Xia, H.; Song, M. Preparation and Characterization of Polyurethane–carbon Nanotube Composites. *Soft Matter* **2005**, *1* (5), 386.

(35)   Tegou, E.; Pseiropoulos, G.; Filippidou, M. K.; Chatzandroulis, S. Low-Temperature Thermal Reduction of Graphene Oxide Films in Ambient Atmosphere: Infra-Red Spectroscopic Studies and Gas Sensing Applications. *Microelectron. Eng.* **2016**, *159*, 146–150.

(36)   Stankovich, S.; Dikin, D. A.; Piner, R. D.; Kohlhaas, K. A.; Kleinhammes, A.; Jia, Y.; Wu, Y.; Nguyen, S. T.; Ruoff, R. S. Synthesis of Graphene-Based Nanosheets via Chemical Reduction of Exfoliated Graphite Oxide. *Carbon N. Y.* **2007**, *45* (7), 1558–1565.

(37)   Tuinstra, F.; Koenig, J. L. Raman Spectrum of Graphite. *J. Chem. Phys.* **1970**, *53* (3), 1126.

(38)   Mehrali, M.; Sadeghinezhad, E.; Akhiani, A. R.; Tahan Latibari, S.; Talebian, S.; Dolatshahi-Pirouz, A.; Metselaar, H. S. C.; Mehrali, M. An Ecofriendly Graphene-Based Nanofluid for Heat Transfer Applications. *J. Clean. Prod.* **2016**, *137*, 555–566.

(39)   Pei, S.; Cheng, H. M. The Reduction of Graphene Oxide. *Carbon N. Y.* **2012**, *50* (9), 3210–3228.

(40)   Arenal, R.; Ferrari, A. C.; Reich, S.; Wirtz, L.; Mevellec, J. Y.; Lefrant, S.; Rubio, A.; Loiseau, A. Raman Spectroscopy of Single-Wall Boron Nitride Nanotubes. *Nano Lett.* **2006**, *6* (8), 1812–1816.

(41)   Gorbachev, R. V.; Riaz, I.; Nair, R. R.; Jalil, R.; Britnell, L.; Belle, B. D.; Hill, E. W.; Novoselov, K. S.; Watanabe, K.; Taniguchi, T.; et al. Hunting for Monolayer Boron Nitride: Optical and Raman Signatures. *Small* **2011**, *7* (4), 465–468.

(42)   Christenson, E. M.; Anderson, J. M.; Hiltner, A.; Baer, E. Relationship between Nanoscale Deformation Processes and Elastic Behavior of Polyurethane Elastomers. *Polymer (Guildf).* **2005**, *46* (25), 11744–11754.

(43)   Petrović, Z. S.; Ferguson, J. Polyurethane Elastomers. *Prog. Polym. Sci.* **1991**, *16* (5), 695–836.

(44)   Chen, Q.; Mangadlao, J. D.; Wallat, J.; De Leon, A.; Pokorski, J. K.; Advincula, R. C. 3D Printing Biocompatible Polyurethane/Poly(lactic acid)/Graphene Oxide Nanocomposites: Anisotropic Properties. *ACS Appl. Mater. Interfaces* **2017**, *9* (4), 4015–4023.

(45)   Petrovic, Z. S.; Javni, I.; Waddon, A.; Banhegyi, G. Structure and Properties of Polyurethane-Silica Nanocomposites. *J. Appl. Polym. Sci.* **2000**, *76* (2), 133–151.

(46)   Razzaq, M. Y.; Anhalt, M.; Frormann, L.; Weidenfeller, B. Thermal, Electrical and Magnetic Studies of Magnetite Filled Polyurethane Shape Memory Polymers. *Materials science and Engineering A*. 2007, pp 227–235.

(47)   Corcione, C. E.; Maffezzoli, A. Glass Transition in Thermosetting Clay-Nanocomposite Polyurethanes. *Thermochimica Acta*. 2009, pp 43–48.

(48)   Ganguli, S.; Roy, A. K.; Anderson, D. P. Improved Thermal Conductivity for Chemically Functionalized Exfoliated Graphite/epoxy Composites. *Carbon N. Y.* **2008**, *46* (5), 806–817.

(49) Mu, Q.; Feng, S. Thermal Conductivity of Graphite/silicone Rubber Prepared by Solution Intercalation. *Thermochim. Acta* **2007**, *462* (1–2), 70–75.

(50) Zhou, W.; Qi, S.; Tu, C.; Zhao, H.; Wang, C.; Kou, J. Effect of the Particle Size of Al2O3 on the Properties of Filled Heat-Conductive Silicone Rubber. *J. Appl. Polym. Sci.* **2007**, *104*, 1312–1318.

(51) Xuan, X.; Li, D. Analytical Study of Joule Heating Effects on Electrokinetic Transportation in Capillary Electrophoresis. *J. Chromatogr. A* **2005**, *1064* (2), 227–237.

(52) Horiuchi, K.; Dutta, P. Joule Heating Effects in Electroosmotically Driven Microchannel Flows. *Int. J. Heat Mass Transf.* **2004**, *47* (14–16), 3085–3095.

(53) Sasagawa, K.; Saka, M.; Abé, H. Current Density and Temperature Distributions near the Corner of Angled Metal Line. *Mech. Res. Commun.* **1995**, *22* (5), 473–483.

(54) Rathore, A. S. Joule Heating and Determination of Temperature in Capillary Electrophoresis and Capillary Electrochromatography Columns. *J. Chromatogr. A* **2004**, *1037* (1–2), 431–443.

(55) Anderson, D. R. Thermal Conductivity of Polymers. *Chem. Rev.* **1966**, *66* (6), 677–690.

(56) Liu, J.; Yang, R. Tuning the Thermal Conductivity of Polymers with Mechanical Strains. *Phys. Rev. B - Condens. Matter Mater. Phys.* **2010**, *81* (17), 1–9.

(57) Choy, C. L. Thermal Conductivity of Polymers. *Polymer (Guildf).* **1977**, *18* (April 1976), 984–1004.

(58) Pop, E.; Varshney, V.; Roy, A. Thermal Properties of Graphene: Fundamentals and Applications. *Mrs Bull.* **2012**, *1273* (December), 1–28.

(59) Shahil, K. M. F.; Balandin, A. A. Graphene-Multilayer Graphene Nanocomposites as Highly Efficient Thermal Interface Materials. *Nano Lett.* **2012**, *12* (2), 861–867.

Chapter 6:

Textile designs for wearable electrochemical (E-Chem) sensors – proof-of-concept studies.

6.1. Introduction

In recent decades, tremendous effort has been made in field of chemical and bio-sensors to replace bulky, expensive and complex analytical instrumental systems used in the health-care sector[1,2]. Different analytical approaches include optical, piezoelectric and electrochemical detection methods have been used to make devices capable of detecting analytes of interest. Among these, electrochemical detection has been the more common techniques use in diagnostics and environmental monitoring devices due to its cost-effectiveness, simplicity and accuracy[1,3]. Increasing demand for heart rate monitors, pedometers and portable real-time monitoring devices for use in sports, soldier performance, aging-associated diseases, and remote patient monitoring has focused attention towards development of the new class of personalized point-of-care systems to provide a real-time feedback of an individual's physiological biomarkers[4–7]. Most of these devices rely on blood samples with the associated need for undesirable invasive sampling. Therefore, in recent years, significant research investigate alternate body fluids other than blood[1,5,8]. Non-invasive wearable biosensor approaches include saliva[9], tear[10] and sweat [11] sensors in addition to breath sensors[1,8,12]. After the first introduction of thread-based microfluidic devices in 2010[13,14], textile substrates owing to their unique characteristics such as cost-effectiveness, wicking properties, flexibility and robustness in wet state, have been considered as a significant platform for the development of wearable sensors[1,4–6,8,11,15,16].

Owing to the variable methods of sample collection and handling required for body fluid, different sensor designs are required in each category. Although there have been some publications using textile substrates to perform electrochemical or electrochemiluminescence detections using pins an threads[17], screen printed electrodes[9,18],

coating threads with conductive inks such as carbon inks[19,20], or separate solid electrodes in contact with textile substrates[10], to our knowledge there have been no publication in creating 3D textile electrochemical cells reported in this chapter. Therefore, in this chapter, two different textile designs using two different methods of fabrication, i.e. knitting and braiding techniques, were proposed as platforms for development of wearable electrochemical sensors utilizing various electrochemical detection techniques, i.e. cyclic voltammetry and amperometry. Moreover, electrochemical reversibility of the system was shown to be improved by surface electrodeposition of polypyrrole (PPy) and gold nanoparticle (AuNp).

6.2. Experiments
6.2.1. Cyclic voltammetry test

All electrochemical measurements were carried out in a beaker-type electrochemical cell with three-electrode system including surface of stainless steel (SS) filament derived electrodes (SS, gold nanoparticle electrodeposited SS or polypyrrole-gold nanoparticle electrodeposited SS) as working electrode, Pt mesh counter electrode and Ag/AgCl reference electrodes (3.5 M KCl) using a potentiostat (CH Instruments, 650D, USA).

6.2.2. Stainless steel surface modification

The surfaces of stainless steel (SS) filament working electrodes were modified by either electrodeposition of gold nanoparticle (AuNp) or polypyrrole (PPy) and AuNps. SS filaments were sonicated in EtOH for 30 minutes to clean surface impurities followed by washing with DI water prior to electrodepositions.

6.2.2.1. Polypyrrole (PPy) electrodeposition

PPy was electrodeposited on SS filament using a CH potentiostat and a standard three-electrode system using a clean SS filament as the working electrode, a platinum mesh as the counter electrode and Ag/AgCl as the reference electrode (3.5 M KCl). PPy was

electrodeposited using a constant potential of + 0.8 V for 60 seconds in an aqueous solution of 0.1 M pyrrole and 0.1 M sodium p-toluenesulfonate. During the deposition process, the colour of SS filament changed to black due to the electro-deposition of pyrrole on SS filament.

6.2.2.2. AuNP electro deposition

AuNP electrodeposition on SS filament was performed using a CH potentiostat instrument using a standard three-electrode system with a clean SS filament as the working electrode, a platinum mesh as the counter electrode and saturated Ag/AgCl as the reference electrode, using an aqueous electrolyte solution of 3.4 mM $HAuCl_4$ and 0.1 M $HClO_4$. Electrodeposition was achieved by applying constant potential of -0.25 V for different times, i.e. 120, 300 and 600 seconds[21]. After electro-deposition the SS filament electrode turned to shiny yellow upon electrodeposition of gold.

6.2.3. Fabrication of 3D textile structures

Two different well-established textile fabrication techniques of knitting and braiding were utilised to assemble 3D textile structures with segmented conductive and non-conductive sections for used as a platform for performing electrochemical tests.

6.2.3.1. 3D knitted structures

3D segmented knitted structures were developed using Brothers double bed knitting machine with 7 gauge needle. A cotton/polyester thread was used as the insulating component, a SS yarn and two parallel 70 denier silver-plated nylon were also used to make electrically conductive structures within the knitted device. Figure 6.1 shows the schematic design for segmented knitted structures.
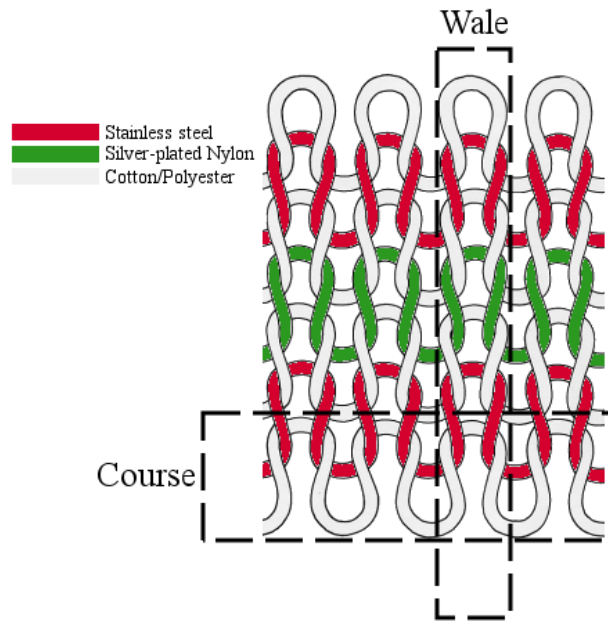
Figure 6.1: Schematic design for segmented knitted structures comprised of cotton/polyester insulating part as SS and silver-plated nylon conductive parts.

Initially the number of machine knitting needles was optimised to establish the optimal diameter of the final tubular knitted structure. It was determined that when 3 needles were used in each side, a knitted structure with the diameter of approximately 4 mm was achieved. 4 courses of conductive yarn followed by 8 courses of insulating yarns were knitted to obtain 4 mm long conductive segments separated with an 8 mm insulating cotton/polyester segment. In total, 50 courses (~ 40 mm) of insulating thread were knitted at each end of structure. Figure 6.2 shows the final segmented 3D knitted structure.
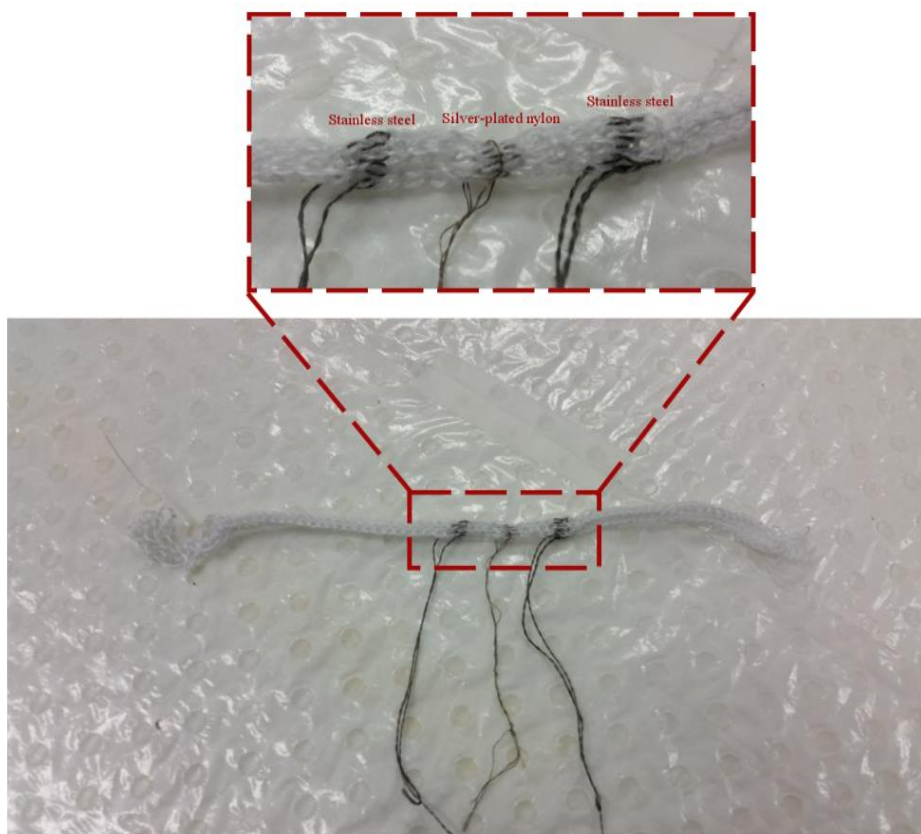
Figure 6.2: Segmented 3D knitted structure platform for electrochemical detection.

6.2.3.2. 3D braided structures

It in collaborative work involving myself and others from our group that 3D braid structures with different number of parallel fibre electrodes can be assembled into a textile based super-capacitor[22]. Using a similar approach in this study, 3D braided structures with parallel conductive and non-conducive yarns as were assembled into a classical 3-electrode structure using the Trenz-Export braiding machine with the resultant utilised in a gravity assisted self-wicking textile electrochemical detection system. 100/36 denier polyester threads were used as insulating components separating both SS filament working and counter electrodes and a 70 denier silver-plated nylon pseudo-reference electrode. 9 spools of polyester threads (as separators and wicking elements), 2 parallel SS filament and one silver-plated nylon in the middle of two SSs with a Ø 700 μm nylon monofilament (fishing line) as a core to was used to assemble a 3D tubular structure with

154

electrically separated electrodes as shown in Figure 6.3.
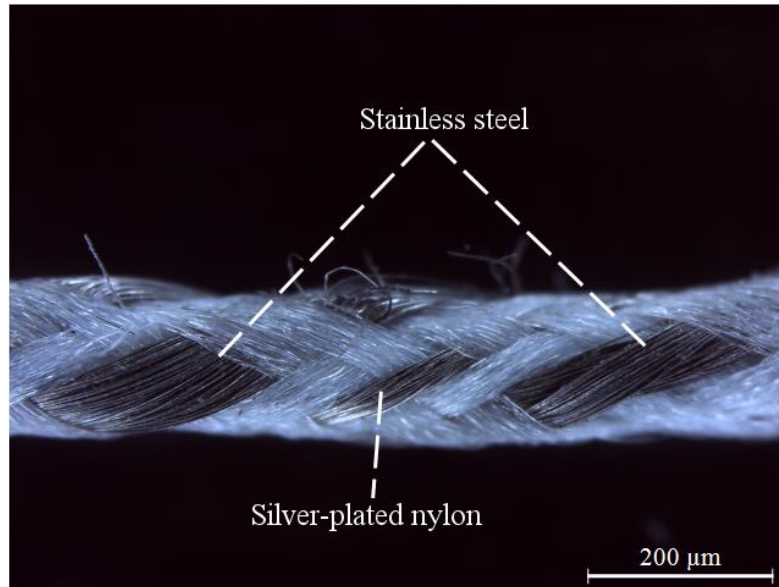
Figure 6.3: 3D tubular braid template for E-chem detections comprised of PET insulating yarns, 2 SS filaments and a silver-plate nylon between 2 SS filaments.

To prove that electrodes in the 3D braided structure were parallel and did not short-circuit with each other, electrodes were separated at both end of the structure and a piece of copper tape was attached to each electrode, Figure 6.4. Then connectivity of each two was tested by a measuring electrical resistivity as shown in Figure 6.5.
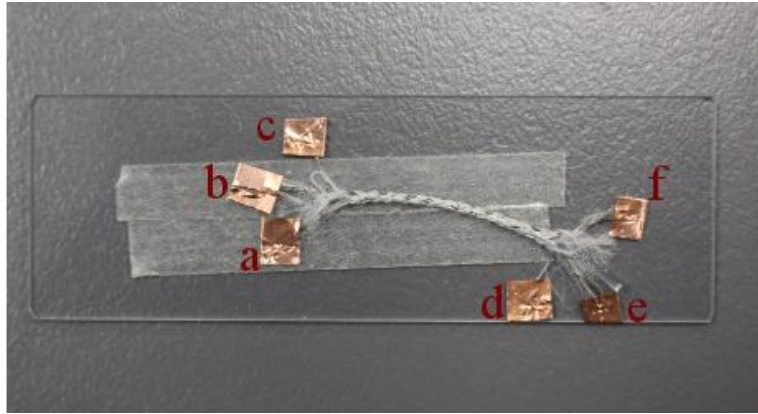
Figure 6.4: braid structure with separated electrodes for connectivity test (a-f show ends of conductive yarns)

Figure 6.5: connectivity test for braid structure showing that each end of an electrode in one side (a-c in **Figure 6.4**) is connected to only one end to the other side (d-f in **Figure 6.4**)

6.3. Results and discussion
6.3.1. Stainless steel surface modification

Since $Fe^{III}(CN)_6^{3-}$/ $Fe^{II}(CN)_6^{4-}$ is a known and well-behaved couple, electrochemically[23,24], potassium ferricyanide was used as the electroactive material along with an NaCl aqueous electrolyte in this study. The redox reactions of $Fe^{III}(CN)_6^{3-}$/ $Fe^{II}(CN)_6^{4-}$ were observed by Cyclic voltammetry (CV) tests over a potential range between 0 mV and 500 mV (CV's with SS electrodes were cycled between -600 mV and 600 mV) in 1 M NaCl aqueous electrolyte. Different concentrations of potassium ferricyanide of 0, 0.2, 0.5, 1, 2, 5, and 10 mM at scan rates of 20, 50, and 100 mV s^{-1} were employed. All electrolyte solutions were deoxygenated by Argon purging for 60 minutes prior CV tests. CVs of a range concentrations of potassium ferricyanide in 1 M NaCl electrolyte were obtained as a function of the scan rate as shown in Figure 6.6. SS filament was used as working electrode while Pt mesh and Ag/AgCl counter and reference electrodes were used, respectively.
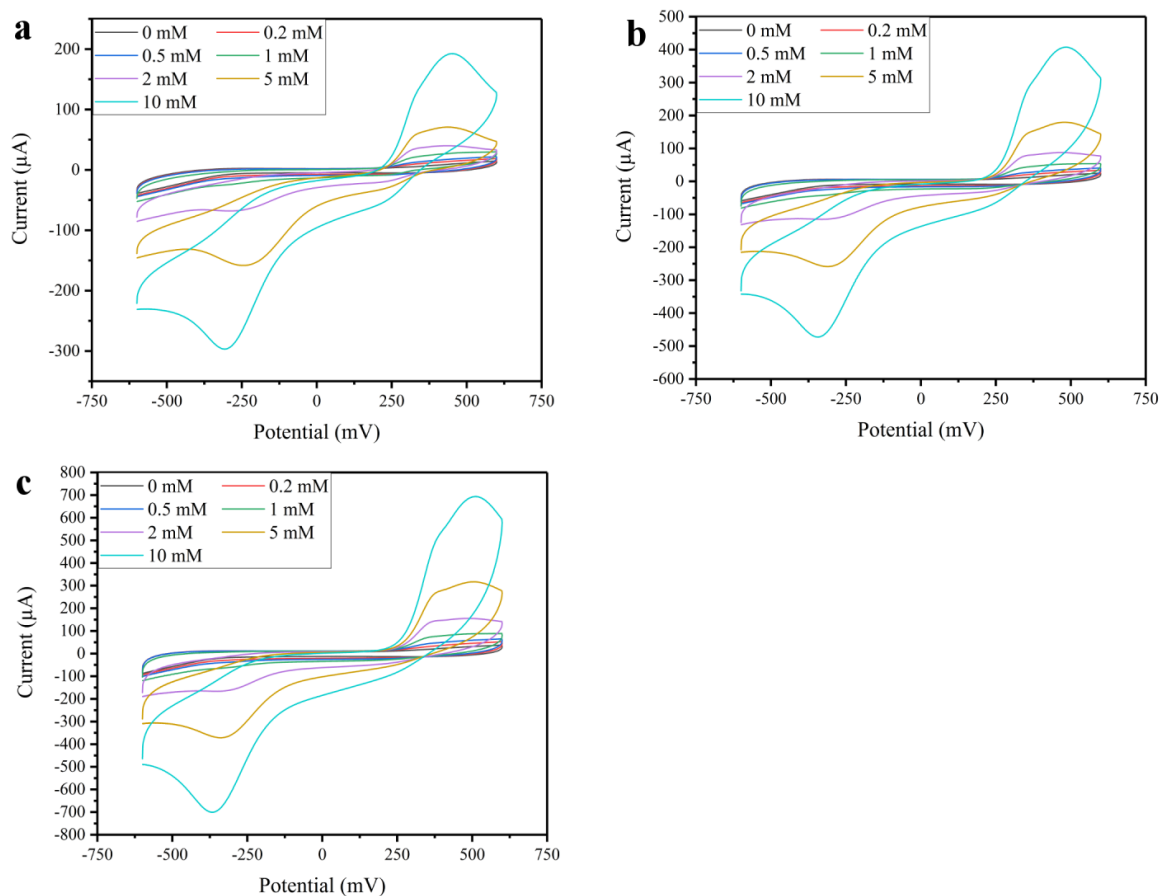
Figure 6.6: Cyclic voltammetry potassium ferricyanide detection on SS filament at scan rates of (a) 20, (b) 50 and (c) 100 mV s^{-1}

Using differential pulse voltammetry at the different concentrations investigated a linear correlation between potassium ferricyanide vs. maximum peak current was observed, Figure 6.7.
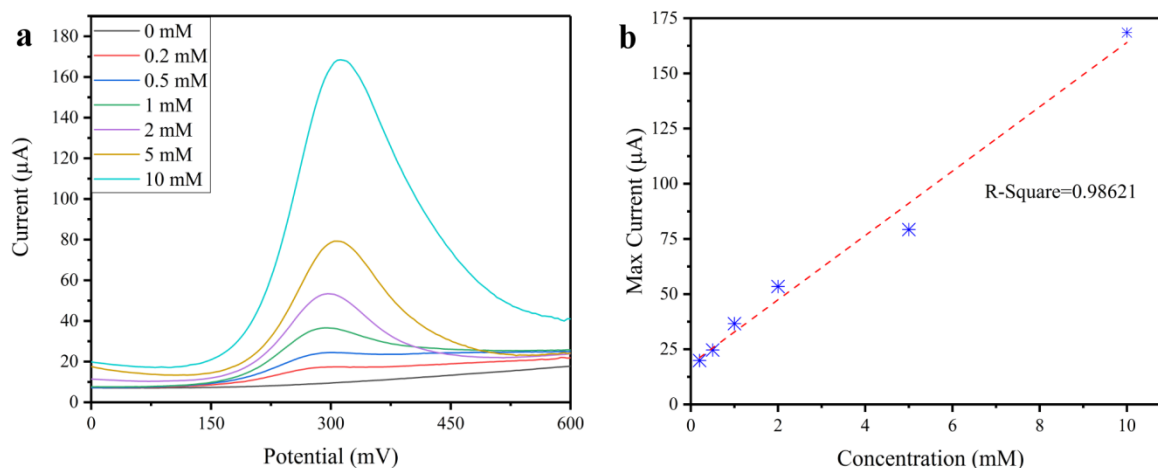
Figure 6.7: (a) Differential pulse voltammetry on different concentrations of potassium ferricyanide and (b) linear relation between concentration of potassium ferricyanide and maximum current shown in DPV

Both anodic and cathodic peaks were clearly observed at 300 mV and -250 mV respectively, with increments of current in proportion to the concentration of potassium ferricyanide, Figure 6.6. However, while there was a linear increase in peak current by increase with concentration (Figure 6.7b), a clearly asymmetric cyclic voltammogram shape associated with a large redox peak separation of 550 mV was observed and was clearly non-ideal when compare to a standard Pt working electrode which displayed the ideal peak shape and separation (~ 59 mV) as shown in Figure 6.8. This indicated that while the SS yarns were capable of acting as an electrode in a electrochemical cell the electrochemical irreversibility of the system was impeded as a result of slow electron exchange of the redox species at the surface of working electrode[23,24].

In order to address the non-ideal surface of SS filaments and enhance the overall electrochemical performance of these yarns, the working electrode SS yarn surface was modified by electrodeposition of AuNps. AuNps were selected due to their outstanding optical, physical and chemical characteristics which includes high electrical conductivity, high specific surface area, resistance to corrosion.[25,26] AuNps have been widely used for surface modification of the working electrode in electrochemistry[27,28] and are well known

to increase the electron exchange rate and consequently improve electrochemical reversibility. AuNps were electrodeposited onto SS filaments for 120, 300 and 600 seconds, as described above. The modified SS-AuNp electrodes were than used as working electrodes to run CVs in 1 M NaCl aqueous electrolyte containing 10 mM potassium ferricyanide. Figure 6.9 shows the normalized current (current divided by maximum current) vs. potential for modified working electrodes.
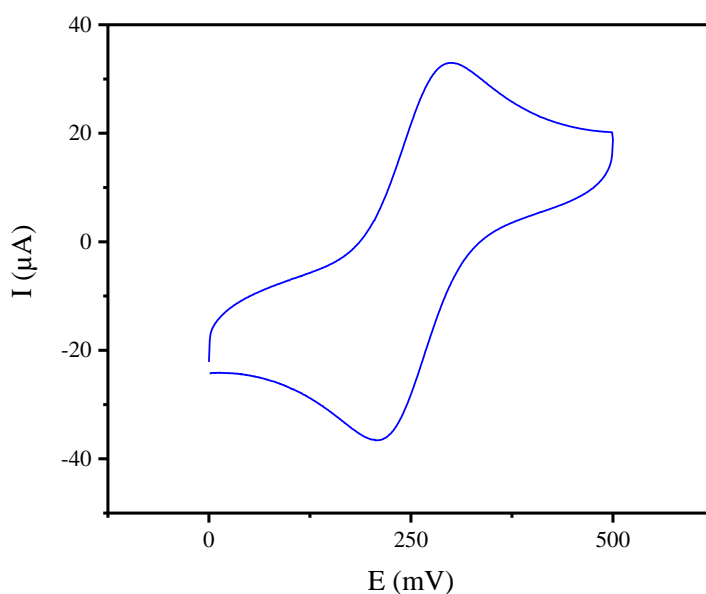
Figure 6.8: CV of 0.5 mM potassium ferricyanide in 1 M NaCl at Pt working electrode

As shown in Figure 6.9, AuNp surface modified electrodes (120 s Au deposition) showed improved reversibility of $Fe^{III}(CN)_6^{3-}$/ $Fe^{II}(CN)_6^{4-}$ reaction rather than pure SS filaments and exhibited higher electron exchange rate, symmetric cyclic voltammograms and small separation of peak potentials (~ 220 mV), compare to what was shown in Figure 6.6 for pure SS filaments. Moreover, it was shown that increasing te electrodeposition time of AuNp from 120 seconds to 300 seconds greatly reduced the redox peak separation to 80 mV, close to ideal peak separation of 59 mV. No significant improvement was observed by increasing the time from 300 to 600 seconds. Therefore, 300 seconds electrodeposition of AuNp was chosen to modify the surface of SS filament working electrodes. Figure 6.10 shows the SEM micrograph of Au particles on the surface of SS filaments.
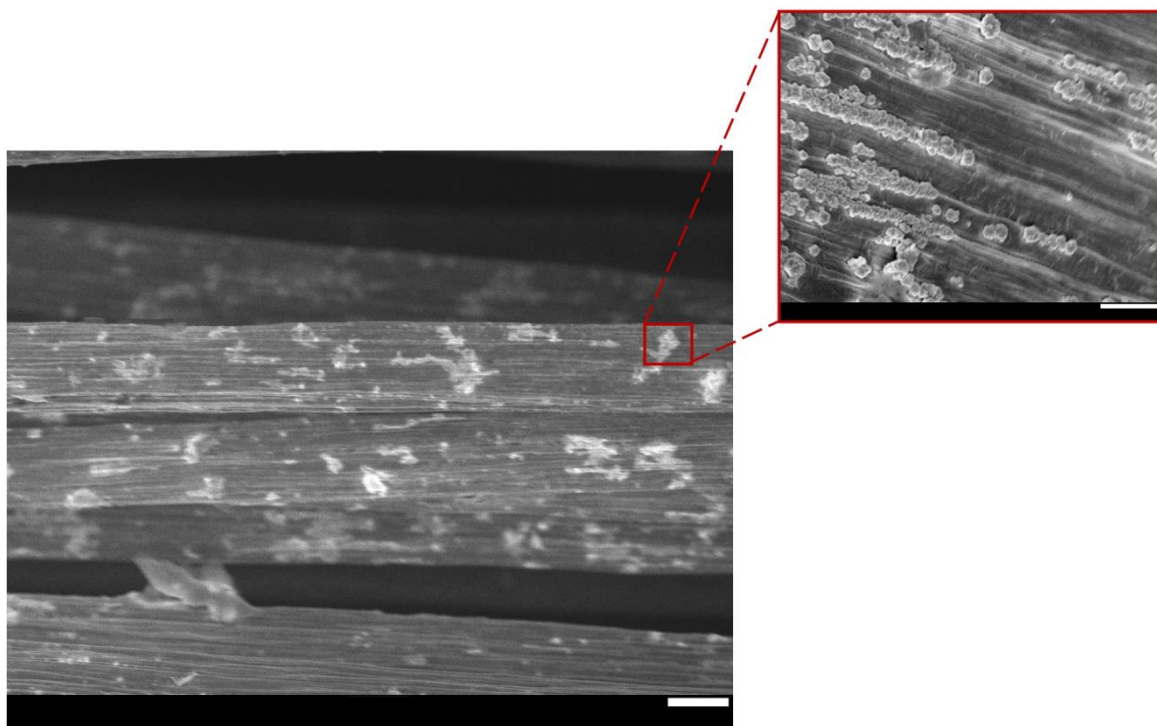
Figure 6.10: SEM micrograph of AuNp electrodeposited SS filament (scale bar= 10 μm) and magnified part to show AuNps morphology (scale part = 1 μm)

Cyclic voltammograms of potassium ferricyanide in 1 M NaCl with gold nanoparticle-modified SS filaments (AuNp-SS) working electrode, Pt mesh as counter and Ag/AgCl as reference electrode is shown in Figure 6.11.
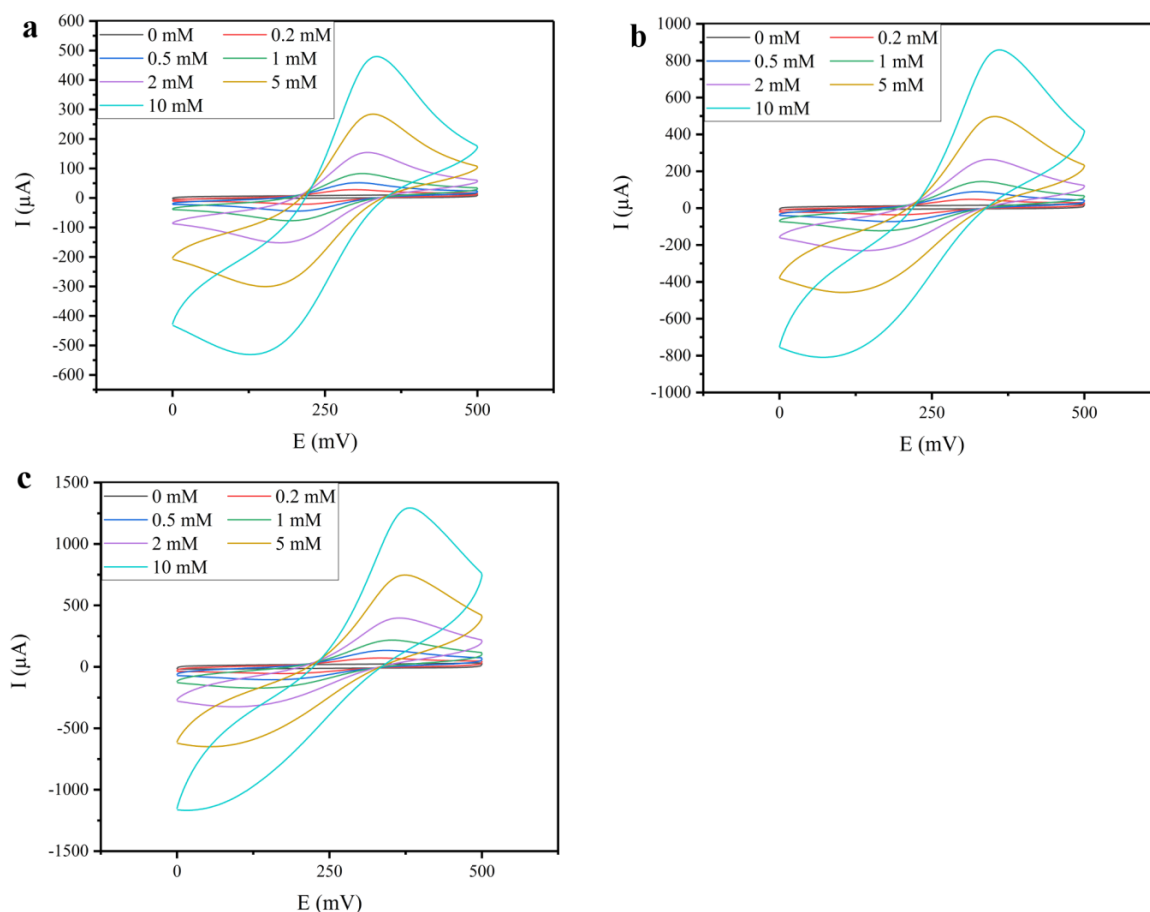
Figure 6.11: CV curves for different concentrations of potassium ferricyanide at (a) 20, (b) 50 and (c) 100 mV s^{-1} scan rates using AuNp-SS working electrode

As shown in Figure 6.11, although modification of SS with AuNp increased the electrochemical reversibility and redox current of $Fe^{III}(CN)_6^{3-}$/ $Fe^{II}(CN)_6^{4-}$, CV curves became asymmetric and distorted at slightly high scan rate (100 mV s^{-1}), indicating electron kinetics was not fast enough for the reaction of $Fe^{III}(CN)_6^{3-}$/ $Fe^{II}(CN)_6^{4-}$ even though AuNp/SS electrode could improve overall electrochemical performance. This limited performance was likely due to non-uniform AuNp distributions across the SS yarn as observed for the SEM images above.

To address these further limitations a thin polypyrrole (PPy) coating was used to increase the adhesion of AuNps on the working electrode. PPy was initially electrodeposited on SS filaments and then AuNps were electrodeposited on PPy-coated SS for 300 seconds[29,30]. Figure 6.12 shows SEM micrographs of PPy-SS and AuNp-PPy-SS filaments.
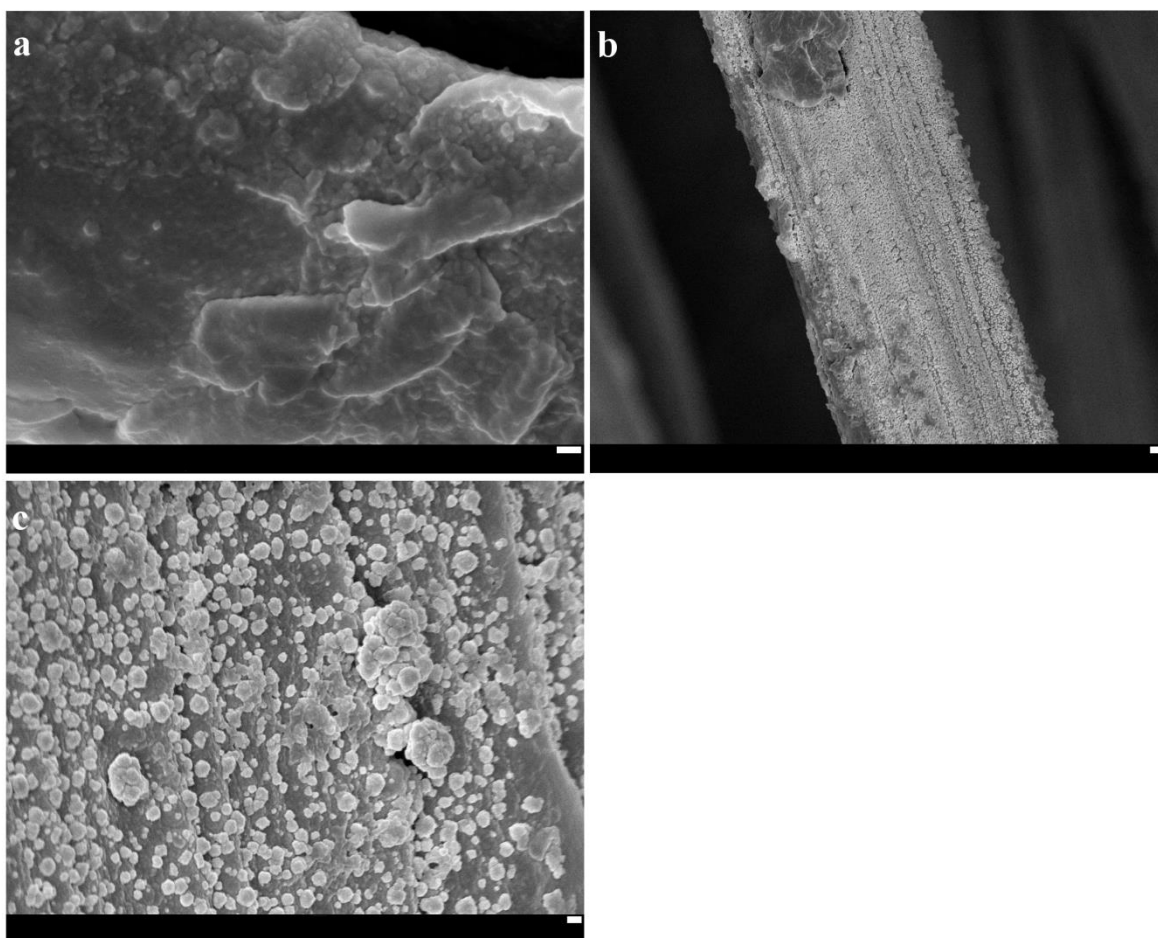
Figure 6.12: SEM micrographs of (a) PPy electrodeposited SS filament (scale bar= 100 nm), (b) AuNp electrodeposited on PPy-SS (scale bar= 1μm) and (c) higher magnification of (b) to show AuNps morphology (scale part = 100 nm)

Figure 6.13 shows electrochemical stability of AuNp-PPy-SS working electrode over 30 cycles at 100 mV s^{-1} in 100 mM NaCl aqueous electrolyte containing 10 mM potassium ferricyanide. Although a diluted electrolyte with much lower ionic strength (compare to what was used for AuNp-SS) was used in this experiment, a significant enhancement was observed in electrochemical reversibility of the system. This suggested that PPy-AuNp

coating provides a porous structure with large effective surface area and high catalytic activity that enhance the kinetics of electron transfer and consequently stability of the system's electrochemical reversibility[31,32].
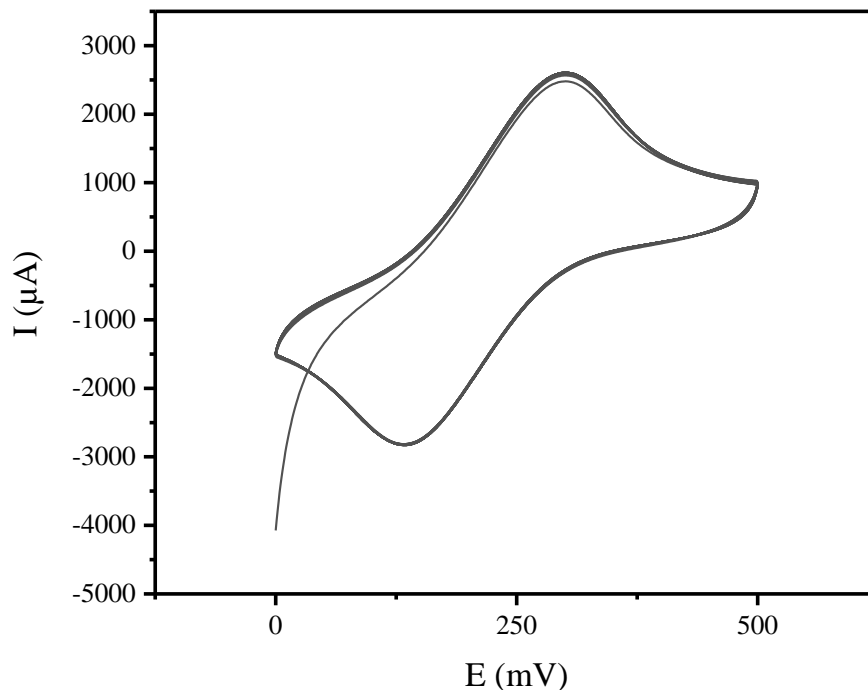
Figure 6.13: 30 Cycles of CV of 10 mM potassium ferricyanide in 100 mM NaCl at 100 mV/S scan rate, working electrode: AuNp-PPy-SS, counter electrode: Pt mesh and reference electrode: Ag/AgCl

Cyclic voltammograms obtained at different concentration of potassium ferricyanide in 100 mM NaCl was shown in Figure 6.14. AuNp-PPy-SS was used as working electrode, Pt mesh as counter and Ag/AgCl as reference electrode.
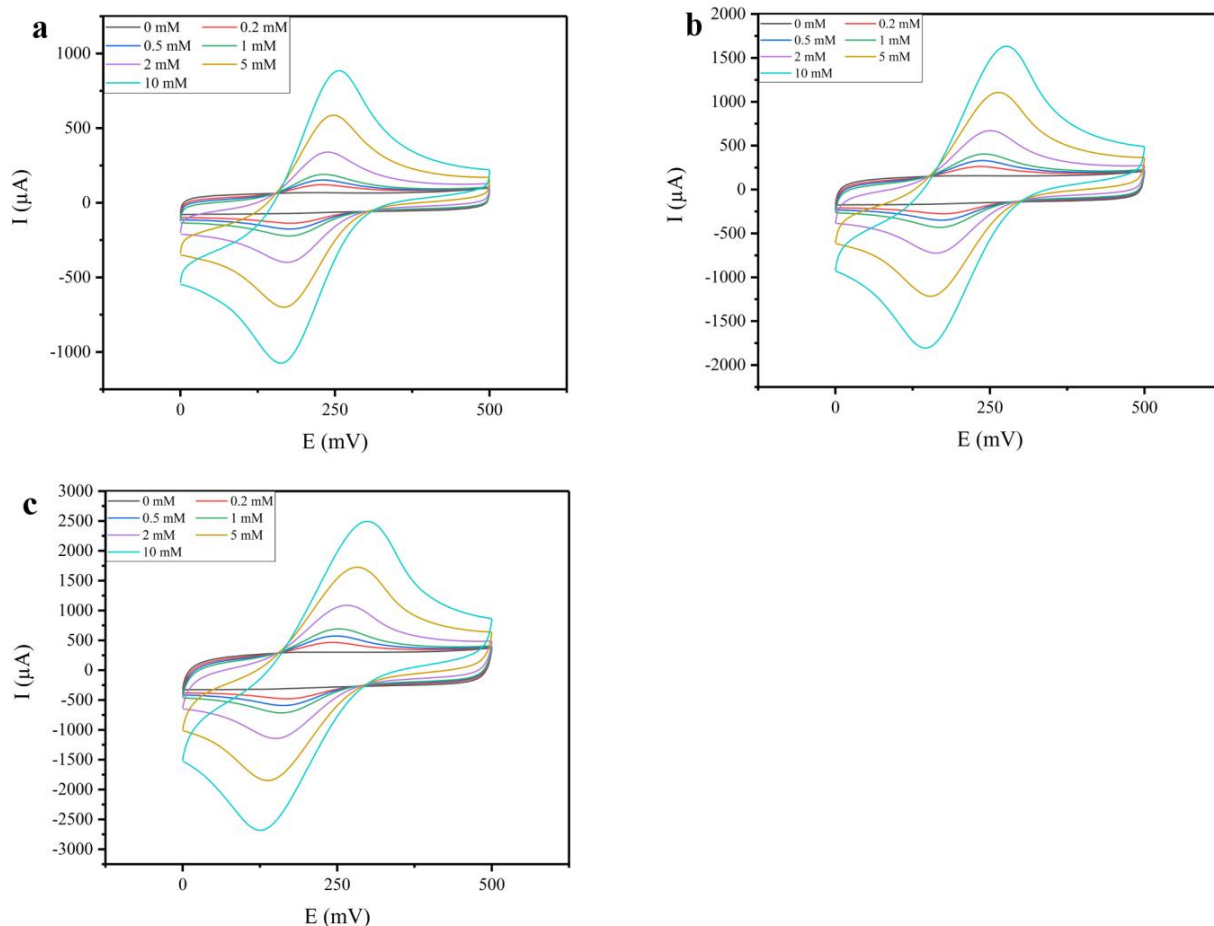
Figure 6.14: CV curves of different concentrations of potassium ferricyanide in 100 mM NaCl at (a) 20, (b) 50 and (c) 100 mV s^{-1} scan rates

As shown in Figure 6.14, CV curves remained symmetric and no change was observed in the separation of peak potentials value confirming that the modified SS electrode with PPy and AuNp (AuNp-PPy-SS electrode) not only performed well electrochemically, but also its performance was stable.

In summary, it was shown that electrochemical performance of SS filaments could be improved by electrodeposition of PPy covered with AuNp. This modification was also proved to be stable. Moreover, as shown in Figure 6.15, there was a linear increase in cathodic peak current by increase in concentration.
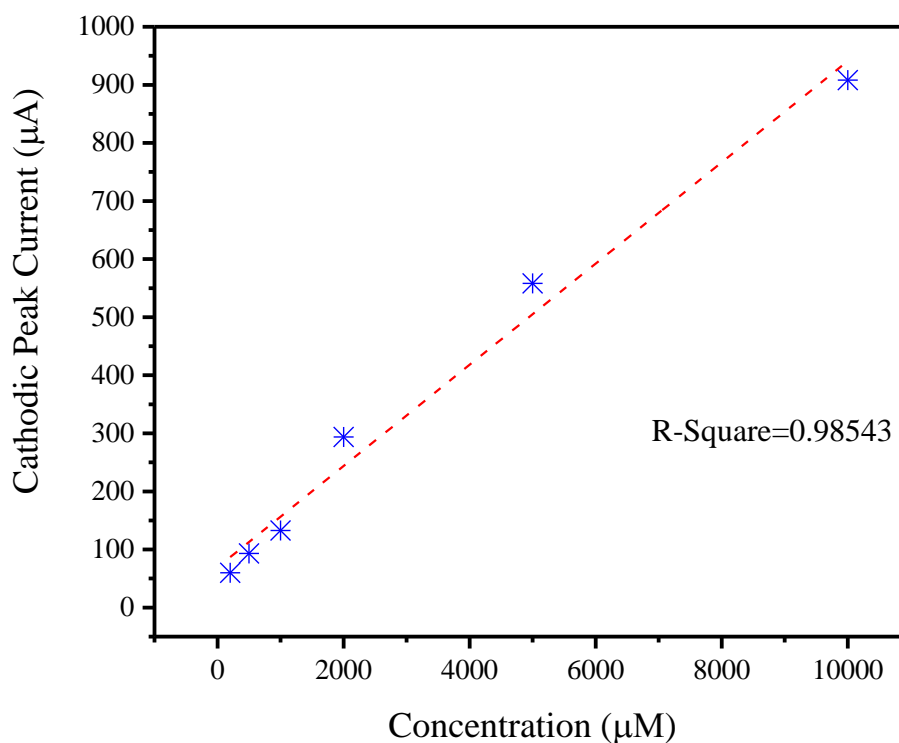
Figure 6.15: Linear increase in peak cathodic current by increase in potassium ferricyanide concentration

6.3.2. Electrochemical detection on 3D braided structure

3D tubular braided structure comprised of three parallel electrodes (2 SS filaments and a silver-plated nylon in the middle) was produced to be used as single device with integrated electrodes for electrochemical detections. Separated electrodes, i.e. working, reference and counter electrodes, in a braided structure is shown in Figure 6.16.
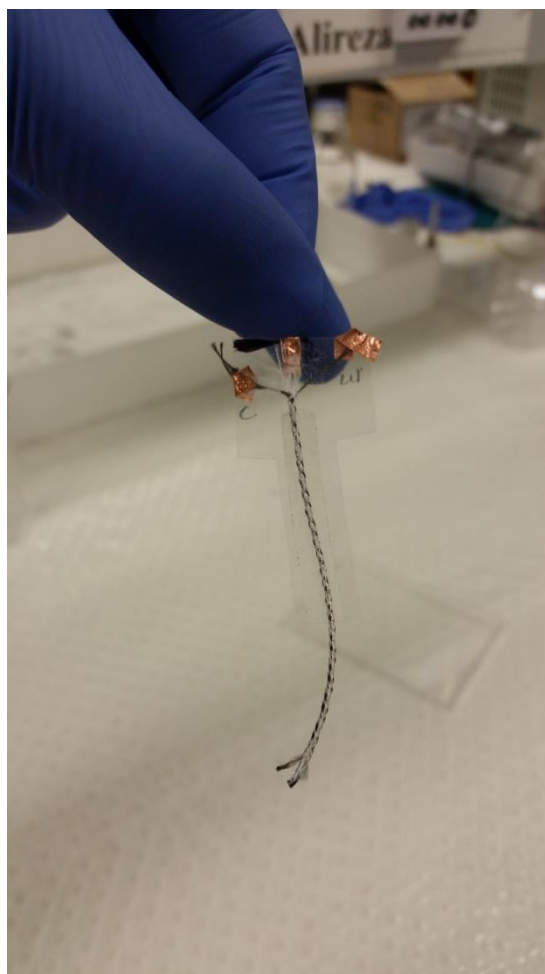
Figure 6.16: Braid structure comprised of 2 SS filaments as counter and working electrodes and a silver-plated electrode (in the middle) as reference electrode which are parallel

Working electrode of the braided structure was modified using the method described above. Figure 6.17 shows the structure with modified working electrode.
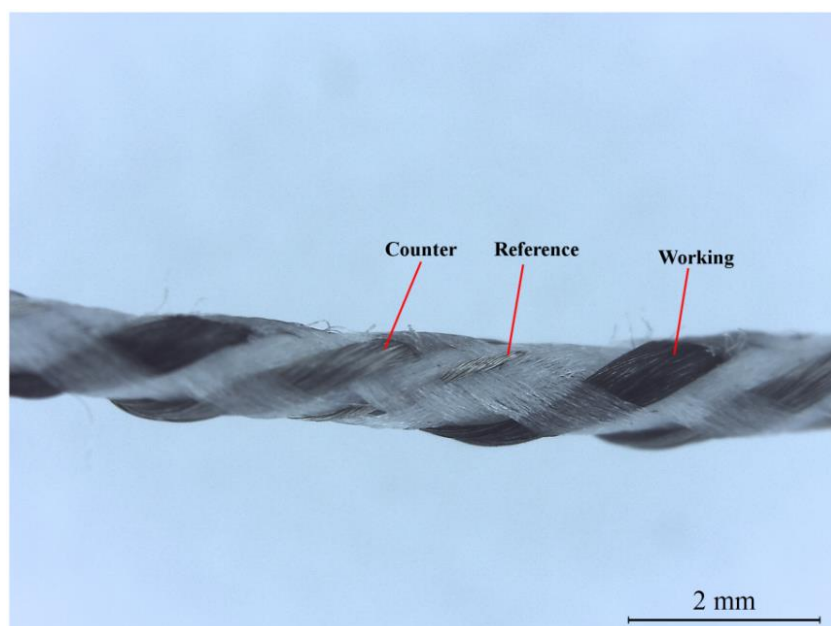
Figure 6.17: 3D braided structure with modified working electrode, i.e. AuNp-PPy-SS electrode.

As a proof of concept, 3D braided structure with modified working electrode was connected to a CH electrochemical workstation, shown in Figure 6.18, and successfully detected 10 mM potassium ferricyanide in 100 mM NaCl utilising the CV technique at the scan rate of 100 mV s^{-1} (Figure 6.19).
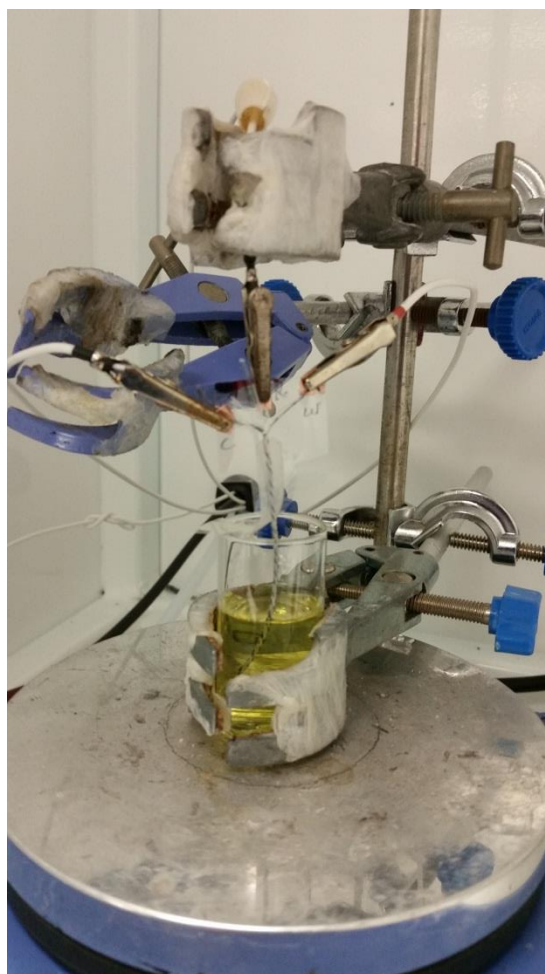
Figure 6.18: CV experimental setup using integrated electrodes in a 3D braided structure
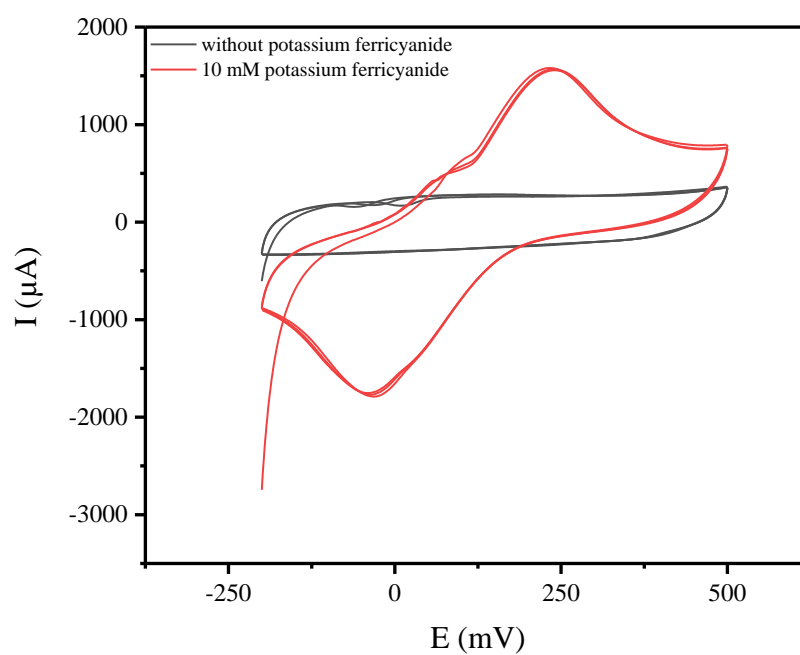
Figure 6.19: Cyclic voltammograms of 10 mM potassium ferricyanide in 100 mM NaCl using integrated electrodes in a 3D braided structure (scan rate 100 mV s^{-1})

6.3.3. Electrochemical detection on 3D knitted structure

The SS filaments used to develop 3D braid structures were unsuitable for the development of knitted structures as they were too thick and stiff and did not produce uniform structures when knitted with cotton/PET yarns. As a consequence, softer SS yarns were purchased and used to develop 3D knitted structures. While SS yarns were soft and thin and could be easily integrated into 3D knitted structures, they couldn't be used to make 3D braids due to their "fluffiness" that causes short circuit issues in braided structures, Figure 6.20. In the knitted configuration, larger insulating gaps between the electrodes were possible thereby preventing the short circuit issues.
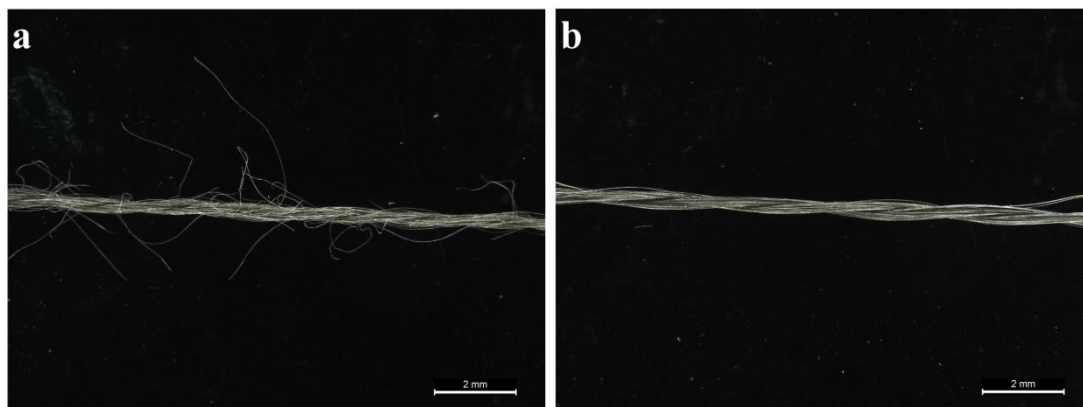
Figure 6.20: (a) SS yarn and (b) SS filament

CVs of a range concentrations of potassium ferricyanide in 1 M NaCl electrolyte were obtained as a function of the scan rate as shown in Figure 6.21. SS yarn was used as working electrode while Pt mesh and Ag/AgCl counter and reference electrodes were used, respectively. Similar to what was observed for SS filaments, shown in Figure 6.6, SS yarns exhibited a clearly asymmetric cyclic voltammogram shape associated with a large redox peak separation of 600 mV indicating a clearly non-ideal electrode.
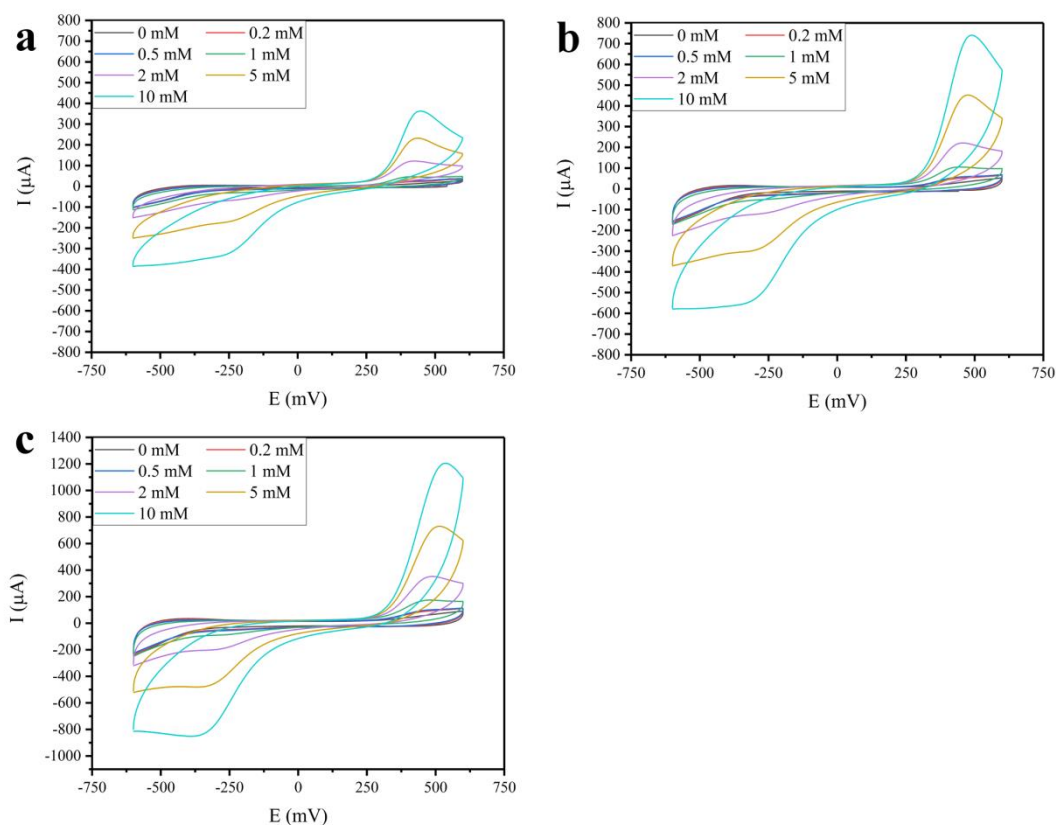
Figure 6.21: Cyclic voltammetry potassium ferricyanide detection on SS yarn at scan rates of (a) 20, (b) 50 and (c) 100 mV s^{-1}

Although SS yarns without surface modifications are non-ideal electrodes for electrochemistry, surface modification, previously shown as an effective way to enhance electrochemical behaviour of the working electrode, can be avoided by utilizing a simple amperometric method to detect potassium ferricyanide was adopted due to the segmented electrode configuration in the textile system. 3D segmented knitted structure comprised of two SS yarn parts as counter and working electrodes and one silver-plated nylon in the middle as pseudo- reference electrode (Figure 6.2) was used for the amperometric detection of a range of concentrations of potassium ferricyanide in 1 M NaCl electrolyte. The 3D knitted structure was first pre-concentrated with electrolyte and then experimental setup shown in Figure 6.22 was used for the amperometric detection. The experiment was set up so that the aqueous supporting electrolyte could gravity siphon from the upper to the lower reservoirs. The experiment was carried out at the constant potential of -400 mV.

10 µL drops of potassium ferricyanide in 1M NaCl with different concentrations, i.e. 0.5, 1, 5 and 10 mM, were applied to the structure and went through the waste container by gravity. Each concentration was repeated 5 times and their corresponding current is shown in Figure 6.23. Electrolyte level in upper petri-dish (electrolyte petri-dish shown in Figure 6.22) kept constant during the experiment to keep the analyte flow rate at a constant rate.
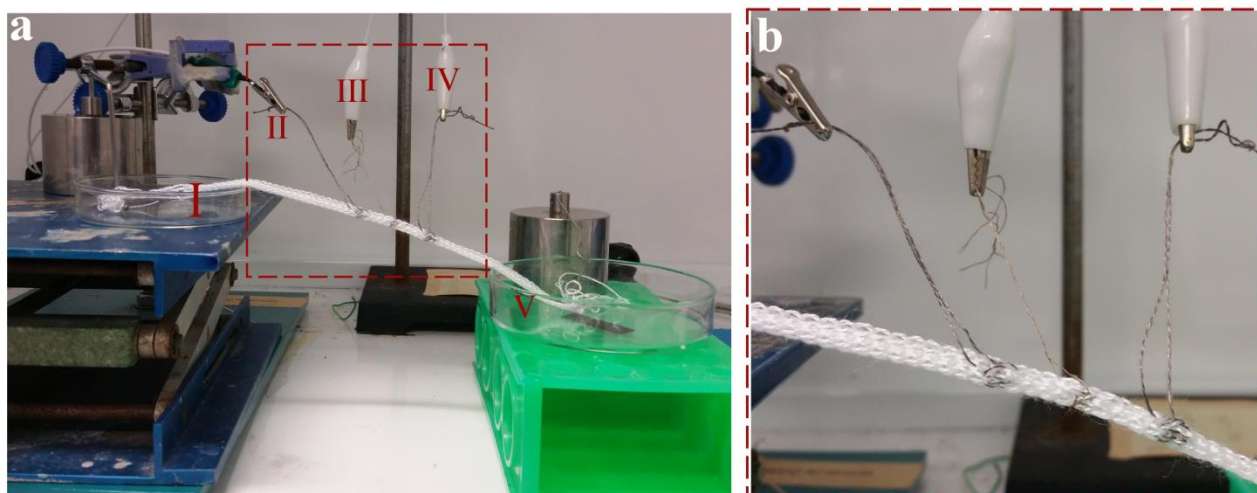
Figure 6.22: (a) Experimental setup for amperometric detection on segmented 3D knitted structure, (I) electrolyte, (II) working electrode, (III) reference electrode, (IV) counter electrode, (V) waste container and (b) closer look of electrode connections
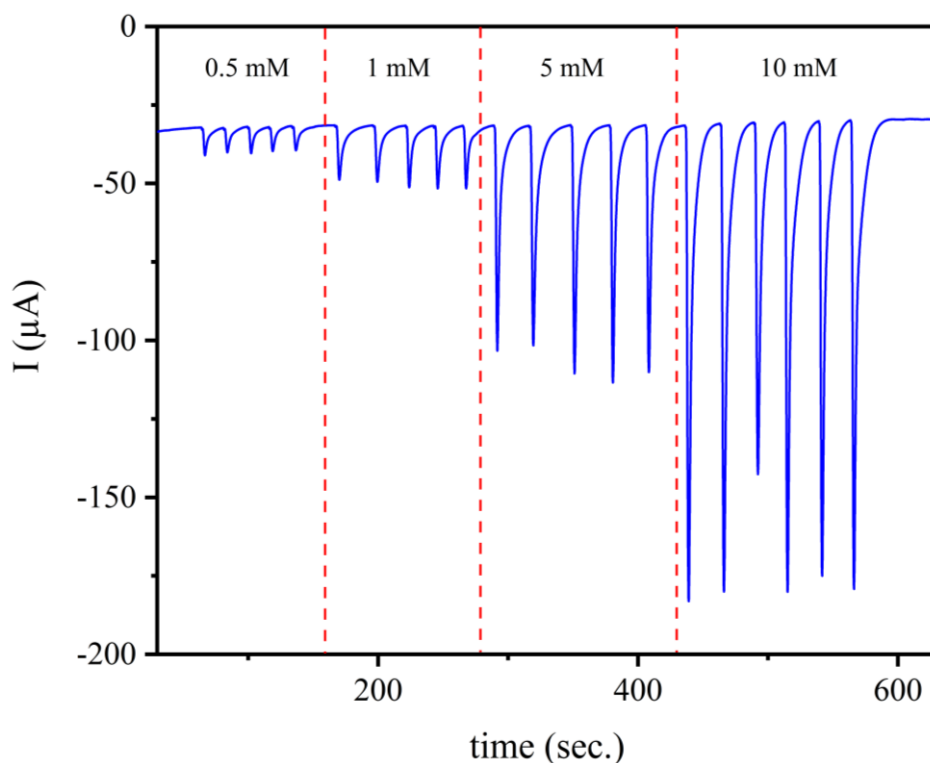
Figure 6.23: Amperometric detection of potassium ferricyanide on segmented 3D knitted structure
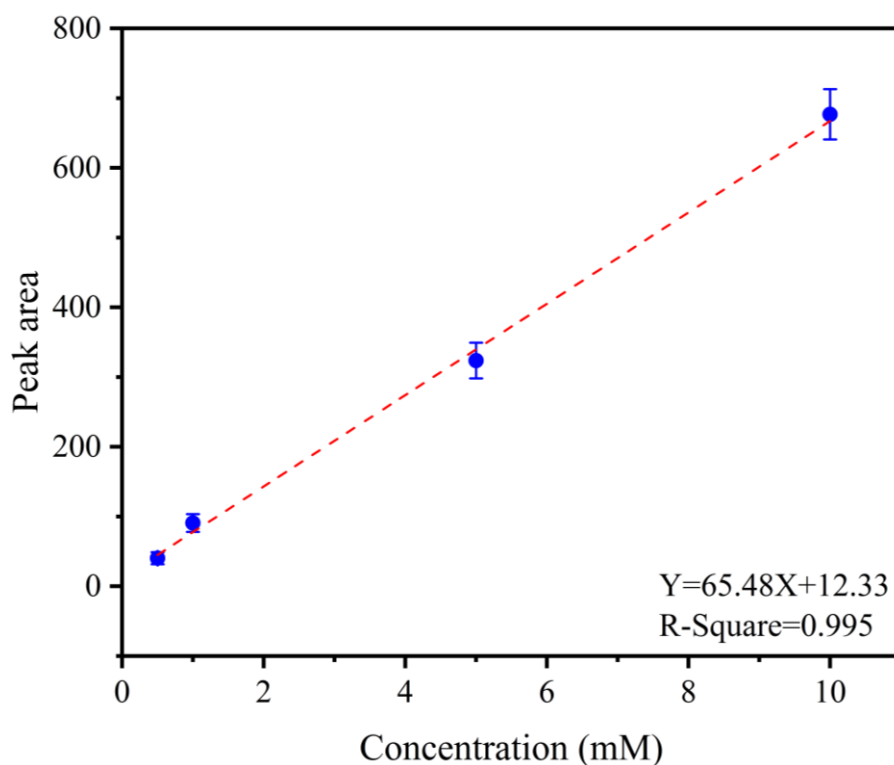
Figure 6.24: Linear decrease in integrated peak area by increase in droplet size

As shown in Figure 6.23, potassium ferricyanide was successfully detected amperometrically on segmented 3D knitted structure and signal intensity was increased by

increase in the analyte's concentration. Absolute value of integrated peak area was calculated and shown to be increased linearly by increase in analyte's concentration, Figure 6.24.

6.4. Conclusion

There is an ever growing demand for wearable chemical and electrochemical sensors that can replace bulky analytical devices in one hand and provide real-time accurate measurements on the other that can be used in a wide variety of applications. Moreover, fabrics and textiles have shown to be promising substrates for making wearable sensors. In this chapter, the surfaces of stainless steel filaments are modified by electrodeposition of PPy and AuNps to achieve an electrochemically reversible system for potassium ferricyanide detection in NaCl electrolyte using CV technique. It was demonstrated that these modified SS working electrode can be incorporated into a 3D braided structure parallel with another SS filament as counter and a silver-plated nylon as reference electrode to make a 3D textile platform on which electrochemical detection was feasible. Such a platform can be easily incorporable into garments and fabrics to form a wearable electrochemical sensor. A knitted 3D textile design also confirmed the feasibility on this approach. This design is comprised of three conductive segments, two SS yarn and a silver-plated nylon in the middle, separated by insulating yarns. It is shown that the latter structure is capable of amperometrically detecting potassium ferricyanide in NaCl electrolyte.

Therefore, it can be concluded that versatile textile-based electrochemical sensors can be designed and made using different textile techniques. Such sensors benefit from being cheap, flexibility and ease of incorporation into everyday garments to provide real time sensing and monitoring.

6.5. References

(1)   Bandodkar, A. J.; Wang, J. Non-Invasive Wearable Electrochemical Sensors: A Review. *Trends Biotechnol.* **2014**, *32* (7), 363–371.

(2)   Turner, A. Biosensors: Then and Now. *Trends Biotechnol.* **2013**, *31* (3), 119–120.

(3)   Malzahn, K.; Windmiller, J. R.; Valdés-Ramírez, G.; Schöning, M. J.; Wang, J. Wearable Electrochemical Sensors for in Situ Analysis in Marine Environments. *Analyst* **2011**, *136* (14), 2912.

(4)   Curto, V. F.; Fay, C.; Coyle, S.; Byrne, R.; O'Toole, C.; Barry, C.; Hughes, S.; Moyna, N.; Diamond, D.; Benito-Lopez, F. Real-Time Sweat pH Monitoring Based on a Wearable Chemical Barcode Micro-Fluidic Platform Incorporating Ionic Liquids. *Sensors Actuators B Chem.* **2012**, *171–172*, 1327–1334.

(5)   Windmiller, J. R.; Wang, J. Wearable Electrochemical Sensors and Biosensors: A Review. *Electroanalysis* **2013**, *25* (1), 29–46.

(6)   Matzeu, G.; Florea, L.; Diamond, D. Advances in Wearable Chemical Sensor Design for Monitoring Biological Fluids. *Sensors Actuators, B Chem.* **2015**, *211*, 403–418.

(7)   Gao, W.; Emaminejad, S.; Nyein, H. Y. Y.; Challa, S.; Chen, K.; Peck, A.; Fahad, H. M.; Ota, H.; Shiraki, H.; Kiriya, D.; et al. Fully Integrated Wearable Sensor Arrays for Multiplexed in Situ Perspiration Analysis. *Nature* **2016**, *529* (7587), 509–514.

(8)   Coyle, S.; Curto, V. F.; Benito-lopez, F.; Florea, L.; Diamond, D. Wearable Bio and Chemical Sensors. In *Wearable sensors: Fundamentals, Implementation and Applications*; Academic Press (via Elsevier), 2014; pp 65–83.

(9)   Malon, R. S. P.; Chua, K. Y.; Wicaksono, D. H. B.; Córcoles, E. P. Cotton Fabric-Based Electrochemical Device for Lactate Measurement in Saliva. *Analyst* **2014**, *139* (12), 3009–3016.

(10)   Agustini, D.; Bergamini, M. F.; Marcolino-Junior, L. H. Tear Glucose Detection Combining Microfluidic Thread Based Device, Amperometric Biosensor and Microflow Injection Analysis. *Biosens. Bioelectron.* **2017**, *98* (May), 161–167.

(11)   Morris, D.; Coyle, S.; Wu, Y.; Lau, K. T.; Wallace, G.; Diamond, D. Bio-Sensing Textile Based Patch with Integrated Optical Detection System for Sweat Monitoring. *Sensors Actuators B Chem.* **2009**, *139* (1), 231–236.

(12)   Guo, L.; Berglin, L.; Li, Y. J.; Matilla, H.; Kalantar MEhrjerdi, A.; Skirfvars, M. " Disappearing Sensor " -Textile Based Sensor for Monitoring Breathing. In *International Conference on Control, Automation and Systems Engineering (CASE)*; IEEE, 2011; pp 1–4.

(13)   Reches, M.; Mirica, K. A.; Dasgupta, R.; Dickey, M. D.; Butte, M. J.; Whitesides, G. M. Thread as a Matrix for Biomedical Assays. *ACS Appl. Mater. Interfaces* **2010**, *2* (6), 1722–1728.

(14)   Li, X.; Tian, J.; Shen, W. Thread as a Versatile Material for Low-Cost Microfluidic Diagnostics. *ACS Appl. Mater. Interfaces* **2010**, *2* (1), 1–6.

(15)   Kang, T.-H. Textile-Embedded Sensors for Wearable Physiological Monitoring Systems, North Carolina State University, 2006.

(16)   De Rossi, D.; Carpi, F.; Galantini, F. Functional Materials for Wearable Sensing, Actuating and Energy Harvesting. *Adv. Sci. Technol.* **2008**, *57*, 247–256.

(17)   Glavan, A. C.; Ainla, A.; Hamedi, M. M.; Fernández-Abedul, M. T.; Whitesides, G. M. Electroanalytical Devices with Pins and Thread. *Lab Chip* **2016**, *16* (1), 112–119.

(18)   Guan, W.; Liu, M.; Zhang, C. Electrochemiluminescence Detection in Microfluidic Cloth-Based Analytical Devices. *Biosens. Bioelectron.* **2016**, *75*, 247–253.

(19)   Choudhary, T.; Rajamanickam, G. P.; Dendukuri, D. Woven Electrochemical Fabric-Based Test Sensors (WEFTS): A New Class of Multiplexed Electrochemical Sensors. *Lab Chip* **2015**, *15* (9), 2064–2072.

(20)   Modali, A.; Vanjari, S. R. K.; Dendukuri, D. Wearable Woven Electrochemical Biosensor Patch for Non-Invasive Diagnostics. *Electroanalysis* **2016**, *28* (6), 1276–1282.

(21)   Hau, N. Y.; Yang, P.; Liu, C.; Wang, J.; Lee, P. H.; Feng, S. P. Aminosilane-Assisted Electrodeposition of Gold Nanodendrites and Their Catalytic Properties. *Sci. Rep.* **2017**, *7* (November 2016), 1–10.

(22)   Zhao, C.; Farajikhah, S.; Wang, C.; Foroughi, J.; Jia, X.; Wallace, G. G. 3D Braided Yarns to Create Electrochemical Cells. *Electrochem. commun.* **2015**, *61*, 27–31.

(23)   Van Benschoten, J. J.; Lewis, J. Y.; Heineman, W. R.; Roston, D. A.; Kissinger, P. T. Cyclic Voltammetry Experiment. *J. Chem. Educ.* **1983**, *60* (9), 772.

(24)   Kissinger, P. T.; Heineman, W. R. Cyclic Voltammetry. *J. Chem. Educ.* **1983**, *60* (9), 702.

(25)   Dai, X.; Nekraseova, O.; Hyde, M. E.; Compton, R. G. Anodic Stripping Voltammetry of arsenic(III) Using Gold Nanoparticle-Modified Electrodes. *Anal. Chem.* **2004**, *76* (19), 5924–5929.

(26)   Bagotsky, V. S. *Fundamentals of Electrohemistry*, Second.; Wiely interscience, 2006.

(27)   Lin, X.; Ni, Y.; Kokot, S. Glassy Carbon Electrodes Modified with Gold Nanoparticles for the Simultaneous Determination of Three Food Antioxidants. *Anal. Chim. Acta* **2013**, *765*, 54–62.

(28)   Duan, J.; He, D.; Wang, W.; Liu, Y.; Wu, H.; Wang, Y.; Fu, M. Glassy Carbon Electrode Modified with Gold Nanoparticles for Ractopamine and Metaproterenol Sensing. *Chem. Phys. Lett.* **2013**, *574*, 83–88.

(29)   García-Hernández, C.; García-Cabezón, C.; Medina-Plaza, C.; Martín-Pedrosa, F.; Blanco, Y.; de Saja, J. A.; Rodríguez-Méndez, M. L. Electrochemical Behavior of polypyrrol/AuNP Composites Deposited by Different Electrochemical Methods: Sensing Properties towards Catechol. *Beilstein J. Nanotechnol.* **2015**, *6* (1), 2052–2061.

(30)   Gutiérrez Pineda, E.; Alcaide, F.; Rodríguez Presa, M. J.; Bolzán, A. E.; Gervasi, C. A. Electrochemical Preparation and Characterization of Polypyrrole/stainless Steel Electrodes Decorated with Gold Nanoparticles. *ACS Appl. Mater. Interfaces* **2015**, *7* (4), 2677–2687.

(31)   Li, J.; Lin, X. Electrocatalytic Oxidation of Hydrazine and Hydroxylamine at Gold Nanoparticle-Polypyrrole Nanowire Modified Glassy Carbon Electrode. *Sensors Actuators, B Chem.* **2007**, *126* (2), 527–535.

(32)   Gong, J.; Wang, L.; Zhang, L. Electrochemical Biosensing of Methyl Parathion Pesticide Based on Acetylcholinesterase Immobilized onto Au-Polypyrrole Interlaced Network-like Nanocomposite. *Biosens. Bioelectron.* **2009**, *24* (7), 2285–2288.

Chapter 7:

Conclusions and future work

7.1. Conclusions

Thread-based microfluidics has attracted significant attention since its emergence in 2010. Although a lot of research work has been done on development of different textile- thread-based microfluidics, there is a lack of understanding fundamental principles of the nature and the role of fibre surface chemistry in the performance of textile-based microfluidic devices. Therefore, this thesis was aimed to understand the effect of fibre surface chemistry on fluid behaviour in textile-based microfluidic devices and consequently to develop functionalized composite fibres suitable for the incorporation into textile structures (either 2D or 3D structures) to induce the desired characteristics to the substrate and improve the performance of textile-based microfluidic device.

Liquid crystalline graphene oxide (LCGO) owing to its very high aspect ratio and sheet size and having carboxyl and hydroxyl functional groups[1–3] was chosen as the filler to be incorporated into low-density polyethylene (LDPE) polymeric matrix. Composite fibres with different surface functional groups and therefore surface chemistries with respect to the LDPE were produced and their properties were investigated.

In **Chapter 3**, LCGO/LDPE composite fibres with different loadings of LCGO were produced by pre-coating the LDPE powder with LCGO and subsequently extruded utilising a conventional melt-spinning technique. These fibres (as well as pure LDPE fibre) were incorporated into 3D textile structures in combination with polyester (PET) thread to make 3D textile-based microfluidic platforms. Finally, the effect of different surface chemistries upon the wicking performance (power free pumping) of 3D textile platforms in different media, i.e. DI water, Tris(hydroxymethyl)aminomethane (TRIS) / N-Cyclohexyl-2-aminoethanesulfonic acid (CHES) buffer and NaCl solution, was investigated. It was found that ionic interaction (repulsion or absorption) between fibres surface and the ion in the solutions used to perform the experiment dominated the flow

178

rate. When DI water and NaCl solution were used, a maximum flow rate was achieved by the tubular knitted 3D textile structure comprised of a commercial PET yarn and 5 w/w% LCGO/LDPE composite fibre. 3D structures comprised of the unmodified PET and LDPE base fibres exhibited the lowest flow rate. In contrast, when Tris/CHES buffer solution was used, the 3D structure comprised of PET and 5 w/w% LCGO/LDPE composite fibres exhibited a flow trend reversal whereby the higher LCGO loadings produced the lowest flow rate due to Tis ion absorption at the fibres surface due to exposed LCGO functional groups of the composite fibre. Under these conditions a maximum flow rate was shown by the structure with no functional groups, i.e. 3D structure comprised of 2PET and PET/LDPE fibres.

Anti-gravitational pumping of DI water using knitted structures comprised of commercial PET and LDPE or LCGO/LDPE composite fibres was also investigated. It was shown that the addition of LCGO-filled fibers into the 3D knitted structures increased the anti-gravitational pumping flow rate. It was found that the flow rate was increased with a direct increase in the amount of LCGO loaded into LDPE. A maximum flow rate of up to 16 µL min^{-1} was achieved with the knitted 3D structure consisting of a commercial PET yarn and 5 w/w% LCGO/LDPE composite fibre.

Fluid movement within a textile structure is primarily driven by a capillary effect. In this thesis it was demonstrated that the flow rate in a textile-based microfluidic structure can be tuned by changing the surface chemistry of the fibres utilised within the textile platform. While there is a degree of tunability in these structures the flow rates are highly condition sensitive and will dependent upon the ionic environment and the solvent reservoir head height. If these textile structures are to be successfully used in electro-fluidic driven devices then a more controllable and precise fluid control will be required in any textile- or thread-based microfluidics approaches. As a consequence, the need to

achieve controllable fluid flow in textiles based systems will require the provision of an external power supply to drive flow. Recently, the electrophoresis technique has been shown to be a powerful tool that has been widely used in textile-based microfluidics. However when an electric field is applied to electrolyte to move an analyte under electrophoretic control Joule-heating will be inevitable. Joule-heating not only increases the fluid temperature, but it also produces temperature gradients in cross-stream and axial flow directions. These temperature effects, cause non-uniformity in fluid properties, and more importantly affect the mass species transport [4]. To address this problem **Chapter 4** and **Chapter 5** focused upon development of thermally conducting composite fibres which may be incorporated into textile substrates in order to minimize the Joule-heating effect.

LGCO was initially investigated as a filler owing to its solvent processability and outstanding thermal conductivity when reduced.[1,2] LDPE was utilised as a filler due its simplicity (simple chemical structure) and due to the fact that was a thermally deductive due to its strain induced crysatalinity[5–7]. LCGO/LDPE composite fibres with different loadings of LCGO were produced using a melt-spinning method. These composite fibres were incorporated into 3D PET knitted structures and their performance in dissipating Joule-heating was investigated. Different electric fields were applied to 3D knitted structures and resultant current and temperature change were monitored. LCGO addition up to 2 w/w% into LDPE resulted in increase in ultimate strength and Young's modulus compare to pure LDPE while maintaining the elongation at break. However a drop in ultimate strength and Young's modulus was observed in 5 w/w% LCGO/LDPE composite fibres due to agglomeration of LCGO resulting weak points in fibres limiting their utility at higher loadings.

The incorporation of LCGO/LDPE composites with filler loadings of lower than 1 w/w%

in 3D PET knitted structures did not improve thermal dissipation ability of the structure. In these fibres, the LCGO sheets were separated by LDPE polymer matrix and therefore had poor inter-connectivity required to form a suitable heat conduction path. This led to huge phonon scattering at the boundaries (between polymeric matrix and the filler) which resulted in the interruption in phonon movements resulting in internal contact thermal resistance. Incorporation of LCG/LDPE fibres with 2 and 5 w/w% loadings of LCGO resulted in improvement in heat dissipation ability and kept the fabricated 3D textile system at a lower working temperature. At these higher loadings, effective connections between the LCGO sheets were noted and consequently heat conduction paths were formed. This phenomenon along with the ability of LCGO to fully integrate and assemble into LDPE the extruded polymeric matrix, driven by its extremely large aspect ratio, could lead to a significant increase in composites' thermal conductivity and therefore its ability to dissipate the heat generated by Joule-heating in the system[8–10].

Despite the promising increase in heat dissipation ability when under electrophoretic conditions through the incorporation of 2 and 5 w/w% LGCO/LDPE fibres, (confirmed by the decrease in the overall textile system's operating temperature) producing LCGO/LDPE composite fibres with LCGO contents of more than 5w/w% was impractical. Unfortunately, the pre-mixing LCGO approach used to produce the fibres resulted in the significant formation of LCGO aggregates within the composite fibre. These aggregates degraded the fibre's mechanical properties thereby limited its utility within the knitting machine used to produce the textile structures.

In **Chapter 5** in order to address melt spinning limitations encountered for LDPE, a solvent base pre-mixing mixing method was investigated to improve the uniformity of the thermally conducting filler within the resultant fibres. In this new approach a wet-spinning technique was adopted for the production of fibres. This approach also required a change

in the type of base polymer, to polyurethane and away from LDPE, due to LDPE's insolubility in common (non-toxic) solvents in order to make thermally conducting fibres. It has been shown by others[11] and consistent with these findings, that thermally conducting composites made by solution mixing typically performed better than melt mixing approaches . A medical grand non-crosslinked PU was chosen as polymeric matrix due to its solubility in various organic solvents and good mechanical properties which made it an excellent candidate for the knitting. LCGO and boron nitride[12,13] nanopowder (BNNP), also a well-known thermally conductive filler, were investigated.

Initially the solubility of PU polymers in DMF and different ratios of EtOH/water was investigated to establish an optimal spinabillity. Then, the wet spinning parameters, i.e. injection flow rate and non-solvent (coagulation bath), were optimized to obtain continuous PU fibres with almost circular cross-section shape. Composite polymeric materials with different loadings of LCGO, i.e. 0.25, 0.5, 1 and 2 w/w%, as well as different loading of BNNP, i.e. 0.5, 1, 2 and 5 w/w%, were prepared by a direct solution mixing method and fibres spun using a wet-spinning method.

The effect of adding fillers in Young's modulus, elongation at break and ultimate strength of resultant fibres were investigated. The addition of the LGCO filler into PU matrix led to overall increase in Young's modulus and ultimate tensile strength while decrease in elongation at break, in a behaviour that was consistent with studies by others[14–18]. The effects of the different loadings of LCGO on the hard and soft segments of PU and their interactions on the mechanical behaviour of the composite fibres were discussed. Similarly the addition of BNNP into PU matrix, resulted in an increase in Young's modulus and ultimate stress. These may be explained by the fact that addition of BNNP filler into PU polymeric matrix enhanced the ability of strain energy dissipation of polymer due to the interfacial adhesion of filler into PU polymeric matrix[14,15,19]. Effect of

BNNP filler on the elongation at break of the composite fibres was similar to what was already reported for silica nanocomposite-filled PU[20] and low loadings of carbon black in PU[21] and resulted in increase in elongation at break.

Both LCGO/PU and BNNP/PU composite fibres were incorporated into 3D PET textile structures using conventional knitting technique and the thermal dissipation ability of the knitted structures were assessed. Different electric fields were applied to 3D knitted structures and resultant current and temperature change were monitored. It was found that although thermal conductivity of reduced LCGO/PU composite increased with increasing LCGO loading, that could be attributed to the different orientation of LCGO sheets in films and fibres, these fibres became more effective in Joule-heating dissipation at the point that they also became electrically conductive (i.e. at LCGO loadings greater than 2w/w%). As a consequence the LCGO was replaced by thermally conducting but electrically insulating BNNP filler. BNNP-filled thermally conducting composite fibres performed very well in dissipating Joule-heating.

It was shown that incorporating thermally conductive fibres into 3D textile structures as heat dissipater potentially can be used as an effective method to dissipate the heat generated by Joule-heating and keep the system as cool as possible for the longer time during electrophoresis experiment. This could be an advantageous and opens up new opportunities for fibre based capillary electrophoresis studies specifically when proteins, living cells and temperature sensitive analytes are being used.

 Finally, in **Chapter 6**, two different textile designs comprised of conducting/non-conducting segments were proposed as textile substrates for wearable electrochemical sensors. Metallic yarns/filaments (stainless steel and silver coated nylon) were employed and their suitability as electrodes determined. Firstly, the effect of modification of working electrode's surface by electrodeposition of polypyrrole (PPy) and gold

nanoparticle (AuNp) upon its electrochemical performance improvement was shown. Utilising braiding fabrication technique, a 3D tubular structure with three parallel electrodes, 2 stainless steel filaments and a silver-plated nylon (used as an internal pseudo reference electrode), was made as a textile platform with integrated electrodes for development of wearable electrochemical sensors. The working electrode of the proposed structure was modified with PPy and AuNp and it was shown that it can be used to detect analytes by a standard cyclic voltammetry technique.

In an alternate approach, a 3D segmented knitted structure comprised of 2 stainless steel yarn and a silver-plated nylon conductive parts separated with cotton/polyester insulating parts was proposed as another design for wearable electrochemical sensors. It was shown that this textile structure could be successfully utilized in a simple gravity flow driven system using a simple electrochemical amperometric detection technique.

In an overall summary, this thesis fundamentally reviewed the effect of fibre's surface chemistry as the basal compartment of a textile structure upon the wicking properties of 3D textile-based microfluidic devices. Then, thermally conducting fibres using different polymeric matrices, LDPE and PU, as well as different filler materials, LCGO and BNNP, were successfully made and incorporated into 3D knitted textile structures. Also, it was shown that the incorporation of these thermally conducting fibres into 3D textile substrates resulted in dissipation of detrimental Joule-heating effects in electrophoretically driven processes. Finally, two different textile platforms comprised of conductive/non-conductive threads made with knitting and braiding techniques were proposed and shown to be capable of electrochemically detecting analytes by cyclic voltammetry or amperometry techniques and therefore, being used to develop wearable electrochemical sensors. It can be concluded that by tuning the surface chemistry of textile fibres (as discussed in **Chapter 3**) and using proper detection methods (**Chapter 6**), this thesis has

set a solid foundation for the future development a wearable µTAD can be made which is capable of collecting the sample, move it to the detection zone and performing quantitative detection.

7.2. Future work

This thesis tried to cover a wide spectrum of textile–based microfluidic issues fundamental study to its application in the field of textile-based microfluidics – a field which is still in its infancy. Although different challenges in making fibres, textile fabrications and microfluidic applications have been tackled in this thesis, there are still many challenges for future study and development.

The effect of changing the fibre's surface chemistry on the wicking properties of the final 3D textile-based microfluidic devices has been discussed in **Chapter 3**. Although, textiles' wicking rate can be improved by tuning fibres' surface chemistry, constant flow rate over the time cannot be achieved due to an increase in the back pressure in reservoirs while fluid is being transferred from one to another. Therefore, it would be useful to investigate if constant flow rate is achievable by applying electric potential to the structure to drive the fluid and therefore exploit those structures as textile-based electroosmotic pumps. Moreover, since the proposed microfluidic pumps cannot be switched off, using some photoresponsive hydrogels[22] to make an actual pump with on/off switch could be also investigated.

Regarding the wicking test and the effect of fibre's surface chemistry explained in this chapter, addition of different fillers like nanoclays that have different functional groups to the polymer matrix is worth investigating. Considering the poor mixing of LCGO and LDPE in LCGO concentrations more than 5 w/w%, replacing LDPE with polymers soluble in organic solvents, by which higher filler loadings is achievable using solution mixing method, could be also explored.

Making thermally conducting composite fibres using melt- and wet-spinning methods have been discussed in **Chapters 4 and 5**. Melt spun fibres seems to be stronger than wet-spun ones, but, solution mixing results in better mixture and thermally conducting fibres. Considering poor efficiency of melt mixing and limitations of solution mixing and wet-spinning, combination of these two methods, i.e. solution mixing to make composites followed by melt-spinning, could eliminate the limitations of wet-spinning, e.g. dependence on viscosity, while improve the efficiency of the mixing.

Chapter 6 proposed different textile designs with integrated electrodes for making wearable electrochemical sensors. Using the same concept and utilizing functionalized fibre segments in textile platforms to trap target molecules or detect biomarkers seems to be a useful tool in biological studies for diagnostics or DNA/RNA extraction and detection and is an area that has significant opportunities for future development.

7.3. References

(1)   Jalili, R.; Aboutalebi, S. H.; Esrafilzadeh, D.; Shepherd, R. L.; Chen, J.; Aminorroaya-Yamini, S.; Konstantinov, K.; Minett, A. I.; Razal, J. M.; Wallace, G. G. Scalable One-Step Wet-Spinning of Graphene Fibers and Yarns from Liquid Crystalline Dispersions of Graphene Oxide: Towards Multifunctional Textiles. *Adv. Funct. Mater.* **2013**, *23* (43), 5345–5354.

(2)   Aboutalebi, S. H.; Gudarzi, M. M.; Zheng, Q. Bin; Kim, J. K. Spontaneous Formation of Liquid Crystals in Ultralarge Graphene Oxide Dispersions. *Adv. Funct. Mater.* **2011**, *21* (15), 2978–2988.

(3)   Aboutalebi, S. H.; Jalili, R.; Esrafilzadeh, D.; Salari, M.; Gholamvand, Z.; Aminorroaya Yamini, S.; Konstantinov, K.; Shepherd, R. L.; Chen, J.; Moulton, S. E.; et al. High-Performance Multifunctional Graphene Yarns: Toward Wearable All-Carbon Energy Storage Textiles. *ACS Nano* **2014**, No. Xx.

(4)   Xuan, X.; Li, D. Analytical Study of Joule Heating Effects on Electrokinetic Transportation in Capillary Electrophoresis. *J. Chromatogr. A* **2005**, *1064* (2), 227–237.

(5)   Choy, C. L. Thermal Conductivity of Polymers. *Polymer (Guildf).* **1977**, *18* (April 1976), 984–1004.

(6)   Anderson, D. R. Thermal Conductivity of Polymers. *Chem. Rev.* **1966**, *66* (6), 677–690.

(7)   Liu, J.; Yang, R. Tuning the Thermal Conductivity of Polymers with Mechanical Strains. *Phys. Rev. B - Condens. Matter Mater. Phys.* **2010**, *81* (17), 1–9.

(8)   Zhao, Y. H.; Zhang, Y. F.; Bai, S. L. High Thermal Conductivity of Flexible Polymer

Composites due to Synergistic Effect of Multilayer Graphene Flakes and Graphene Foam. *Compos. Part A Appl. Sci. Manuf.* **2016**, *85*, 148–155.

(9)   Guo, H.; Li, X.; Li, B.; Wang, J.; Wang, S. Thermal Conductivity of Graphene/poly(vinylidene Fluoride) Nanocomposite Membrane. *Mater. Des.* **2017**, *114*, 355–363.

(10)   Zhao, Y. H.; Wu, Z. K.; Bai, S. L. Study on Thermal Properties of Graphene Foam/graphene Sheets Filled Polymer Composites. *Compos. Part A Appl. Sci. Manuf.* **2015**, *72*, 200–206.

(11)   Ng, H. Y.; Lu, X.; Lau, S. K. Thermal Conductivity of Boron Nitride-Filled Thermoplastics: Effect of Filler Characteristics and Composite Processing Conditions. *Polym. Compos.* **2005**, *26* (6), 778–790.

(12)   Eichler, J.; Lesniak, C. Boron Nitride (BN) and BN Composites for High-Temperature Applications. *J. Eur. Ceram. Soc.* **2008**, *28* (5), 1105–1109.

(13)   Li, T.; Hsu, S. L. Enhanced Thermal Conductivity of Polyimide Films via a Hybrid of Micro- and Nano-Sized Boron Nitride. *J. Phys. Chem. B* **2010**, *114*, 6825–6829.

(14)   Cai, D.; Jin, J.; Yusoh, K.; Rafiq, R.; Song, M. High Performance Polyurethane/functionalized Graphene Nanocomposites with Improved Mechanical and Thermal Properties. *Compos. Sci. Technol.* **2012**, *72*, 702–707.

(15)   Wu, C.; Huang, X.; Wang, G.; Wu, X.; Yang, K.; Li, S.; Jiang, P. Hyperbranched-Polymer Functionalization of Graphene Sheets for Enhanced Mechanical and Dielectric Properties of Polyurethane Composites. *J. Mater. Chem.* **2012**, *2*, 7010–7019.

(16)   Javadi, M.; Gu, Q.; Naficy, S.; Farajikhah, S.; Crook, J. M.; Wallace, G. G.; Beirne, S.; Moulton, S. E. Conductive Tough Hydrogel for Bioapplications. *Macromol. Biosci.* **2017**.

(17)   Chen, Q.; Mangadlao, J. D.; Wallat, J.; De Leon, A.; Pokorski, J. K.; Advincula, R. C. 3D Printing Biocompatible Polyurethane/Poly(lactic acid)/Graphene Oxide Nanocomposites: Anisotropic Properties. *ACS Appl. Mater. Interfaces* **2017**, *9* (4), 4015–4023.

(18)   Seyedin, M. Z.; Razal, J. M.; Innis, P. C.; Jalili, R.; Wallace, G. G. Achieving Outstanding Mechanical Performance in Reinforced Elastomeric Composite Fibers Using Large Sheets of Graphene Oxide. *Adv. Funct. Mater.* **2015**, *25* (1), 94–104.

(19)   Petrović, Z. S.; Ferguson, J. Polyurethane Elastomers. *Prog. Polym. Sci.* **1991**, *16* (5), 695–836.

(20)   Petrovic, Z. S.; Javni, I.; Waddon, A.; Banhegyi, G. Structure and Properties of Polyurethane-Silica Nanocomposites. *J. Appl. Polym. Sci.* **2000**, *76* (2), 133–151.

(21)   Seyedin, S.; Razal, J. M.; Innis, P. C.; Wallace, G. G. A Facile Approach to Spinning Multifunctional Conductive Elastomer Fibres with Nanocarbon Fillers. *Smart Mater. Struct.* **2016**, *25* (3), 35015.

(22)   Coleman, S.; ter Schiphorst, J.; Azouz, A.; Ben Bakker, S.; Schenning, A. P. H. J.; Diamond, D. Tuning Microfluidic Flow by Pulsed Light Oscillating Spiropyran-Based Polymer Hydrogel Valves. *Sensors Actuators, B Chem.* **2017**, *245*, 81–86.

Appendices

Appendix I: MATLAB to calculate Young's modulus for LCGO/LDPE composite fibres

```matlab
clear,clc;
close all;
commandwindow;
TT=[];
aT=xlsread('LDPE_LCGO_Modulusfile.xlsx','Sheet1','A4:AD200');
[m n]=size(aT);
STP=17;
MD=cell(6,5);
MD{1,4}='Average(MPa)';
MD{1,5}='STD';
R=2;
C=1;
for i=1:n/2
    A=aT(:,(2*i-1):2*i);
    x=A(:,1);
    x(isnan(x))=[];
    y=A(:,2);
    y(isnan(y))=[];
    y=smooth(y,10);

    t=STP+1;
    a=fitlm(x(STP:t),y(STP:t));
    Tr=a.Rsquared.Ordinary;
    while (Tr>0.990) || (t-STP<5)
        TT=[TT Tr];
        t=t+1;
        a=fitlm(x(STP:t),y(STP:t));
        Tr=a.Rsquared.Ordinary;
    end
    no=t-1;
    Mo=(y(no)-y(STP))/(.01*(x(no)-x(STP)));
    MD{R,C}=Mo;

    if (mod(i,3)==0) && (i<(n/2))
        plot(x,y);
        plot([x(STP) x(no)],[y(STP) y(no)],'--r');
        figure;
        MD{R,C+1}=mean(double([MD{R,1} MD{R,2} MD{R,3}]));
        MD{R,C+2}=std(double([MD{R,1} MD{R,2} MD{R,3}]));
        R=R+1;
        C=1;

    else
        hold on
        plot(x,y);
        plot([x(STP) x(no)],[y(STP) y(no)],'--r');
        C=C+1;
    end


end
MD{R,4}=mean(double([MD{R,1} MD{R,2} MD{R,3}]));
MD{R,5}=std(double([MD{R,1} MD{R,2} MD{R,3}]));
MD
xlswrite('LDPE_LCGO_Modulusfile.xlsx',MD,'Sheet2','B2:F7');
```

Appendix II: MATLAB to calculate Young's modulus for LCGO/PU composite fibres

```
clear,clc;
close all;
commandwindow;
TT=[];
aT=xlsread('PU_LCGO_Modulusfile.xlsx','Sheet1','A4:AD4000');
[m n]=size(aT);
STP=10;
MD=cell(6,5);
MD{1,4}='Average(MPa)';
MD{1,5}='STD';
R=2;
C=1;
for i=1:(n/2)

   A=aT(:,(2*i-1):2*i);
   x=A(:,1);
   x(isnan(x))=[];
   y=A(:,2);
   y(isnan(y))=[];
   y=smooth(y,10);

   t=STP+1;
   a=fitlm(x(STP:t),y(STP:t));
   Tr=a.Rsquared.Ordinary;
   while (Tr>0.990) || (t-STP<5)
      TT=[TT Tr];
      t=t+1;
      a=fitlm(x(STP:t),y(STP:t));
      Tr=a.Rsquared.Ordinary;
   end

   no=t-1;
   Mo=(y(no)-y(STP))/(.01*(x(no)-x(STP)));
   MD{R,C}=Mo;

   if (mod(i,3)==0) && (i<(n/2))
      plot(x,y);
      plot([x(STP) x(no)],[y(STP) y(no)],'--r');
      figure;
      MD{R,C+1}=mean(double([MD{R,1} MD{R,2} MD{R,3}]));
      MD{R,C+2}=std(double([MD{R,1} MD{R,2} MD{R,3}]));
      R=R+1;
      C=1;

   else
      hold on
      plot(x,y);
      plot([x(1) x(no)],[y(1) y(no)],'--r');
      C=C+1;
   end
end
MD{R,4}=mean(double([MD{R,1} MD{R,2} MD{R,3}]));
MD{R,5}=std(double([MD{R,1} MD{R,2} MD{R,3}]));
MD
xlswrite('PU_LCGO_Modulusfile.xlsx',MD,'Sheet2','B2:F7');
```

Appendix III: MATLAB to calculate Young's modulus for BNNP/PU composite fibres

```
clear,clc;
close all;
commandwindow;
TT=[];
aT=xlsread('PU_BN_Modulusfile.xlsx','Sheet1','A4:AD4000');
[m n]=size(aT);
STP=10;
MD=cell(6,5);
MD{1,4}='Average(MPa)';
MD{1,5}='STD';
R=2;
C=1;
for i=1:n/2
   A=aT(:,(2*i-1):2*i);
   x=A(:,1);
   x(isnan(x))=[];
   y=A(:,2);
   y(isnan(y))=[];
   y=smooth(y,10);

   t=STP+1;
   a=fitlm(x(STP:t),y(STP:t));
   Tr=a.Rsquared.Ordinary;
   while (Tr>0.990) || (t-STP<5)
      TT=[TT Tr];
      t=t+1;
      a=fitlm(x(STP:t),y(STP:t));
      Tr=a.Rsquared.Ordinary;
   end
   no=t-1;
   Mo=(y(no)-y(STP))/(.01*(x(no)-x(STP)));
   MD{R,C}=Mo;

   if (mod(i,3)==0) && (i<(n/2))
      plot(x,y);
      plot([x(STP) x(no)],[y(STP) y(no)],'--r');
      figure;
      MD{R,C+1}=mean(double([MD{R,1} MD{R,2} MD{R,3}]));
      MD{R,C+2}=std(double([MD{R,1} MD{R,2} MD{R,3}]));
      R=R+1;
      C=1;

   else
      hold on
      plot(x,y);
      plot([x(1) x(no)],[y(1) y(no)],'--r');
      C=C+1;
   end


end
MD{R,4}=mean(double([MD{R,1} MD{R,2} MD{R,3}]));
MD{R,5}=std(double([MD{R,1} MD{R,2} MD{R,3}]));
MD
xlswrite('PU_BN_Modulusfile.xlsx',MD,'Sheet2','B2:F7');
```

Appendix IV: Manuscripts prepared (or submitted)

1. **Farajikhah, S.**; Cabot, J. M.; Innis, P. C.; Paull, B.; Wallace, G. G. Life-saving threads; advances in textile-based analytical devices. *ACS Applied Materials and Interfaces (under review).*

Abstract: Novel approaches that incorporate electrofluidic and microfluidic technologies are reviewed to illustrate the translation of traditional enclosed structures into open and accessible textile based platforms. Through the utilisation of on-fibre and on-textile separations it is possible to invert the enclosed capillary column or microfluidic "chip" platform, to achieve efficient surface accessible separations whilst maintaining a microfluidic format. The open fibre/textile arrangement immediately provides new possibilities to interrogate, manipulate, redirect, extract, characterise and quantify solutes and target species at any point in time during analyte separation. This approach is revolutionary in its approach, and provides many potential advantages not otherwise afforded by the more traditional platform.

2. **Farajikhah, S.**; Talebian, S.; Sayyar, S.; Cabot, J. M.; Innis, P. C.; Paull, B.; Wallace, G. G. Insight into the Effect of Surface Chemistry on the Performance of Textile-Based Microfluidics; Route Towards Making Power-Free Textile-based Microfluidic Pump. Prepared for submission to *Adv. Func. Mater.*

Abstract: Microfluidic pumps to obtain controlled movement of fluids are essential components for making all sorts of microfluidic devices such as integrated lab-on-a-chip devices, medical devices, etc. Difficulties encountered with miniaturization of conventional microfluidic pumps have raised a great deal of attention towards development of pumps, which eliminates the need for an external power source and problems associated with bubbles. In this work, for the first time a power-free knitted 3D textile-based microfluidic pump has been manufactured. This pump incorporates polyester yarns and a composite low-density polyethylene (LDPE) - liquid crystalline graphene oxide (LCGO) fibre. The addition of LCGO increases surface polarity causing a decrease in the capillarity pressure and therefore higher capillary force along the channel of the knitted structure. Composite fibers were produced via a twin-screw melt extrusion approach to produce ca. 131 ± 17 μm fibers consisting of LDPE as matrix with a LCGO filler from 0 to 5 w/w%. This system eliminated the need for any external power supplies. Fluid was shown to move up to 6x faster in 3D knitted structures comprised of composite fibre when compare to 3D knitted structure prepared from polyester yarns only (without any composite fibre). Most significantly, the flow rate achievable was found to be proportional to the LCGO loading, providing the potential to control flow through fibre composition.

3. **Farajikhah, S.**; Van Amber, R. R.; Sayyar, S.; Shafei, S.; Fay, C.; Beirne, S.; Javadi, M.; Wang X.; Innis, P. C.; Paull, B.; Wallace, G. G. Processable Thermally Conducting Polyurethane Composite Fibres. Prepared for submission to *Small.*

Abstract: Increasing demand for wearable electronics and smart textiles leads to a great deal of attention into development of electrically conducting fibres. Although, tremendous efforts have been made to present electrically conducting fibres incorporable into garment, production of processable thermally conducting fibres is almost neglected. Owing to very rapid development of miniaturized wearable electronic devices, making thermally conducting fibres to be used for as heat sinks for heat management of such devices is inevitable. In this study, thermally conducting and electrically insulating boron nitride nanopowder (BNNP) fillers have been used to effectively enhance the thermal conductivity and mechanical properties of the polyurethane polymer fibres. Thermal conductivity enhancement of more than 160 % is achieved by very low loading of BNNP

(less than 5 wt.%). Proposed thermally conducting fibres are also incorporated into 3D textile structures as a proof of processability.

4. **Farajikhah, S.**; Van Amber, R. R.; Sayyar, S.; Shafei, S.;Wu, L.; Wang X.; Innis, P. C.; Paull, B.; Wallace, G. G. Utilizing Thermally Conductive Fibers to Facilitate Joule-Heating Dissipation in Textile-Based Microfluidic Devices; a Comparative Study on Boron Nitride- and Graphene Oxide-Filled Fibres. Under preparation for submission to *Adv. Func. Mater.*

Abstract: For the first time fabrication of a 3D textile structure using thermally conducting liquid crystal graphene oxide (LCGO)- and boron nitride nanopowder (BNNP)-filled composite fibres combined with polyester threads as a useful solution to dissipate the heat and minimize Joule-heating effects during analytical experiments such as textile based electrophoretic separations is reported. A range of electric fields are applied to the knitted structures, assembled from these fibres and yams, and current and system's temperature are tracked. In unmodified textile structures the presence of a Joule-heating effect results in increase the system's temperature. The addition of the thermally conductive composite fibres into 3D PET structure resulted in a minimization of the Joule-heating effects resulting in the lower temperature rise compare to that of 3D structures without thermally conducting fibres. Moreover, spherical geometry of BNNP fillers along with their very high (~ 5 eV) band gap make them great candidates for production of thermally conducting fibres to dissipate Joule-heating in experiments like textile-based electrophoretic separations.

5. **Farajikhah, S.**; Choi, J.; Esrafilzadeh, D.; Underwood, J.; Innis, P. C.; Paull, B.; Wallace, G. G. 3D textile structures with integrated electroactive electrodes for wearable electrochemical sensors. Prepared for submission to *Analyst.*

Abstract: Owing to rapid changes in life style, there is an ever growing attention towards low-cost wearable electrochemical sensors. In this paper, textile fabrication techniques as low-cost production methods have been proposed to make textile-based platforms with integrated electroactive electrodes for making low cost wearable electrochemical sensing devices.